# A Quantitative approach to EHD friction prediction based on rheometry and molecular dynamics simulations

Ruibin Xu

N° d'ordre : 2023ISAL0086

**THESE de DOCTORAT DE L'INSA LYON,**
**membre de l'Universié de Lyon**

**École Doctorale** N°ED162
**Mécanique, Énergétique, Génie Civil et Acoustique (MEGA)**

**Spécialité/ discipline de doctorat :**
Génie Mécanique

Soutenue publiquement le 10 Novembre 2023, par :
**Ruibin XU**

# A Quantitative Approach to EHD Friction Prediction Based on Rheometry and Molecular Dynamics Simulations

Devant le jury composé de :

| | | | |
|---|---|---|---|
| Ashlie MARTINI | Professeur | University of California Merced - USA | Rapporteure |
| Gerhard POLL | Professeur | Leibniz University Hannover - Germany | Rapporteur |
| Norbert BADER | Maître de Conférences | University of Twente - Netherlands | Examinateur |
| Noël BRUNETIERE | Directeur de Recherhce | CNRS-Université de Poitiers-ISAE ENSMA | Examinateur |
| Nicolas FILLOT | Professeur | INSA Lyon | Directeur de thèse |
| Laetitia MARTINIE | Maître de Conférences | INSA Lyon | Co-directrice de thèse |

## Département FEDORA – INSA Lyon - Ecoles Doctorales

| SIGLE | ECOLE DOCTORALE | NOM ET COORDONNEES DU RESPONSABLE |
|---|---|---|
| CHIMIE | **CHIMIE DE LYON**<br>**https://www.edchimie-lyon.fr**<br>Sec. : Renée EL MELHEM<br>Bât. Blaise PASCAL, 3e étage<br>secretariat@edchimie-lyon.fr | **M. Stéphane DANIELE**<br>C2P2-CPE LYON-UMR 5265<br>Bâtiment F308, BP 2077<br>43 Boulevard du 11 novembre 1918<br>69616 Villeurbanne<br>**directeur@edchimie-lyon.fr** |
| E.E.A. | **ÉLECTRONIQUE, ÉLECTROTECHNIQUE, AUTOMATIQUE**<br>**https://edeea.universite-lyon.fr**<br>Sec. : Stéphanie CAUVIN<br>Bâtiment Direction INSA Lyon<br>Tél : 04.72.43.71.70<br>secretariat.edeea@insa-lyon.fr | **M. Philippe DELACHARTRE**<br>INSA LYON<br>Laboratoire CREATIS<br>Bâtiment Blaise Pascal, 7 avenue Jean Capelle<br>69621 Villeurbanne CEDEX<br>Tél : 04.72.43.88.63<br>**philippe.delachartre@insa-lyon.fr** |
| E2M2 | **ÉVOLUTION, ÉCOSYSTÈME, MICROBIOLOGIE, MODÉLISATION**<br>**http://e2m2.universite-lyon.fr**<br>Sec. : Bénédicte LANZA<br>Bât. Atrium, UCB Lyon 1<br>Tél : 04.72.44.83.62<br>secretariat.e2m2@univ-lyon1.fr | **Mme Sandrine CHARLES**<br>Université Claude Bernard Lyon 1<br>UFR Biosciences<br>Bâtiment Mendel<br>43, boulevard du 11 Novembre 1918<br>69622 Villeurbanne CEDEX<br>**sandrine.charles@univ-lyon1.fr** |
| EDISS | **INTERDISCIPLINAIRE SCIENCES-SANTÉ**<br>**http://ediss.universite-lyon.fr**<br>Sec. : Bénédicte LANZA<br>Bât. Atrium, UCB Lyon 1<br>Tél : 04.72.44.83.62<br>secretariat.ediss@univ-lyon1.fr | **Mme Sylvie RICARD-BLUM**<br>Institut de Chimie et Biochimie Moléculaires et Supramoléculaires (ICBMS) - UMR 5246 CNRS - Université Lyon 1<br>Bâtiment Raulin - 2ème étage Nord<br>43 Boulevard du 11 novembre 1918<br>69622 Villeurbanne Cedex<br>Tél : +33(0)4 72 44 82 32<br>**sylvie.ricard-blum@univ-lyon1.fr** |
| INFOMATHS | **INFORMATIQUE ET MATHÉMATIQUES**<br>**http://edinfomaths.universite-lyon.fr**<br>Sec. : Renée EL MELHEM<br>Bât. Blaise PASCAL, 3e étage<br>Tél : 04.72.43.80.46<br>infomaths@univ-lyon1.fr | **M. Hamamache KHEDDOUCI**<br>Université Claude Bernard Lyon 1<br>Bât. Nautibus<br>43, Boulevard du 11 novembre 1918<br>69 622 Villeurbanne Cedex France<br>Tél : 04.72.44.83.69<br>**hamamache.kheddouci@univ-lyon1.fr** |
| Matériaux | **MATÉRIAUX DE LYON**<br>**http://ed34.universite-lyon.fr**<br>Sec. : Yann DE ORDENANA<br>Tél : 04.72.18.62.44<br>yann.de-ordenana@ec-lyon.fr | **M. Stéphane BENAYOUN**<br>Ecole Centrale de Lyon<br>Laboratoire LTDS<br>36 avenue Guy de Collongue<br>69134 Ecully CEDEX<br>Tél : 04.72.18.64.37<br>**stephane.benayoun@ec-lyon.fr** |
| MEGA | **MÉCANIQUE, ÉNERGÉTIQUE, GÉNIE CIVIL, ACOUSTIQUE**<br>**http://edmega.universite-lyon.fr**<br>Sec. : Stéphanie CAUVIN<br>Tél : 04.72.43.71.70<br>Bâtiment Direction INSA Lyon<br>mega@insa-lyon.fr | **M. Jocelyn BONJOUR**<br>INSA Lyon<br>Laboratoire CETHIL<br>Bâtiment Sadi-Carnot<br>9, rue de la Physique<br>69621 Villeurbanne CEDEX<br>**jocelyn.bonjour@insa-lyon.fr** |
| ScSo | **ScSo***<br>**https://edsciencessociales.universite-lyon.fr**<br>Sec. : Mélina FAVETON<br>INSA : J.Y. TOUSSAINT<br>Tél : 04.78.69.77.79<br>melina.faveton@univ-lyon2.fr | **M. Bruno MILLY**<br>Université Lumière Lyon 2<br>86 Rue Pasteur<br>69365 Lyon CEDEX 07<br>**bruno.milly@univ-lyon2.fr** |

*ScSo : Histoire, Géographie, Aménagement, Urbanisme, Archéologie, Science politique, Sociologie, Anthropologie

# Contents

## Abstract

This thesis presents a quantitative approach to elastohydrodynamic (EHD) friction prediction, based on a combination of experimental rheometry data and molecular dynamics (MD) simulations. The approach is applied to two fluids of different natures: a lubricant squalane (SQ) and a traction-like fluid benzyl benzoate (BB). The Newtonian viscosity of the fluids is determined using measurements from high-pressure viscometers (HPV) taken from the literature, and a novel Newtonian viscosity model is proposed in this work, which is based on an existing thermal scaling model in the literature. Subsequently, a comprehensive Eyring stress law, covering a wide range of temperature and pressure conditions, is constructed from non-equilibrium molecular dynamics (NEMD) simulations. The obtained Newtonian viscosity and Eyring stress are used to build Eyring-type generalised viscosity models for both fluids. These are implemented into a finite element (FE) model of a lubricated contact in the elastohydrodynamic regime, taking into account non-Newtonian and thermal effects (TEHLnN) for friction prediction. The results are compared with friction measurements performed in a tribometer under the same contact conditions and show good agreement. Notably, the friction plateau and the thermal thinning regime observed experimentally are accurately reproduced by the TEHLnN model. Further research was carried out to investigate the origin of friction plateaus. The results suggest that friction plateaus result from a combination of non-Newtonian effects and thermal effects. The work also reveals that the thermal effect arises almost simultaneously with the non-Newtonian effect. This work presents a crucial step towards "true" friction prediction and quantitative EHL, bringing together experimental rheometry, molecular dynamics simulations, and contact modelling.



**Keywords**: EHD friction, Friction plateau, Eyring model, Molecular dynamics (MD) simulations

## Résumé

Cette thèse présente une approche quantitative de la prédiction du frottement élastohydrodynamique (EHD), basée sur une combinaison de données expérimentales de rhéométrie et de simulations de dynamique moléculaire (MD). L'approche est appliquée à deux fluides de natures différentes : un lubrifiant, le squalane (SQ), et un fluide de type traction, le benzoate de benzyle (BB). La viscosité newtonienne des fluides est déterminée en utilisant des mesures de viscosimètres à haute pression (HPV) tirées de la littérature, ainsi qu'un nouveau modèle de viscosité newtonienne proposé dans ce travail, basé sur un modèle de mise à l'échelle thermique existant dans la littérature. Par la suite, une loi de contrainte d'Eyring complète, couvrant une large gamme de conditions de température et de pression, est construite à partir de simulations de dynamique moléculaire hors équilibre (NEMD). La viscosité newtonienne obtenue et la contrainte d'Eyring sont utilisées pour construire des modèles de viscosité généralisée de type Eyring pour les deux fluides. Celles-ci sont implémentées dans un modèle à éléments finis (FE) d'un contact lubrifié dans le régime élastohydrodynamique, en prenant en compte les effets non-Newtoniens et thermiques (TEHLnN) pour la prédiction du frottement. Les résultats sont comparés avec des mesures de frottement effectuées dans un tribomètre sous les mêmes conditions de contact et montrent une bonne concordance. Notamment, le plateau de frottement et le régime d'amincissement thermique observés expérimentalement sont reproduits avec précision par le modèle TEHLnN. Des recherches supplémentaires ont été menées pour étudier l'origine des plateaux de frottement. Les résultats suggèrent que les plateaux de frottement résultent d'une combinaison d'effets non-Newtoniens et thermiques. Les travaux révèlent également que l'effet thermique se produit presque simultanément avec l'effet non newtonien. Ce travail représente une étape cruciale vers une prédiction quantitative du frottement, en rassemblant la rhéométrie expérimentale, les simulations de dynamique moléculaire et la modélisation du contact.



**Mots clés** : Frottement EHD, Plateau de frottement, Modèle Eyring, Simulations dynamique moléculaire (DM)

# Résumé étendu

## Introduction et objectifs

Le transport et l'industrie consomment les deux tiers de l'énergie totale consommée chaque année [1]. Parmi eux, la surmontée du frottement représente la plus grande partie de la consommation d'énergie, soit entre 25 à 30% dans les transports, tandis que dans l'industrie, elle est d'environ 15 à 20% [1]. Réduire les pertes par frottement entraînerait d'importantes économies d'énergie, avec des avantages économiques et environnementaux en résultant. Sur une période supplémentaire de 15 à 20 ans, on estime que les pertes par frottement pourraient être réduites de plus de 60%, économisant 385 000 millions de litres de carburant et réduisant les émissions de $CO_2$ de 960 millions de tonnes par an [2, 3].

Les roulements à éléments roulants (REBs) sont un composant mécanique couramment utilisé conçu pour minimiser le frottement dans les articulations pivotantes. Les REBs modernes (voir Figure 1) sont généralement composés des éléments suivants : deux anneaux disposés en cercles concentriques (connus sous le nom d'anneau intérieur et d'anneau extérieur), des éléments roulants positionnés entre les anneaux, et une cage pour guider ces éléments roulants. Les REBs transmettent la charge en mouvement à travers ces éléments roulants. Ces éléments induisent un frottement roulant, qui remplace le frottement glissant, le premier étant généralement bien moindre que le second sous des charges équivalentes.

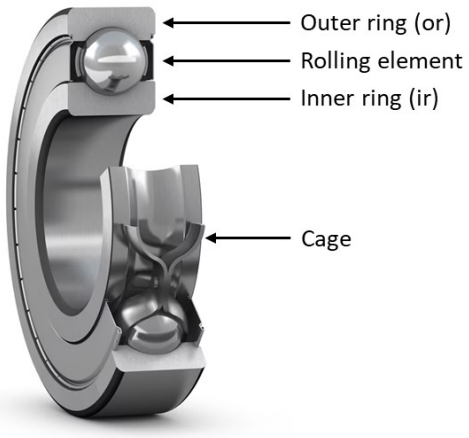


Figure 1: Les roulements à billes à gorges profondes. Source:https://www.skf.com/us/products/rolling-bearings/ball-bearings/deep-groove-ball-bearings.

En plus des problèmes environnementaux mentionnés ci-dessus, il existe également une motivation économique. Le marché mondial des roulements a été évalué à 118,7 milliards de dollars américains en 2020 et devrait croître à un taux de croissance annuel composé de 8,5% de 2021 à 2028 (voir Figure 2).

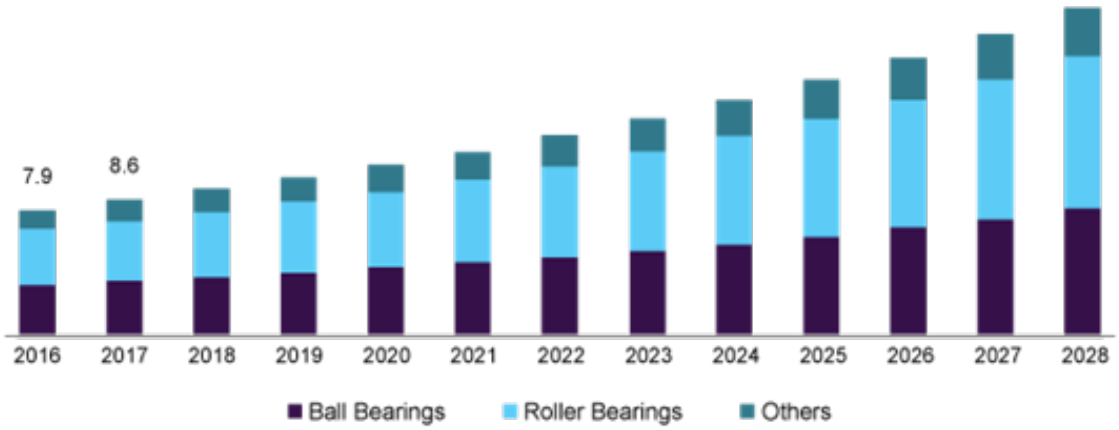


Figure 2: Marché allemand des roulements par produit, 2016-2028 (en milliards USD). Source:www.grandviewresearch.com/industry-analysis/bearings-market.

La demande de roulements à faible maintenance, à haut rendement et à longue durée de vie croît avec le marché. Il est donc important de disposer de modèles de prédiction du frottement fiables et pertinents pour optimiser la conception des roulements et réduire les pertes par frottement.

Dans la plupart des roulements, le contact entre des surfaces non conformes fonctionne sous le régime de lubrification élastohydrodynamique (EHL), où un film de lubrifiant très mince (environ 100 nm) sépare les surfaces et est soumis à une très haute pression ($> 1$ GPa). Dans ces conditions, le taux de cisaillement peut atteindre des valeurs élevées ($10^4 - 10^7\ s^{-1}$), et la haute pression augmente considérablement la viscosité du lubrifiant. De plus, la pression dans le contact EHL n'est pas uniformément répartie à travers le film (voir la ligne noire dans la Figure 3). Les deux créent également un échauffement par cisaillement significatif et non uniforme, résultant en un grand gradient de température à travers le film (voir la ligne rouge dans la Figure 3). Toutes ces complexités engendrent plusieurs difficultés dans la prédiction du frottement. Premièrement, il y a un manque de caractérisation expérimentale des propriétés du lubrifiant sous de telles conditions extrêmes (c'est-à-dire haute pression, taux de cisaillement élevé). Deuxièmement, les phénomènes physiques associés à ces conditions sévères ne sont pas totalement compris (c'est-à-dire d'éventuelles transitions de phase, mécanisme d'accommodation de vitesse) et le couplage complexe des conditions de fonctionnement en contact rend difficile l'interprétation du résultat et la déduction d'une compréhension de la mécanique. Cependant, la construction de modèles pertinents et robustes (c'est-à-dire non empiriques) doit être basée sur une compréhension complète de la mécanique de contact.

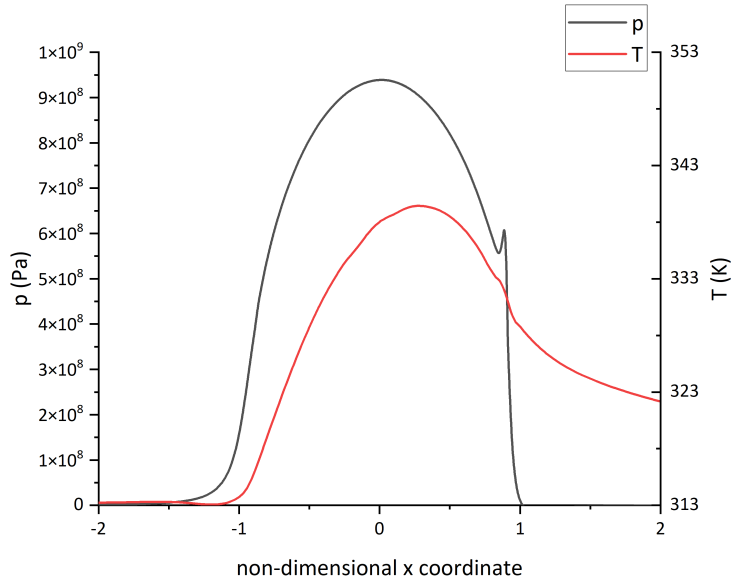


Figure 3: Distributions typiques de la pression (ligne noire) et de la température (ligne rouge) dans un contact EHD. Résultats de la simulation d'un contact acier-acier lubrifié au squalane, à la température ambiante $T_0$=313K, pression hertzienne $p_h$=900MPa, vitesse d'entraînement $u_e$=0,8$^m/_s$ et slide-to-roll ratio=0,6.

## Objectifs

L'objectif principal de cette recherche est de proposer une stratégie pour parvenir à une prédiction quantitative du frottement dans le régime EHL. La complexité de cette tâche provient des conditions extrêmes de pression, d'épaisseur du film, de taux de cisaillement, d'échauffement par cisaillement, et du fort couplage entre ces conditions de fonctionnement. Expérimentalement, les méthodes de caractérisation rhéologique sont limitées à des gammes restreintes de pression et de taux de cisaillement. Les simulations de dynamique moléculaire semblent être une approche prometteuse pour combler le manque en caractérisation des fluides, mais elles sont limitées en termes de temps de calcul et de complexité de la composition chimique du lubrifiant. Le défi réside dans l'intégration des caractérisations expérimentales et numérique (dynamique moléculaire) des lubrifiants (sous haute pression et haut taux de cisaillement à diverses températures) dans un modèle numérique basé sur la mécanique des milieux continus des contacts EHD. Ce modèle doit prendre en compte la génération et le transfert de chaleur au sein du lubrifiant et vers les surfaces.

Cette thèse se compose de quatre chapitres. Dans le **Chapitre 1**, l'état de l'art des méthodes existantes de prédiction de frottement est examiné. Dans le **Chapitre 2**, la stratégie et les outils de l'approche actuelle sont détaillés. Tout d'abord, les mesures expérimentales et les simulations de dynamique moléculaire (MD) sont décrites pour fournir une stratégie de caractérisation du fluide. Ensuite, un modèle de contact basé sur la mécanique des milieux continus est construit.Dans le **Chapitre 3**, les résultats de la caractérisation du fluide sont présentés. La loi rhéologique est dérivée des données obtenues. Dans le **Chapitre 4**, le frottement d'un contact EHD thermique non-Newtonien est prédit, et comparé aux mesures de frottement sur des bancs d'essai expérimentaux.

# Etat de l'art

## Comportement de frottement en régime EHD

La présente étude se concentre sur le frottement en régime de lubrification à film complet. Dans un tel régime, lorsque la pression dans le contact devient suffisamment élevée (jusqu'à 3 GPa) pour déformer significativement les surfaces (quelques micromètres), on parle de régime de lubrification élastohydrodynamique (EHD). La haute pression entraîne un changement significatif de la viscosité du lubrifiant [4]. Comme c'est le cas pour les contacts secs, le frottement dû au cisaillement du lubrifiant dans le contact EHD à film complet est généralement quantifié par le coefficient de frottement $C_f$, défini comme le rapport entre la force tangentielle $F_T$ (opposée au glissement) et la charge normale appliquée $F_N$.

$$C_f = \frac{F_T}{F_N} \tag{1}$$

Le rapport de glissement à roulement (slide-to-roll ratio, SRR) est souvent utilisé en parallèle avec le coefficient de frottement. Lorsque $C_f$ est tracé par rapport au SRR sur le même graphique, comme le montre la Figure 4, on peut observer que le frottement traverse différents régimes à mesure que le SRR augmente. À faible SRR, le frottement augmente presque linéairement avec le SRR, ce qui est souvent attribué à la réponse Newtonienne du lubrifiant. Cette dépendance linéaire persiste jusqu'à ce que le coefficient de frottement atteigne une valeur critique. Ensuite, le coefficient de frottement augmente plus lentement avec le SRR. Cela indique que le frottement passe par un régime de fluidification sous contrainte. Enfin, à des SRR très élevés, une baisse significative du coefficient de frottement peut être observée. Cela est dû au chauffage par cisaillement, impliquant une augmentation de la température dans le film de fluide. Ce dernier régime est connu sous le nom de régime de fluidification thermique (thermal thinning).

Cependant, à des SRR modérés à élevés, le coefficient de frottement peut atteindre une valeur maximale et peut présenter un régime de plateau, comme le montre le centre de la Figure 4. Cela signifie que le coefficient de frottement ne augmente plus avec le SRR, mais en devient indépendant. À partir de cette force de frottement maximale, une contrainte de cisaillement moyenne maximale $\tau_L$ peut être déduite. Dans la littérature, ce plateau de frottement est parfois appelé phénomène de "contrainte de cisaillement limite" (limiting shear stress, LSS). Le LSS a été proposé pour la première fois par Smith [5]. Il a attribué cela au fait que si la contrainte dans le film de lubrifiant dépasse un seuil, il se "briserait" comme un solide plastique.

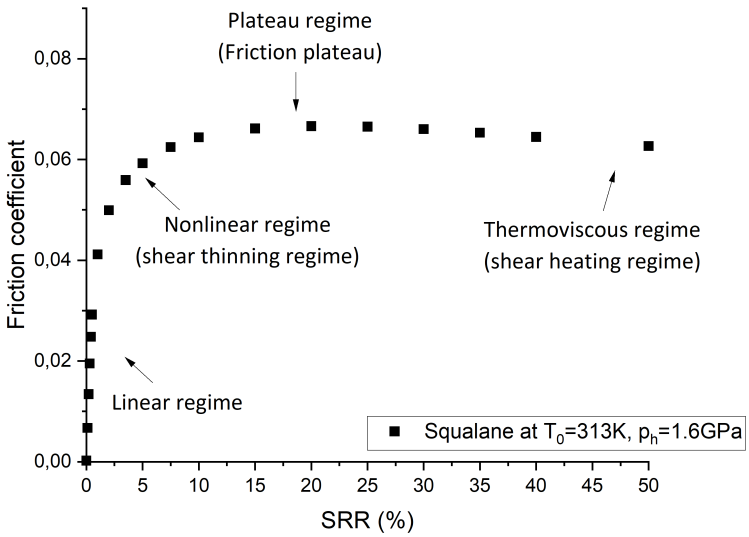


Figure 4: Courbe typique du coefficient de frottement en fonction du TRS. Données expérimentales de la présente étude.

Comme la courbe de frottement, dans la Figure 5, le comportement ultime d'un lubrifiant en masse pourrait apparaître avec une contrainte de cisaillement maximale $\tau_{lim}$ ou $\tau_{LSS}$. Il est important de comprendre et de prédire quantitativement ce phénomène car il représente la contrainte maximale qu'un lubrifiant pourrait supporter localement dans un contact EHD (Élastohydrodynamique).

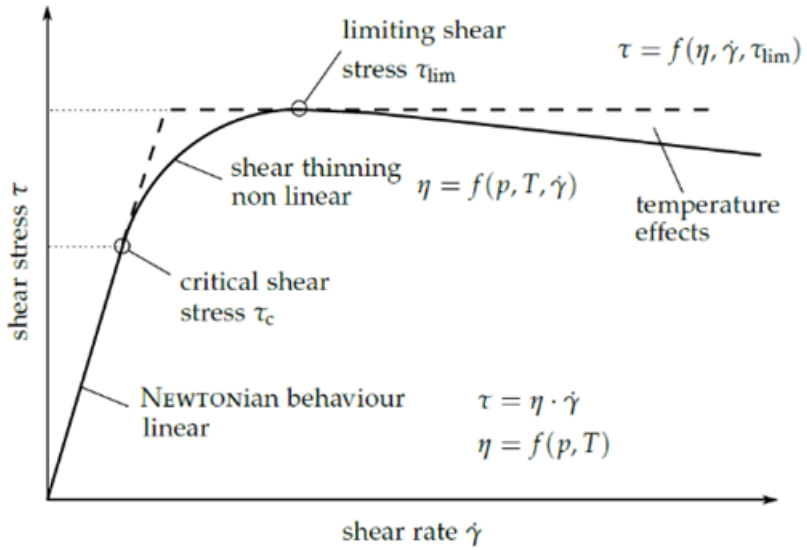


Figure 5: Modèle pour la contrainte de cisaillement et le taux de cisaillement dans un lubrifiant en vrac. Adapté de [6].

Cependant, puisque le frottement est mesuré en contact (tribologie), il devrait être distingué de

la contrainte de cisaillement mesurée dans le fluide en vrac (rhéologie). De plus, malgré certaines similitudes, la viscosité d'un fluide n'est pas toujours équivalente à la viscosité apparente calculée à partir de valeurs moyennes dans des expériences tribologiques. Autrement dit, on ne devrait pas simplement égaler $\tau_a$ (de la Figure 4) à $\tau$ (de la Figure 5), ni égaler $\tau_L$ à $\tau_{LSS}$. Comme le souligne Bair [7], une courbe de contrainte n'est pas une courbe d'écoulement. Et la réponse des fluides au taux de cisaillement n'est pas la même que la relation entre la contrainte de cisaillement moyenne et le taux de cisaillement moyen obtenue à partir de courbes de traction. Cette confusion est largement répandue dans la communauté EHD [8, 9, 10]. LSS décrit une propriété de volume de fluide, qui est une propriété rhéologique mesurée dans un rhéomètre ou équivalent où le fluide est uniformément chargé. Alors que dans un tribomètre, il subit une large répartition de pression. La contrainte mesurée dans un rhéomètre doit être considérée comme la conséquence de la propriété du matériau, la contrainte dérivée du frottement mesuré dans un tribomètre est une valeur moyenne dans tout le contact. Par conséquent, dans cet article, le terme approprié pour décrire cette valeur de frottement limitante est plateau de frottement. Plus important encore, les propriétés rhéologiques du fluide doivent être caractérisées de manière indépendante du contact. Les prédictions de frottement devraient être basées sur ces propriétés a priori.

## Scénario et caractérisation du frottement limité

De nombreuses hypothèses concernant l'origine du plateau de frottement peuvent être trouvées dans la littérature. Trois principales familles d'explications seront présentées :

- la cinématique locale du lubrifiant.
- les propriétés inhérentes du lubrifiant.
- le chauffage visqueux dans le lubrifiant.

Ces scénarios sont déjà détaillés dans les recherches [11, 12].

### Cinématique locale

Une hypothèse pour expliquer l'origine du plateau de frottement est la cinématique locale de l'écoulement du fluide. Cette hypothèse peut être divisée en trois scénarios principaux : a. glissement aux niveau des parois, b. localisation du cisaillement et c. écoulement de type plug. Il est à noter que dans certains scénarios de cinématique locale, la modification de l'écoulement laminaire est induite par la vitrification du lubrifiant. Dans ce cas, le glissement aux niveau des parois et la localisation du cisaillement sont étroitement liés. Dans d'autres cas, elle est induite par la dissipation thermique dans le film de fluide, ce qui relie le glissement aux niveau des parois et écoulement de type plug.

**Glissement aux niveau des parois** L'hypothèse des conditions aux limites sans glissement entre les interfaces liquide-solide est discutable en pratique. Des preuves de glissement aux limites dans les contacts ont été démontrées à la fois expérimentalement [13, 14] et par des simulations de dynamique moléculaire [15, 16] sous des conditions de fonctionnement spécifiques. Schnell [17] a été le premier à démontrer expérimentalement que le glissement aux niveau des parois peut se produire entre une surface hydrophobe et de l'eau. Des études ultérieures ont montré que ce phénomène se produit non seulement dans des fluides simples (par exemple, l'eau et l'hexadécane) [17, 18] mais aussi dans des fluides complexes (par exemple, des polymères) [19], et non seulement sur la surface hydrophobe [17, 20] mais aussi sur la surface lisse, même sous des conditions de mouillage total [19]. Cette observation est étayée par des simulations de dynamique moléculaire [15]. Li et al. [21] ont en outre

suggéré que la longueur de glissement augmente de manière non linéaire avec le taux de cisaillement et exponentiellement avec la pression. Kaneta et al. [22], ont trouvé que le film de lubrifiant présente un comportement solide dans le cas du roulement pur et des preuves de glissement aux niveau des parois se produisent aux, ou près des, interfaces lorsque le film est très mince. Pit et al. [18] soupçonnent que le glissement aux niveau des parois était à l'origine du comportement du plateau de frottement lorsqu'ils ont montré des preuves de glissement aux niveau des parois dans un contact de deux disques de saphir avec de l'hexadécane. Malgré ces preuves, le glissement aux niveau des parois n'a pas été directement observé dans les contacts EHD représentatifs, probablement en raison des temps de transit extrêmes, des faibles épaisseurs de film et de la présence de mouvement relatif au niveau des surfaces de contact.

**Localisation du cisaillement** Le deuxième scénario suppose que le plateau de frottement se produit lorsque la déformation par cisaillement devient localisée et forme des bandes de cisaillement dans le film de lubrifiant. Plint [23] a été le premier à utiliser la localisation du cisaillement pour expliquer le plateau de frottement. Des observations de localisation thermique ont été faites par Bair et al. en 1993 [24] dans des cellules de visualisation d'écoulement à haute pression, c'est-à-dire en dehors du contact. Tandis que les résultats expérimentaux récents ont identifié la localisation du cisaillement isothermique [25]. Bair et McCabe [26] montrent que deux types de bandes de cisaillement peuvent être observées, l'une alignée avec la direction de l'écoulement et l'autre alignée avec la direction transversale au film. La contrainte de cisaillement dans le film de lubrifiant pourrait être inégalement répartie en raison de la génération de chaleur, et ainsi la contrainte serait "localisée" et formerait une bande de cisaillement. Cela devrait être dû à la forte dépendance entre la viscosité du lubrifiant et la température ainsi qu'à la faible conductivité thermique des lubrifiants. Cela entraîne un gradient de température dans le film de lubrifiant, ce qui peut conduire à un cisaillement inhomogène. Ils ont pu distinguer deux types de bandes de cisaillement, induites thermiquement et induites mécaniquement, en fonction des conditions de fonctionnement. Néanmoins, Bair n'a jamais relié ces résultats dans des expériences rhéologiques à ses résultats tribologiques, de sorte qu'ils n'ont pas pu être utilisés pour expliquer la formation de plateaux de frottement. Et ces bandes de cisaillement n'ont jamais été observées dans un contact EHD vivant. Cependant, cela n'empêche pas certains chercheurs de suggérer que la localisation du cisaillement peut provoquer un plateau de frottement [11, 27].

**L'écoulement de type plug** Le dernier scénario a été proposé pour la première fois par Jacobson [28]. Il a suggéré qu'une grande partie du lubrifiant se comporte comme un noyau solide ou plug en raison de sa viscosité extrêmement élevée, tandis qu'une zone très mince près de la surface de contact est cisaillée. Le noyau est dans un état liquide vitreux. Depuis lors, l'existence de ce mécanisme a été démontrée par des résultats expérimentaux obtenus par différentes méthodes, tels que Šperka et al. [29] et Ponjavic et al. [30]. Dans une étude ultérieure utilisant des simulations de dynamique moléculaire, Ewen et al. [31] ont constaté que la présence d'un plateau de frottement s'accompagne d'une transition de la localisation du cisaillement à l'écoulement de type plug. Bien que des recherches supplémentaires soient nécessaires pour confirmer cette relation, l'écoulement de type plug se présente comme un scénario intéressant car il peut faire le lien entre plusieurs scénarios précédemment énoncés. Le noyau est principalement considéré comme étant dans un état vitreux, ce qui en fait un cas de localisation du cisaillement où le cisaillement est localisé dans une zone près de la surface. Et si l'épaisseur de la région de cisaillement devient petite par rapport à la taille moléculaire, elle pourrait être considérée comme un glissement de paroi. Bien qu'il y ait de plus en plus de preuves que les contraintes de cisaillement très élevées dans les contacts EHD produisent des transitions cinématiques locales, ces transitions sont difficiles à caractériser expérimentalement et leur effet sur la réponse au

frottement et le mécanisme physique plus profond ne sont pas bien compris [11, 32]. De plus, ces mécanismes peuvent impliquer d'autres paramètres liés à la complexité du contact. Par exemple, Porras-Vazquez et al. [16] montrent avec des simulations de dynamique moléculaire qu'un changement de rugosité de surface ou de mouillabilité peut changer la cinématique locale. Cependant, si l'épaisseur du film est suffisamment élevée, la réponse à le frottement n'est pas impactée.

**Propriété intrinsèque du lubrifiant : structure moléculaire et changement de phase**

Le plateau de frottement étant une caractéristique inhérente du lubrifiant est l'hypothèse principale répandue dans la littérature [33], mais il existe deux approches qui sont dissociées. Pour certains chercheurs, la génération du plateau de frottement est considérée comme dépendant de la nature du fluide, c'est-à-dire de la structure de la molécule [31, 34]. Alors que pour d'autres, la génération du plateau de frottement dépend de son état thermodynamique [16, 35].

Les résultats de Zhang et al. [34] ont montré que les fluides de traction atteignaient leurs limites sous les conditions de test, tandis que les huiles de base à faible frottement ne le faisaient pas. Ils en ont conclu que la structure moléculaire du fluide de base a un effet significatif sur le frottement dans les contacts EHD. Ewen et al. [31] ont utilisé à la fois des expériences de tribomètre et des simulations de dynamique moléculaire pour étudier deux lubrifiants : le squalane, le DEHS, et deux fluides de traction DM2H, DCMP. Ils ont conclu que le plateau de frottement peut se produire dans les fluides de traction mais pas dans les lubrifiants, et que cette différence est liée à la structure de la molécule.

Cependant, la conjecture de la "propriété intrinsèque" a toujours été contestée par une autre vision légèrement différente selon laquelle la génération du plateau de frottement ne dépend pas de la nature du lubrifiant mais de son état thermodynamique (liquide ou vitreux) [16, 35]. Par conséquent, le plateau de frottement est réalisable sous des conditions thermodynamiques spécifiques quelle que soit la nature du fluide. Ces conditions varient en fonction du lubrifiant. Des études antérieures [36, 37, 38, 39] semblent montrer que la transition vitreuse de la molécule du fluide est une condition nécessaire à l'apparition du plateau de frottement. Pour un fluide de type traction (benzoate de benzyle), Ndiaye et al. [40] ont corrélé la pression à laquelle un plateau de frottement peut être mesuré expérimentalement avec la pression de transition vitreuse nominale du fluide, mesurée dans un volume de fluide [35]. Ils ont montré que pour des pressions hertziennes inférieures à la pression de transition vitreuse du fluide, aucun plateau de frottement n'est observé car la viscosité apparente macroscopique des contacts semble augmenter exponentiellement avec la pression. Dès que la pression hertzienne dépasse la pression de transition vitreuse du lubrifiant, la viscosité apparente du contact se stabilise et les tests de frottement montrent un plateau. Cette corrélation a ensuite été confirmée par Porras-Vasquez et al. [16], qui ont effectué des simulations NEMD sur deux fluides (squalane et benzoate de benzyle) et comparé les résultats numériques avec des mesures expérimentales de frottement. En se basant sur les diagrammes de phase, deux conditions de fonctionnement correspondant soit à un état liquide soit à un état solide sont sélectionnées. Ils ont constaté que pour les deux fluides et dans les simulations numériques comme dans les expériences de tribomètre, aucun plateau de frottement n'était observé dans les conditions de fonctionnement à l'état liquide, mais dans les conditions à l'état solide.

**Effets thermiques**

Des conditions sévères dans le contact EHD peuvent induire une dissipation visqueuse qui augmente localement la température du lubrifiant dans le contact, jusqu'à 100 ℃ localement [41, 42]. Ceci est plus susceptible de se produire lorsque les conditions de contact combinent des facteurs tels qu'une

haute pression allant jusqu'à plusieurs GPa [11], des taux de cisaillement élevés allant jusqu'à $10^7 s^{-1}$ et une haute viscosité du fluide. L'étude des effets thermiques en EHL est apparue pour la première fois dans l'étude de Cheng et al. [43, 44] en 1965, et par la suite, de nombreux auteurs ont proposé différentes explications à la montée de la température dans le film d'huile [45, 46, 47]. L'augmentation de la température dans le contact EHD peut entraîner une diminution significative de la viscosité du fluide. Pourtant, cela a longtemps été négligé dans la littérature. Dans les premières études théoriques sur l'EHL, comme celles de Dowson et Higginson [48] ou Grubin [49], les conséquences des effets thermiques sur la viscosité étaient ignorées et la viscosité dans le film d'huile était supposée dépendre uniquement de la pression. Ce fut Crook [50, 51] en 1961 qui a révélé pour la première fois l'impact du chauffage par cisaillement sur la viscosité des lubrifiants. C'est également Crook [51] qui a établi le premier lien entre le chauffage par cisaillement et le frottement. Il attribue les valeurs maximales de frottement à la réduction de la viscosité due à la génération de chaleur, tandis que la réduction du frottement à des taux de cisaillement très élevés signifie que l'effet thermique devient dominant. Cependant, dans plusieurs études sur le frottement en EHD, les conditions de fonctionnement sont supposées être isothermes. Cela signifie que le chauffage par cisaillement ne peut expliquer le plateau de frottement. Ndiaye [12] a constaté que des plateaux de frottement étaient observés dans des contacts réduisant le chauffage par cisaillement et fonctionnant dans des conditions apparemment isothermes. Il est cependant important de noter qu'ils n'ont pas mesuré ou contrôlé directement la température à l'intérieur du contact, mais ont plutôt contrôlé la température à l'entrée du contact et déterminé la génération de chaleur en surveillant la température de l'huile dans le réservoir. Des preuves plus directes proviennent des simulations. Par exemple, Habchi et al. [52], Porras-Vasquez et al. [16] et Ewen et al. [53] ont réalisé différentes simulations dans un environnement (nominalement) isotherme, et un plateau de frottement a été observé. De plus, les résultats de ces simulations ont été comparés avec succès aux données expérimentales. En conclusion, l'effet du chauffage par cisaillement sur la réponse au frottement reste flou. Actuellement, le chauffage par cisaillement est principalement associé au plateau de frottement dans la théorie de la localisation du cisaillement [23, 24, 25, 26, 54].

### Caractérisation du plateau de frottement

En supposant que le plateau de frottement est une propriété inhérente du fluide et selon ce raccourci que les propriétés rhéologiques du fluide peuvent être obtenues à partir de la courbe de frottement, les chercheurs décrivent directement le plateau de frottement à l'aide de modèles empiriques dérivés d'expériences tribologiques [55, 56, 57, 58, 59, 60, 61, 62, 63, 64]. Cependant, comme ces lois empiriques sont dérivées de la courbe de traction plutôt que de la courbe de flux, elles ne reflètent pas la nature du fluide lui-même, ce qui les empêche d'être de véritables prédictions. Ce type d'approche de prédiction de le frottement est présenté sous la forme classique de l'équation 2.

$$F_T = \tau_a \times S \quad with \quad \begin{cases} \tau_a = \eta\dot{\gamma} & for \quad \eta\dot{\gamma} < \tau_L \\ \tau_a = \tau_L & for \quad \eta\dot{\gamma} > \tau_L \end{cases} \tag{2}$$

Des modèles de $\tau_L$ ou $\tau_{LSS}$ ont été proposés dans la littérature. La plupart des modèles [9, 40, 65, 66, 67, 68] sont dérivés de tests tribologiques tandis que d'autres proviennent de tests rhéologiques [42, 69]. Il semble que la valeur de $\tau_L$ ou $\tau_{LSS}$ dépend de la nature du fluide, de la pression, de la température et probablement aussi de la surface de contact. De plus, la valeur de $\tau_L$ donnée par ces modèles est une valeur unique et intégrée qui ne prend pas en compte la variation locale. Ceci ne peut pas être utilisé pour dériver une méthode de prédiction de frottement généralisée et ne

prend pas en compte les mécanismes physiques derrière les phénomènes limitants de contrainte de cisaillement/frottement.

### Vers une prédiction quantitative du frottement

le frottement dans l'EHL est régie par le comportement rhéologique des lubrifiants. Afin de prédire le frottement, la première exigence est de caractériser avec précision leurs propriétés rhéologiques, en particulier un modèle de viscosité doit être défini.

Dans certains travaux antérieurs [70], les chercheurs ont tenté d'utiliser la viscosité apparente dérivée des tests tribologiques pour caractériser le frottement. À mesure que des mesures de frottement plus précises sont devenues disponibles, ils se sont tournés vers la caractérisation de le frottement directement en ajustant des équations aux courbes de traction [9, 65, 71]. Sur la base de ces caractérisations, de nombreux modèles empiriques ont été développés [57, 58, 59, 72]. Malgré ces efforts, ces méthodes utilisent des données dérivées d'expériences tribologiques pour reproduire la valeur de frottement des mêmes expériences. Ces méthodes fonctionnent a posteriori et leur utilisation est limitée aux conditions de fonctionnement, ce qui rend impossible leur extension à d'autres conditions ou lubrifiants.

Des avancées significatives dans la prédiction de le frottement ont été réalisées depuis l'avènement de la technologie des viscosimètres haute pression pour mesurer les propriétés rhéologiques des fluides en vrac. En utilisant ces données indépendantes du contact, les chercheurs ont réussi à prédire le frottement EHD à la fois dans des environnements isothermes [60, 61, 62, 73] et thermiques [63] dans les régimes newtoniens et de cisaillement mince. Ces travaux pionniers ont inspiré de nombreuses études ultérieures sur le contact EHD thermique, telles que [56, 55, 74, 75]. Malgré la qualité des résultats obtenus, un inconvénient typique de ces approches de prédiction est l'incapacité à prédire le plateau de frottement. Par conséquent, les modèles de plateau de frottement dérivés des résultats de l'expérience tribologique sont généralement utilisés pour ajouter manuellement une limite supérieure et reproduire les courbes de frottement expérimentales.

À ce stade, nous pouvons résumer les principaux inconvénients des approches existantes pour prédire le frottement comme suit :

- Elles sont basées sur l'hypothèse que les plateaux de frottement sont un comportement intrinsèque du fluide, sur lequel il n'y a pas de consensus.
- Ces modèles de plateau de frottement sont purement empiriques, dérivés de données dépendantes du contact. Ce qui ne prend pas en compte la complexité du contact réel et n'est pas prédictif. Pour faire une véritable prédiction de le frottement, la première exigence est de déterminer les propriétés rhéologiques des fluides a priori, et cette détermination doit être indépendante du contact.

En raison des défis expérimentaux associés à la caractérisation des fluides sur des rhéomètres indépendants dans des conditions similaires à un contact EHL (pression et cisaillement extrêmes), les simulations numériques comme la dynamique moléculaire présentent une opportunité intéressante.

D'autre part, il y a deux modèles de viscosité généralisés les plus utilisés dans la littérature, à savoir le modèle de Carreau [76] (Équation 3) et le modèle d'Eyring [77] (Équation 1.9).

$$\eta = \eta_N \left(1 + \frac{\dot{\gamma}^2}{\dot{\gamma}_c}\right)^{\frac{N-1}{2}} \tag{3}$$

$$\eta = \frac{\tau_e}{\dot{\gamma}} \sinh^{-1}\left(\frac{\eta_N \dot{\gamma}}{\tau_e}\right) \tag{4}$$

Selon [78], le modèle de Carreau s'ajuste très bien aux données MD tant que $\eta_N$ (la soi-disant "viscosité Newtonienne"), la vitesse de cisaillement critique $\dot{\gamma}_c$, et l'exposant de Carreau $N$ varient avec la pression et la température. Cela contraste avec la littérature précédente où le modèle de Carreau était utilisé avec des $\dot{\gamma}_c$ et des $N$ constants [79]. Pendant ce temps, dans [80], la viscosité du squalane est caractérisée en utilisant des données MD et des résultats ajustés avec le modèle d'Eyring sur une large gamme de pressions, de températures et de vitesses de cisaillement. Dans leur approche, deux paramètres d'ajustement de la loi d'Eyring ont été déterminés, à savoir $\eta_N$ et la contrainte d'Eyring $\tau_e$.

Ces résultats fournissent une voie potentielle pour décrire avec précision la rhéologie des fluides dans des conditions EHL. Par conséquent, une caractérisation a priori de la rhéologie des fluides est cruciale. Cela inclut la viscosité Newtonienne ($\eta_N$), la vitesse de cisaillement critique ($\dot{\gamma}_c$), la contrainte d'Eyring ($\tau_e$), et éventuellement l'exposant de Carreau (selon le modèle utilisé), et leurs variations avec la pression, la température et la vitesse de cisaillement. Celles-ci pourraient être réalisées avec l'aide de simulations MD et constitueraient un complément idéal aux approches expérimentales. Ensemble, ils pourraient former la base d'une approche de caractérisation de fluide quantitative pour capturer le comportement intrinsèque du fluide, indépendamment des expériences de tribologie.

Enfin, pour s'aligner avec les mesures expérimentales de frottement, un modèle de prédiction de frottement quantitatif devrait incorporer le comportement rhéologique intrinsèque précédemment défini du lubrifiant et prendre en compte la distribution de la pression et de la température sur la zone de contact. Cela peut être réalisé en résolvant les relations d'équilibre de la mécanique des milieux continus (masse, force, équilibre énergétique) à l'intérieur et autour du contact, comme décrit dans [55, 61, 74].

# Strategie et methodologie

## Stratégie

L'approche proposée pour la prédiction de le frottement se compose de deux parties : (I) la caractérisation numérique des propriétés rhéologiques des fluides à l'échelle moléculaire et (II) la mise en œuvre de ces propriétés dans un modèle de continuum à l'échelle du contact. La première partie implique de prédire les propriétés intrinsèques des fluides dans un environnement isotherme et isobare à l'aide de simulations de dynamique moléculaire (MD). La seconde, à l'échelle de la zone de contact, prend en compte la répartition des paramètres de fonctionnement tels que la pression, la température et l'épaisseur du film. Un modèle de contact par éléments finis (FE) est construit pour simuler un contact ponctuel EHD réaliste en tenant compte de l'effet thermique et des lubrifiants non-newtoniens. Cela devrait conduire à une prédiction numérique de le frottement comparable aux mesures expérimentales sur des tribomètres.

### Choix du modèle rhéologique

L'une des approches classiques pour modéliser la rhéologie non Newtonienne dans la littérature utilise les modèles de type Carreau [56, 60, 61, 63, 73], qui décrivent adéquatement le régime linéaire et de fluage, mais échouent à capturer le régime de plateau tant que le taux de cisaillement critique $\dot{\gamma}_c$ et l'exposant de Carreau $N$ sont choisis comme constants.

D'un autre côté, le modèle d'Eyring est basé sur le concept d'activation thermique. Les modèles macroscopiques reliant le comportement à l'échelle moléculaire à le frottement macroscopique ont été initiés par les travaux de Prandtl [81, 82] et Eyring [77], où les deux auteurs ont développé indépendamment leur théorie sur le même concept : le taux d'un processus dépend de l'énergie thermique possédée par un atome ou une molécule et des forces mécaniques qui lui sont appliquées. Parce que cette approche combine les énergies mécaniques et thermiques, elle est connue sous le nom de concept de "l'activation thermique augmentée par contrainte", ou concept SATA.

### Modèle Eyring

Henry Eyring a développé son célèbre modèle de viscosité en utilisant le concept SATA en 1936 [77]. Le modèle d'Eyring suppose que le début de l'écoulement est causé par le réarrangement des molécules individuelles d'un plan moléculaire adjacent. La dérivation mathématique de l'équation d'Eyring peut être trouvée dans [70].

L'équation d'Eyring de viscosité et de contrainte de cisaillement est montrée dans l'Equation 5. Le modèle d'Eyring est issu du concept SATA et est remarquablement simple, avec seulement deux paramètres. Cela fait qu'il est largement utilisé par les chercheurs en EHD.

$$\eta = \frac{\tau_e}{\dot{\gamma}} \sinh^{-1}\left(\frac{\eta_N \dot{\gamma}}{\tau_e}\right) \tag{5a}$$

$$\tau = \tau_e \sinh^{-1}\left(\frac{\eta_N \dot{\gamma}}{\tau_e}\right) \tag{5b}$$

Dans ce travail, le modèle d'Eyring est choisi par rapport aux modèles de type Carreau pour deux raisons. La première raison de ce choix est sa forme mathématique, qui tend à décrire un plateau

de contrainte de cisaillement à des taux de cisaillement élevés. Cela peut être mis en évidence en calculant la pente de la viscosité réduite logarithmique $R_{visco}$. Le résultat de $R_{visco}$ en fonction de $\dot{\gamma}_{red.} = \dot{\gamma}/\dot{\gamma}_c$ est montré dans la Figure 6. Les détails du calcul sont fournis dans l'Appendice A.

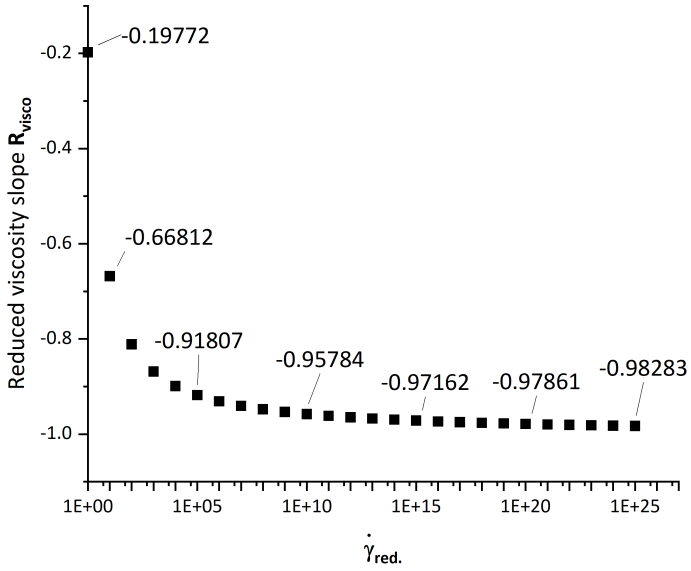


Figure 6: Taux de variation (pente) de la viscosité réduite $\eta_{red.}$ en fonction du taux de cisaillement réduit $\dot{\gamma}_{red.}$.

La figure montre que la pente de la viscosité réduite logarithmique $R_{visco}$ par rapport à $\dot{\gamma}_{red.}$ tend vers -1, ce qui implique que la viscosité devient proportionnelle à $\dot{\gamma}^{-1}$. En conséquence, la contrainte de cisaillement dans le fluide, $\tau = \eta\dot{\gamma}$, tend vers une constante, ce qui est la définition de la contrainte de cisaillement limite. Par conséquent, le modèle d'Eyring est intrinsèquement capable de décrire le comportement limite des lubrifiants en vrac.

La deuxième raison de choisir Eyring est sa capacité à s'ajuster avec précision aux données sur une large gamme de conditions de fonctionnement malgré sa simplicité. La viscosité du squalane est décrite avec précision par le modèle d'Eyring dans la plupart des conditions EHL (pression et température), comme l'ont constaté Jadhao et Robbins [80] (voir Figure 2.4), Lin et Kedzierski [83], et Prentice et al. [84]. De plus, Jadhao et Robbins ont démontré que le modèle d'Eyring pouvait décrire la viscosité réduite $\eta_{red.} = \eta/\eta_N$ du SQ sur 25 ordres de grandeur du taux de cisaillement réduit $\dot{\gamma}_{red.}$ (voir Figure 2.5). En revanche, le modèle de Carreau avec N = 0,5 (écrit comme n dans la figure) ne parvient pas à reproduire la variation du taux de fluidification en cisaillement sur la même plage. Cela implique une meilleure polyvalence du modèle d'Eyring pour les conditions EHL, puisque le $\dot{\gamma}_c$ (et donc le $\dot{\gamma}_{red.}$) varie considérablement sur la large distribution des conditions de fonctionnement dans les contacts EHD. En effet, la pression passe de zéro à quelques gigapascals dans la zone de contact, et le taux de cisaillement peut atteindre $10^8 s^{-1}$.

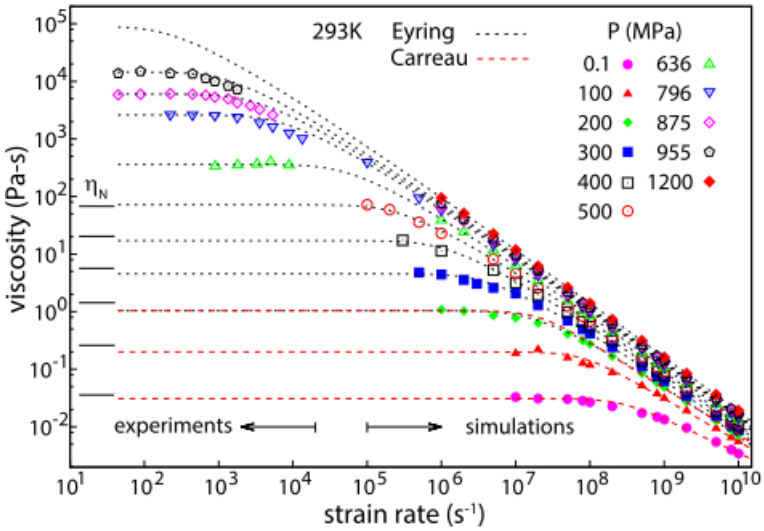


Figure 7: Variation de la viscosité du SQ à 293K par rapport au taux de contrainte. Les données proviennent d'expériences rhéologiques et de simulations NEMD, les différents symboles distinguent les différentes pressions. Adapté de [80].

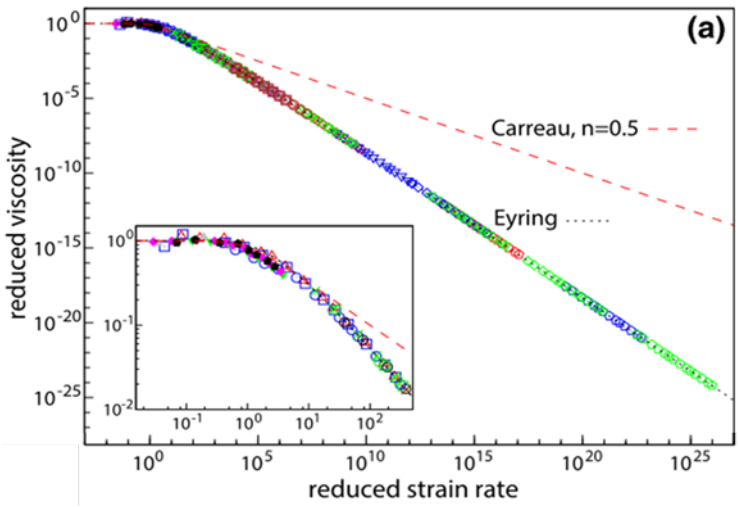


Figure 8: Viscosité réduite $\eta_{red.}$ en fonction du taux de contrainte réduit $\dot{\gamma}_{red.}$. Les données proviennent d'expériences rhéologiques et de simulations NEMD. Adapté de [80].

Le modèle d'Eyring ne nécessite que deux paramètres variant avec la pression et la température : la viscosité à faible cisaillement (Newtonienne) $\eta_N$ et la contrainte d'Eyring $\tau_e$. $\eta_N$ reflète la dépendance de la viscosité par rapport à la température et à la pression du fluide au repos. $\tau_e$ détermine le début de la fluidification par cisaillement du fluide. Par rapport au modèle de Carreau, qui a trois paramètres d'ajustement, cette simplicité facilite grandement le processus de caractérisation. De plus, en ajustant deux paramètres sur des données indépendantes du contact, le modèle d'Eyring résultant est considéré comme prédictif.

#### Choix des fluides étudiés

L'approche de prédiction de le frottement proposée dans ce travail doit être indépendante du fluide lubrifiant. Par conséquent, deux fluides aux comportements tribologiques opposés sont choisis : un lubrifiant (squalane, SQ) et un fluide de type traction organique (benzoate de benzyle, BB). Le SQ est un lubrifiant organique de formule $C_{14}H_{12}O_2$. Il a été un fluide de référence en EHL pendant 60 ans [85]. Les molécules de SQ ont une structure d'alcane linéaire, longue et flexible, comme le montre la Figure 9(a). Le BB est un fluide organique de formule $(CH_3)_2CH(CH_2)_3CH(CH_3)(CH_2)_3(CH_2)_3CH(CH_3)$. Il est proposé comme référence pour imiter le comportement des fluides de traction. Les molécules de BB ont une structure encombrante et petite, comme le montre la Figure 9(b).

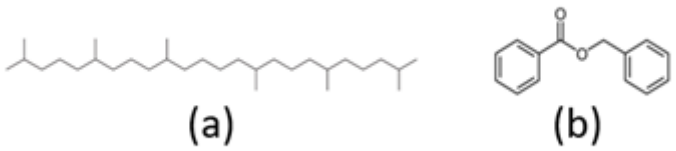


Figure 9: Représentation schématique de la molécule de (a) squalane et de la molécule de (b) benzoate de benzyle.

## Caractérisation des fluides : approche expérimentale et simulation MD

Pour caractériser pleinement le comportement rhéologique des fluides sélectionnés, les propriétés suivantes sont requises : la densité et la viscosité généralisée. Étant donné que cette dernière est donnée par le modèle d'Eyring dans cette étude, la viscosité Newtonienne et la contrainte d'Eyring doivent également être déterminées. En raison de l'absence d'une méthode pour déterminer expérimentalement la contrainte d'Eyring, elle sera déterminée par des simulations MD et sera donc présentée ultérieurement dans la section 2.3.

### Caractérisation des fluides : approche expérimentale et simulation MD

Pour caractériser pleinement le comportement rhéologique des fluides sélectionnés, les propriétés suivantes sont requises : la densité et la viscosité généralisée. Comme cette dernière est donnée par le modèle d'Eyring dans cette étude, il faut donc également déterminer la viscosité Newtonienne et la contrainte d'Eyring. En raison de l'absence d'une méthode pour déterminer expérimentalement la contrainte d'Eyring, elle sera déterminée par des simulations de dynamique moléculaire.

#### Expériences rhéologiques

La détermination de la viscosité Newtonienne a été largement étudiée dans la littérature [86, 87, 88], en particulier sa dépendance à la pression, car c'est le paramètre à l'origine de la plus grande variation de la viscosité. Une description précise de cette variation sur la plage de pression d'intérêt est essentielle pour la prédiction de le frottement [70]. Pour les conditions de contact EHD, la pression peut être de l'ordre de, ou supérieure à, la pression de transition vitreuse du lubrifiant, provoquant ainsi l'entrée du

lubrifiant dans un état vitreux et entraînant une forte augmentation de la viscosité. Cela nécessite des appareils rhéologiques capables d'appliquer des pressions très élevées tout en mesurant une quantité représentative du comportement du fluide. Actuellement, les viscosimètres à haute pression (HPV) sont les outils les plus efficaces pour ce type de mesure, bien qu'ils ne permettent pas de mesurer à des pressions proches de, ou supérieures à, la transition vitreuse. Le SQ et le BB ont été caractérisés rhéologiquement par rapport à la pression et à la température à l'aide de HPV. Une autre alternative possible est la simulation numérique à l'échelle moléculaire, qui sera présentée par la suite.

Les données de mesure rhéologique, recueillies soit expérimentalement soit numériquement, sont ensuite utilisées pour ajuster un modèle rhéologique, tel que le modèle WLF-Yasutomi [89] ou le modèle de mise à l'échelle thermique [64], qui sont décrits ci-après et seront utilisés ultérieurement pour prédire le frottement. De plus, le volume relatif du fluide est mesuré par la méthode expérimentale, comme les dilatomètres ou les piézomètres à soufflet [90]. Ces données sont ensuite ajustées à l'équation d'état empirique pour donner l'état du fluide à différentes pressions $p$ et températures $T$. Dans la présente étude, l'équation d'état de Tait classique [91] est utilisée. La densité $\rho$ peut également être dérivée de l'équation de Tait via la densité de référence $\rho_R$ mesurée par des densimètres à la pression atmosphérique $p_{atm}$ et à la température de référence $T_R$.

**Approche dynamique moléculaire**

Pour compléter les données rhéologiques, en particulier pour la réponse non Newtonienne (contrainte d'Eyring) des deux fluides et pour les conditions de fonctionnement inaccessibles aux méthodes expérimentales, des outils de caractérisation numérique à l'échelle locale sont nécessaires. Dans ce contexte, les simulations de dynamique moléculaire (MD) sont une approche appropriée car elles permettent d'accéder au comportement des lubrifiants à l'échelle moléculaire. De plus, il est possible de contrôler la pression et la température et d'atteindre des conditions EHL nominales qui sont inaccessibles dans les expériences rhéologiques. Plusieurs études MD de fluides confinés sous de telles conditions ont été publiées ces dernières années. Toutes les simulations MD réalisées dans cette étude sont codées dans LAMMPS [92] et exécutées sur le cluster LaMCoS ou le cluster P2CHPD, l'un des trois centres de calcul régionaux de Lyon, situé à l'Université de Lyon I. La simulation MD nous permet d'appliquer des conditions extrêmes contrôlées, telles que des pressions élevées et des taux de cisaillement élevés, à des températures constantes.

**Algorithme MD** Les simulations de MD reposent sur les interactions physiques entre les particules à l'échelle atomique par l'intermédiaire d'un champ de force donné. L'évolution des systèmes au fil du temps est calculée en résolvant les équations du mouvement de Newton. À chaque instant $t$ de la simulation, la position de chaque particule est connue. En fonction du champ de force choisi, l'énergie potentielle de chaque particule, la force agissant sur elle (définie comme le gradient de l'énergie potentielle) et son accélération sont calculées successivement. L'algorithme de Verlet [93] est ensuite utilisé pour calculer la nouvelle position de chaque particule.

Un pas de temps d'une femtoseconde ($1^{-15}s$) est choisi dans la présente étude. Le choix du champ de force dépend de la description de la molécule. Selon la littérature, pour les simulations de dynamique moléculaire de systèmes contenant des molécules linéaires à longue chaîne, les champs de force AA (tout-atome) sont recommandés [94], tels que les champs de force "long chain optimised potential for liquid simulations all-atom" (L-OPLS-AA) [95, 96]. Il a été démontré que les champs de force L-OPLS-AA donnent des résultats proches des données expérimentales sur les coefficients de frottement. Dans cette étude, les champs de force L-OPLS-AA sont utilisés dans les simulations de dynamique moléculaire pour le SQ et le BB, le même choix que dans l'étude de Porras-Vazquez [97]. Enfin, les

simulations de dynamique moléculaire peuvent être réalisées soit à l'équilibre (EMD) soit avec des énergies externes apportées au système (dynamique moléculaire hors équilibre, NEMD).

**Simulation EMD** Dans cette étude, nous tentons d'abord de caractériser la viscosité Newtonienne à l'équilibre en utilisant des simulations de dynamique moléculaire à l'équilibre (EMD). La boîte de simulation mesure environ 5 nm*5 nm*5 nm et contient 150 molécules pour le SQ et 360 molécules pour le BB. Des conditions périodiques aux limites sont appliquées dans les trois directions du système. La procédure de simulation des simulations EMD commence par la phase d'équilibrage, qui implique de minimiser l'énergie du système pour atteindre l'équilibre. Ce processus permet au système d'adopter une configuration stable et énergétiquement favorable avant de passer aux étapes suivantes de la simulation. Plus tard, le thermostat et le barostat de Nosé-Hoover [98] sont appliqués au système : d'abord, un ensemble canonique (NVT) est appliqué, ce qui signifie que le nombre total de molécules, le volume et la température sont maintenus constants pendant le processus. Cette étape dure pendant une période de 10 000 pas de temps pour stabiliser la température du système. Deuxièmement, l'ensemble isotherme-isobare (NPT) est appliqué, ce qui signifie que le nombre total de molécules, la pression et la température sont maintenus constants pendant le processus. Cette étape prend dix fois plus de temps que la précédente (100 000 pas de temps) pour atteindre la stabilisation de la pression souhaitée de la simulation tout en maintenant la stabilité de la température. Enfin, avec la pression et la température stabilisées, la simulation est exécutée dans l'ensemble thermodynamique canonique (NVE), ce qui signifie que le nombre total de molécules, le volume et l'énergie totale sont maintenus constants tout au long du processus. Cette étape est réalisée pendant le temps requis et le calcul de la viscosité ou du coefficient de diffusion est effectué dans cette dernière étape. En pratique, cette dernière étape est exécutée sans limite de temps prédéfinie pour obtenir le meilleur rapport signal-bruit. Toutes les simulations EMD de la présente étude utilisent la même configuration : un nœud, quinze cœurs et quinze gigaoctets de RAM sont exécutés pendant la durée maximale autorisée par le cluster (5,5 jours pour le cluster P2CHPD et 8 jours pour le cluster LaMCoS). Le temps de simulation typique est de plusieurs dizaines de nanosecondes (avec un maximum de 71,5 ns).

Deux méthodes sont testées : la méthode de Green-Kubo et la méthode de diffusion (Stokes-Einstein).

**Méthode Green-Kubo** Green-Kubo [99, 100] a démontré que les propriétés de transport (coefficient de diffusion et viscosités Newtoniennes) peuvent être reliées à la durée des fluctuations. Elles peuvent être exprimées comme des intégrales de fonctions d'autocorrélation. La viscosité Newtonienne $\eta_N$ est liée à la moyenne d'ensemble du tenseur de contrainte hors diagonale $P_{ij}$. Il a trois composants : $P_{xy}$, $P_{xz}$, et $P_{yz}$.

$$\eta_N = \frac{V}{3k_BT}\int_0^{+\infty} \langle P_{ij}(t)P_{ij}(0)\rangle \, dt \tag{6}$$

Dans l'Équation 6, $k_B$ est la constante de Boltzmann, $V$ est le volume du fluide, et $T$ est la température de l'échantillon. La viscosité calculée par la méthode de Green-Kubo est présentée en Appendice B.

**Méthode Stokes-Einstein** Une autre méthode pour déduire la viscosité Newtonienne des simulations EMD consiste à appliquer l'équation de Stokes-Einstein (Équation 7). Cette équation combine l'approche d'Einstein pour la description du mouvement brownien [101] et la théorie de Stokes sur la traînée des particules dans les fluides à faible nombre de Reynolds [102]. La viscosité Newtonienne est dérivée du coefficient de diffusion :

$$\eta_N = \frac{k_B T}{6\pi D r_c} \tag{7}$$

Dans l'Équation 2.17, $r_c$ est la longueur caractéristique, qui représente le rayon de la molécule de fluide simulée à une pression et température données. Pour calculer le coefficient de diffusion $D$, on mesure le déplacement carré moyen (MSD) des molécules (dans le régime de diffusion). Le MSD mesure la distance moyenne au carré des molécules due au mouvement brownien par rapport à leur position initiale [93]. Trois régimes différents des molécules peuvent être identifiés dans le temps : balistique, cage et régime de diffusion. Comme illustré dans la Figure 10.

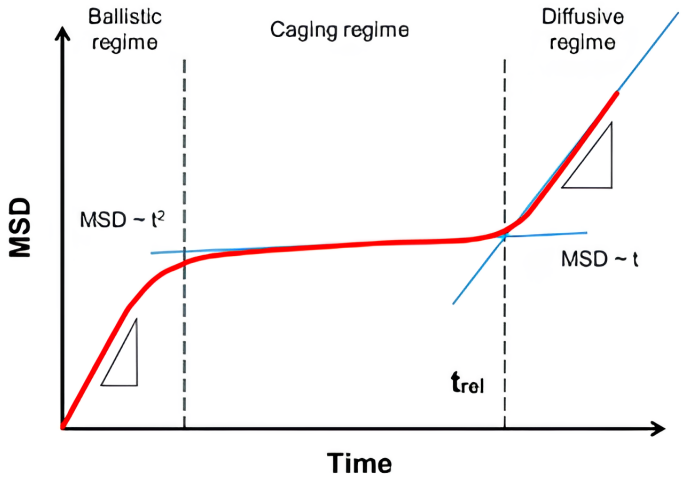


Figure 10: MSD en fonction du temps. Adapté de [97].

Einstein a d'abord relié le coefficient de diffusion au MSD en fonction du temps d'observation $t_{obs}$. Selon sa théorie, pour un $t_{obs}$ très long (qui tend vers l'infini), le MSD est proportionnel à $t_{obs}$. Le coefficient de proportionnalité est le coefficient de diffusion [93, 103]. Ceci indique que $D$ est défini comme indiqué dans l'Équation 8, où $n$ est la dimension du système. Il convient de noter que $t_{obs}$ implique le temps d'observation dans l'expérience, et pour les simulations numériques, cette notion correspond au temps de simulation $t_{simu}$.

$$D = \frac{1}{2n} \lim_{t \to \infty} \frac{\mathrm{d}MSD}{\mathrm{d}t} \tag{8}$$

Le calcul de $D$ nécessite une vérification (pour déterminer si le système est diffusif ou non) et un post-traitement des résultats de la simulation (calcul de la pente de la courbe MSD) conformément à l'Équation 8.

**Simulation NEMD** En fonction du système simulé, les simulations NEMD peuvent être divisées en NEMD en vrac et NEMD confiné. Le premier simule un ensemble de molécules sans surfaces de contact, similaire au système en EMD. Le second simule à la fois les surfaces de contact et le fluide à l'intérieur. Différentes méthodes NEMD peuvent également être identifiées en fonction de la manière dont le cisaillement est appliqué au système. Pour les systèmes en vrac, le cisaillement peut être appliqué soit en déformant la boîte de simulation (algorithme SLLOD [104]) soit en échangeant

artificiellement la quantité de mouvement entre les deux régions extrêmes des molécules de fluide (algorithme Müller-Plathe [105]). Pour le système NEMD confiné, le cisaillement est appliqué en appliquant directement un mouvement aux surfaces de contact (murs coulissants [106, 107]). Les différences entre ces trois méthodes sont résumées dans le tableau 1.

| Type de simulation | NEMD en vrac | | NEMD confiné |
|---|---|---|---|
| Nom de la méthode | SLLOD | Müller-Plathe | Murs coulissants |
| Origine du cisaillement | Déformation de la boîte de simulation | Échange en quantité de mouvement | Mouvement appliqué sur surfaces de contact |
| Système simulé | Molécules | | Molécules + surfaces de contact |

Table 1: Les trois méthodes NEMD différentes.

Dans ce travail, la méthode des murs coulissants est choisie pour caractériser la contrainte d'Eyring du fluide. Pour le caractériser à une pression $p$ et une température $T$ données, des simulations sont réalisées dans des conditions isobares et avec la présence d'un thermostat, la température est bien contrôlée, donc elle peut aussi être considérée comme un environnement isotherme.

Les systèmes NEMD contiennent des molécules de fluide confinées entre des surfaces solides de fer rugueux. Une nano-rugosité des surfaces de fer est créée par la loi d'auto-échelle fractale [31], où l'exposant de Hurst est fixé à 0,8 [108], et la rugosité quadratique moyenne (RMS) est fixée à 0,8 nm pour quantifier la rugosité. Les atomes de fer sont liés par le champ de force empirique classique de la méthode des atomes embarqués (EAM) [109], qui est largement utilisé dans le cas des systèmes métalliques [110, 111]. La section transversale de la surface solide mesure environ 5nm*5nm dans les directions x et y et a une épaisseur d'environ 3-5nm dans la direction z, comme illustré dans la Figure 11. Des conditions aux limites périodiques sont imposées dans les directions x et y. Aucune hypothèse n'est faite sur le profil de vitesse des systèmes NEMD confinés. Selon une étude précédente de Porras-Vazquez et al. [16], une épaisseur minimale de film d'huile de 10 nm est nécessaire pour prévenir les effets de surface comme le stratifiage dans les structures de fluide en raison du confinement. Par conséquent, un système contenant 720 molécules SQ ou 1440 molécules BB est utilisé, comme illustré dans les Figures 11 et 12.

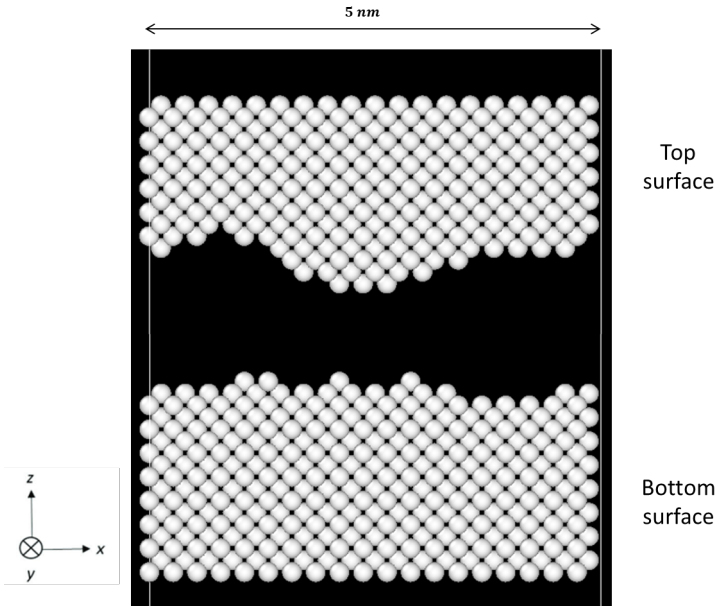


Figure 11: La surface rugueuse du système NEMD confiné.

Le processus de simulation comporte trois étapes : équilibrage, compression et cisaillement. Toutes les étapes sont exécutées en utilisant l'ensemble canonique thermodynamique (NVE), comme précédemment décrit dans la simulation EMD. Cela signifie que le nombre total de molécules, le volume et l'énergie totale sont maintenus constants pendant la procédure, ce qui signifie également que l'action interne du système est conservée. Un thermostat Nosé-Hoover est appliqué à l'ensemble du système (fluides et solides) pour contrôler la température, mais seulement dans la direction y pour éviter d'affecter le cisaillement dans la direction x et la pression dans la direction z. Un coefficient d'amortissement de 0,1 ps est choisi pour le thermostat.

L'énergie du système est d'abord minimisée. Cette étape dure 0,5 ns pour randomiser les positions des molécules de fluide ($5\times10^5$ étapes temporelles). Ensuite, pendant l'étape de compression, une pression constante est appliquée sur la surface supérieure avec le même thermostat utilisé pour contrôler la température, fonctionnant pendant 2 ns ($2 \times 10^6$ étapes temporelles). Enfin, lors de l'étape de cisaillement, une vitesse constante est appliquée à chaque surface solide pour créer un cisaillement. La vitesse est imposée sur les surfaces supérieure et inférieure, mais dans des directions opposées. De manière similaire à ce qui est fait dans les simulations EMD, l'étape de cisaillement est ensuite exécutée sans limite de temps prédéfinie pour obtenir le meilleur rapport signal/bruit, avec la même configuration qu'en EMD (CPU, RAM, temps d'horloge maximum) ; le temps de simulation typique est de plusieurs dizaines de ns. Les résultats ont prouvé être capables d'éviter une augmentation de température dans toutes les conditions testées. Le système NEMD confiné utilisé dans la présente étude est illustré dans la Figure 12.

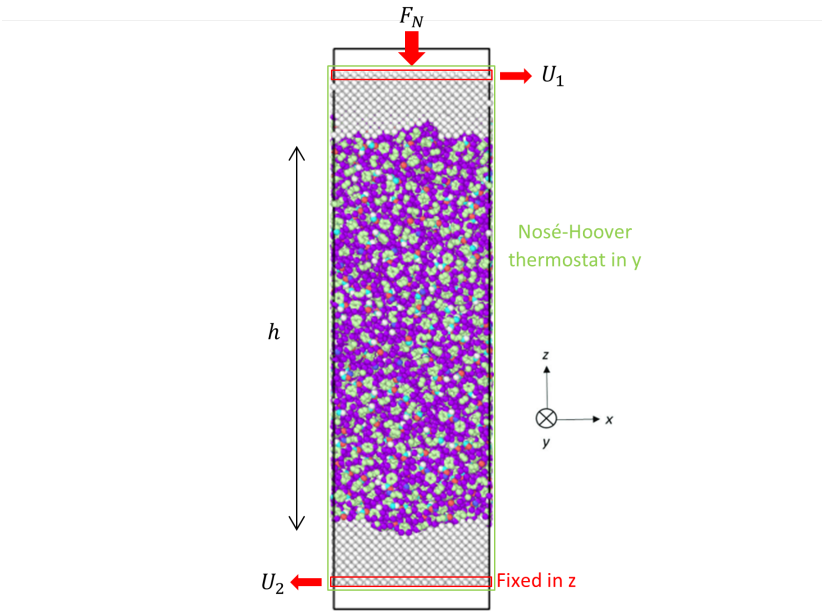


Figure 12: Système NEMD confiné des 1440 molécules de BB utilisées dans cette étude.

## Modélisation du contact ponctuel TEHD

Sur la base des travaux de Habchi et al. [63], Doki-Thonon [74], Wheeler [75] et Wheeler et Raisin [112], un modèle de contact TEHLnN (Thermal EHL non-Newtonian) stationnaire a été développé dans les travaux antérieurs en utilisant le logiciel d'analyse par éléments finis COMSOL Multiphysics. Le modèle calcule simultanément le profil de pression dans le film de fluide (équation de Reynolds généralisée); la déformation élastique des surfaces (conduisant au calcul du profil d'épaisseur du film); le champ de température dans le fluide et les solides en contact (via les équations d'équilibre énergétique); et l'équation d'équilibre des forces (équilibre de charge). Pour résoudre ces équations, la loi constitutive rhéologique du fluide est nécessaire. Cela inclut sa densité et sa viscosité en fonction de $p$, $T$ et $\dot{\gamma}$.

### Equations principales

### Équation de Reynolds généralisée

Le champ de pression dans un contact ponctuel EHD thermique en régime permanent avec un lubrifiant non newtonien est donné par l'équation de Reynolds généralisée de Yang et al. [113], comme indiqué dans l'Équation 9.

$$\frac{\partial}{\partial x}\left[\left(\frac{\rho}{\eta}\right)_e \frac{\partial p}{\partial x}\right] + \frac{\partial}{\partial y}\left[\left(\frac{\rho}{\eta}\right)_e \frac{\partial p}{\partial y}\right] - \frac{\partial}{\partial x}\left(\rho_x^*\right) = 0 \tag{9}$$

Les directions x et y sont dans le plan de contact et la direction z est dans la direction de l'épaisseur du film $h$. Comparée à sa version classique [114], l'équation de Reynolds généralisée prend en compte la variation des propriétés du fluide à l'intérieur du film de lubrifiant en utilisant des valeurs intégrées calculées à partir de l'opérateur $\left(\frac{\rho}{\eta}\right)_e$. L'équation de Reynolds est résolue uniquement dans une

région 2D $\partial\Omega_c$, $\Omega_c$ représente la surface de contact à la surface d'une géométrie élastique linéaire 3D $\Omega$ représentant un solide de contact équivalent, comme on peut le voir sur la Figure 13. Les conditions aux limites pour l'équation de Reynolds sont une pression nulle aux bords de la zone de Reynolds $\partial\Omega_c$. Les propriétés rhéologiques à travers l'épaisseur du film sont ensuite utilisées pour résoudre l'équation de Reynolds généralisée. Le calcul de ces valeurs est effectué dans une géométrie 3D indépendante de la masse équivalente, pour prendre en compte la distribution de $p$, $T$, et $\dot{\gamma}$ dans l'épaisseur du film, comme le montre la partie en pointillés sur la zone de contact $\partial\Omega_c$ sur la Figure 13.

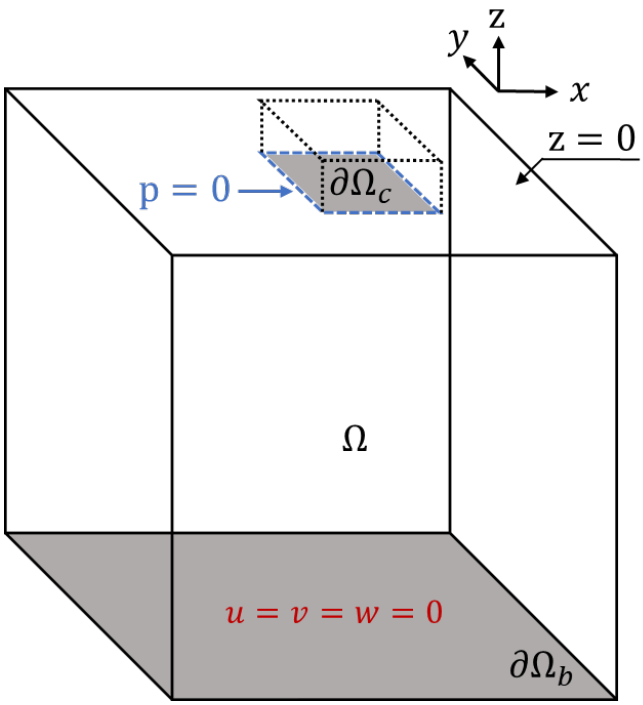


Figure 13: Géométrie du modèle élastique (masse équivalente $\Omega$), zone de Reynolds $\partial\Omega_c$ et géométrie du modèle non newtonien (représentée par des pointillés). Les conditions aux limites sont marquées en bleu et rouge.

### Équation d'élasticité

La pression calculée à l'intérieur de la zone de contact $\partial\Omega_c$ sert de condition aux limites pour calculer le déplacement élastique de la surface supérieure sur le solide équivalent $\Omega$, comme le montre l'Équation 10.

$$\nabla \cdot \sigma = 0 \qquad o \qquad \sigma = \begin{bmatrix} \sigma_{xx} & \tau_{xy} & \tau_{xz} \\ \tau_{xy} & \sigma_{yy} & \tau_{yz} \\ \tau_{xz} & \tau_{yz} & \sigma_{zz} \end{bmatrix} \tag{10}$$

La surface inférieure $\partial\Omega_b$ (surface grise sur la Figure 13) est fixée. Dans le domaine $\partial\Omega_c$, la contrainte normale dans la direction z $\sigma_{zz}$ est fixée à la pression $-p$ calculée par l'équation de Reynolds généralisée. Les autres frontières sont libres de se déplacer.

### Épaisseur du film et équations d'équilibre de charge

Pour les contacts sphère-plan que nous avons étudiés dans le présent travail, l'épaisseur du film $h$ sur la zone de contact est donnée par l'Équation 11.

$$h(x,y) = h_0 + \frac{x^2+y^2}{2R} + \delta(x,y) \tag{11}$$

où $\delta(x,y) = w(x,y,z=0)$, c'est-à-dire sur le domaine $\partial\Omega_c$ sur la Figure 13. Le terme $h_0$ est le résultat de l'équation d'équilibre de charge, qui relie la pression générée dans le lubrifiant à la charge normale $W$.

$$\iint_S p(x,y)dxdy = W \tag{12}$$

### Équations thermiques

Le champ de température est obtenu en résolvant les équations de chaleur au sein d'une géométrie 3D, comme le montre la Figure 14. Elle comprend les domaines $\Omega_t$ et $\Omega_b$, représentant les solides supérieur et inférieur, et $\Omega_f$ en gris clair représentant le fluide. Deux zones en gris foncé représentent les interfaces solide-fluide.

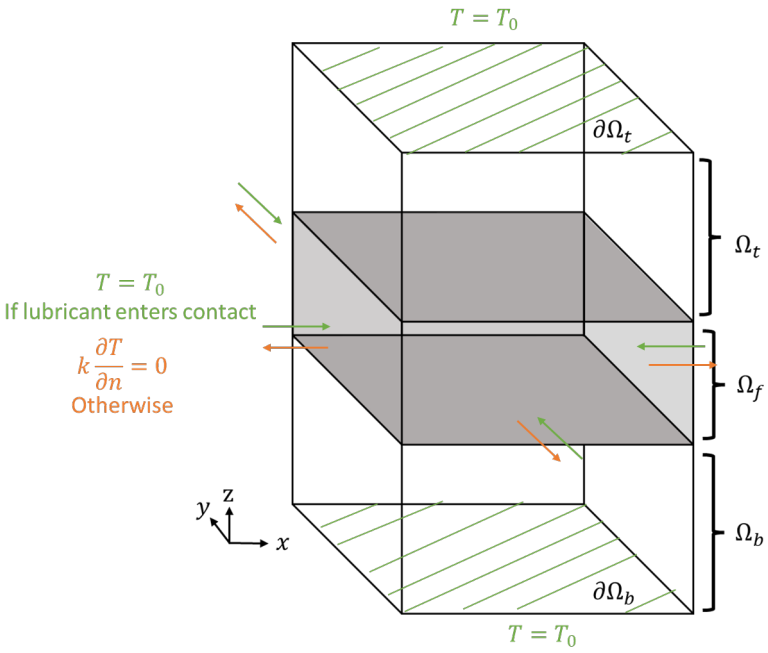


Figure 14: Géométrie du modèle thermique et conditions aux limites correspondantes pour les solides et le fluide. Les zones blanches $\Omega_t$ et $\Omega_b$ représentent les solides supérieur et inférieur, la zone grise $\Omega_f$ représente le fluide et les surfaces grises foncées représentent les interfaces solide-liquide.

Dans les solides, en l'absence de mouvement dans la direction y, la chaleur est transférée par conduction, décrite par l'Équation 13. Cette équation est résolue pour les solides supérieur et inférieur, où $u_x$ est la vitesse de la surface solide dans la direction x, $c$ est la capacité thermique spécifique, $k$ est la conductivité thermique et l'indice $_s$ représente les propriétés du solide.

$$\rho_s c_s u_x \frac{\partial T}{\partial x} - \nabla.\left(k_s \nabla T\right) = 0 \tag{13}$$

L'équation de chaleur dans le film de fluide est écrite comme l'Équation 14. $u_{fx}(x,y,z)$ et $u_{fy}(x,y,z)$ représentent la vitesse du fluide en tout point du film de lubrifiant dans les directions x et y.

$$\rho_f c_f \left(u_{fx}(x,y,z)\frac{\partial T}{\partial x} + u_{fy}(x,y,z)\frac{\partial T}{\partial y}\right) - \frac{\partial}{\partial z}\left(k\frac{\partial T}{\partial z}\right) = Q_{comp} + Q_{shear} \tag{14}$$

$Q_{comp}$ et $Q_{shear}$ représentent respectivement les sources de chaleur de compression et de cisaillement, comme le montre l'Équation 15 [74].

$$\begin{aligned} Q_{comp} &= -\frac{T}{\rho_f}\frac{\partial \rho_f}{\partial T}\left(\vec{u_f}\cdot\vec{\nabla}p\right) \\ Q_{shear} &= \eta\left[\left(\frac{\partial u_{fx}}{\partial z}\right)^2 + \left(\frac{\partial u_{fy}}{\partial z}\right)^2\right] \end{aligned} \tag{15}$$

Pour le problème stationnaire dans cette étude, les conditions aux limites pour les équations de chaleur sont les suivantes : pour les surfaces supérieure et inférieure ($\partial\Omega_t$ et $\partial\Omega_b$ sur la Figure 14), la température est fixée comme la température initiale $T_0$. Pour les autres surfaces, $T = T_0$ si le fluide ou le solide entre dans la zone de contact ; sinon, $k\frac{\partial T}{\partial n} = 0$ [74].

### Expériences tribologiques

Pour évaluer l'approche de modélisation quantitative, des expériences tribologiques ont été réalisées pour BB et SQ, en utilisant le tribomètre à bille-sur-disque Jerotrib au LaMCoS - INSA de Lyon décrit dans [40]. Les courbes de frottement mesurées sur le BB et le SQ ont d'abord été fournies dans [40] et [115] respectivement. Étant donné que ces expériences ont été réalisées indépendamment de cette thèse par d'autres chercheurs à LaMCoS, les lecteurs sont invités à consulter les références ci-dessus pour plus de détails.

# Characterisation du fluid

Ce chapitre présente la détermination des paramètres, à savoir la viscosité Newtonienne $\eta_N$ et la contrainte d'Eyring $\tau_e$, pour l'équation constitutive d'Eyring des deux fluides étudiés. Ces paramètres sont essentiels pour modéliser avec précision le comportement rhéologique des fluides dans les conditions EHL.

## Caractérisation de la viscosité Newtonienne (faible cisaillement)

Les simulations EMD ont été utilisées pour déterminer la viscosité Newtonienne d'un fluide. Les valeurs de viscosité Newtonienne obtenues ont été comparées aux mesures du viscosimètre haute pression de Bair [116] pour SQ et de Ndiaye et al. [40] pour BB. Les conditions de simulation pour les deux fluides sont résumées dans le tableau 2.

| | SQ | BB |
|---|---|---|
| p [MPa] | 0.1 - 2000 | 0.1 - 2000 |
| T [K] | 313 - 2000 | 313 - 2000 |

Table 2: Conditions de simulation de SQ et BB.

### Viscosité Newtonienne par la méthode Stokes-Einstein

Le concept de la méthode de Stokes-Einstein a été décrit précédemment. Cette méthode nécessite deux informations : le coefficient de diffusion$D$ et la longueur caractéristique$r_c$, qui peuvent tous deux être calculés par des simulations EMD. Dans cette étude,$D$ est dérivé en traçant la courbe MSD et$r_c$ est dérivé en estimant le volume de chaque molécule. Un ensemble d'équations d'Arrhenius est établi pour modéliser les coefficients de diffusion en utilisant le$D$ calculé (et les$E_a(p)$ et$D_0$ correspondants) et$r_c$ est ensuite utilisé dans les équations de Stokes-Einstein pour calculer la viscosité Newtonienne en fonction de la température et de la pression. Un résumé du modèle de viscosité Newtonienne est présenté dans l'Équation 16.

$$
\begin{gathered}
\eta_N(p,T)[\text{Pa.S}] = \frac{k_B T}{6\pi D(p,T) r_c} \\
D^{SQ}(p,T)[\text{m}^2/\text{s}] = D_0^{SQ} \exp\left(\frac{-E_a^{SQ}(p)}{k_B T}\right) \quad D^{BB}[\text{m}^2/\text{s}] = D_0^{BB} \exp\left(\frac{-E_a^{BB}(p)}{k_B T}\right) \\
E_a^{SQ}(p)[\text{kJ}/\text{mol}] = 20.672 + 0.012p \qquad E_a^{BB}(p) = 20.519 + 0.011p \\
D_0^{SQ}[\text{m}^2/\text{s}] = 4.17 \times 10^{-8} \qquad D_0^{BB}[\text{m}^2/\text{s}] = 1.06 \times 10^{-7} \\
r_c^{SQ}[\text{Å}] = 5.44 \qquad r_c^{BB}[\text{Å}] = 4.11
\end{gathered}
\tag{16}
$$

Les résultats prédits sont comparés aux données expérimentales pour valider cette approche. La viscosité Newtonienne mesurée dans la même gamme de conditions de fonctionnement par le viscosimètre haute pression pour SQ [116] et BB [40] est utilisée. La Figure 3.9 montre les comparaisons.

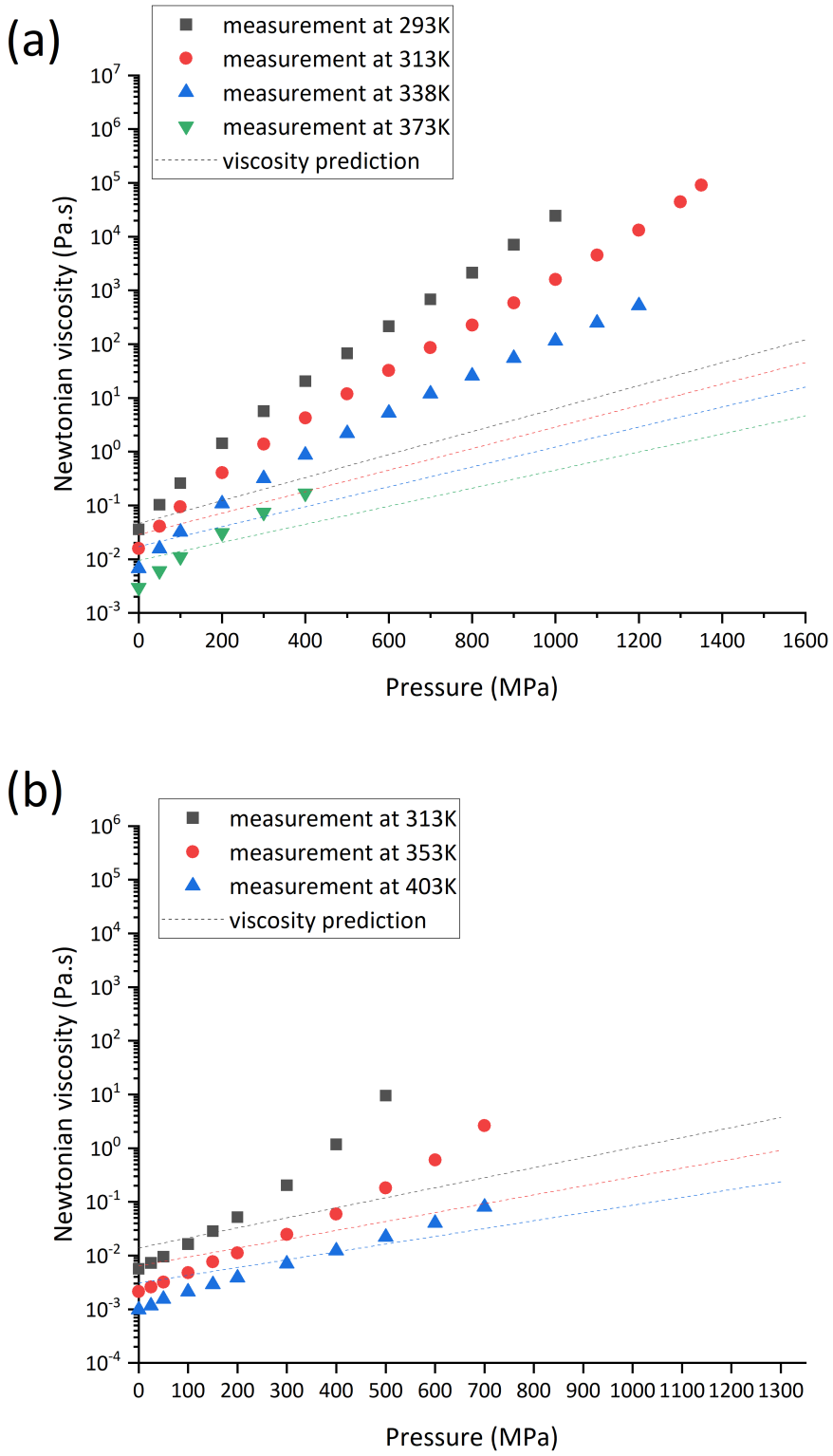


Figure 15: Comparaison entre les mesures de viscosité Newtonienne (symboles, SQ [116] et BB [40]), et la prédiction par la méthode de Stokes-Einstein (lignes pointillées) de (a) SQ et (b) BB.

Comme prévu, la méthode de Stokes-Einstein prédit une corrélation exponentielle entre la viscosité Newtonienne et la pression, donnant une tendance “linéaire” sur le graphique log-lin. Cependant, la prédiction et les données expérimentales montrent des tendances différentes. Alors que cette différence entre les deux ensembles de données est relativement petite autour de la pression atmosphérique, où la prédiction et la mesure sont du même ordre de grandeur, elle augmente de plusieurs ordres de grandeur à mesure que la pression augmente. De plus, la méthode de Stokes-Einstein ne parvient pas à prédire la croissance plus rapide qu’exponentielle (ou comportement super-Arrhenius) [87, 88] observée pour le fluide à hautes pressions.

Les causes possibles de cette erreur sont analysées une par une. Des exemples incluent des erreurs dans le calcul de$D$ et$r_c$, ou des erreurs cumulatives tout au long du processus. Cependant, aucun de ces facteurs n’est suffisant pour expliquer le décalage des résultats prédits et l’apparition d’un comportement plus rapide qu’exponentiel, la véritable signification de la “viscosité Newtonienne” mesurée expérimentalement est discutée.

La viscosité Newtonienne calculée à partir du coefficient de diffusion reflète les propriétés du fluide en vrac dans le régime diffusif, c’est-à-dire les propriétés d’un fluide détendu à l’équilibre. La diffusion ou l’écoulement est un concept d’échelle temporelle ; sur des échelles de temps suffisamment longues, même la matière considérée comme solide peut « s’écouler », comme le mouvement de la croûte terrestre. Pour les expériences comme pour les simulations, il existe une limite au calcul du coefficient de diffusion (ou viscosité) à l’équilibre. Ce processus peut devenir excessivement long et « trop ennuyeux à observer » [117], en raison de l’augmentation du temps de relaxation$t_{rel}$ causée par l’augmentation de la pression. Des exemples de cette situation peuvent être l’incapacité d’entrer dans l’état de diffusion dans le temps de simulation limité en raison du très long$t_{rel}$ ( $t_{simu} < t_{rel}$), d’où l’incapacité de calculer$D$ (et donc$\eta_N$ sur une approche de diffusion), comme décrit précédemment. Dans les expériences, comme celles utilisant un viscosimètre à bille tombante, la bille tombe trop lentement en raison de la viscosité extrêmement élevée, rendant impossible la mesure de sa valeur ($t_{obs} < t_{rel}$). Par conséquent, la mesure expérimentale de la « viscosité Newtonienne », en réalité, est une mesure de la viscosité à faible cisaillement [116]. Égaler la viscosité à faible cisaillement et la viscosité Newtonienne est basé sur l’hypothèse qu’à des taux de cisaillement très faibles, la réponse du fluide est Newtonienne. Cette supposition pose des problèmes à deux égards. Premièrement, dans la mesure de la viscosité à faible cisaillement, des forces extérieures sont appliquées à l’échantillon, le plaçant dans un état de non-équilibre. Cela diverge légèrement de la définition de la viscosité Newtonienne (définie à l’équilibre) et de la viscosité prédite par la méthode de Stokes-Einstein, basée sur des simulations réalisées à l’équilibre. De plus, il reste à déterminer si la réponse du fluide est Newtonienne dans tous les cas, car les hautes pressions entraînent des temps de relaxation plus longs et des taux de cisaillement critiques plus faibles. Dans ce dernier cas, même un « faible cisaillement » pourrait encore initier un amincissement au cisaillement. Dans le premier cas, l’augmentation de$t_{rel}$ peut poser des problèmes dans l’état de l’échantillon pendant la mesure. En effet, dans ces conditions sévères, l’échelle de temps de relaxation pourrait être égale ou même dépasser la durée de la simulation ou de l’expérience [118]. Dans un tel cas, les valeurs de viscosité mesurées expérimentalement ne reflèteraient pas le fluide dans un état liquide. Concevablement, ces mesures de deux phases différentes sont très susceptibles de montrer des tendances différentes, rappelant la transition exponentielle à plus rapide qu’exponentielle largement observée dans les viscosimètres avec une augmentation du taux de cisaillement [88]. De plus, il est important de noter que ces deux problèmes peuvent se cumuler. Cela signifie que dans certaines mesures de viscosité à faible cisaillement, la viscosité mesurée pourrait correspondre à la viscosité d’amincissement au cisaillement d’un fluide dans un état solide, qui peut différer du concept de viscosité Newtonienne.

Comme les résultats de prédiction montrent des écarts de plusieurs ordres de grandeur, nous pouvons conclure qu'à ce stade, la méthode de Stokes-Einstein basée sur des paramètres dérivés de la simulation EMD ne peut pas fournir une prédiction satisfaisante du frottement dans des conditions EHL. Par conséquent, une autre méthode est choisie pour caractériser la viscosité Newtonienne.

**Détermination du modèle de viscosité Newtonienne**

Les pressions auxquelles sont effectuées les mesures expérimentales de viscosité (pression maximale de 1350 MPa pour SQ et 700 MPa pour BB) sont inférieures à la pression trouvée dans les contacts EHD réels. Néanmoins, les modèles de viscosité sont couramment ajustés sur ces résultats expérimentaux dans la littérature pour être extrapolés aux conditions EHL. Le plus couramment utilisé est le modèle WLF-Yasutomi (modifié), déjà publié pour SQ [85] et BB [40]. Cependant, la loi WLF-Yasutomi a une limitation mathématique, à savoir la pression de transition vitreuse $p_g$. Compte tenu de la possible haute pression des conditions EHL sur lesquelles la présente étude est axée, cette limitation doit être contournée. Par conséquent, un autre modèle de viscosité newtonienne, la loi d'échelle de viscosité créée dans la présente étude (voir l'Équation 17), est utilisé.

$$\varphi = \left(\frac{T}{T_R}\right)\left(\frac{V}{V_R}\right)^g$$
$$\eta_N = A\exp\left(B\varphi^{-q} + C\varphi^{-Q}\right), \qquad 0 < q < 1, \qquad 1 < Q$$

Le paramètre d'échelle $\varphi$ de la loi d'échelle de viscosité nécessite la connaissance du volume relatif, qui est défini par l'équation d'état de Tait. La loi d'échelle de viscosité créée dans ce travail peut être ajustée aux mesures expérimentales de viscosité des deux fluides, conduisant aux paramètres d'ajustement donnés dans le tableau 3.

| | A[Pa.s] | B[K] | C[K] | q [-] | Q [-] | g [-] | SD [%] |
|---|---|---|---|---|---|---|---|
| SQ[Cette étude] | $3.531 \times 10^{-5}$ | 6.016 | 0.133 | 0.999 | 3.954 | 3.521 | 10.77 |
| BB[Cette étude] | $6.807 \times 10^{-5}$ | 4.280 | 0.155 | 0.871 | 6.037 | 4.569 | 4.13 |

Table 3: Paramètres de la loi d'échelle de viscosité de SQ et BB.

Les courbes de viscosité résultantes sont illustrées à la Figure 16. Les mesures expérimentales de viscosité (symboles solides) et les deux lois de viscosité newtonienne (lignes pointillées pour WLF-Yasutomi, lignes en pointillés pour la mise à l'échelle de la viscosité) sont comparées. Il peut être observé que pour une température donnée, les deux lois coïncident bien avec les données expérimentales, fournissant une description cohérente de la viscosité newtonienne à basse pression, 0-1400 MPa pour SQ et 0-700 MPa pour BB. Notamment, aucun modèle ne semble prédire avec précision le comportement plus rapide que l'exponentiel autour de 1400 MPa pour SQ, ce qui conduit à une possible plus grande déviation des mesures expérimentales avec l'augmentation des pressions.

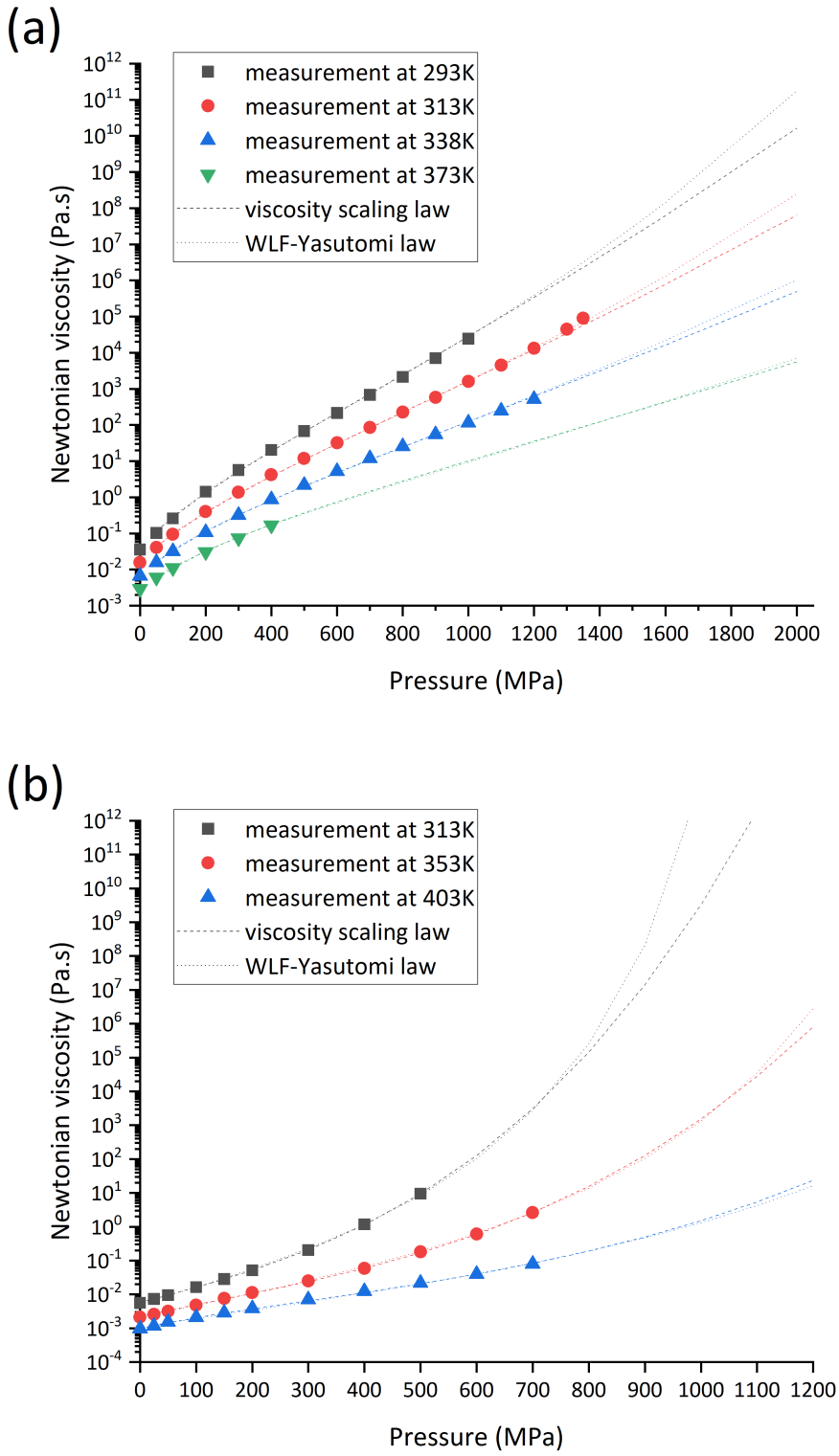


Figure 16: Comparaison entre les mesures de viscosité newtonienne (symboles, SQ [116] et BB [40]), la loi WLF-Yasutomi (lignes pointillées) et la loi d'échelle de viscosité créée dans ce travail (lignes en pointillés) de (a) SQ et (b) BB.

## Caractérisation de la contrainte Eyring

Pour caractériser la réponse du fluide au cisaillement, il est important de garantir que la simulation offre un bon rapport signal sur bruit, ce qui nécessite que l'étape de "cisaillement" de la simulation soit la plus longue possible. Le profil de température de chaque résultat a été tracé pour vérifier qu'il n'y avait pas d'augmentations de température excessives. Le profil de vitesse a été tracé pour vérifier si un profil de vitesse de Couette avait été atteint. La contrainte en régime permanent obtenue a été utilisée pour le post-traitement afin d'obtenir la viscosité non newtonienne et la contrainte d'Eyring. La plage de conditions de simulation NEMD pour SQ et BB est présentée dans le tableau 4.

| | T [K] | p [MPa] |
|---|---|---|
| SQ | 293 - 373 | 100 - 2000 |
| BB | 293 - 373 | 200 - 1000 |

Table 4: Conditions testées en NEMD pour SQ et BB.

L'étude précédente de Jadhao et Robbins [80, 119] a conduit à la dérivation de la contrainte d'Eyring à partir de simulations MD en ajustant la loi d'Eyring (forme approximative à des taux de cisaillement très élevés) sur les données de taux de contrainte de cisaillement. Dans la présente étude, la loi d'Eyring originale est directement ajustée aux données de contrainte de cisaillement versus taux de cisaillement pour calculer la contrainte d'Eyring.

Le processus d'ajustement peut être réalisé en utilisant la méthode des moindres carrés. Cependant, bien que la loi d'Eyring n'ait que deux paramètres : $\tau_e$ et $\eta_N$ , le processus d'ajustement semble incertain lorsque les deux paramètres sont autorisés à varier. Par conséquent, en pratique, ce processus d'ajustement est simplifié en fixant les valeurs de $\eta_N$ données par la mesure expérimentale, ou, si nécessaire, à la valeur interpolée par le modèle de viscosité newtonienne choisi pour cette étude. Ainsi, le seul paramètre à ajuster par la méthode des moindres carrés à partir du résultat NEMD est la contrainte d'Eyring. Cette approche est choisie afin de dériver une contrainte d'Eyring cohérente avec $\eta_N$. Cela signifie que la paire de paramètres ($\eta_N$, $\tau_e$ ) représente le meilleur ajustement des données NEMD par la loi d'Eyring.

### Squalane

La contrainte d'Eyring de SQ, notée $\tau_e^{SQ}$, est d'abord calculée. En complément, $\tau_e^{SQ}$ provenant de la littérature [80] ou calculée en appliquant la même méthode proposée dans ce travail sur les résultats NEMD de la littérature [31, 16] sont superposées aux résultats de la présente étude dans la Figure 17.

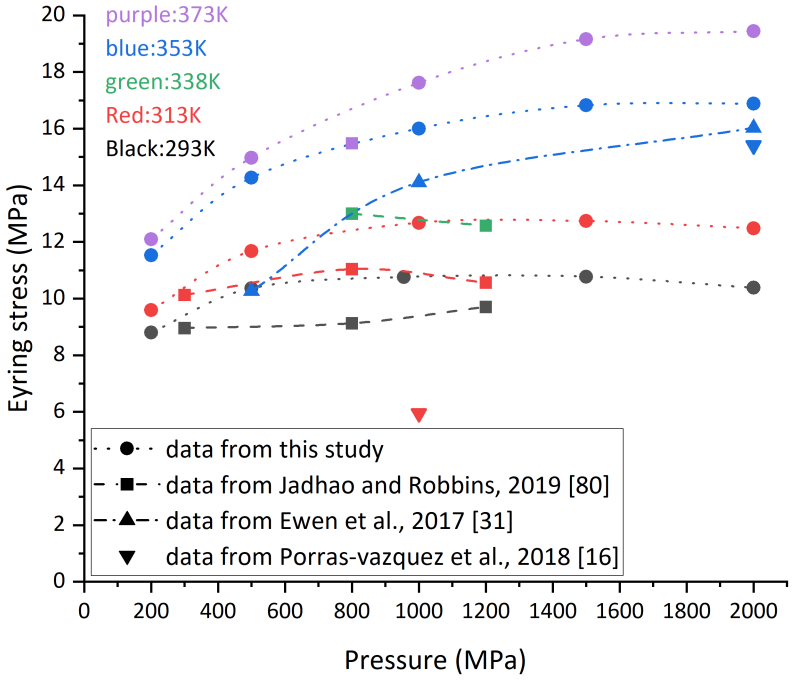


Figure 17: Contrainte d'Eyring de SQ en fonction de la pression, et pour différentes températures. Comparaison entre les résultats de cette étude (NEMD confiné, points et lignes pointillées) et les données de la littérature : Jadhao et Robbins [80] (NEMD en volume, carrés et lignes pointillées), Ewen et al. [31] (NEMD confiné, triangles et ligne pointillée-tiret). Porras-Vazquez et al. [16] (NEMD confiné, triangles inversés). Différentes couleurs sont utilisées pour distinguer les températures.

La comparaison montre qu'il n'y a pas de consensus clair sur la valeur de la contrainte d'Eyring de SQ, et des divergences existent entre les différents auteurs. Cependant, les $\tau_e^{SQ}$ dérivés de la simulation de la présente étude sont comparables à ceux de la littérature. Ces divergences peuvent résulter des différences entre les simulations NEMD. Pour ces raisons, et dans le but d'unifier la méthodologie de recherche, seules les données de la présente étude sont utilisées par la suite. La variation de la contrainte d'Eyring de SQ $\tau_e^{SQ}$ par rapport à la pression $p$ [MPa] et à la température $T$ [K] est ajustée par une fonction donnée dans l'Équation 17 (valide dans la plage des $p$ et $T$ testées). Les paramètres résultants sont donnés dans le Tableau 5. Ce modèle sera implémenté dans le modèle de contact FEM. Les données de contrainte d'Eyring issues des simulations NEMD et l'équation dérivée sont superposées dans la Figure 18.

$$\tau_e^{SQ}[MPa] = A(T)\left(1 - \exp\left(-\frac{p}{B(T)}\right)\right) + C(T)$$
$$A(T) = a_1 * T + a_2 \qquad B(T) = b_1 * T + b_2 \qquad C(T) = c_1 * T + c_2 \tag{17}$$

| a1 [MPa/K] | a2 [MPa] | b1 [MPa/K] | b2 [MPa] | c1 [MPa/K] | c2 [MPa] |
|---|---|---|---|---|---|
| 0.0598 | -11.4683 | 4.6973 | -1209 | 0.0505 | -10.0967 |

Table 5: Paramètres de l'équation de la contrainte d'Eyring de SQ.

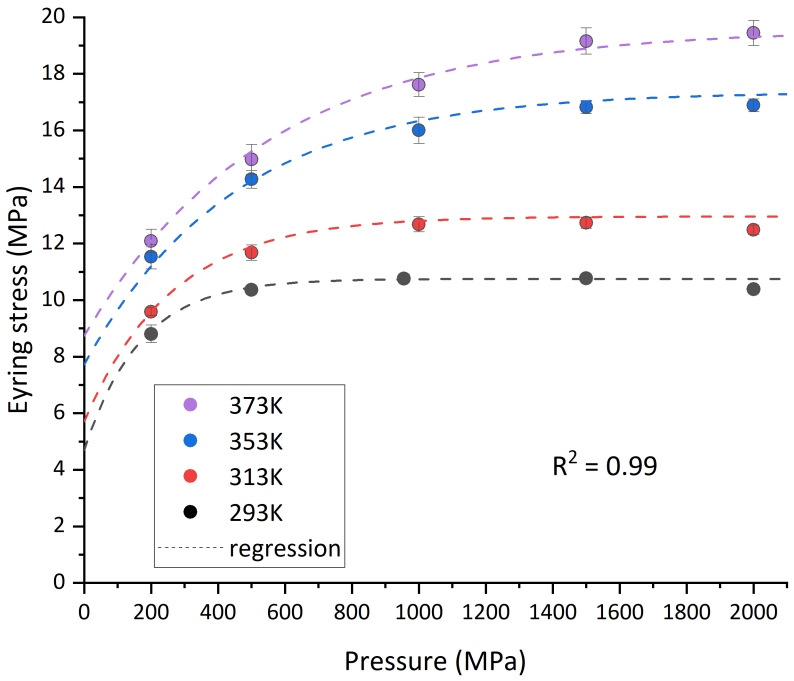


Figure 18: Contrainte d'Eyring de SQ de cette étude (symboles) et équation de la contrainte d'Eyring (écrite comme "régression", lignes pointillées) en fonction de la pression et de la température.

**Benzyl Benzoate**

According to the results depicted in Figure 19, the Eyring stress for BB, denoted as $\tau_e^{BB}$, displays a rather straightforward relationship with pressure and temperature. Notably, within the range of the tested pressures and temperatures, $\tau_e^{BB}$ appears to be directly proportional to the pressure, albeit with a negative gradient. A similar trend was observed by Evans and Johnson [65] for another traction fluid known as Santotrac 50. A linear fit of the results associates $\tau_e^{BB}$ with the pressure $p$ [MPa] and temperature $T$ [K], as described in Equation 18.

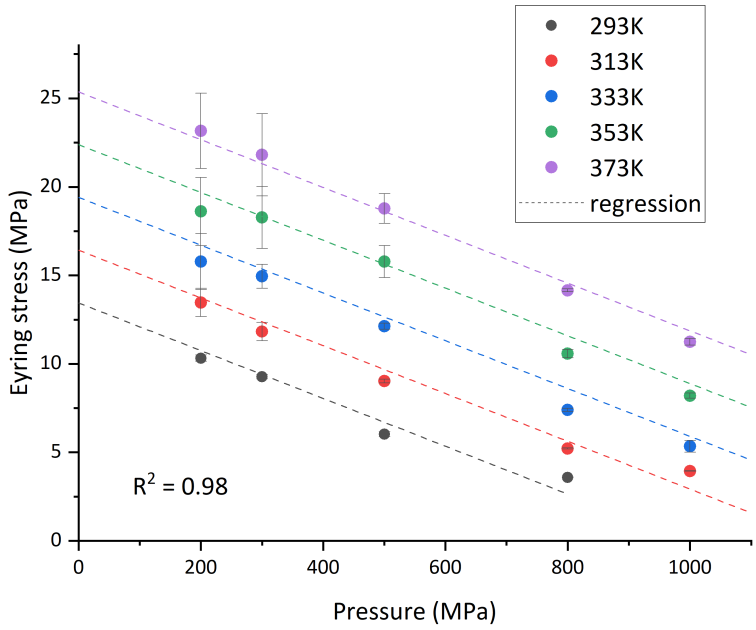


Figure 19: BB Eyring stress as deduced from this research (depicted by symbols) juxtaposed with the linear regression (represented by dashed lines) in relation to both pressure and temperature.

$$\tau_e^{BB}[MPa] = 0.149T - 0.014p - 30.21 \tag{18}$$

In a manner analogous to the case with SQ, the defining equation for $\tau_e^{BB}$ remains valid strictly within the examined pressure range (spanning from 200 MPa to 1000 MPa) and temperature (ranging between 293 K and 373 K). It's an evident assertion that the Eyring stress cannot plunge to zero, or even manifest negative values with an escalation in pressure. Yet, upon a closer examination of Figure 19, it becomes apparent that $\tau_e^{BB}$ tends towards a minimal, yet non-zero, asymptotic value. Currently, the available data is inadequate to substantiate this supposition. However, this hypothesis could be the subject of scrutiny in subsequent investigations.

## Modèle de synthèse de la viscosité des fluides

Selon la viscosité newtonienne et le stress d'Eyring des fluides, les modèles de viscosité généralisés pour les deux fluides sont construits pour prédire la viscosité à une pression, une température et un taux de cisaillement donnés. Ces deux paramètres sont dérivés soit de mesures expérimentales (viscosité newtonienne) soit de résultats de simulation (stress d'Eyring). Pour SQ, les données de viscosité newtonienne proviennent d'un viscosimètre à haute pression [120] réalisé par Bair [116], tandis que les résultats de simulation proviennent de Jadhao et Robbins [80]. Pour BB, les données de viscosité newtonienne proviennent des mêmes mesures de Ndiaye et al. [40] et les résultats de simulation de la présente étude sont utilisés pour comparaison.

Comme dernière étape pour valider les modèles de viscosité généralisés, la viscosité non-newtonienne prédite a été comparée pour les deux fluides aux mesures expérimentales effectuées sur des rhéomètres à haute pression. Les données de viscosité non-newtonienne de SQ proviennent de Bair et al. [73].

Celles de BB proviennent d'expériences rhéologiques réalisées à LaMCoS par Bouscharain [121]. Les comparaisons sont montrées à la Figure 20, où (a) est SQ à 293K et des pressions de 100 MPa à 955 MPa. (b) est BB à 303 K, 313 K, et des pressions de 300 MPa et 400 MPa.

Il peut être observé que la viscosité généralisée prédite par le modèle d'Eyring est en bon accord avec les mesures expérimentales et les données de simulation NEMD. Les modèles prévoient avec précision le plateau de viscosité newtonienne (à partir des mesures de viscosimètre à haute pression), les données de viscosité-taux à des taux de cisaillement modérés (à partir des mesures de rhéomètre) et les données de viscosité-taux à des taux de cisaillement modérés à élevés (à partir de la simulation NEMD). Une déviation est observée dans la prédiction de la transition plateau-éclaircie par cisaillement de SQ par rapport aux mesures de rhéomètre de Bair et al. à 796 MPa, 875 MPa et 955 MPa (indiquée par la flèche noire à la Figure 20). La transition non-newtonienne expérimentale est retardée par rapport à celle prédite. Jadhao et Robbins ont rapporté un résultat similaire [80] lorsqu'ils ont tenté d'adapter le modèle d'Eyring aux mêmes données expérimentales, ils ont également trouvé que pour ces données de Bair et al. [73], le modèle Carreau s'adapte mieux dans cette région. Ces prédictions quantitatives de viscosité généralisée démontrent la faisabilité et la fiabilité de l'approche de modélisation de la viscosité proposée dans cette étude. La prédiction de frottement peut alors être effectuée avec ces modèles à l'échelle du contact.

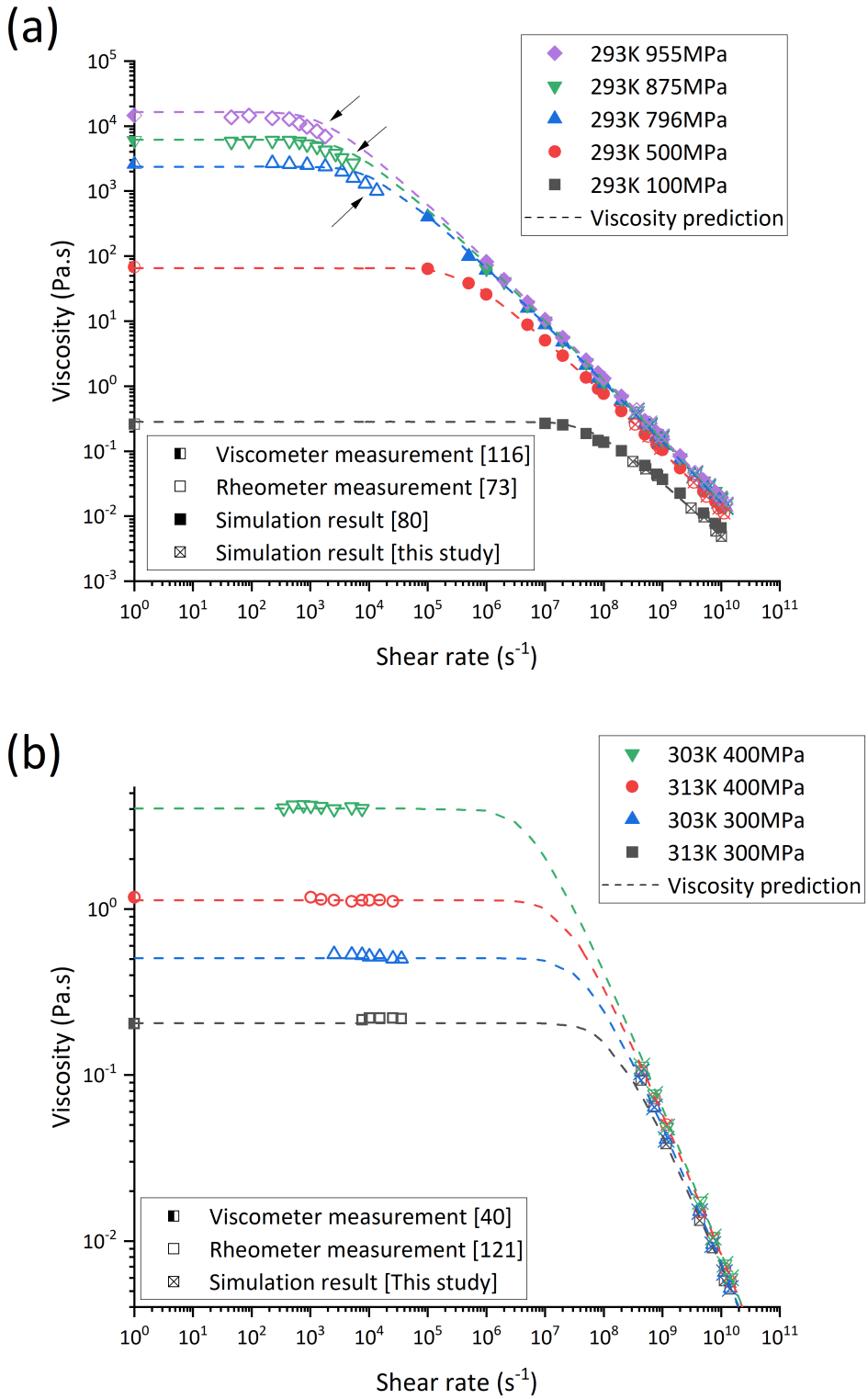


Figure 20: (a) Comparaison de la prédiction de viscosité généralisée SQ (Eyring, lignes en pointillés) à 293 K et des pressions de 100 MPa à 955 MPa, avec des mesures de viscosimètre à haute pression de Bair [116] (symboles fermés à moitié gauche), des mesures de rhéomètre de Bair et al. [73] (symboles ouverts), des résultats de simulation de Jadhao et Robbins [80] (symboles fermés) et de cette étude (symboles ouverts avec une croix) (b) Comparaison de la prédiction de viscosité généralisée BB (Eyring, lignes en pointillés) à 303 K, 313 K, et des pressions de 300 MPa et 400 MPa, avec des données de viscosité newtonienne de Ndiaye et al. [40], des mesures de rhéomètre de Bouscharain [121] (symboles ouverts) et des résultats de simulation de cette étude (symboles ouverts avec une croix).

# Prediction du frottement EHD

## Prédiction du frottement à partir du modèle TEHLnN

Le modèle complet de viscosité d'Eyring établi dans le Chapitre 3 est implémenté dans le modèle de contact TEHLnN décrit au Chapitre 2 pour prédire le frottement. Les simulations numériques du contact sont choisies pour être réalisées dans les mêmes conditions opérationnelles que la mesure expérimentale du frottement afin de comparer la prédiction numérique aux données expérimentales. Les conditions de l'expérience sont résumées dans le tableau 6.

| **Fluide** | SQ | BB |
|---|---|---|
| Température ambiante $T_0$ [K] | 313 | 313, 333 |
| Charge de contact $W$ [N] | 46, 108, 254 | 32, 61 |
| Pression de Hertz maximale $p_h$ [MPa] | 900, 1200, 1600 | 800, 1000 |
| Vitesse d'entraînement $u_e$ [$^m/_s$] | 0.8 | 2.5(313 K), 5(333 K) |
| Rapport glissement/roulement SRR [%] | 0.1-80 | 0.1-50 |

Table 6: Conditions expérimentales tribologiques de SQ et BB.

Ces conditions tribologiques sont d'abord tracées par rapport aux données de viscosité Newtonienne pour voir à quel point elles sont représentatives. Elles sont présentées sous forme de croix noires dans la Figure 21. Ces dernières représentent la viscosité newtonienne de SQ ou BB à la température ambiante (réservoir de lubrifiant) et la pression de Hertz des expériences du tribomètre. Les valeurs de viscosité sont obtenues à partir de la mesure expérimentale du viscosimètre ou extrapolées en utilisant le modèle de viscosité sélectionné. Comme le montre la Figure 21, pour SQ, les conditions d'essai correspondent à une viscosité à l'intérieur ou proche de la plage de mesure expérimentale, tandis que pour BB, les conditions d'essai sont situées plus loin dans la zone extrapolée.

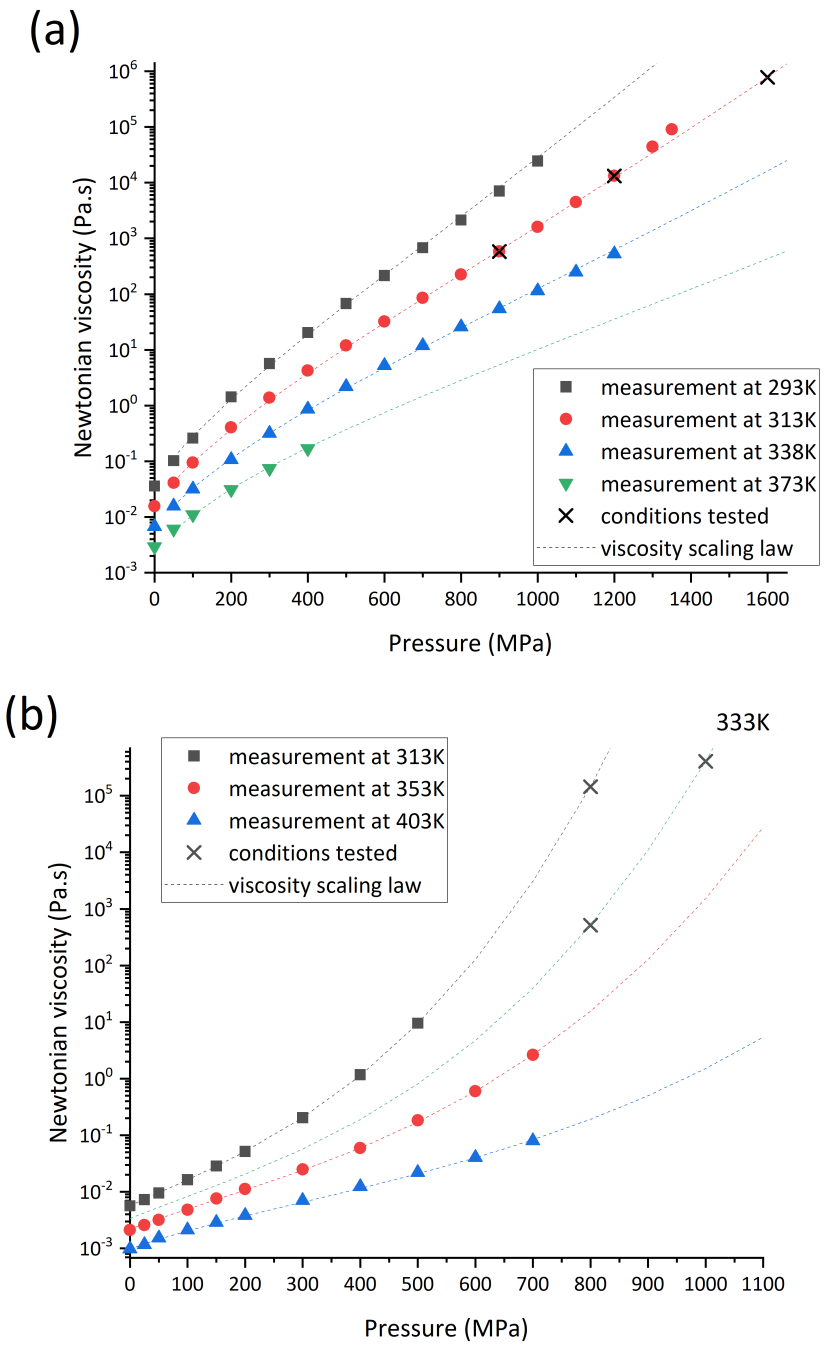


Figure 21: Comparaison entre les mesures de viscosité (symboles pleins) et les prédictions des lois d'échelle de viscosité (lignes en pointillés). (a) SQ, données expérimentales de [116]. (b) BB, données expérimentales de[40]. Les conditions opérationnelles pour les expériences de frottement de cette étude sont marquées par des croix noires.

Pour un contact acier-acier, les courbes de frottement mesurées et prédites sont montrées dans la Figure 22 (SQ) et la Figure 23 (BB). Les prédictions TEHLnN sont représentées par des points rouges, et les mesures tribologiques sont représentées par des carrés noirs.

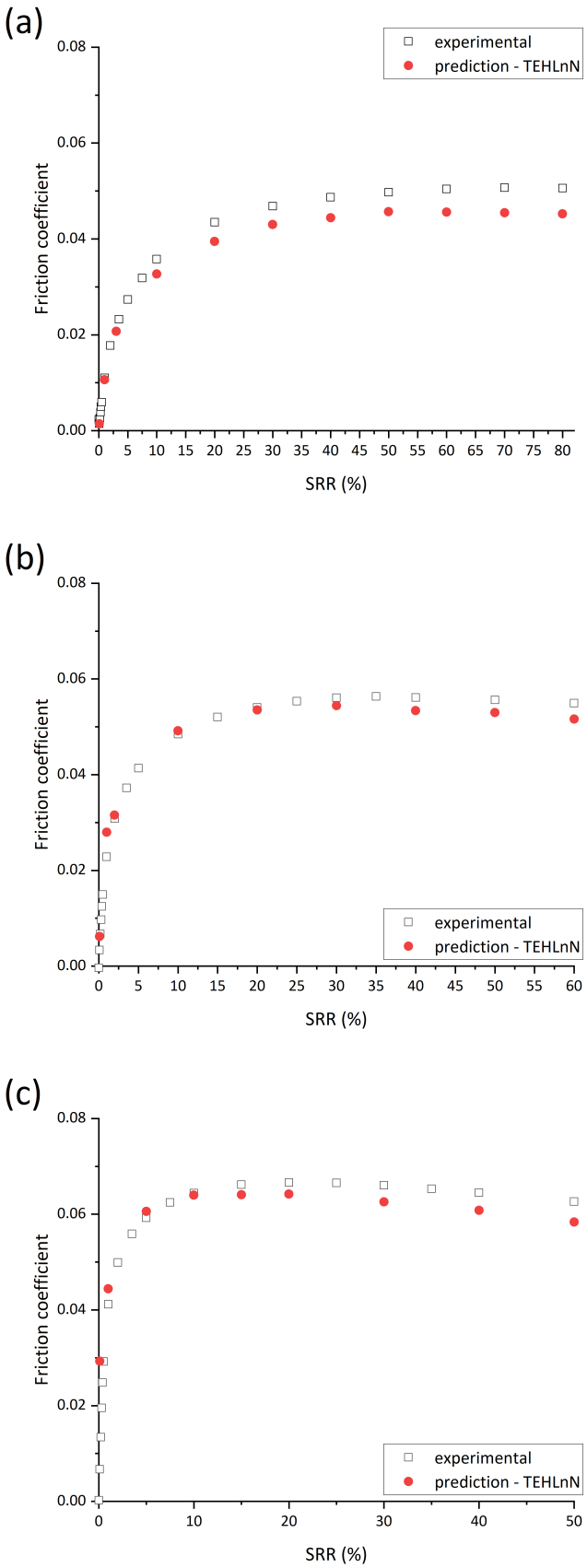


Figure 22: Comparaison entre les mesures expérimentales de frottement de cette étude (carrés noirs) et les prédictions numériques de la simulation TEHLnN (points rouges). (a) SQ $T_0$=313K, $p_h$=900MPa. (b) SQ $T_0$=313K, $p_h$=1200MPa. (c) SQ $T_0$=313K, $p_h$=1600MPa.

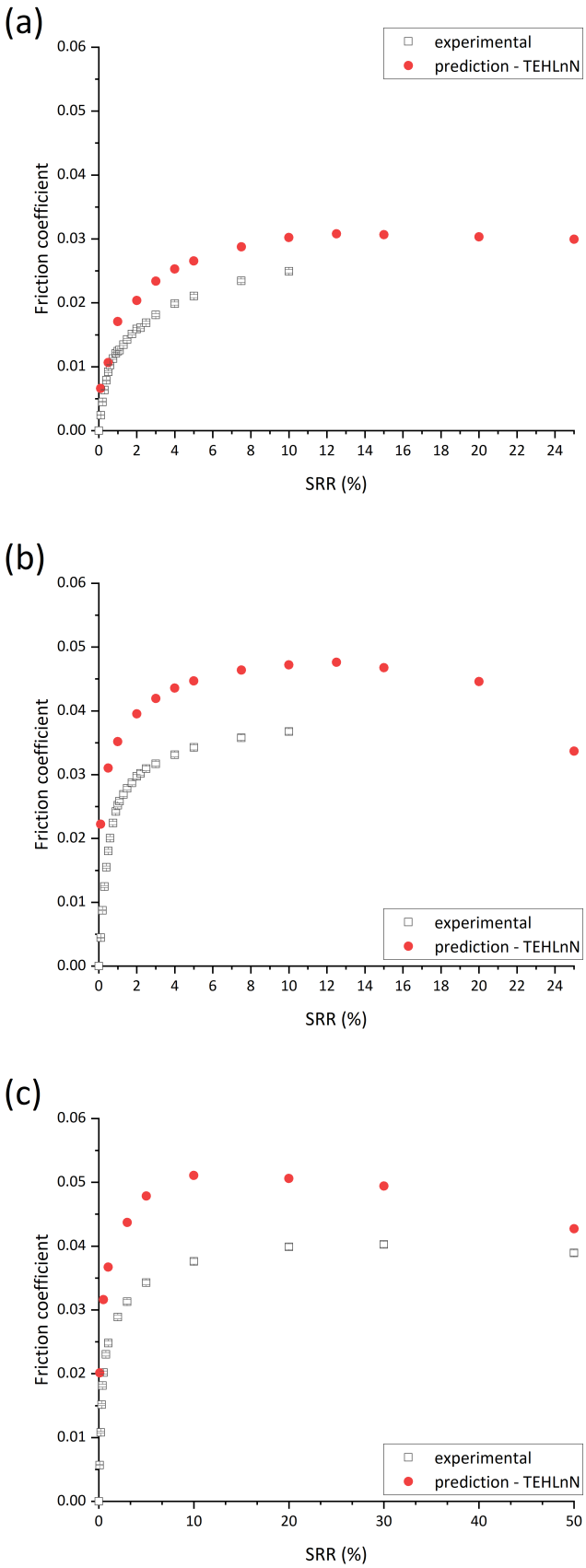


Figure 23: Comparaison entre les mesures expérimentales de frottement de [40] (carrés noirs) et la prédiction numérique de la simulation TEHLnN (points rouges). (a) BB $T_0$=333K, $p_h$=800MPa. (b) BB $T_0$=333K, $p_h$=1000MPa. (c) BB $T_0$=313K, $p_h$=800MPa.

Dans le cas de SQ, la simulation TEHLnN a prédit quantitativement le coefficient de frottement, y compris les régimes linéaire et de fluidification du cisaillement des courbes de frottement. Plus intéressant encore, ils ont réussi à prédire la non-linéarité du coefficient de frottement en fonction de la vitesse glissante, en particulier pour les pressions plus élevées. Cela démontre la validité du modèle de viscosité Eyring en fonction de la pression et de la vitesse de cisaillement pour décrire le comportement non-newtonien du lubrifiant à haute pression et à haute vitesse de cisaillement.

Pour BB, même si les prédictions de la simulation sont assez proches des données expérimentales, quelques différences peuvent être observées. Cela pourrait être attribué à une simplification du modèle, à des erreurs d'extrapolation de la viscosité à haute pression, ou encore à d'autres phénomènes non pris en compte dans le modèle.

En conclusion, l'intégration du modèle de viscosité d'Eyring au modèle TEHLnN a permis d'obtenir des prédictions du frottement plus précises, en particulier pour les conditions à haute pression et à haute vitesse de cisaillement, démontrant l'importance de prendre en compte le comportement non-newtonien des lubrifiants dans ces conditions.

### Étude de la génération du plateau de frottement

Malgré les divergences observées pour BB, la simulation TEHLnN prédit toujours quantitativement le frottement mesuré expérimentalement des deux fluides et en particulier du plateau de frottement. Autrement dit, le plateau de frottement peut être reproduit dans un modèle de contact réaliste qui prend en compte à la fois les effets non-Newtoniens modélisés par le modèle de viscosité d'Eyring et les effets thermiques dus à la compression et à la source de chaleur de cisaillement dans l'équation de l'énergie. Pour pouvoir discuter plus en détail de l'origine du plateau de frottement, ces deux effets devaient être découplés. Pour cela, deux simulations supplémentaires sont effectuées pour chaque condition de fonctionnement dans les Figures 22 et 23, les simulations non-Newtoniennes isothermes empêchent la montée en température due à la génération de chaleur. Et des simulations Newtoniennes thermiques ont été réalisées en considérant uniquement la viscosité indépendante du cisaillement (prise comme $\eta_N$).

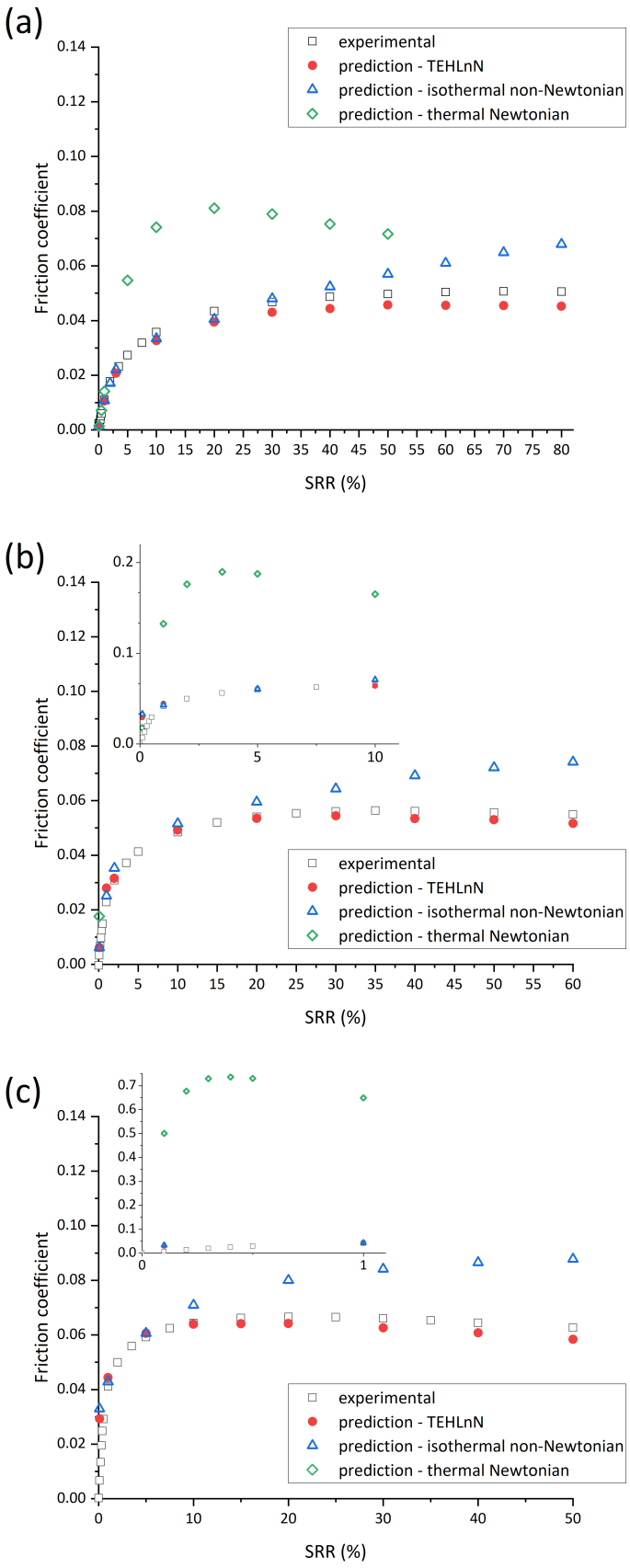


Figure 24: Comparaison entre les mesures expérimentales de cette étude (carrés noirs) et les résultats de prédiction de la simulation non-Newtonienne thermique (points rouges), de la simulation non-Newtonienne isotherme (triangles bleus) et de la simulation Newtonienne thermique (diamant vert). (a) SQ $T_0$=313K, $p_h$=900MPa. (b) SQ $T_0$=313K, $p_h$=1200MPa. (c) SQ $T_0$=313K, $p_h$=1600MPa.

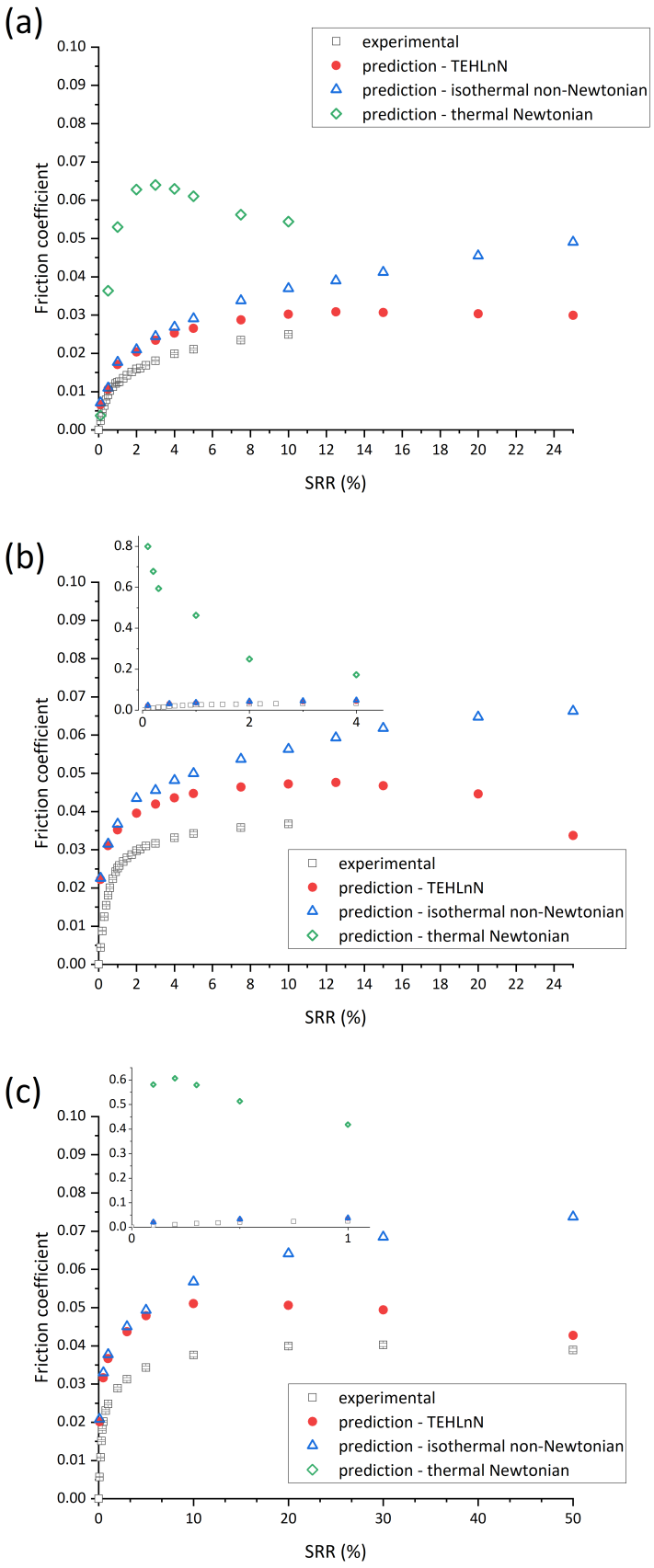


Figure 25: Comparaison entre les mesures expérimentales de [40] (carrés noirs) et les résultats de prédiction de la simulation non-Newtonienne thermique (points rouges). (a) BB $T_0$=333K, $p_h$=800MPa. (b) BB $T_0$=333K, $p_h$=1000MPa. (c) BB $T_0$=313K, $p_h$=800MPa.

Selon les résultats montrés dans les Figures 24 et 25, ni les effets thermiques ni les effets non-Newtoniens seuls ne peuvent reproduire le plateau de frottement observé expérimentalement. En conséquence, le plateau de frottement semble être dû à une combinaison d'amincissement par cisaillement (effet non-Newtonien) et d'amincissement thermique (effet thermique). Le régime "en plateau" des courbes de frottement ne semble pas être dû uniquement à une propriété intrinsèque du lubrifiant. Il dépend également de l'échauffement visqueux dans le contact, y compris des matériaux constituant les corps solides et des conditions de contact.

Cette conclusion peut également être liée à la variation de $\dot{\gamma}_{red.} = \dfrac{\dot{\gamma}}{\dot{\gamma}_c}$ dans la zone de contact. En fait, lorsque les conditions de contact changent, le taux de cisaillement critique $\dot{\gamma}_c$ change également. Par conséquent, le $\dot{\gamma}_{red.}$ change pour le même SRR. Combiné à l'effet thermique, cela détermine le frottement sous des conditions spécifiques. Cela peut expliquer pourquoi les plateaux de frottement ont tendance à se produire à des pressions de contact élevées (pour le même SRR) : un taux de cisaillement critique plus bas dû à une haute pression le rend plus facile à atteindre un haut $\dot{\gamma}_{red.}$, et la viscosité plus élevée rend également l'effet thermique plus prononcé. De plus, on pourrait supposer, sur la base de ces déductions, que l'apparition de plateaux de frottement est générique. Un $\dot{\gamma}_{red.}$ suffisamment élevé et un effet thermique suffisamment fort (à un taux de cisaillement élevé)

finiront par saturer le frottement ou même le faire baisser. Bien que l'on ne sache pas encore lequel de ces deux effets est en position dominante dans ce processus, car la présente étude démontre qu'aucun des deux ne peut reproduire indépendamment le plateau de frottement observé dans l'expérience.

Étant donné l'influence non négligeable des effets thermiques sur le frottement EHD, il est raisonnable de conjecturer que, dans les mêmes conditions de contact (pression, température et taux de cisaillement/SRR), différentes caractéristiques thermodynamiques introduites en faisant varier les solides en contact peuvent modifier la dissipation thermique et ainsi provoquer des réponses frottementnelles différentes. Ainsi, le frottement dans un ensemble de contacts acier-saphir a également été prédit et comparé à ceux dans des contacts acier-acier dans les mêmes conditions, dont les détails sont donnés dans l'Annexe D. Malheureusement, la différence dans les propriétés thermiques des deux solides n'est pas suffisamment significative pour conclure fermement sur leur influence sur leur frottement, d'autres études sont nécessaires.

# Conclusion generale

Cette thèse propose une stratégie originale pour prédire le frottement dans le contact élastohydrodynamique (EHD), fondée sur une caractérisation a priori du fluide.

Dans le premier chapitre, un état de l'art sur le frottement EHD est présenté. Ce chapitre met en lumière la difficulté de modéliser correctement le seuil de frottement observé expérimentalement. Jusqu'ici, de nombreux chercheurs ont eu recours à des modèles empiriques pour introduire artificiellement des plateaux de frottement, se privant ainsi d'une approche véritablement "prédictive".

Le deuxième chapitre détaille la stratégie proposée, articulée autour de deux volets majeurs : la détermination des propriétés rhéologiques du fluide, en se concentrant spécifiquement sur la viscosité généralisée, et la mise en place d'un modèle de contact EHD thermique capable de reproduire les champs de pression et de température du véritable contact. Le modèle de viscosité d'Eyring est privilégié pour sa simplicité et sa caractérisation facile grâce à ses deux paramètres. La caractérisation des propriétés rhéologiques en conditions EHL est toutefois complexe, d'où le recours aux simulations de dynamique moléculaire pour compléter les données existantes. Deux fluides, le squalane (SQ) et le benzoate de benzyle (BB), sont sélectionnés pour la démonstration.

Dans le troisième chapitre, les paramètres du modèle d'Eyring sont définis. La viscosité Newtonienne est d'abord approchée par des simulations de dynamique moléculaire en équilibre. Toutefois, face à des limitations, un modèle dérivé d'expériences est finalement retenu. Les simulations de dynamique moléculaire hors équilibre permettent ensuite de déterminer la contrainte d'Eyring. Les modèles de viscosité généralisée pour les deux fluides sont alors établis.

Le quatrième chapitre décrit le développement du modèle de contact TEHLnN pour la prédiction du frottement. Le modèle d'Eyring est intégré, permettant une prédiction du frottement à partir de quantités physiques indépendantes du contact. Bien que les prédictions montrent quelques écarts, elles parviennent à anticiper quantitativement le frottement pour les deux fluides. L'analyse subséquente suggère que c'est le modèle de viscosité d'Eyring qui est responsable des écarts. Des simulations supplémentaires montrent que le plateau de frottement est le résultat combiné d'effets non-Newtoniens et thermiques.

En conclusion, cette thèse offre une nouvelle perspective sur la prédiction du frottement EHD, en s'appuyant sur une caractérisation préalable du fluide et en soulignant l'importance des effets non-Newtoniens et thermiques combinés.

# Nomenclature

| | |
|---|---|
| $a$ | Hertzian contact circle's radius |
| $a_1, a_2, b_1, b_2, c_1, c_2$ | SQ Eyring stress model parameters |
| $A_1, A_2, B_1, B_2, C_1, C_2$ | WLF model parameters |
| $A, B, C, q, Q$ | Viscosity scaling model parameters |
| $A_{Ea}, B_{Ea}$ | Fitting parameters of activation energy law |
| $a_v$ | Volume-temperature variation constant(Tait) |
| $\beta_K$ | Bulk modulus-temperature coefficient(Tait) |
| $C_f$ | Friction coefficient |
| $c, c_i$ | Specific heat capacity of $i$ component |
| $D$ | Diffusion coefficient |
| $D_m$ | Compliance matrix |
| $D_0$ | Pre-exponential factor of diffusion coefficient |
| $\delta$ | Elastic displacement of solid surface |
| $E_i, \nu_i$ | Young's modulus and Poisson's ratio of solid $i$ respectively |
| $E', \nu'$ | Equivalent Young's modulus and Poisson's ratio |
| $E_a$ | Activation energy |
| $E_k$ | Kinetic energy |
| $\eta$ | Generalised viscosity |
| $\eta_N$ | Newtonian viscosity |
| $\eta_g$ | Glass transition viscosity |
| $\eta_R, \eta_0$ | Newtonian viscosity value at reference state ($p_{atm}$,$T_R$) and initial state ($p_{atm}$,$T_0$) respectively |
| $\eta_{red.}$ | Reduced viscosity |
| $\eta_e, \eta'_e$ | Generalised Reynolds equation integral terms |

| | |
|---|---|
| $\varepsilon_{ij}$ | Deformation of solid in the j-direction in a plane having i as a normal |
| $F$ | Force |
| $\dot{\gamma}$ | Shear rate |
| $\dot{\gamma}_c$ | Critical shear rate |
| $\dot{\gamma}_{red.}$ | Reduced shear rate |
| $h$ | Film thickness |
| $h_0$ | Film thickness constant parameter |
| $H$ | Dimensionless film thickness |
| $k_i$ | Thermal conductivity of $i$ component |
| $K_0$ | Initial bulk modulus(Tait) |
| $K_0'$ | Initial pressure rate of change of bulk modulus(Tait) |
| $K_{00}$ | Pre-exponential factor of initial bulk modulus(Tait) |
| $m_i$ | Mass of $i$ component |
| $MSD$ | Mean square displacement |
| $N$ | Carreau exponent |
| $N_m$ | Number of molecules in the simulation box |
| $n$ | Dimension factor |
| $\Omega$ | Equivalent mass |
| $\Omega_c$ | Contact domain |
| $\partial\Omega_c$ | Contact domain's boundray |
| $\Omega_t, \Omega_b$ | Top and bottom solids respectively |
| $\Omega_f$ | Fluid domain |
| $\partial\Omega_t, \partial\Omega_b$ | Top and bottom surfaces respectively |
| $p$ | Pressure |
| $p_h$ | Hertzian pressure |
| $p_H$ | Hertzian dry contact pressure field |
| $p_{atm}$ | Atmospheric (initial) pressure |
| $p_g$ | Glass transition pressure |
| $\overline{p}$ | Mean pressure in the contact area |
| $\varphi$ | Viscosity scaling parameter |
| $P_{ij}$ | Off-diagonal stress tensor |
| $Q_{comp}, Q_{shear}$ | Compression and shear heat sources respectively |

| | |
|---|---|
| $\rho_R, \rho_0$ | Density value at reference state ($p_{atm}$,$T_R$) and initial state ($p_{atm}$,$T_0$) respectively |
| $\rho_e, \rho'_e, \rho''_e, \rho^*_x$ | Generalised Reynolds equation integral terms |
| $r_s$ | Stokes or Stokes-Einstein radius |
| $r_h$ | Hydrodynamic radius |
| $r_c$ | Characteristic length |
| $R$ | Equivalent radius of curvature |
| $R_x, R_y$ | Radius of curvature in x and y-direction |
| $R_{visco}$ | Logarithmic reduced viscosity slope |
| $S$ | Contact area |
| $SRR$ | Slide-to-roll ratio |
| $\sigma$ | Stress tensor |
| $\sigma_{ii}$ | Normal stress component in the i-direction |
| $t$ | Time |
| $t_{rel}$ | Relaxation time |
| $t_{simu}$ | Simulation time |
| $t_{obs}$ | Experimental obervation time |
| $T$ | Temperature |
| $T_0$ | Ambient (initial) temperature |
| $T_R$ | Reference temperature |
| $T_g$ | Glass transition temperature |
| $T_g$ | Glass transition temperature constant parameter |
| $\tau$ | Shear stress |
| $\tau_a$ | Average shear stress in contact |
| $\tau_{lim}, \tau_{LSS}$ | Maximum shear stress or limiting shear stress |
| $\tau_L$ | Maximum average shear stress in contact |
| $\tau_e$ | Eyring stress |
| $\tau_{ij}$ | Shear stress component in the j-direction in a plane having i as a normal |
| $U$ | Elastic displacement vector of solid |
| $u_i$ | Velocity of $i$ component |
| $\Delta u$ | Sliding velocity |
| $u_e$ | Entrainment velocity |

| | |
|---|---|
| $u, v, w$ | Elastic displacement components in the x, y and z-direction respectively |
| $u_{fx}, u_{fy}$ | Fluid flow velocity components in the x and y-directions respectively |
| $V$ | Volume |
| $V_t$ | Volume of simulation box |
| $V_R$ | Volume at reference state |
| $W$ | Contact load |
| $x, y, z$ | Space dimensions |
| $X, Y, Z$ | Dimensionless space dimensions |

# Introduction

Transport and industry consume two-thirds of the total energy consumed annually [1]. Among them, overcoming friction is the largest part of energy consumption, accounting for between 25 to 30% in transport, while in the industry, it is around 15 to 20% [1]. Reducing friction losses would lead to significant energy savings, with consequent economic and environmental benefits. For example, advanced friction control technologies could reduce friction losses in passenger cars by around 18% over the next five to ten years, saving 117,000 million litres of fuel per year. This benefit is increasingly recognised in the context of growing environmental concerns and the implementation of carbon-neutral policies in all countries. Over a further 15 to 20 years, it is estimated that friction losses could be reduced by more than 60%, saving 385,000 million litres of fuel and reducing $CO_2$ emissions by 960 million tonnes per year [2, 3].

Rolling element bearings (REBs) are a commonly used mechanical component designed to minimise friction in pivot joints. Modern REBs (see Figure 26) typically consist of the following parts: two rings arranged in concentric circles (known as the inner ring and outer ring), rolling elements positioned between the rings, and a cage to guide the rolling elements. REBs carry the moving load through these rolling elements. The rolling elements induce rolling friction, which substitutes the sliding friction, with the former generally being much smaller than the latter under equivalent loads.

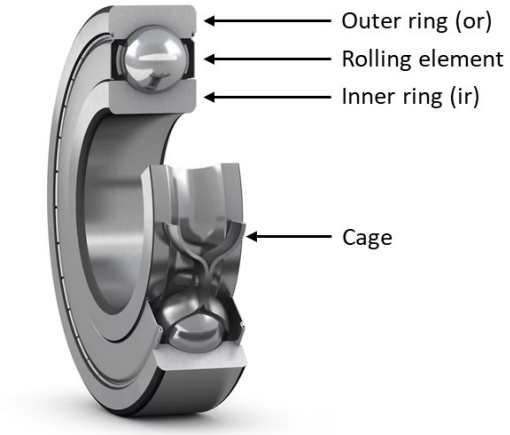


Figure 26: Deep groove ball bearings.
https://www.skf.com/us/products/rolling-bearings/ball-bearings/deep-groove-ball-bearings.

In addition to the environmental issues mentioned above, there is also an economic motivation. The global bearing market was valued at USD 118.7 billion in 2020 and is expected to grow at a compound

annual growth rate of 8.5% from 2021 to 2028 (see Figure 27).

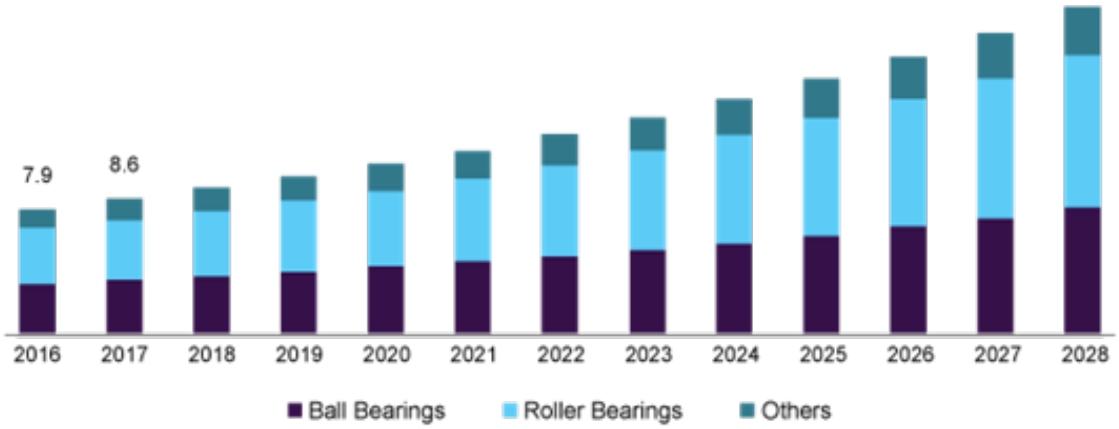


Figure 27: Germany bearings market by product, 2016-2028 (in Billion USD)
www.grandviewresearch.com/industry-analysis/bearings-market.

The demand for bearings with low maintenance, high efficiency and long life is growing with the market. It is therefore important to have reliable and relevant friction prediction models to optimise bearing design and reduce friction losses.

In most rolling bearings, contact between non-conforming surfaces operates under the elastohydrodynamic lubrication (EHL) regime, where a very thin film of lubricant ($\sim$ 100 nm) separates the surfaces and is subjected to very high pressure ($>$ 1 GPa). In these conditions, the shear rate can reach high values, and the high pressure significantly increases the viscosity of the lubricant. Besides, the pressure in the EHD contact is not uniformly distributed throughout the film but increases from the inlet ($p_{atm}$) towards the centre until the maximum value (considered as the Hertzian pressure $p_h$) and then decreases towards the $p_{atm}$ at the outlet (see black line in Figure 28). High shear rate ($10^4 - 10^7\ s^{-1}$) and pressure distribution also lead to significant, non-uniform shear heating, resulting in a large temperature gradient across the film (see red line in Figure 28). All these complexities bring up several difficulties in the prediction of friction. Firstly, there is a lack of experimental characterisation of lubricant properties under such severe conditions (i.e. high pressure, high shear rate). Secondly, physical phenomena associated with these severe conditions are not totally understood (i.e. possible phase transitions, velocity accommodation mechanism), and the complex coupling of operating conditions in contact makes it difficult to interpret the result and derive an understanding of mechanics. However, the construction of relevant and robust (i.e. non-empirical) models must be based on a full understanding of contact mechanics.

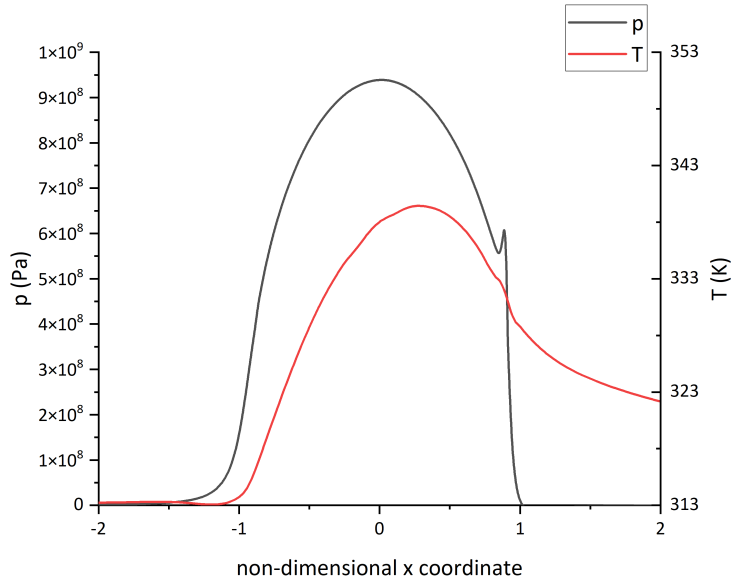


Figure 28: Typical pressure (black line) and temperature (red line) distributions in an EHD contact. Simulation results from this study of a steel-steel contact lubricated with squalane, at the ambient temperature $T_0$=313K, Hertzian pressure $p_h$=900MPa, entrainment velocity $u_e$=0.8$^m/_s$ and slide-to-roll ratio=0.6.

## Objectives

The main objective of this research is to propose a strategy for achieving quantitative friction prediction in the EHL regime. The complexity of this task arises from the extreme conditions of pressure, film thickness, shear rate, shear heating, and the strong coupling between these operating conditions. Experimentally, rheological characterisation methods are limited to restricted ranges of pressure and shear rate. Molecule dynamics simulations appear to be a promising approach to fill the gap in fluid characterisation, yet they are constrained in terms of computational time and complexity of the chemical composition of the lubricant. The challenge lies in the integration of experimental and molecular dynamics characterisations of lubricants (under high pressure and high shear rate at various temperatures) into a continuum mechanics-based numerical model of EHD contacts. This model must consider heat generation and transfer within the lubricant and towards the surfaces.

## Outline

This thesis consists of four chapters.

In **Chapter 1**, the state-of-the-art of existing friction prediction methods is reviewed.

In **Chapter 2** the strategy and tools of the present approach are detailed. First, experimental measurements and molecular dynamics (MD) simulations are described to provide a strategy for fluid characterisation. Second, a contact model based on continuum mechanics is constructed.

In **Chapter 3** the results of fluid characterisation are presented. The rheological law is derived from the data obtained.

In **Chapter 4** friction of a thermal non-Newtonian EHD contact is predicted, and compared to friction measurements on experimental test rigs.

# State of the art

Tribology is the scientific study of friction and wear between surfaces in relative motion. Although the term "tribology" wasn't introduced until the 1960s by Jost in his report [122], the first quantitative analysis of friction dates back to the 15th century. It was then that Leonardo da Vinci introduced the concept of the coefficient of friction, defined as the ratio of friction to the applied normal load. His observations also led him to identify two fundamental laws of tribology for dry contact. He concluded that two objects of the same weight but with different contact areas will have the same friction (friction is independent of the nominal contact area) and that friction doubles when the weight doubles (friction is proportional to the normal load) [123]. These two observations were formalised as "laws" by Amonton in 1699 [124]. Later, in 1785, Coulomb experimentally discovered that friction in a dry contact is independent of the relative sliding velocity [125].

Friction leads to energy consumption and wear. One way to reduce this is by lubricating the contact. Compared to the term "tribology", the history of lubrication is considerably older. Primitive humans may have noted that crushed plants and mud facilitated the dragging of stones—a primordial form of lubrication [126, 127]. More intensive use of lubricants had to wait until the invention of the wheel and bearings. Archaeological evidence [128] suggests that ancient civilisations (Egypt, Mesopotamia, and China) already used lubricants to ease the transport of building materials and lubricate their chariots. The Greco-Romans are believed to have used grease mixed with lime and olive oil as a lubricant. Roman statesman Cato the Elder documented in his book "De Agri Cultura" how the by-products of olive oil production were used to lubricate axles [128]. In the Middle Ages, with the widespread use of iron and copper machinery, the second generation of lubricants appeared. These were composed of animal oils, vegetable oils, or a mix of the two. Up until this point, lubrication was still based on empirical selection rather than scientific analysis [129].

The modern scientific understanding of friction, lubrication, and wear began in the 19th century, with the advent of more complex, faster, and larger machines bringing about the need for more intricate and specialised lubricants. With the growth of the oil industry, petroleum lubricants rapidly dominated the field [129]. During this period, several landmark studies were conducted by scientists and engineers, including Hertz [130] and Reynolds [114]. Reynolds' equation describes simplified fluid mechanics of a thin viscous flow of an incompressible fluid and, crucially, it connects the kinematics of the contacting surfaces and its geometry to the generation of pressure in the lubricant. This type of lubrication is termed "hydrodynamic" (as opposed to "hydrostatic" lubrication, where pressure is generated by an external system). The phenomenon of pressure generation is vital to understanding the load-bearing capacity of lubricant films. Indeed, the Reynolds equation serves as the basis for all modern lubrication theories. A comprehensive understanding of these lubrication theories is essential

for optimising the design of mechanical components, extending their lifespan, and minimising energy loss and wear.

## 1.1 Lubrication regimes

Friction or friction coefficient (defined as friction divided by load) in a lubricated contact is a non-linear function of the contact load, the lubricant viscosity and the lubricant sliding velocity. This theory was first proposed by Stribeck in 1902 [131]. According to the Stribeck curve, as shown in Figure 1.1, operating conditions can lead to three different lubrication regimes depending on the thickness of the film separating the solid surfaces.

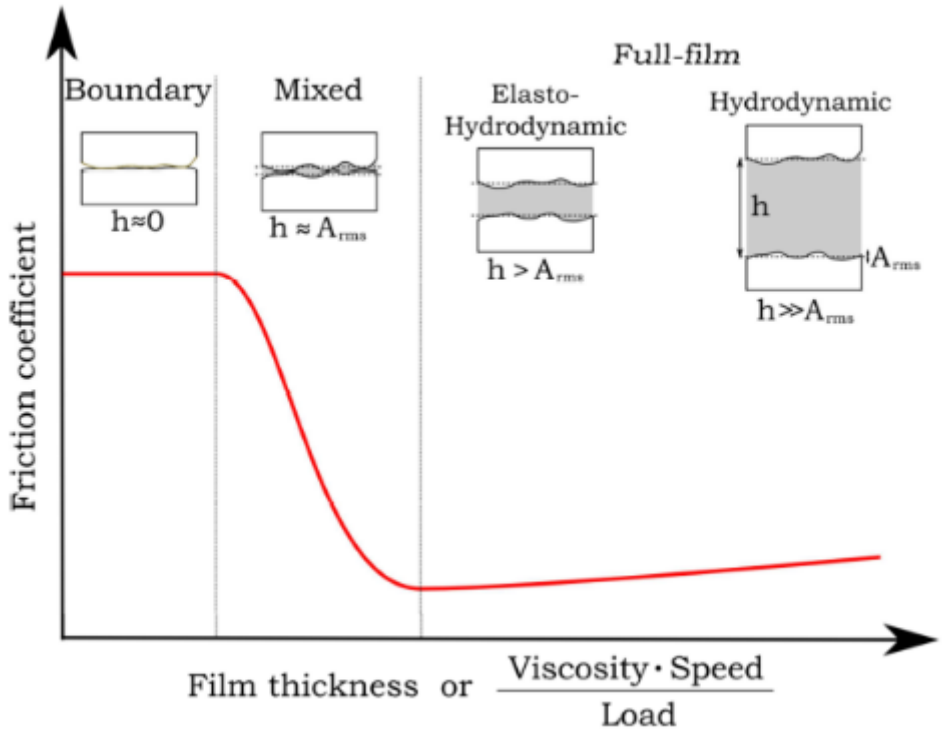


Figure 1.1: Stribeck curve, illustrating the dependence of friction coefficient with the film thickness $h$ or the operating conditions of the lubricated contact. A relation is drawn between the oil film thickness and the root-mean-square roughness $A_{rms}$ of the contacting bodies in each lubrication regime. Adapted from [97].

The three lubrication regimes are boundary lubrication, mixed lubrication, and full-film lubrication. At low sliding speeds, low lubricant viscosity and/or high loads, direct contact between surfaces transpires. This is recognised as the boundary lubrication regime. In this regime, friction exhibits the characteristics of dry friction and is independent of speed. As the fluid viscosity or sliding speed increases, or the load decreases, more lubricant enters the contact, thus augmenting the thickness of the lubricant film. When the film thickness escalates up to a level approximating the average height of the surface asperities, the contact enters the mixed lubrication regime. In this regime, friction diminishes as the film thickness increases to its lower limit. At this juncture, the lubricant film's thickness is roughly three times the average height of the asperities. There is no direct contact between the surfaces, and all the load is borne by the hydrodynamic pressure generated within the

lubricant film. This final regime is referred to as full-film lubrication. In this regime, friction values are low and wear is virtually negligible.

The present study focuses on the full film lubrication regime. With the contacting surfaces separated by a lubricant film, two sub-regimes can be distinguished. Conformal surfaces (e.g. as in journal or thrust bearings) lead to a wide contact area and the pressure is not high enough to cause significant elastic deformation of the surfaces (typically less than 50 MPa). This sub-regime is known as the hydrodynamic (HD) lubrication regime. When the pressure in the contact becomes high enough (up to 3GPa) to deform the surfaces significantly (a few micrometres), it is considered as the elastohydrodynamic (EHD) lubrication regime, which is often associated with non-conforming contact surfaces (e.g. as in rolling element bearings or gears) [132].

High pressure in such regimes leads to a significant change in the viscosity of the lubricant [4]. Predictive film thickness models are based on the fact that the formation of oil film depends on the entrainment velocity and the viscosity at the contact entrance, while friction in the contact depends mainly on the viscosity at the contact centre. Early research focused on predicting film thickness was fulfilled in the 1950s [48, 49]. Nowadays the film thickness predictions are achieved and show very good agreement against experimental results [75, 133, 134].

## 1.2 Friction behaviour in EHD regime

As is the case for dry contacts, friction due to lubricant shearing in the full film EHD contact is typically quantified by the friction coefficient $C_f$, defined as the ratio between the tangential force $F_T$ (opposed to the sliding) and the normal applied load $F_N$.

$$C_f = \frac{F_T}{F_N} \tag{1.1}$$

where the tangential force $F_T$ can enable to derive the contact mean stress $\tau_a$ over the contact area $S$ such as:

$$F_T = \tau_a \times S \tag{1.2}$$

In experiments, friction is measured at a given sliding speed. The average shear stress $\tau_a$ can subsequently be derived from the estimated contact surface area as per the Hertz theory [130]. The Hertz theory delineates the form and size of the contact area and provides an estimation of pressure distribution. On the other hand, another value, namely the slide-to-roll ratio (SRR), is often employed alongside the coefficient of friction. SRR, denoted as SRR=$\frac{\Delta u}{u_e}$, is defined as the ratio between the sliding velocity $\Delta u = u_t - u_b$ and the entrainment velocity $u_e = \frac{(u_t+u_b)}{2}$, where $u_t$ and $u_b$ represent the sliding velocities of the upper and lower surfaces, respectively.

When $C_f$ is plotted with respect to SRR on the same graph, as shown in Figure 1.2, it can be seen that the friction experiences different regimes as the SRR increases. At low SRR, friction increases almost linearly with SRR, which is often attributed to the Newtonian response of the lubricant. This linear dependence holds until the friction coefficient reaches a critical value. Thereafter, the friction coefficient increases slower with SRR. This indicates that friction experiences a shear-thinning regime. These two regimes are shown in the left part of Figure 1.2.

Finally, at very high SRRs, a significant decrease in friction coefficient can be observed, as shown in the right part of the curve in Figure 1.2. This is due to shear heating involving an increase in temperature in the fluid film. This last regime is known as the thermal thinning regime.

However, at moderate to high SRR, the friction coefficient may reach a maximum value and may exhibit a plateau regime, as shown in the centre of Figure 1.2. This means that the friction coefficient no longer increases with the SRR but becomes independent of it, the same way as dry friction. From this maximum friction force, a maximum average shear stress $\tau_L$ can be derived (see Equation 1.2). In the literature, this friction plateau is sometimes referred to as the "limiting shear stress" (LSS) phenomenon. The LSS was first proposed by Smith [5]. He attributed this to the fact that if the stress in the lubricant film exceeds a threshold, it would "break" like a plastic solid. A similar conclusion was reached by Plint [23]. Later, he developed a theory involving a shear plane within the lubricant film which accommodates the difference in speed between the contact surfaces, with solidified lubricant layers on either side of this plane moving at the speed of the two contact surfaces [135]. However, since friction is measured in contact (tribology), it should be distinguished from the shear stress measured in the bulk fluid (rheology). This will be discussed again in the following sections.

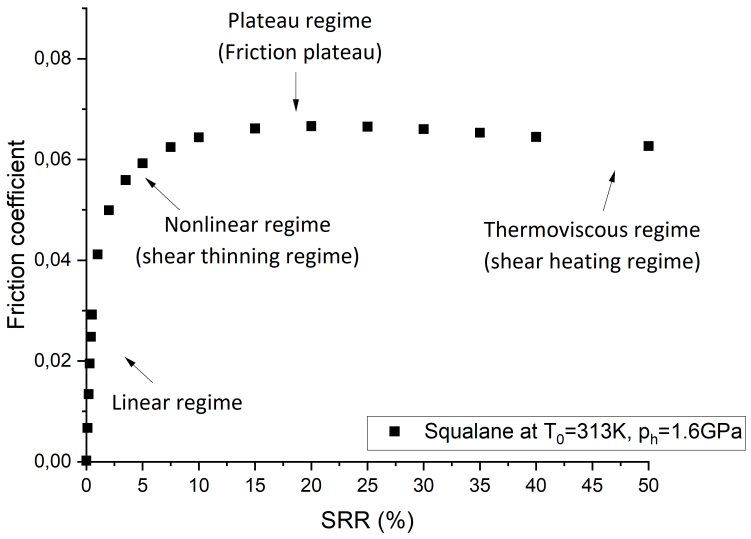


Figure 1.2: A typical friction coefficient versus SRR curve. Experimental data from the present study.

Prediction of friction requires accurately characterising the rheological properties of bulk fluid, as described in the following.

For a Newtonian fluid, the viscosity would be defined as $\tau = \eta\dot{\gamma}$, where $\dot{\gamma}$ is the shear rate. To be able to take into account the previous physical phenomena happening in the EHD contact, we will rather define a generalised viscosity as given by Equation 1.3.

$$\tau = \eta(p, T, \dot{\gamma})\dot{\gamma} \tag{1.3}$$

For the lubricant probed over the range of experimentally accessible pressures and temperatures, an increase in pressure increases viscosity, while an increase in temperature decreases it [136, 137].

In terms of viscosity variation with shear rate, a Newtonian and a shear thinning (non-Newtonian) regime can be identified, as shown in Figure 1.3.

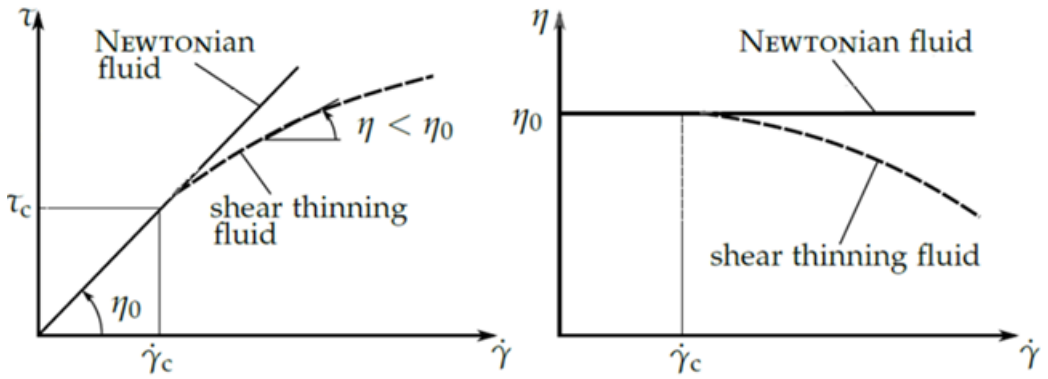


Figure 1.3: Evolution of the bulk shear stress (left) and the dynamic viscosity (right) at constant pressure and temperature with the applied shear rate. A Newtonian fluid presents a constant viscosity, which translates into a constant slope in the shear stress diagram. Adapted from [138].

Like the friction curve, in Figure 1.4, the ultimate behaviour of a bulk lubricant could appear with a maximum shear stress $\tau_{lim}$ or $\tau_{LSS}$. It is important to understand and predict this phenomenon quantitatively as it represents the maximum stress a lubricant could sustain locally in an EHD contact. Ultimately, this would make it possible to minimise energy losses due to friction in contacts by optimising the design of mechanical components and the formulation of lubricants. It is also the most important factor in selecting the lubricant to be used according to Bair and Winer [139].

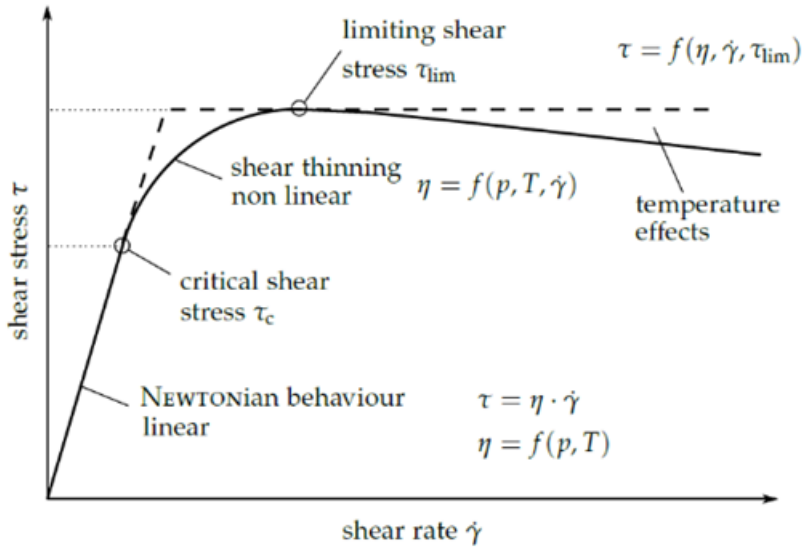


Figure 1.4: Model for shear stress-shear rate in bulk lubricant. Adapted from [6].

While there are reliable models and numerous experimental validations for predicting lubricant thickness [140], the theory fails to predict friction quantitatively [41, 141]. Although progress has recently

been made in predicting friction in the Newtonian and shear thinning regimes [55, 56, 142], predicting friction in the plateau regime remains one of the problems challenging the tribological community. This is mainly due to the lack of characterisation of the rheological properties of the fluid under high pressure and high shear rates (simultaneously). In recent years, there has been a great deal of interest in studying experimentally the rheological properties of fluids under typical EHD nominal conditions. Unfortunately, despite the effort that has been put into developing these empirical models, no rheometric instrument has yet been able to reach the very severe conditions found in some EHD contacts. The high-pressure rheometers have technical limitations and are limited to lower contact pressures (∼1 GPa), and shear stress (few MPa), sometimes far from EHD conditions.

It should be emphasised that, despite some similarities, the viscosity of a fluid is not always equivalent to the apparent viscosity calculated from average values in tribological experiments. That is, one should not simply equate $\tau_a$ (of Figure 1.2) with $\tau$ (of Figure 1.3 and 1.4), nor equate $\tau_L$ with $\tau_{LSS}$. As Bair [7] points out, a stress curve is not a flow curve. The response of fluids to shear rate is not the same as the relationship between mean shear stress and mean shear rate obtained from traction curves. This confusion widely exists in the EHD community [8, 9, 10]. It arises from the assumption that the generation of the friction plateau is an inherent property of the fluid (which is explained in detail below) and that the rheological properties of the fluid can be derived from the friction curve.

LSS describes a fluid volume property, which is a rheological property measured in a rheometer or equivalent. In such a test, the fluid is uniformly loaded, but in a tribometer, it experiences a wide pressure distribution. The stress measured in a rheometer should be considered as the consequence of material property, whereas the stress derived from friction measured in a tribometer is an average value in the whole contact. Therefore, in this paper, the appropriate term to describe this limiting friction value is friction plateau. Most importantly, the rheological properties of the fluid should be characterised in a contact-independent manner. Friction predictions should be based on these a priori properties.

## 1.3 Scenario and characterisation of limited friction

Many hypotheses for the origin of the friction plateau can be found in the literature. In this section, three main families of explanations will be presented:

- the local kinematics of the lubricant.
- the inherent properties of the lubricant.
- the viscous heating in the lubricant.

These scenarios are already detailed in research [11, 12].

### 1.3.1 Local kinematics

One hypothesis to explain the origin of the friction plateau is the local kinematics of the fluid flow. This hypothesis could be divided into three main scenarios: a. wall slip, b. shear localisation and c. plug flow. Note that in some local kinematics scenarios, modification of the laminar flow is induced by the vitrification of the lubricant. In this case Section 1.3.2 and Section 1.3.1 are closely related. In some others, it is induced by the thermal dissipation in the fluid film, which relates Section 1.3.2 and Section 1.3.3.

**a Wall slip**

The assumption of no-slip boundary conditions between liquid-solid interfaces is questionable in practice. Evidence of boundary slip in contacts has been demonstrated both experimentally [13, 14] and by molecular dynamic simulations [15, 16] under specific operating conditions. Schnell [17] first demonstrated experimentally that wall slip can occur between a hydrophobic surface and water. Subsequent studies have further demonstrated that this phenomenon occurs not only in simple fluids (e.g. water and hexadecane) [17, 18] but also in complex fluids (e.g. polymers) [19], and not only on the hydrophobic surface [17, 20] but also on the smooth surface, even under total wetting conditions [19]. This observation is supported by molecular dynamics simulations [15]. Li et al. [21] further suggested that the slip length increases non-linearly with shear rate and exponentially with pressure.

Further experimental results provided evidence for wall slip in contact. For example, Wong et al. [143] recorded a series of real-time interferograms on impact dimple with a polybutene oil (PB1300) using an optical EHD experimental platform. They also varied the velocity in the ball-disc contact. These impact pit interferograms are shown in Figure 1.5.

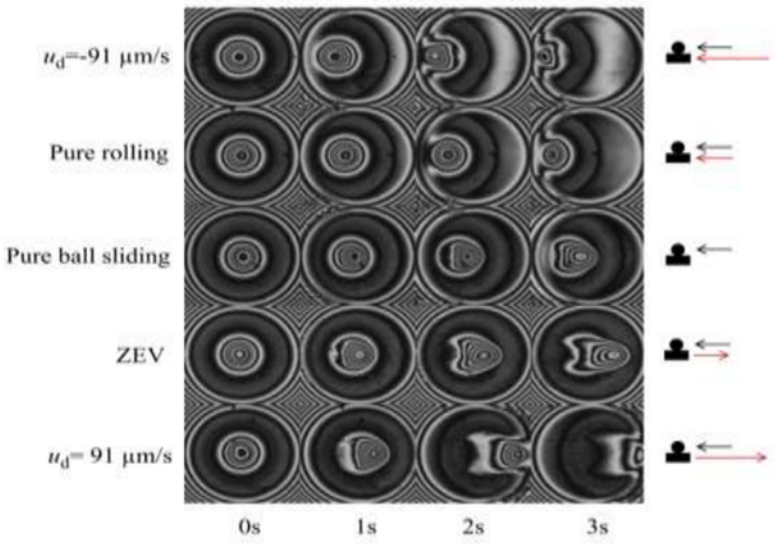


Figure 1.5: Interferograms of the impact dimple displacement at different configurations for constant ball velocity and t=4s. Adapted from [143].

The black and red arrows on the right-hand side of the diagram indicate the magnitude and direction of the velocity in the test. It was concluded by the authors that their displacement depends only on the motion of the disc and not on the motion of the ball. Furthermore, by varying only the speed of the ball, with a maximum of 75 $\mu m/s$, they found that the speed of the dimple was constant and approximately equal to the speed of the disc. Beyond this value, the speed of the dimple increases as the ball speed increases. They concluded that there was a wall slip at both the lubricant-ball interface and the lubricant-disc interface.

In other studies [144, 145], tests carried out with polyphenyl ether (5P4E) at room temperature with a maximum pressure of 1.33 GPa showed no dimple displacement at all. They attributed this to the lubricant being in a glassy state. Kaneta et al. [22], by direct measurement of the film thickness in the EHD contact, also found that the lubricant film exhibits solid-like behaviour in the pure rolling

case and evidence of wall slip occurs at, or near, the interfaces when the film is very thin.

Finally, Pit et al. [18] suspect that wall slip was the origin of the friction plateau behaviour when they showed evidence of wall slip in a two-sapphire disc contact with hexadecane. They concluded from their result that the molecular scale roughness will greatly inhibit the occurrence of wall slip. In the absence of wall slip, momentum will be transferred from the surface to the fluid, thus increasing the effective friction. Despite this evidence, wall slip has not been directly observed in representative EHD contacts, presumably due to the extreme transit times, low film thicknesses and the presence of relative motion at the contact surfaces.

**b Shear localisation**

The second scenario assumes that friction plateau occurs when shear deformation becomes localised and forms shear bands in the lubricant film. Thermal localisation has been observed experimentally by Bair et al. [24]. The recent experimental results identified another type of shear localisation [25]: isothermal shear localisation. Isothermal localisation occurs when the pressure is close to the glass transition pressure of the lubricant. This implied that the shear localisation can be either thermally induced or mechanically induced.

Plint [23] first uses shear localisation to explain the friction plateau. He explained the friction plateau measured on two-roller machines by the limiting shear strength of the lubricant (hydrocarbon-based lubricant). As the value of the plateau depended on the temperature of the lubricant, he suggested that a shear failure developed in the fluid film and described this localised deformation as a thermally softened region. Unfortunately, the formation of these shear bands is very difficult to characterise, since conventional rheology and tribology measurements are average measurements in a volume of fluid, whereas by definition it is a local process. Nevertheless, observations of these shear bands were made in 1993 in high-pressure flow visualisation cells, i.e. outside contact (see Bair et al. [24] for more details). 10 years later, Bair and McCabe [26] took this exploration a step further. They show that two types of shear bands can be observed (Figure 1.6), one aligned with the flow direction and the other aligned with the cross-film direction. They also successfully predicted the formation of the shear band using the Mohr-Coulomb slip model. The shear stress in the lubricant film could be unevenly distributed due to heat generation, and thus the stress would be "localised" and form a shear band. This should be due to the strong dependence between lubricant viscosity and temperature and the poor thermal conductivity of lubricants. This results in a temperature gradient in the lubricant film, which can lead to inhomogeneous shear. They were able to distinguish between two types of shear bands, thermally-induced and mechanically-induced, depending on the operating conditions.

Nevertheless, Bair never linked these findings in rheological experiments to his tribological results, so they could not be used to explain the formation of friction plateaus. These shear bands have never been observed in a living EHD contact. However, this does not stop some researchers from suggesting that shear localisation may cause a friction plateau [11, 27].

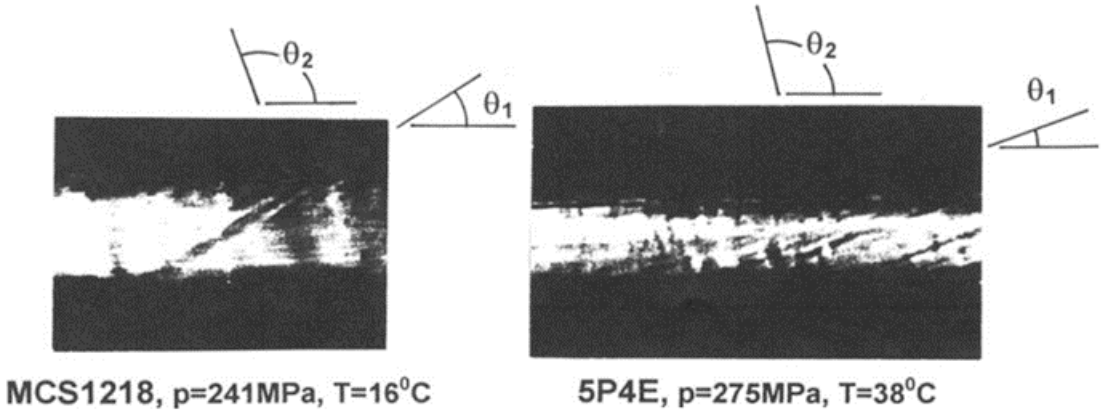


Figure 1.6: Micrographs of mechanical shear bands observed in a high-pressure flow visualisation cell at the given state conditions. Adapted from [26].

### c Plug flow

The last scenario was first proposed by Jacobson [28]. He suggested that a large portion of lubricant behaves as a solid core or plug due to extremely high viscosity while a very thin zone near the contacting solid surface is sheared. The core is in a liquid-glassy state. A schematic of the plug flow is shown in Figure 1.7.

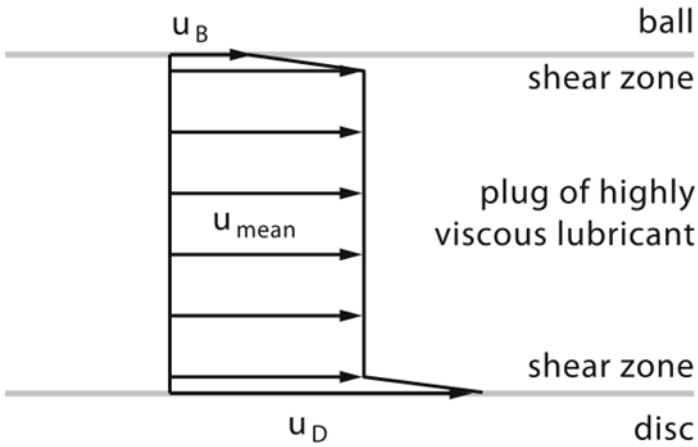


Figure 1.7: Plug flow mechanism and shear zones in through-film profile. Adapted from [29].

Since then, the existence of this mechanism has been demonstrated by experimental results obtained by different methods. For instance, Šperka et al. [29] used the Particle Tracking Velocimetry (PTV) technique to determine the velocity profiles in an EHD contact (with Hertzian pressure around 600 MPa) of mineral oil with graphite nanoparticles. They showed that the velocities of particles are different through the film thickness at the entrance of contact but later become uniform in the contact and approximately equal to the mean velocity of the lubricant. They attributed this result to the formation of a plug-flow mechanism where a large portion of lubricant flows at mean velocity and velocity gradient occurs near solid surfaces (Figure 1.8). Ponjavic et al. [30] used photo bleached-fluorescence imaging velocimetry to visualise a contact of polybutene with a sphere and a flat surface. Their results show the existence of critical pressure below which the velocity profile is nearly linear

and above which a plug flow could occur. This critical pressure was found to be dependent on the molecular weight of the tested oils (PB920, PB1300, PB2300).

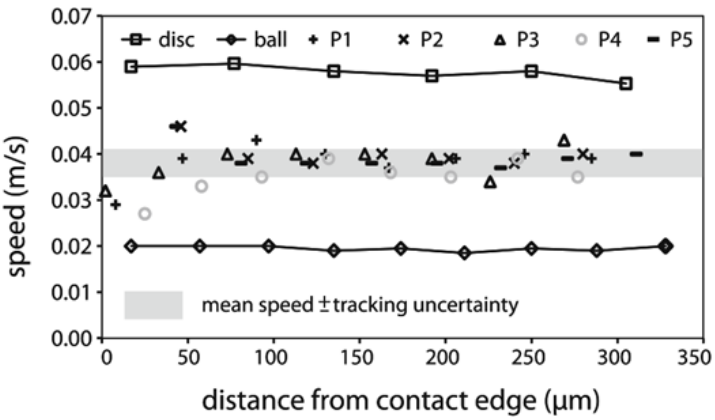


Figure 1.8: Optically tracked particle speed profiles compared with the speed of disc and ball. The grey area depicts the mean lubricant speed, including tracking speed uncertainty. Adapted from [29].

In a later study of friction in EHD contact using molecular dynamics simulations, Ewen et al. [31] found that for cases where friction plateau did not occur, only Couette flow or shear localisation is observed in the fluid. In contrast, the presence of friction plateau is accompanied by a transition from shear localisation to plug flow. Although more research is needed to confirm this relation, plug flow presents itself as an interesting scenario because it can link several scenarios stated previously. The core is mostly considered to be in a glassy state, making it a case of shear localisation where the shear is localised in a zone near the surface. And if the thickness of the shear region becomes small to the molecular size, it could be considered as wall slip.

Although there is growing evidence that very high shear stresses in EHD contacts produce local kinematic transitions that lead to deviations from Couette flow in both bulk lubricant and in contact, such transitions are difficult to characterise experimentally, and their effect on the friction response and the deeper physical mechanism are not well-understood [11, 32].

Moreover, these mechanisms may involve other parameters relating to contact complexity. For instance, Porras-Vazquez et al. [16] show with MD simulations that a change of surface roughness or wettability could change the local kinematics. However, if the film thickness is high enough, the friction response is not impacted.

### 1.3.2 Intrinsic property of the lubricant: molecular structure vs phase change

Friction plateau being an inherent characteristic of the lubricant is the main assumption widespread in the literature [33], but there exist two approaches that are dissociated. For some researchers, the generation of friction plateau is thought to depend on the nature of the fluid, i.e. the structure of the molecule [31, 34]. While for the others the friction plateau generation is dependent on its thermodynamic state [16, 35].

Research relating EHD friction to the molecular structure of the lubricants was initially driven by the formulation of traction fluids used when high friction was required. Hentschel [146] found that irregularly shaped molecules have higher friction than spherical or elliptical molecules. Subsequently,

Muraki [147] studied both cyclic and branched molecules and found that the EHD friction coefficient measured with the latter increased with branching. Tsubouchi et al. [148] further summarised five characteristics that favour high EHD friction: (1) high molecular stiffness, (2) large size, (3) short chain length, (4) high melting point and (5) low molecular polarity. This is because, at very high pressures and strain rates, intermolecular slip is hindered if the molecules cannot be easily rotated or deformed. Besides, high polarity prevents molecules from stacking closely together. Conversely, it would rather allow the molecules to maintain a certain space, making them easy to rotate or deform. In addition, molecules with a linear structure are more likely to align in different layers, minimising their interactions and reducing friction.

Zhang et al. [34] carried out a series of tribometer tests on 38 base oils. The isothermal EHD friction curves obtained showed that the traction fluids reached their limits under the test conditions (slid-to-roll ratio up to 50%), while the low friction base oils did not. They concluded that the molecular structure of the base fluid has a significant effect on friction in EHD contacts. Around the same time, Ewen et al. [31] used both tribometer experiments and molecular dynamic simulations of a lubricant sheared between two confined surfaces to investigate the effect of molecular structure, pressure and shear rate on friction in EHD contact for four fluids, two lubricants: Squalane, DEHS, and two traction fluids DM2H, DCMP. The results of their experiments and simulations are shown in Figure 1.9.

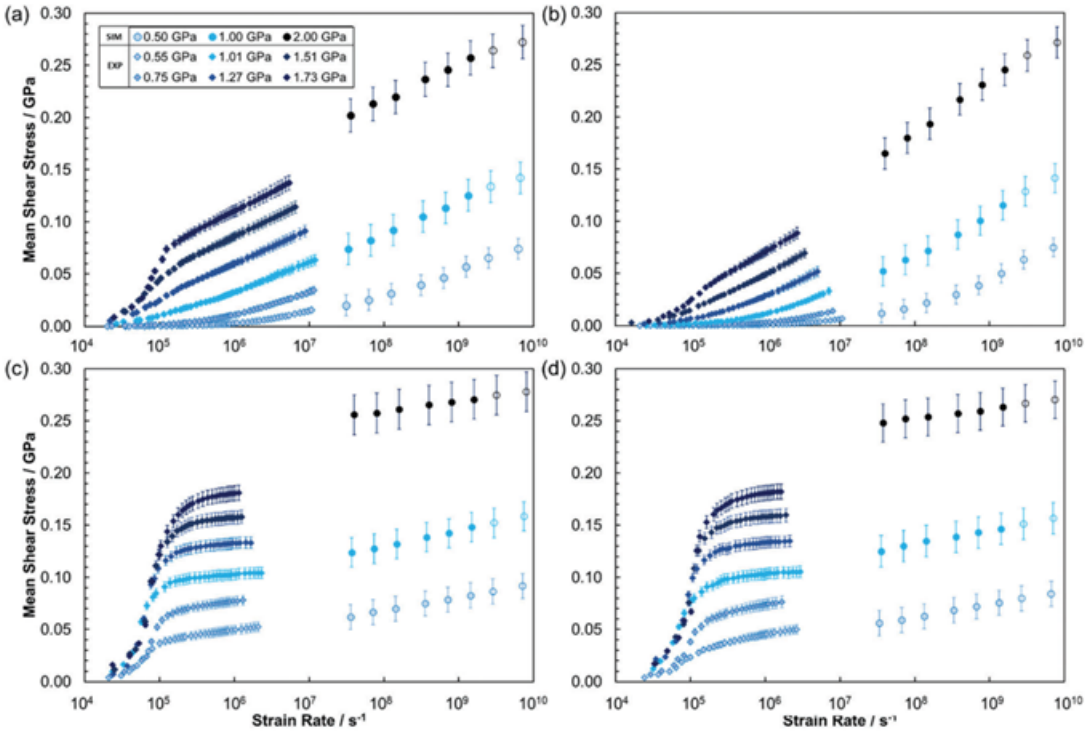


Figure 1.9: Mean shear stress vs log(strain rate) for fluids at 80℃ and 0.5-2.0 GP; Squalane (a), DEHS (b), DM2H (c), DCMP (d). Thermally-corrected experimental data are shown as filled diamonds. Isothermal NEMD data are shown as filled circles, and the NEMD data with a temperature rise are shown as open circles. Adapted from [31].

They conclude from the experimental results that friction plateau is observed under the test conditions for the two traction fluids in Figure 1.9 (c) and (d). In addition, no significant differences are observed

in the mean shear stress measured on fluids with similar molecular structures. For lubricants in Figure 1.9 (a) and (b), no friction plateau is observed and the difference in mean shear stress between them has been attributed to the number and type of branched chains the molecules have. For NEMD simulation results, good agreement was found between simulations and experiments, especially for lubricants. For traction fluids, the overestimated stress and friction plateau values noted for MD simulations may come from the force field or the difference in thermal dissipation due to lower film thickness in simulations than in experiments. They concluded that friction plateau can occur in traction fluids but not in lubricants, and the difference is related to the structure of the molecule.

However, the "intrinsic property" conjecture has always been challenged by another slightly different approach. It states that the friction plateau generation does not depend on the nature of the lubricant but on its thermodynamic (liquid or glassy) state [16, 35]. Therefore the friction plateau is achievable under specific thermodynamic conditions whatever the nature of the fluid. These conditions vary according to the lubricant.

Glass transition refers to the molecular structure of the fluid starting to behave like a solid due to the freezing of the microscopic Brownian diffusion. This transition is difficult to define, as it depends on thermodynamics [149]. 35 years ago, Alsaad and coworkers [36] already characterized the influence of pressure and temperature on the onset of glass transition of 5P4E thanks to Brillouin Light Scattering and dilatometry experiments. They compared the pressure and temperature nominal conditions of transition in a volume of fluid with the operating conditions in a contact. They concluded that glass transition could be expected to occur in EHD contact and influence friction and film thickness. Other studies directly derived glass transition characterisation from friction experiments. Johnson and Cameron [37] measured a friction plateau (or limitation of traction) at intermediate sliding speed (0.1-0.5 $^{m}/_{s}$) that could be explained by a plastic solid behaviour of the lubricant beyond critical shear stress. Johnson and Roberts [38] also highlighted a viscoelastic transition of mineral oil with increasing pressure, characterised by a point contact disk machine. Ohno et al. [39] further demonstrated that as the pressure increases, the behaviour of the lubricant transitions from the viscous regime to the viscoelastic regime and eventually to the elastoplastic regime.

Although these results are based on experiments without simultaneous friction measurements and therefore do not directly explain the physical origin of the friction plateau, they seem to show that the molecule of the fluid undergoing glass transition is a necessary condition for the friction plateau to occur. For a traction-like fluid (benzyl benzoate), Ndiaye et al. [40] correlated the pressure at which a friction plateau can be measured experimentally with the nominal glass transition pressure of the fluid, measured in a volume of fluid [35]. They showed that for Hertzian pressures below the glass transition pressure of the fluid, no friction plateau is observed. For such pressures, the macroscopic apparent viscosity of the contacts, expressed as the ratio of the average shear stress to the central shear rate, appears to increase exponentially with pressure. On the other hand, as soon as the Hertzian pressure exceeds the glass transition pressure of the lubricant, the apparent viscosity of the contact stabilised and fiction tests show a plateau.

This correlation was subsequently confirmed by Porras-Vasquez et al. [16], who performed non-equilibrium molecular dynamic simulations (see Chapter 2) on two fluids (squalane and benzyl benzoate). They compared their numerical results with experimental friction data measured on a tribometer. Based on the phase diagrams they constructed for the two fluids, they selected two operating conditions corresponding to either a liquid or a solid-like state. They found that for both fluids and in both numerical simulations and tribometer experiments, no friction plateau was observed in the liquid state operating conditions (Figure 1.10 (a) and (c)). However, for the solid-state conditions,

the friction plateau was observed for both fluids in simulations and experiments (Figure 1.10 (b) and (d)).

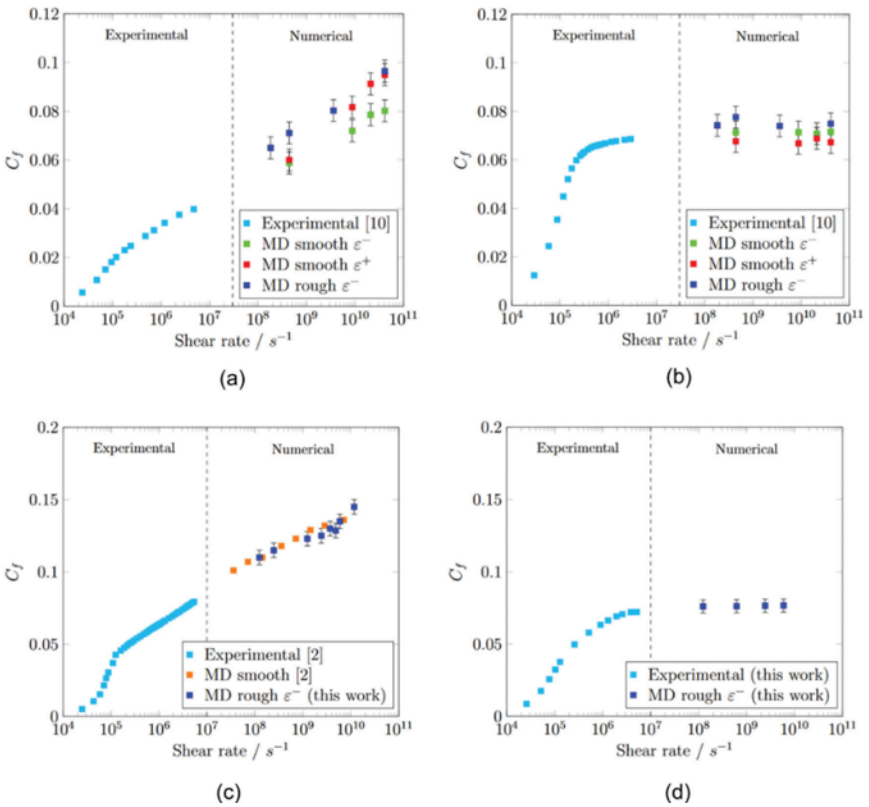


Figure 1.10: Coefficient of friction versus shear rate for Benzyl Benzoate at 313K at (a) 0.5GPa and (b) 2GPa, and Squalane at (c) 353K and 2GPa and (d) 313K and 1.2GPa. For the latter case, a direct comparison is made between simulations and friction measurements. The dashed line marks the separation between experimental (left) and MD results (right). Adapted from [16].

They also compared numerical simulations carried out on smooth and rough surfaces. Their results showed that the coefficient of friction is of the same order of magnitude regardless of the surface. This led them to conclude that in systems with sufficient oil film thickness, the friction response is independent of the contact surface.

### 1.3.3 Thermal effects

Severe conditions in EHD contact may induce viscous dissipation which locally increases the lubricant temperature in the contact, up to 100 ℃ locally [41, 42]. This is more likely to occur when the contact conditions are a combination of factors such as high pressure up to several GPa [11], high shear rates up to $10^7 s^{-1}$, and high fluid viscosity. The study of the thermal effects in EHL first appeared in the study by Cheng et al. [43, 44] in 1965, and subsequently, many authors have proposed different ways to explain the rise of temperature in oil film [45, 46, 47]. As mentioned previously, the temperature increase in EHD contact can lead to a significant decrease in fluid viscosity. Yet, it has long been neglected in the literature. Thus, in early theoretical studies of EHL such as in Dowson and Higginson's work [48] or Grubin's work [49], the consequence of thermal effects on viscosity was ignored, and the viscosity value in the oil film was assumed to be an only pressure-dependent. It was

Crook [50, 51] in 1961 who first revealed the impact of shear heating on the viscosity of lubricants.

It was also Crook [51] who first made the connection between shear heating and friction. He attributes the maximum friction values to the reduction in viscosity due to heat generation, while the reduction in friction at very high shear rates means that the thermal effect becomes dominant. However, in several studies (particularly some of those mentioned below) the operating conditions, either experimental or numerical, are assumed to be isothermal. This means that shear heating cannot explain the friction plateau. Ndiaye [12] found that friction plateaus were observed in contacts with carefully selected operating conditions to minimise shear heating and operate in apparent isothermal conditions. However, it is important to note that they did not directly measure or control the temperature inside the contact, but rather controlled the temperature at the contact entrance and determined the heat generation by monitoring the temperature of oil in the reservoir. More direct evidence comes from simulations. For example, Habchi et al. [52], Porras-Vasquez et al. [16] and Ewen et al. [53] performed different simulations in a (nominal) isothermal environment, and friction plateau was observed. Furthermore, the results of these simulations were successfully compared with the experimental data. In conclusion, the effect of shear heating on the friction response remains unclear. At present, shear heating is mainly associated with friction plateau in shear localisation theory [23, 24, 25, 26, 54].

## 1.4 Characterisation of friction plateau

Assuming that the friction plateau is an inherent property of the fluid and according to this shortcut that the rheological properties of the fluid can be obtained from the friction curve, researchers directly describe the friction plateau using empirical models derived from tribological experiments [55, 56, 57, 58, 59, 60, 61, 62, 63, 64]. There are of course more practical reasons for this, namely the difficulty of reproducing the extreme conditions of EHD contacts in rheological experiments [11]. However, as these empirical laws are derived from the traction curve rather than the flow curve, they do not reflect the nature of the fluid itself, which prevents them from being true predictions. This type of friction prediction approach is presented in the classical form of Equation 1.4.

$$F_T = \tau_a \times S \quad with \quad \begin{cases} \tau_a = \eta\dot{\gamma} & for \quad \eta\dot{\gamma} < \tau_L \\ \tau_a = \tau_L & for \quad \eta\dot{\gamma} > \tau_L \end{cases} \tag{1.4}$$

The pioneering experimental work on friction plateau characterisation was done by Johnson and Tevaarwerk [9] in 1977. They performed friction experiments using a disc machine and investigated the dependence of the limiting stress value on pressure. According to their theory, there is a linear relationship between the mean shear stress derived from the friction plateau $\tau_L$ and the mean pressure in contact $\overline{p} = \frac{2}{3}p_h$, where $p_h$ is the Hertzian pressure (maximum pressure) in the contact area. The relation is shown in the Equation 1.5

$$\tau_L = \tau_0 + \alpha\overline{p} \tag{1.5}$$

Again, it is important to note that in their research $\tau_L$ was determined by tribological experiments and should be distinguished from the rheologically determined LSS value $\tau_{LSS}$. $\tau_0$ is an extrapolation of the friction plateau value at zero pressure. However, it has no physical meaning as there is no friction plateau at this pressure. Its typical value was in the range of 1-5 MPa, extrapolated by

Jacobson [150]. $\alpha$ is called the $\tau_L$-pressure coefficient with a typical value in the range of 0.05-0.1, measured by Johnson and Tevaarwerk [9].

This model was further developed by others, including Höglund and Jacobson [66, 67], Hirst and Moore [68], and Evans and Johnson [65]. They extended the test to a wider range of fluids, including mineral oil, synthetic oil and grease, different contact surfaces, including steel and tungsten, and a wider range of pressures and temperatures. All the researchers show that $\tau_L$ is proportional to the mean pressure in contact, regardless of the type of fluid. Höglund and Jacobson [66] found that there is a critical pressure at which the increase in $\tau_L$ with pressure changes from non-linear to linear. They called this critical pressure the "solidification pressure", sometimes interpreted as the glass transition pressure [12]. They also found that this critical pressure increases with temperature.

For the difference due to fluid type, Höglund and Jacobson [66, 67] found that all mineral oils show a consistent $\tau_L$-pressure dependence, meaning that they have consistent $\partial\tau_L/\partial p$. In the case of synthetic oils, it is highly dependent on their chemical nature (molecular structure). Finally, for different contact surfaces (steel and tungsten carbide), Hirst and Moore [68] showed that the $\tau_L$ value is independent of the nature of the contact surfaces. However, considering that conventional tungsten and steel have very similar thermal diffusivity ($k/(\rho c_s)$), where $k$ is the thermal conductivity, $\rho$ the density and $c_s$ the specific heat capacity of solid), this last conclusion may not be entirely correct because of the similarity of the thermal effect in two different contact surfaces.

Moreover, $\tau_L$ may be temperature dependent. Höglund and Jacobson [66] first showed that $\alpha$ decreases with temperature. Later, Evans and Johnson [65] tested two lubricants (HVI and 5P4E) and a traction fluid (Santotrac). They found that lubricant's $\tau_L$ is independent of temperature, but for traction fluid, $\tau_L$ decreases when temperature increases.

In addition to the above studies based on tribological experiments, there have also been studies based on rheological experiments. In 1990, Bair and Winer [69] characterised the pressure and temperature dependence of $\tau_{LSS}$ using a high shear stress rheometer with two fluids (a mineral oil LVI260 and a synthetic oil 5P4E). Their results show that, at a given temperature, the $\tau_{LSS}$ increases with pressure but the $\tau_{LSS}$-pressure coefficient is not a constant. Due to the lower pressures in the experiments (<200 MPa), the tested fluids considered did not enter the glassy state. This finding is similar to the previously mentioned Höglund and Jacobson [66] result that the $\tau_L$ of the fluid exhibits a nonlinear increase before a critical pressure, which is considered to be the glass transition pressure.

Later in 1992, Bair and Winer [42] carried out further studies of Evans and Johnson [65] performed in a high-pressure rheometer to investigate the pressure and temperature dependence of $\tau_{LSS}$. They extended the tests to a wider range of pressures, above and below the glass transition pressure, and more temperatures. The results are shown in Figure 1.11. According to the results, for the lubricant 5P4E, $\tau_{LSS}$ depends on both pressure and temperature. This variation follows a model shown in Equation 1.6

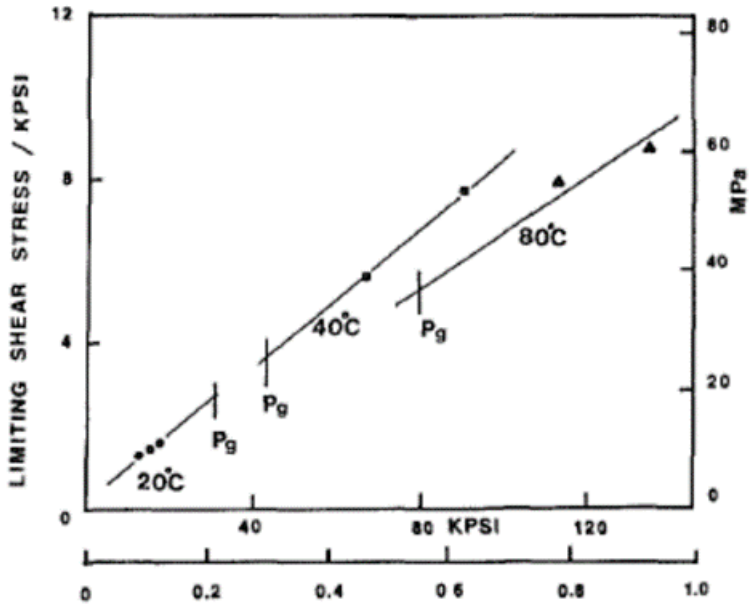


Figure 1.11: Pressure and temperature dependence of LSS. Adapted from [139].

$$\tau_{LSS}(p,T) = \lambda(T) \times p \quad with \quad \lambda(T) = 0.095 - 0.0035T \tag{1.6}$$

Note that in Equation 1.6, $p$ and $T$ are coupled, and $p$ is the pressure in the cell therefore homogeneous everywhere in the fluid. Similar models for $\tau_L(p,T)$ with coupled $p$ and $T$ proposed by others can be found in the literature [151, 152].

In a recent study, Ndiaye et al. [40] proposed for the first time an uncoupled $\tau_L$ model. They used a ball-disc tribometer to test two fluids, the benzyl benzoate and a lubricant (Shell T9). The $\tau_L$ is described by the Equation 1.7

$$\tau_L(p,T) = \Lambda\overline{p} - \beta T + \tau_0 \tag{1.7}$$

where $\Lambda$ is the $\tau_L$-pressure coefficient, $\beta$ is the $\tau_L$-temperature coefficient and $\tau_0$ is a constant. These parameters depend on the nature of the fluid. Here the average pressure $\overline{p}$ was used since they derived this model from tribological experiments in contact.

Finally, we can conclude that the value of $\tau_L$ or $\tau_{LSS}$ depends on the nature of the fluid, pressure, temperature and probably also on the contact surface. Despite the many attempts, the limitations of these approaches are obvious. Most models [9, 40, 65, 66, 67, 68] are derived from tribological tests and are therefore not predictive. Besides, the $\tau_L$ value given by these models is a single, integrated value that does not take into account local variation. This cannot be used to derive a generalised friction prediction method. More importantly, these models are empirical and do not take into account the physical mechanisms behind the limiting phenomena of shear stress/friction.

## 1.5 Towards a quantitative friction prediction

Friction in EHL is governed by the rheological behaviour of lubricants. In order to predict friction, the first requirement is to accurately characterise their rheological properties. Following Equation 1.3, a viscosity model must be defined.

In some early work [70], researchers attempted to use apparent viscosity derived from tribological tests to characterise friction. As more accurate friction measurements became available, they turned to characterising friction directly by fitting equations to traction curves, such as the Johnson and Tevaarwerk equation [9]. This model was later accepted by researchers and further refined to better fit experimental results and to account for temperature rise and pressure distribution in contact [65, 71]. Based on these characterisations, numerous empirical models have been developed, including sophisticated numerical models such as those of Jacod et al. [57, 72] and also some simple analytical tools for engineering purposes such as Olver and Spikes [58] and Morales-Espejel and Wemekamp [59]. Despite these efforts, these methods use data derived from tribological experiments to reproduce the friction value of the same experiments. Such methods work a posteriori and their use is limited to operating conditions, making it impossible to extend them to other conditions or lubricants.

Significant advances in friction prediction have been made since the breakthrough of high-pressure viscometer technology to measure the rheological properties of bulk fluids. The contact-independent data collected over the range of pressure and temperature experienced in a contact enable accurate friction prediction if a relevant viscosity model could be derived from them. Using these data, researchers have successfully predicted EHD friction for both isothermal [60, 61, 62, 73] and thermal environments [63] in Newtonian and shear thinning regimes. These pioneering works have inspired many subsequent studies of thermal EHD contact, such as Doki-Thonon [74], Wheeler [75], Liu et al.[56] and Björling et al. [55]. Despite the quality of the results obtained, a typical drawback of these prediction approaches is the inability to predict the friction plateau. Therefore, friction plateau models derived from the tribological experiment results are usually used to manually add an upper limit and reproduce the experimental friction curves.

At this point, we can summarise the main drawbacks of existing approaches to predict friction as follows:

- They are based on the assumption that friction plateaus are intrinsic fluid behaviour, on which there is no consensus.
- These friction plateau models are purely empirical, derived from contact-dependent data. Which do not take into account the complexity of the real contact and are not predictive. To make a true friction prediction, the first requirement is to determine the rheological properties of the fluids a priori, and this determination should be contact-independent.

Due to the experimental challenges associated with characterising fluid on independent rheometers under conditions similar to an EHD contact (extreme pressure and shear), numerical simulations like molecular dynamics present an interesting opportunity.

Voeltzel et al. [78] proposed a complete characterisation of an ionic liquid using MD simulations, along with a Carreau (generalised viscosity) model [76], as demonstrated in Equation 1.8.

$$\eta = \eta_N \left(1 + \frac{\dot{\gamma}^2}{\dot{\gamma}_c}\right)^{\frac{N-1}{2}} \tag{1.8}$$

They discovered that the Carreau model fits the MD data very well as long as $\eta_N$ (the so-called "Newtonian viscosity"), the critical shear rate $\dot{\gamma}_c$, and the Carreau exponent $N$ vary with pressure and temperature. This is in contrast to previous literature where the Carreau model was used with constant $\dot{\gamma}_c$ and $N$ [79].

Meanwhile, Jadhao and Robbins [80] characterised the viscosity of squalane using MD data and fitted results with the Eyring model [77] (as shown in Equation 1.9) across a wide range of pressures, temperatures, and shear rates. In their approach, two fitting parameters of the Eyring law were determined, namely $\eta_N$ and the Eyring stress $\tau_e$.

$$\eta = \frac{\tau_e}{\dot{\gamma}} \sinh^{-1}\left(\frac{\eta_N \dot{\gamma}}{\tau_e}\right) \tag{1.9}$$

These findings provide a potential route to accurately describe the rheology of fluids under EHL conditions. Therefore, an a priori fluid characterisation of fluid rheology is crucial. This includes the Newtonian viscosity ($\eta_N$), the critical shear rate ($\dot{\gamma}_c$), Eyring stress ($\tau_e$), and possibly the Carreau exponent (depending on the model used), and their variations with pressure, temperature, and shear rate. These could be achieved with the help of MD simulations and would provide an ideal complement to experimental approaches. Together, they could form the foundation of a quantitative fluid characterisation approach to capture the intrinsic fluid behaviour, independent of tribology experiments.

Finally, to align with experimental friction measurements, a quantitative friction prediction model would need to incorporate the previously defined rheological intrinsic behaviour of the lubricant and take into account the pressure and temperature distribution across the contact area. This can be achieved by solving the equilibrium relations of continuum mechanics (mass, force, energy equilibrium) inside and around the contact, as outlined by Habchi et al. [61], Doki-Thonon [74], and Björling et al. [55].

## 1.6 Conclusion

Lubricants in EHD contact are exposed to severe conditions: high pressures, high shear rates, and abrupt changes in pressure and temperature in relation to shear rate behaviour across the contact area. These extreme conditions lead to distinctive macroscopically observed friction, diverging from a linear increase and into a friction plateau. Various hypotheses and scenarios have been proposed in the literature to account for this, yet none have been experimentally validated, and there is no accepted consensus in the literature.

Significant strides in friction prediction have been made alongside enhancements in experimental rheological fluid property characterisation. However, an a priori description of the fluid's limiting response remains absent. As a result, the current prediction approach is unable to predict the friction plateau. It still relies on empirical models derived from tribological experiments, which prevents it from being deemed truly predictive. Numerical methodologies, such as molecular dynamics simulations, appear to be the ideal tools to bridge this gap, providing a necessary a priori complement to the rheological characterisation of the lubricant. Ultimately, a quantitative EHD friction prediction would need to incorporate an appropriate intrinsic characterisation of the lubricant into continuum mechanics equations able to consider the pressure and temperature distribution across the EHD contact area.

# Strategy and methodology

The proposed friction prediction approach consists of two parts: (I) the numerical characterisation of the rheological properties of fluids at the molecular scale and (II) the implementation of these properties in a continuum model at the contact scale. The former involves predicting the intrinsic properties of the fluids in an isothermal, isobaric environment with the help of molecular dynamic (MD) simulations. The latter at the scale of the contact area, considers the distribution of the operating parameters such as pressure, temperature, and film thickness. A finite element (FE) contact model is built to simulate a realistic EHD point contact considering the thermal effect and non-Newtonian lubricants. It should lead to a numerical friction prediction comparable to experimental measurements on tribometers.

## 2.1 Strategy

### 2.1.1 Overall strategy

Thus far, despite recent significant advancements [6, 87, 88, 153, 154], the limitations of experimental characterisation tools for lubricants have impeded the formulation of robust constitutive equations under extreme pressure and shear conditions. This has hindered the prediction of friction plateaus in contact. Owing to this insufficient rheological characterisation, the study leans towards numerical approaches.

As previously mentioned, molecular dynamics (MD) simulations overcome experimental challenges by not being constrained by ranges of temperature, pressure, or shear rate. However, MD simulations and experiments face contrasting difficulties. While experiments struggle to attain high sliding and high pressure, simulations at low sliding necessitate longer simulation times to achieve a steady state, which is occasionally unattainable due to computing power limitations. Consequently, these two tools complement one another in characterizing the fluid bulk properties.

On the other hand, friction as a macroscopic quantity is challenging to obtain directly from MD simulations. Indeed, due to limited computing power, current MD simulations are confined to a relatively small scale and are not applicable to the scale of a real contact area (e.g. as in rolling element bearings). Consequently, MD simulations cannot reproduce the complexity of the EHD contact (described in Chapter 1). Simulations on a larger scale (in terms of time and space) are necessary. A finite element method (FEM) appears to be a suitable numerical approach to solving continuum mechanics equations. This approach enables coupling the flow with the solid surface deformations and the thermal dissipation in the contact. However, a constitutive equation for the

lubricant is required in the FEM model.

Until now, previous continuum approaches [55, 56, 57, 58, 59, 60, 61, 62, 63, 64] implemented two distinct constitutive equations: a rheological law for low shear stresses and an empirical friction plateau model for high shear stress, as presented in Section 1.4. This facilitated the modelling of a friction plateau but with the disadvantage of being non-predictive, as previously mentioned. In the current approach, we attempt to implement a single rheological model that accurately describes the shear-thinning behaviour of fluids while also being able to predict the generation of a friction plateau.

To validate this approach, the numerical friction data will be compared with friction measurements.

### 2.1.2 Choice of the rheology model

One of the classical approaches to model non-Newtonian rheology in the literature uses the Carreau-type models [56, 60, 61, 63, 73], which adequately describes the linear and shear-thinning regime but fails to capture the plateau regime as long as the critical shear rate $\dot{\gamma}_c$ and Carreau exponent $N$ chosen as constant.

On the other hand, the Eyring model is based on the thermal activation concept. Macroscopic models linking molecular scale behaviour to macroscopic friction originated with the work of Prandtl [81, 82] and Eyring [77], where both authors independently developed their theory based on the same concept: the rate of a process depends on the thermal energy possessed by an atom or molecule and the mechanical forces exerted on it. These models were originally developed for chemical processes, but have been extended to viscous shear flows. The essence of these processes is the rate of molecules diffusing in a volume of fluid at rest, i.e., the rate of molecules crossing the energy barriers. It is calculated as the Arrhenius equation (at equilibrium, i.e., in the absence of external forces):

$$r_0 = Ae^{(-E_a/k_BT)} \tag{2.1}$$

where $A$ is a constant, $E_a$ is the thermal activation energy, $k_B$ is the Boltzmann constant and $T$ is the absolute temperature as shown in Figure 2.1(a). The molecular diffusion is activated if its thermal energy $k_BT$ exceeds the energy barrier $E_a$.

In the non-equilibrium case, a force $f$ is applied to the system. It will decrease the height of the energy barrier by a factor $f\Delta x$ in the direction of the applied force and increase it by the same amount in the opposite direction, as shown in Figure 2.1(b). $\Delta x$ is the activation distance, which is the distance required for the particle to reach the top of the energy barrier. The new process rate in the direction of the force $r_f$ and in the opposite direction $r_b$ are as follows

$$\begin{aligned} r_f &= Ae^{-E_a - f\Delta x/k_BT} \\ r_b &= Ae^{-E_a + f\Delta x/k_BT} \end{aligned} \tag{2.2}$$

In the system where the processes in both directions are possible, a net rate could be written as

$$r_{net} = A(e^{-E_a - f\Delta x/k_BT} - e^{-E_a + f\Delta x/k_BT}) = 2k_0 \sinh\left(\frac{f\Delta x}{k_BT}\right) \tag{2.3}$$

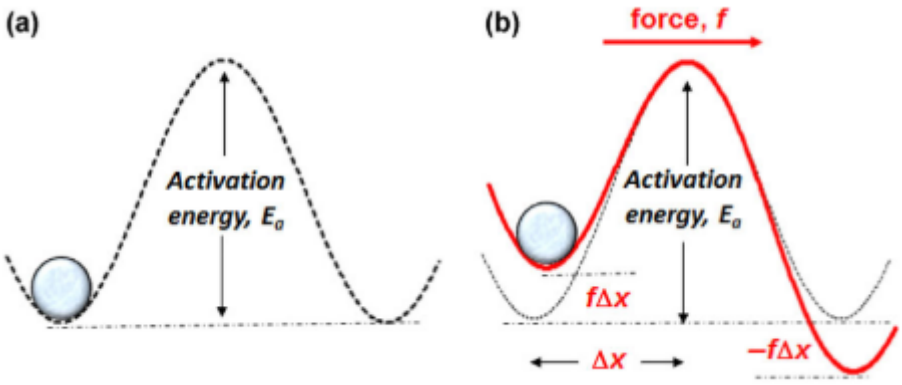


Figure 2.1: (a) Activation energy barrier in the absence of an applied force on the molecule represented as a sphere. (b) Influence of an applied force f on the effective energy barrier. Adapted from [70].

Because this approach combines mechanical and thermal energies, it is known as the "stress augmented thermal activation", or SATA concept.

### Eyring model

Henry Eyring developed his famous model of viscosity using the SATA concept in 1936 [77]. The Eyring model assumes that the onset of flow is caused by the rearrangement of individual molecules of an adjacent molecular plane, as shown in Figure 2.2. The mathematical derivation of the Eyring equation can be found in [70].

In Eyring's theory, without an external force on the fluid, there will be no flow because the barrier height is a unique $E_a$ that allows the flow process to occur with equal probability in both directions.

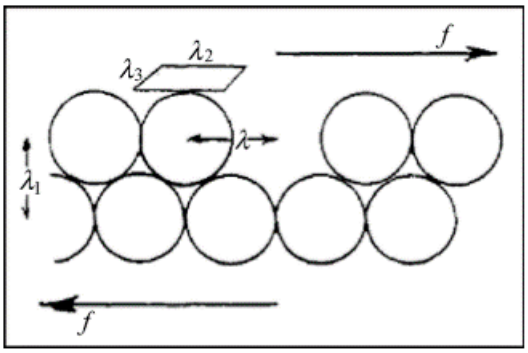


Figure 2.2: Eyring's schematic model of viscous flow of simple molecules. Adapted from [70].

With an applied force, it produces a difference in velocity between adjacent planes. An expression for $\Delta u$ could be derived from Equation 2.3.

$$\Delta u = 2k_0\lambda \sinh\left(\frac{f\Delta x}{k_B T}\right) \tag{2.4}$$

where $\lambda$ is the distance the molecule travels in one jump or the distance between two energy minima

which corresponds to the two lowest positions in Figure 2.1. So $\lambda = 2\Delta x$ as it is twice the activation distance. Taking $\lambda_1$ as the distance between the molecular plans, the shear rate is written as:

$$\dot{\gamma} = \frac{\Delta u}{\lambda_1} = \frac{2k_0\lambda}{\lambda_1}\sinh\left(\frac{f\lambda}{2k_BT}\right) \tag{2.5}$$

Further, assuming that $\lambda_2$ $\lambda_3$ is the area of the molecule on which the force is acting, the shear stress could be written as $\tau = \frac{f}{\lambda_2\lambda_3}$, replacing $f$ in 2.5 by the shear stress, the expression for the effective viscosity $\eta$, defined as the shear stress divided by the shear rate $\eta = \frac{\tau}{\dot{\gamma}}$, could be written as:

$$\eta = \frac{\tau}{\dot{\gamma}} = \frac{\tau\lambda_1}{2k_0\lambda\sinh\left(\frac{\tau\lambda\lambda_2\lambda_3}{2k_BT}\right)} \tag{2.6}$$

For very low applied shear stress (low shear rate) $\tau \ll \frac{k_BT}{\lambda\lambda_2\lambda_3}$, the expression $\sinh(\frac{\tau\lambda\lambda_2\lambda_3}{2\mathrm{k_B T}})$ becomes just $\frac{\tau\lambda\lambda_2\lambda_3}{2k_BT}$, the low shear viscosity (Newtonian viscosity) could be derived from equation 2.6.

$$\eta \xrightarrow{low\ shear} \eta_N = \frac{k_BT\lambda_1}{k_0\lambda^2\lambda_2\lambda_3} \tag{2.7}$$

The term $\frac{2k_BT}{\lambda\lambda_2\lambda_3}$ is called the Eyring stress $\tau_e$. It describes the threshold in stress at which the behaviour becomes non-Newtonian (shear thinning regime), similar to the critical shear stress $\tau_c$ that can be seen in Figure 1.4. Using $\tau_e$ and Equation 2.7 to substitute Equation 2.6, one have:

$$\frac{\eta}{\eta_N} = \frac{\tau}{\tau_e\sinh\left(\frac{\tau}{\tau_e}\right)} \tag{2.8}$$

Equation 2.8 is the shear thinning behaviour described by the Eyring model, which is expressed as the effective viscosity over its maximum (Newtonian) value. Substitute $\eta$ with $\tau$ and $\dot{\gamma}$, one have:

$$\begin{aligned} \frac{\tau}{\eta_N\dot{\gamma}} &= \frac{\tau}{\tau_e\sinh\left(\frac{\tau}{\tau_e}\right)} \\ \sinh\left(\frac{\tau}{\tau_e}\right) &= \frac{\eta_N\dot{\gamma}}{\tau_e} \\ \frac{\tau}{\tau_e} &= \sinh^{-1}\left(\frac{\eta_N\dot{\gamma}}{\tau_e}\right) \end{aligned} \tag{2.9}$$

Finally, the Eyring equation of viscosity and shear stress is shown in Equation 2.10. The Eyring model originated from the SATA concept, and it is remarkably simple, with only two parameters. All makes it widely used by EHD researchers.

$$\eta = \frac{\tau_e}{\dot{\gamma}} \sinh^{-1}\left(\frac{\eta_N \dot{\gamma}}{\tau_e}\right) \tag{2.10(a)}$$

$$\tau = \tau_e \sinh^{-1}\left(\frac{\eta_N \dot{\gamma}}{\tau_e}\right) \tag{2.10(b)}$$

However, whether the Eyring model can be applied to all types of fluids is controversial. Eyring and his co-workers believed that the model only gave "a satisfactory explanation for the viscosity of simple fluids" [155]. Fortunately, most lubricants used today are mixtures of small molecules with low viscosity, which is close to the type of fluid for which the Eyring model was developed [70].

In the following, the Eyring model is chosen over the Carreau-type models for two reasons. The first reason for this choice is its mathematical form, which tends to describe a shear stress plateau at high shear rates. This can be highlighted by calculating the logarithmic reduced viscosity slope $R_{visco} = \dfrac{\partial \log_{10}(\eta_{red.})}{\partial \log_{10}(\dot{\gamma}_{red.})}$. Where the reduced viscosity is defined as $\eta_{red.} = \eta/\eta_N$ and the reduced shear rate as $\dot{\gamma}_{red.} = \dot{\gamma}/\dot{\gamma}_e$, with $\dot{\gamma}_e$ being the Eyring rate, which is equal to $\tau_e/\eta_N$. The Eyring rate represents the shear rate threshold at which significant shear thinning occurs, sometimes called the critical shear rate $\dot{\gamma}_c$, in the present study, these two notions are unified using $\dot{\gamma}_c$ and therefore $\dot{\gamma}_{red.} = \dot{\gamma}/\dot{\gamma}_c$. The result of $R_{visco}$ as a function of $\dot{\gamma}_{red.}$ is shown in Figure 2.3. Calculation details are provided in Appendix A.

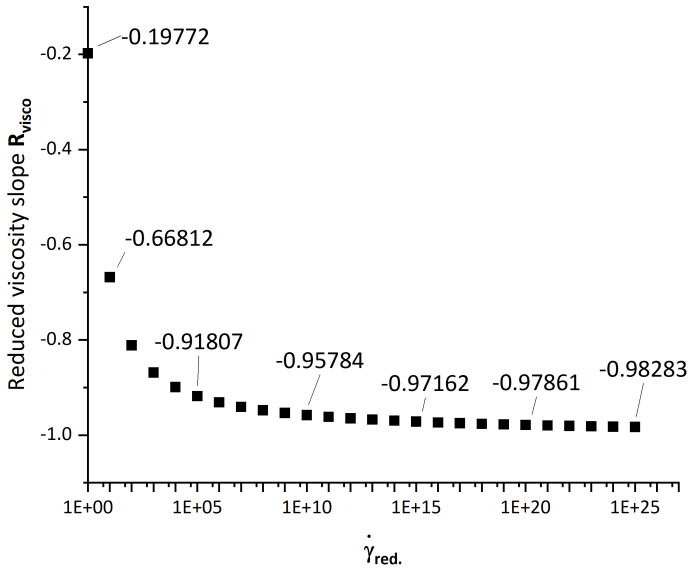


Figure 2.3: Variation rate (slope) of the reduced viscosity $\eta_{red.}$ as a function of reduced shear rate $\dot{\gamma}_{red.}$.

The figure demonstrates that the logarithmic reduced viscosity slope $R_{visco}$ versus $\dot{\gamma}_{red.}$ tends to -1, implying that the viscosity becomes proportional to $\dot{\gamma}^{-1}$. Consequently, the shear stress in the fluid, $\tau = \eta\dot{\gamma}$, tends towards a constant, which is the definition of limiting shear stress. Therefore, the Eyring model is intrinsically capable of describing the limiting behaviour of bulk lubricants.

The second reason to choose Eyring is its ability to accurately fit data over a wide range of operating conditions despite its simplicity. Jadhao and Robbins [80] studied the rheological properties of SQ and bi-disperse Lennard-Jones (LJ) fluids using confined NEMD simulations. Examining the shear-thinning viscosity, they discovered that the transition from Carreau to Eyring is generic for the studied fluids and is triggered by the increase in Newtonian viscosity. For SQ, transition takes place at Newtonian viscosities higher than 1 Pa.s, as illustrated in Figure 2.4. A similar transition from Carreau to Eyring was also observed in another polyol ester lubricant (PEC6) by Lin and Kedzierski [83]. This transition could be explained by the SATA concept [77]. Indeed, the fundamental principle of the Eyring model is that particles must cross a single energy barrier to initiate flow. At low viscosity, the wide range of molecular conformations leads to a wide distribution of similar energy barriers (in all directions), which does not align with the single energy barrier assumption of Eyring's theory. However, at high viscosity, the particle only needs to cross the lowest energy barrier (which is unique). This lowest energy barrier is considered to be the one in the direction of shear and lowered by the applied force, as shown in Figure 2.1(b). And the decreased amount of the energy barrier is expressed by the parameter $-E_a - f\Delta x$ shown in Equation 2.2. This is thought to be the fundamental reason for this Carreau to Eyring transition [106]. In the low viscosity case, the higher number of fitting parameters in the Carreau law enables obtaining a better fit on short ranges of shear rates.

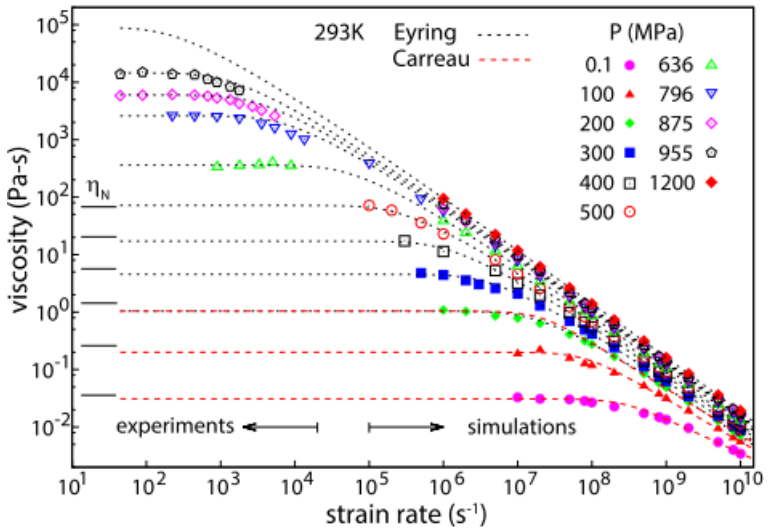


Figure 2.4: SQ viscosity variation at 293K with respect to strain rate. Data come from rheological experiments and NEMD simulations, the different symbols distinguish the different pressures. Adapted from [80].

The viscosity of squalane is accurately described by the Eyring model under most EHL conditions (pressure and temperature), as found by Jadhao and Robbins [80] (see Figure 2.4), Lin and Kedzierski [83], and Prentice et al. [84]. Besides, Jadhao and Robbins demonstrated that the Eyring model could describe the reduced viscosity $\eta_{red.}$ of SQ over 25 orders of magnitude of the reduced shear rate $\dot{\gamma}_{red.}$ (see Figure 2.5). In contrast, the Carreau model with N = 0.5 (written as n in the figure) fails to reproduce the variation in shear thinning rate over the same range. This implies better versatility of the Eyring model for EHL conditions since the $\dot{\gamma}_c$ (and consequently $\dot{\gamma}_{red.}$) drastically varies over the wide distribution of operating conditions in the EHD contacts. Indeed, pressure increases from zero to a few gigapascals in the contact area, and the shear rate can reach $10^8 s^{-1}$.

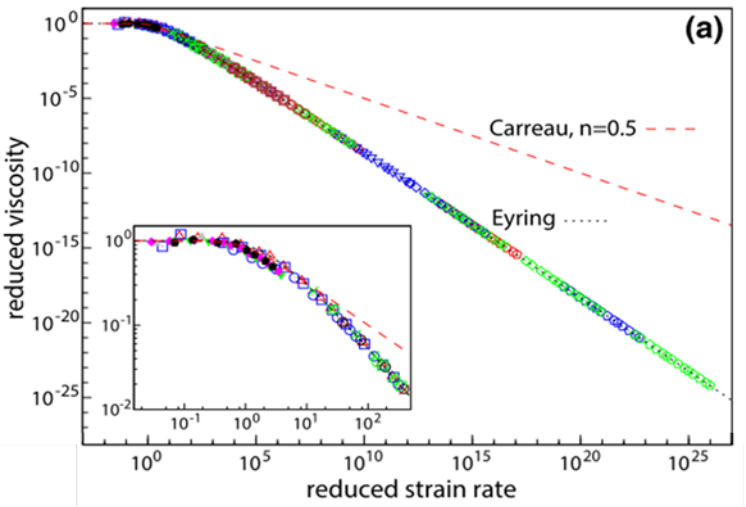


Figure 2.5: Reduced viscosity $\eta_{red.}$ as a function of reduced strain rate $\dot{\gamma}_{red.}$. Data come from rheological experiments and NEMD simulations. Adapted from [80].

As seen in Equation 2.10, the Eyring model requires only two parameters varying with pressure and temperature: the low shear (Newtonian) viscosity $\eta_N$ and the Eyring stress $\tau_e$. $\eta_N$ reflects the temperature and pressure viscosity dependence of the fluid at rest. $\tau_e$ determines the onset of the fluid shear thinning. Compared to the Carreau model, which has three fitting parameters, this simplicity significantly facilitates the characterisation process. Moreover, by fitting two parameters on data independent from the contact, the resulting Eyring model is considered predictive.

### 2.1.3 Choice of the fluids studied

The friction prediction approach proposed in this work should be independent of the lubricating fluid. Therefore, two fluids with opposite tribology behaviour are chosen: a lubricant (squalane, SQ) and an organic traction-like fluid (benzyl benzoate, BB).

SQ is an organic lubricant with the formula $C_{14}H_{12}O_2$. It has been a reference fluid in EHL for 60 years [85]. Its properties are well-characterised by a large amount of data that can be found in the literature, such as Bair et al. [85, 116]; Comuñas et al. [156]. These data will be further used as a reference or for comparison in this study. Like most molecules of base oil lubricants, SQ molecules have a linear alkane structure, which is long and flexible, as shown in Figure 2.6(a). The primary function of a lubricant is to provide a protective oil film between the contact surfaces and to reduce friction. Therefore, it needs to be viscous enough to maintain the film thickness but not too viscous in order not to increase friction.

BB is an organic fluid with the formula $(CH_3)_2CH(CH_2)_3CH(CH_3)(CH_2)_3(CH_2)_3CH(CH_3)$. It is proposed as a reference (see Habchi et al. [61], Porras-Vazquez et al. [16]) to mimic traction fluid behaviour. The rheological properties of BB have been rarely studied in the literature, but a few references are available [12, 97]. Traction fluids must provide an adequate traction coefficient or energy transmission under certain conditions, such as in continuous variable transmission (CVT) gearboxes. In contrast to SQ, BB molecules have a bulky and small structure, as shown in Figure 2.6(b). The saturated ring makes the molecules difficult to rotate and thus increases the traction force. Traction fluids also need to be able to form a high-viscosity oil film at high pressures and

a low-viscosity oil film at low temperatures [97]. Studies of rheological properties using the Eyring model for BB, similar to those of SQ, are missing in the literature on BB. Though BB is a complex molecular, at this point we assume that the Eyring model will be suitable to reproduce BB rheological behaviour. This assumption will be discussed later.

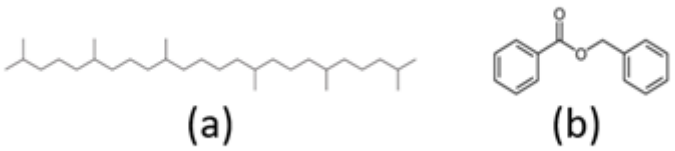


Figure 2.6: Schematic representation of (a) Squalane molecule and (b) Benzyl Benzoate molecule.

## 2.2 Fluid characterisation: experimental approach from the literature

To fully characterise the rheological behaviour of the selected fluids, the following properties are required: density and generalised viscosity. Since the latter is given by the Eyring model in this study, therefore, Newtonian viscosity and Eyring stress also need to be determined. Due to the lack of a method to determine Eyring stress experimentally, it will be determined by MD simulations and will therefore be presented later in Section 2.3. This section focuses on the rheological experiment methods to characterise Newtonian viscosity and density.

### 2.2.1 Rheological experiments

The determination of the Newtonian viscosity has been extensively studied in the literature [86, 87, 88], in particular, its dependence on pressure, as it is the parameter at the origin of the greatest variation in viscosity. An accurate description of this variation over the pressure range of interest is essential for friction prediction [70]. For EHD contact conditions, the pressure can be of the order of or greater than the glass transition pressure of the lubricant, causing the lubricant to enter a glassy state and resulting in a sharp increase in viscosity. This requires rheological apparatus capable of applying very high pressures and still measuring a quantity representative of the fluid behaviour. At present, high-pressure viscometers (HPV) are the most efficient tools for this type of measurement, although they do not allow measurement at pressures close to or higher than the glass transition. SQ and BB have been rheologically characterised versus pressure and temperature using HPVs. Three distinct HPVs have been used to measure the viscosity of SQ, described in [157, 158]. They have made it possible to probe SQ from atmospheric pressure up to 1200 MPa and at temperatures between 293 K and 373 K. Viscosity data was provided in [116]. BB has been probed from atmospheric pressure up to 700 MPa and at temperatures between 313 K and 403 K. Viscosity data was first provided in [40]. Another possible alternative is numerical simulation at the molecular scale, which will be presented hereafter.

The rheological measurement data, collected either experimentally or numerically, are then used to fit a rheological model, such as the WLF-Yasutomi [89] model or the thermal scaling model [64], which are described hereafter and will be later used to predict friction.

Besides, the relative volume of the fluid is measured by the experimental method, such as dilatometers or bellows piezometers [90]. These data are later fitted to the empirical equation of state to give the state of the fluid at different $p$ and $T$. In the present study, the classical Tait equation of state [91] is used. The density $\rho$ can also be derived from the Tait equation via the reference density $\rho_R$ measured by density meters at atmospheric pressure $p_{atm}$ and at the reference temperature $T_R$.

**a William-Landel-Ferry (WLF) Yasutomi model**

The quantitative analysis of the lubricant viscosity has to be based on equations of state such as temperature-pressure correlations, which are not always available, although the viscosity itself could easily be measured with a viscometer [4]. The William-Landel-Ferry (WLF) model [137] first allowed the temperature dependence of viscosity to be described. To make it suitable for EHL conditions, Yasutomi et al. [159] proposed a modified version of the WLF model to describe the dependence of viscosity on both temperature and pressure, derived from the concept of free volume. The free volume is the volume within a fluid that allows the free movement of molecules. As the free volume approaches zero, the mobility of molecules decreases and the viscosity increases [160]. The WLF-Yasutomi model is widely used in EHD studies and has undergone several iterations since its creation. The most recent version by Bair [89] is shown in Equation 2.11. Its mathematical form is a function that grows exponentially with pressure and diverges as it approaches a critical thermodynamic condition ($p_g$ and $T_g$), identified as the glass transition.

$$\eta_N = \eta_g \times \exp\left(\frac{-2.303C_1 \times (T - T_g(p)) \times F(p)}{C_2 + (T - T_g(p)) \times F(p)}\right) \tag{2.11}$$

where $A_1, A_2, B_1, B_2, C_1, C_2$ are fit parameters, $T_g(p)$ is the glass transition temperature, and $F(p)$ is the dimensionless relative thermal expansivity of free volume:

$$\begin{aligned} T_g(p) &= T_{g0} + A_1 \times \ln(1 + A_2 \times p) \\ F(p) &= (1 + B_1)^{B_2} \end{aligned} \tag{2.12}$$

$\eta_g$ is the viscosity value at the glass transition. Commonly the literature uses the value of $\eta_g = 10^{12}$ Pa.s [149, 161, 162].

In addition to providing a good description of viscosity in the pressure range of experimental measurement, the WLF-Yasutomi model also provides a reliable extrapolation for fluids with high inflexion pressure (strong fluid) for pressures up to 300 MPa above the measured pressure [89], but is less reliable for fluids with low inflexion pressure (fragile fluid) [163]. However, this model has a major drawback due to its mathematical form: it has a mathematical limit $p_g$ and cannot describe viscosity in the glassy state (for $p > p_g$), which considerably limits its use in EHL conditions.

**b Viscosity scaling model**

The viscosity of many organic liquids could be described by a thermal scaling law $\eta_N = f(\varphi)$ depending on a scaling parameter $\varphi$, written as:

$$\varphi = \left(\frac{T}{T_R}\right)\left(\frac{V}{V_R}\right)^g \tag{2.13}$$

$\varphi$ is determined by the relative temperature $^{T}/_{T_R}$ and the relative volume $^{V}/_{V_R}$, with $T_R$ and $V_R$ are respectively the reference temperature and reference volume. The relative volume could be expressed from any equation of state (as Tait [91] or Murnghan [164]). $g$ is a material constant related to the internal energy of molecule [165]. Several scaling laws $f$ could be found in the literature. In the present study, a viscosity scaling law based on the normalised Ashurst-Hoover equation proposed by Bair and Laesecke [64] is created:

$$\eta_N = A \exp\left(B\varphi^{-q} + C\varphi^{-Q}\right), \qquad 0 < q < 1, \qquad 1 < Q \tag{2.14}$$

The fitting parameters $A, B, C, q, Q$ are obtained by adjusting the law on experimental viscosity measurements. e.g. measurements from high-pressure viscometers. It is important to note that in this study, our aim was only to find the mathematical model that best fits the viscosity measurement data. Even though this model and Bair and Laesecke [64] model have similar parameters, the physical meaning of each parameter is not necessarily the same. The advantage of this law is that it has no mathematical limits compared to the WLF-Yasutomi equation.

#### c Tait equation of state

The Tait equation of state is used to give the variation of the relative volume of fluid with pressure and temperature required by the viscosity scaling model created in the present study (see Equation 2.13).

$$\begin{gathered} \frac{V}{V_R} = \left[1 + a_v\left(T - T_R\right)\right] \times \left[1 - \frac{1}{1 + K_0'} \ln\left(1 + \frac{p}{K_0}\left(1 + K_0'\right)\right)\right] \\ \frac{V}{V_R} = \frac{\rho_R}{\rho} \end{gathered} \tag{2.15}$$

where $K_0 = K_{00} \exp\left(-\beta_K T\right)$, and $K_0'$, $a_v$, $K_{00}$ and $\beta_K$ are the parameters of the Tait equation of state. The parameters for SQ are taken from Bair [116] and the reference density is taken from Mylona et al. [166]. The parameters for BB are derived from the results of the same test as SQ performed by Bair [167] and the reference density of BB has been measured at LaMCoS - INSA de Lyon with an Anton Paar DMA4500M density meter. Values are given in Table 2.1.

| | $K_0'$ [-] | $a_v$[K$^{-1}$] | $K_{00}$[GPa] | $\beta_K$[K$^{-1}$] | $\rho_R$[kg/m$^3$] at 313.15K | SD [%] |
|---|---|---|---|---|---|---|
| SQ[116] | 11.74 | $8.36 \times 10^{-4}$ | 8.658 | $6.232 \times 10^{-3}$ | 795.8[166] | 0.05 |
| BB[167] | 10.44 | $7.47 \times 10^{-4}$ | 13.707 | $6.107 \times 10^{-3}$ | 1102.3[This study] | 0.07 |

Table 2.1: Parameters of Tait equation of state and density measurements for SQ and BB.

## 2.3 Fluid characterisation: molecular dynamic approach

To complement these data, especially for the non-Newtonian response (Eyring stress) of both fluids and for operating conditions inaccessible to experimental methods, numerical characterisation tools at the local scale are needed. In this context, MD simulations are a suitable approach as they provide access to the behaviour of lubricants at the molecular scale. In addition, it is possible to control

pressure and temperature and to reach nominal EHL conditions that are inaccessible in rheological experiments. Several MD studies of confined fluids under such conditions have been published in recent years. These include not only simple Lennard-Jones molecules [32, 168, 169] but also more complex and realistic molecules [16, 31, 80, 170]. The results of MD simulations have been shown to be comparable in evolution with viscosity measurements (rheology) [73, 119] and friction measurements (tribology) [16, 31].

All the MD simulations performed in this study are coded in LAMMPS [92] and run on the LaMCoS cluster or the P2CHPD cluster, one of the three regional computing centres of Lyon, located at the University of Lyon I. The MD simulation allows us to apply controlled extreme conditions, such as high pressures and high shear rates, at constant temperatures.

### 2.3.1 MD Algorithm

MD simulations are based on the physical interactions between particles at the atomic scale through a given force field. The evolution of systems over time is calculated by solving Newton's motion equations. At each time $t$ of the simulation, the position of each particle is known. Depending on the chosen force field, the potential energy of each particle, the force acting on it (defined as the gradient of the potential energy) and its acceleration are calculated successfully. The Verlet algorithm [93] is then used to calculate the new position of each particle.

A time step of one femtosecond ($10^{-15}s$) is chosen in the present study. The choice of the force field depends on the description of the molecule. Two families can be classically adopted: the all-atom (AA) and the united-atom (UA) force fields. In the AA force field, each atom in the molecule is explicitly treated and parameterised. In the UA force field, non-polar hydrogen atoms are grouped with carbon atoms and treated as "pseudo-atoms" such as $CH$, $CH_2$ or $CH_3$. According to the literature, the UA force fields provide an accurate structure but consistently underestimate the friction coefficients and friction-velocity behaviour from experimental observations [106]. Therefore, for MD simulations of systems containing long-chain linear molecules, AA force fields are recommended [94], such as the "long chain optimised potential for liquid simulations all-atom" (L-OPLS-AA) force fields [95, 96]. The L-OPLS-AA force fields have been used to simulate many different lubricants, such as SQ [16, 31] and diethylhexyl sebacate [31], as well as traction fluid DM2H, Santotrac 2000 [31] and BB [16]. These simulations have been shown to give results close to experimental data on friction coefficients. In this study, the L-OPLS-AA force fields are used in MD simulations for both SQ and BB, the same choice as in the study of Porras-Vazquez [97].

Finally, MD simulations can be performed either at equilibrium (EMD) or with external energies brought to the system (non-equilibrium molecular dynamics, NEMD).

### 2.3.2 EMD simulation

In this study, we first attempt to characterise the Newtonian viscosity at the equilibrium using EMD simulations. EMD simulate the bulk fluid in an isobaric-isothermal state at equilibrium to characterise the fluid viscosity in volume. Two methods are tested: the Green-Kubo and the diffusion (Stokes-Einstein) methods. The initial system sample is made using the open-source LAMMPS builder project by Ewen and Echeverri [171], which uses Moltemplate [172] and ASE [173] modules. The simulation box measures approximately 5 nm*5 nm*5 nm and contains 150 molecules for SQ and 360 molecules for BB. Periodic boundary conditions are applied in the three directions of the system. The EMD system used in the present study is shown in Figure 2.7.

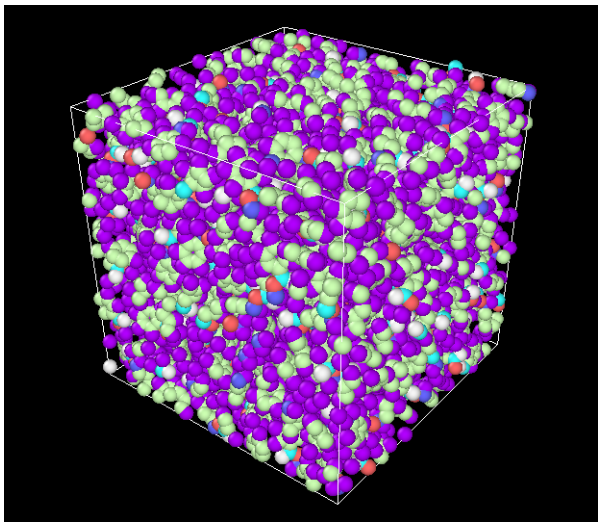

Figure 2.7: EMD system of the 360 molecules of BB used in this study.

The simulation procedure of the EMD simulations began with the equilibrium stage, which involved minimising the system energy to reach equilibrium. This process allows the system to adopt a stable and energetically favourable configuration before proceeding to the subsequent stages of the simulation. Later, the Nosé-Hoover thermostat and barostat [98] are applied to the system: first, a canonical ensemble (NVT) is applied, which means that the total number of molecules, the volume, and the temperature are kept constant during the process. This stage lasts for a period of 10,000 time steps to stabilise the system temperature. Secondly, the isothermal-isobaric ensemble (NPT) is applied, which means that the total number of molecules, the pressure, and the temperature are kept constant during the process. This stage takes ten times as long as the previous one (100,000 time steps) to achieve the desired pressure stabilisation of the simulation while maintaining temperature stability. Finally, with both pressure and temperature stabilised, the simulation is run in the thermodynamic canonical ensemble (NVE), which means that the total number of molecules, the volume, and the total energy are kept constant throughout the process. This stage is carried out for the required time and the calculation of the viscosity or diffusion coefficient is carried out in this last stage. In practice, this last stage is run for no preset time limit to obtain the best signal-to-noise ratio. All EMD simulations in the present study use the same configuration: one node, fifteen cores, and fifteen gigabytes of RAM run for the maximum wall-clock time allowed by the cluster (5.5 days for the P2CHPD cluster and 8 days for the LaMCoS cluster). The typical simulation time amounts to several tens of nanoseconds (with a maximum of 71.5 ns).

#### a Green-Kubo method

At equilibrium, the Newtonian viscosity of the fluid can be estimated within the linear response regime of stress to strain rate. Green-Kubo [99, 100] demonstrated that transport properties (diffusion coefficient and Newtonian viscosities) can be related to the duration of fluctuations. They can be expressed as integrals of autocorrelation functions. The Newtonian viscosity $\eta_N$ is related to the ensemble average of the off-diagonal stress tensor $P_{ij}$. It has three components: $P_{xy}$, $P_{xz}$, and $P_{yz}$.

$$\eta_N = \frac{V}{3k_BT}\int_0^{+\infty} \langle P_{ij}(t)P_{ij}(0)\rangle \, dt \tag{2.16}$$

In Equation 2.16, $k_B$ is the Boltzmann constant, $V$ is the volume of the fluid, and $T$ is the temperature of the sample. Viscosity calculated by the Green-Kubo method is presented in Appendix B.

**b Stokes-Einstein method**

Another method to derive the Newtonian viscosity from EMD simulations consists of applying the Stokes-Einstein equation (Equation 2.17). This equation combines the approach of Einstein for the description of Brownian motion [101] and Stokes' theory of particle drag in low Reynolds number fluids [102]. The Newtonian viscosity is derived from the diffusion coefficient:

$$\eta_N = \frac{k_B T}{6\pi D r_s} \tag{2.17}$$

In Equation 2.17, $r_s$ is the Stokes or Stokes-Einstein radius. It is widely used synonymously with the hydrodynamic radius $r_h$ [174]. $r_s$ (or $r_h$) is defined as the radius of a non-slip hard sphere with the same diffusion rate as that of the particles. Generally, this radius is determined by the Stokes-Einstein equation from known Newtonian viscosity $\eta_N$ and diffusion coefficient $D$. For the Stokes-Einstein equation to hold, this radius should also be independent of temperature [175]. Numerous studies on different fluids have shown that these two radii are comparable to the size of the average building units of the fluid [175, 176, 177, 178, 179]. It is therefore a reasonable approximation to use the physical radius of the molecules. In this study, this length is unified as the "characteristic length" and denoted by $r_c$, which represents the radius of the simulated fluid molecule at a given pressure and temperature.

To calculate the diffusion coefficient, the mean square displacement (MSD) of molecules is measured. The MSD measures the average squared distance of molecules due to Brownian motion from their initial position [93]. Three different regimes of the molecules can be identified in time, as shown in Figure 2.8.

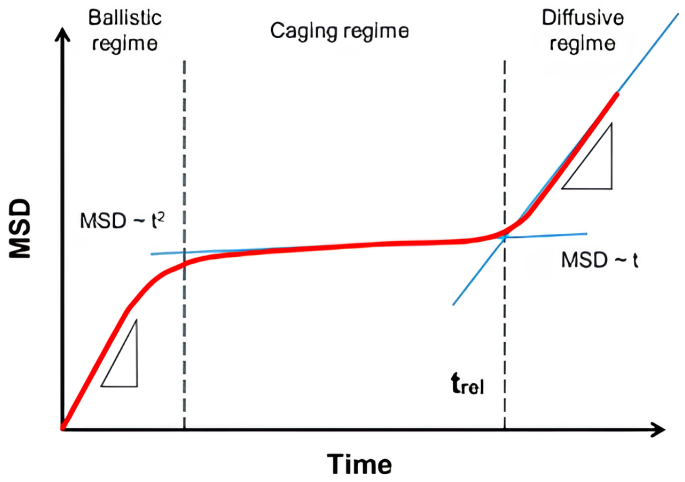


Figure 2.8: MSD as a function of time. Adapted from [97].

For a very short time at the beginning of the simulation, a molecule is subjected to its initial inertia and moves in a uniform linear motion until it collides with neighbouring molecules. This regime is

known as the ballistic regime. After this short inertia-dominated regime, molecules collide randomly and become temporarily trapped in a "cage" of surrounding molecules leading to restricted mobility. This regime is known as the caging regime and induces a plateau in the MSD evolution in time. This caging regime lasts up to the relaxation time $t_{rel}$, when the molecule has accumulated enough energy to overcome the energy barrier and begins to diffuse, entering the diffusive regime. It should be noted that in the diffusion regime, the MSD increases almost linearly with time (MSD $\sim$ $t^1$ ), and $D$ is linked to the relaxation time $t_{rel}$ [180] by:

$$t_{rel} = \frac{4r_c^2}{D} \tag{2.18}$$

Indeed, Einstein first related the diffusion coefficient to the MSD as a function of observation time $t_{obs}$. According to his theory, for a very long $t_{obs}$ (which tends to infinity), the MSD is proportional to $t_{obs}$. The coefficient of proportionality is the diffusion coefficient [93, 103]. This indicates that $D$ is defined as shown in Equation 2.19, where $n$ is the dimension of the system. It is worth noting that $t_{obs}$ implies the observation time in the experiment, and for numerical simulations, this notion corresponds to the simulation time $t_{simu}$.

$$D = \frac{1}{2n} \lim_{t\to\infty} \frac{\mathrm{d}MSD}{\mathrm{d}t} \tag{2.19}$$

The calculation of $D$ necessitates verification (whether the system is diffusive or not) and post-processing of the simulation results (calculation of the slope of the MSD curve) in accordance with Equation 2.19. Details are provided in Chapter 3.

### 2.3.3 NEMD simulation

Depending on the system simulated, NEMD simulations can be divided into bulk NEMD and confined NEMD. The former simulates a bulk of molecules without contact surfaces, similar to the system in EMD. The latter simulates both the contact surfaces and the fluid within it. Different NEMD methods could also be identified depending on how the shear is applied to the system. For bulk systems, shear can be applied either by deforming the simulation box (SLLOD algorithm [104]) or by artificially exchanging the momenta between the two extreme regions of the fluid molecules (Müller-Plathe algorithm [105]). For the confined NEMD system, the shear is applied by directly applying motion to the contact surfaces (Sliding walls [106, 107]). The differences between these three methods are summarised in Table 2.2.

| Simulation type | Bulk NEMD | | Confined NEMD |
|---|---|---|---|
| Method name | SLLOD | Müller-Plathe | Sliding walls |
| Origin of shear | Deformation of simulation box | Exchange in momenta | Motion applied on contact surfaces |
| System simulated | Molecule bulk | | Molecule bulk + contact surfaces |

Table 2.2: The three different NEMD methods.

According to Ewen et al. [53], the Müller-Plathe method always underestimates viscosity due to the absence of external forces, which is inconsistent with experiments and therefore not considered in the

present study. The "sliding walls" method (Confined NEMD) has the longest history of use. It was invented by Ashurst and Hoover [181] in 1975 and has been developed in recent years with several fluids tested, including SQ [16, 31] and BB [16]. On the other hand, the SLLOD method emerged later in the 1980s [80] and has also undergone significant development in recent years. Bair et al. [107] published the first non-Newtonian rheology comparison between NEMD simulation prediction using the SLLOD algorithm and rheometer measurements. Since then, several studies have been successfully carried out using bulk NEMD, such as the study by Liu et al. [182] and Jadhao and Robbins [119]. These studies have shown that the NEMD method (sliding walls and SLLOD) provides a good characterisation of the behaviour of fluids under shear.

In general, bulk NEMD simulation is performed at constant volume, and the flow profile is always assumed to be linear (Couette flow) [106]. As a consequence, it is considered to be more representative of the rheological characteristics of the fluid. The results are often validated with rheometer measurements [107, 119, 182].

The confined NEMD simulations are performed at constant pressure, with the presence of surfaces, the shear is transferred to the fluid through the solid surface motion, as in real contact. Although there is a large difference given the complexity of real contacts, such as pressure distribution, thermal effects, and the topography of the surface, some researchers considered the confined NEMD to be close to real contact [106]. In the literature, results of confined NEMD are used to compare with tribological experiment measurements [16, 106]. In this work, the sliding wall method is chosen to characterise the Eyring stress of the fluid. To characterise it at a given $p$ and $T$, simulations are performed under isobaric conditions and with the presence of a thermostat, the temperature is well controlled, so it can also be considered as an isothermal environment.

Like EMD systems, the confined NEMD systems of both fluids are also built using the LAMMPS builder project [171] with Moltemplate [172] and ASE [173]. The systems contain confined fluid molecules between solid surfaces of rough iron. A nano-roughness of iron surfaces is created by the self-fractal scaling law [31], where the Hurst exponent is set to 0.8 [108], and the root mean square (RMS) roughness is set to 0.8 nm to quantify the roughness. Iron atoms are bounded by the classical empirical embedded atom method (EAM) force field [109], which is widely used in the case of metallic systems [110, 111]. The cross-section of the solid surface is approximately 5nm*5nm in the x and y directions and has a thickness of about 3-5nm in the z-direction, as shown in Figure 2.9. Periodic boundary conditions are imposed in the x and y directions. No assumption is made on the velocity profile of confined NEMD systems. According to a previous study by Porras-Vazquez et al. [16], a minimum oil film thickness of 10 nm is required to prevent surface effects like layering in the fluid structures due to confinement. Therefore, a system containing 720 SQ molecules or 1440 BB molecules is used, as shown in Figure 2.9 and 2.10.

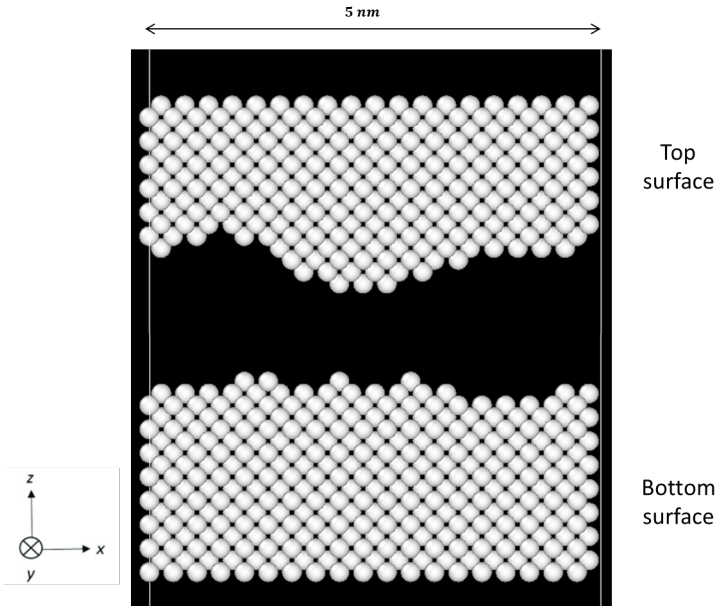


Figure 2.9: The rough surface of confined NEMD system.

The simulation process has three stages: equilibration, compression, and shear. All stages are run using the thermodynamic canonical ensemble (NVE), as previously described in the EMD simulation. It refers to the total number of molecules, the volume, and the total energy being kept constant during the procedure, which also means that the internal action of the system is conserved. For NEMD simulations, the inevitable consequence of the NVE ensemble is an increase in temperature since no heat dissipation can take place while external energy (compression and shear) is constantly added. Yet, the fluid characterisation should be carried out for a given temperature and pressure, in other words, in an isothermal and isobaric process. Therefore, to avoid the unrealistic temperature rise, the use of a thermostat becomes a necessity. In previous studies [31, 97], the temperature of confined NEMD simulations was controlled by a Langevin thermostat located inside the solid surface. This thermostat is clearly limited in its ability to control temperature rise, especially for the central part of the film thickness, as it takes time for the heat to transfer. To correctly characterise the real response of the fluid to shear, a more effective method to control temperature is necessary. As a consequence, we apply a Nosé-Hoover thermostat to the whole system (both fluids and solids) but only in the y-direction to avoid affecting shear in the x-direction and pressure in the z-direction. A damping coefficient of 0.1 ps is chosen for the thermostat.

The energy of the system is first minimized. The system is then equilibrated using a Nosé-Hoover thermostat with a damping coefficient of 0.1 ps applied to the whole system. This stage runs for 0.5 ns to randomize the positions of fluid molecules ($5 \times 10^5$ time steps). Then, in the compression stage, a constant pressure is applied on the upper surface with the same thermostat used to control temperature, running for 2 ns ($2 \times 10^6$ time steps). Finally, in the shear stage, a constant velocity is applied to each solid surface to create shear. The velocity is imposed on both the top and bottom surfaces but in opposite directions. Similarly to what is done in EMD simulations, the shearing stage is then run for no preset time limit to obtain the best signal-to-noise ratio, with the same configuration as in EMD (CPU, RAM, maximum wall-clock time) typical simulation time is several tens of ns, details are described in Section 3.2. The results are proven to be able to avoid temperature rise under all the conditions tested, as shown in Chapter 3. The confined NEMD system used in the

present study is shown in Figure 2.10.

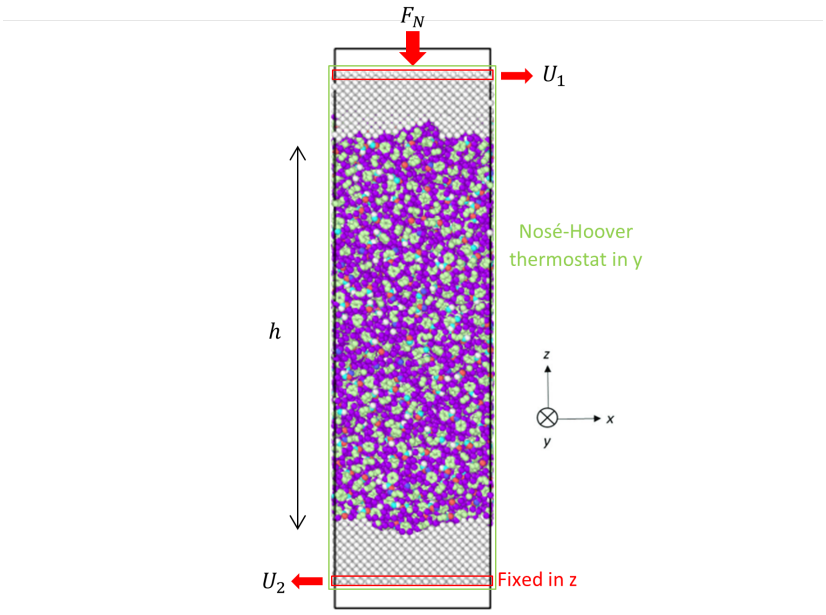


Figure 2.10: confined NEMD system of the 1440 molecules of BB used in this study.

The primary output of these confined NEMD simulations is the shear stress versus shear rate response. The shear rate is implicitly applied through the enforced velocity of the moving walls. The shear stress is derived as the total tangential force exerted on the atoms in the red region depicted in Figure 2.10, divided by the area (which is $5 \times 5\ nm^2$). More details are presented in Chapter 3.

## 2.4 TEHD point contact modelling

Based on the work from Habchi et al. [63], Doki-Thonon [74], Wheeler [75], and Wheeler and Raisin [112], a stationary thermal EHL non-Newtonian (TEHLnN) contact model was developed in the former work in the finite element analysis software COMSOL Multiphysics. The model simultaneously calculates the pressure profile in the fluid film (generalised Reynolds equation); the elastic deformation of the surfaces (leading to the calculation of the film thickness profile); the temperature field in the fluid and contacting solids (via energy equilibrium equations); and the force balance equation (load equilibrium). To solve the equations, the rheological constitutive law of the fluid is required. This includes its density and viscosity as functions of $p$, $T$, and $\dot{\gamma}$.

### 2.4.1 Main equations

#### a Generalised Reynolds equation

The pressure field in a steady-state thermal EHD point contact with non-Newtonian lubricant is given by the generalised Reynolds equation from Yang et al. [113], as shown in Equation 2.20.

$$\frac{\partial}{\partial x}\left[\left(\frac{\rho}{\eta}\right)_e \frac{\partial p}{\partial x}\right] + \frac{\partial}{\partial y}\left[\left(\frac{\rho}{\eta}\right)_e \frac{\partial p}{\partial y}\right] - \frac{\partial}{\partial x}\left(\rho_x^*\right) = 0 \tag{2.20}$$

x and y directions are in the contact plane and the z-direction is in the film thickness $h$ direction. Compared to its classical version [114], the generalised Reynolds equation takes into account the variation of fluid properties within the lubricant film using integrated values calculated from the operator $\left(\frac{\rho}{\eta}\right)_e$, shown in Equation 2.21.

$$\begin{aligned} \left(\frac{\rho}{\eta}\right)_e &= \frac{\eta_e}{\eta'_e}\rho'_e - \rho''_e \\ \rho^*_x &= \rho'_e \eta_e u_e - \rho_e u_b \end{aligned} \tag{2.21}$$

The entrainment velocity $u_e$ is derived from the top and bottom surface velocities, respectively $u_t$ and $u_b$, as $u_e = \frac{(u_t+u_b)}{2}$. The equivalent fluid properties across the film thickness are defined in Equation 2.22:

$$\begin{gathered} \rho_e = \int_0^h \rho_f dz \\ \rho'_e = \int_0^h \rho_f \left(\int_0^z \frac{1}{\eta} dz'\right) dz \qquad \rho''_e = \int_0^h \rho_f \left(\int_0^z \frac{z'}{\eta} dz'\right) dz \\ \frac{1}{\eta_e} = \int_0^h \frac{1}{\eta} dz \qquad \frac{1}{\eta'_e} = \int_0^h \frac{z}{\eta} dz \end{gathered} \tag{2.22}$$

where the subscript $_f$ stands for properties of the fluid, $\eta(x, y, z)$ is the viscosity described here by the Eyring model (see Section 2.1.2), which depends on pressure, temperature, and shear stress (or shear rate). The Eyring viscosity model depends on two parameters: the Newtonian viscosity $\eta_N$ is here defined by a viscosity scaling model based on experimental measurement (see Section 3.1.3), and the Eyring stress extracted from homemade NEMD simulation (see Section 3.2.5) as defined in Section 2.3.3. $\rho(x, y, z)$ is the density described by the Tait equation of state [91] (see Section 3.1.3). The Reynolds equation is solved only in a 2D region $\partial\Omega_c$, $\Omega_c$ represents the contact surface at the surface of a 3D linear elastic geometry $\Omega$ representing an equivalent contact solid, as seen in Figure 2.11. The boundary conditions for the Reynolds equation are zero pressure at the edges of the Reynolds area $\partial\Omega_c$.

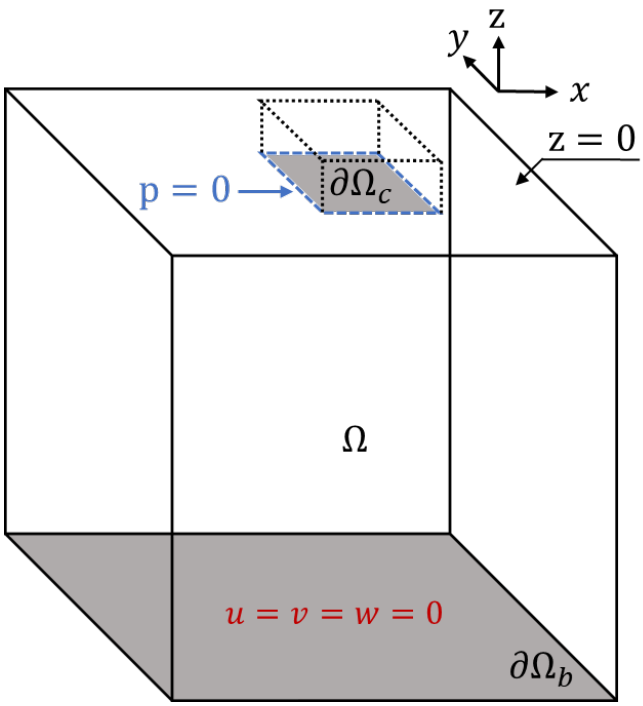


Figure 2.11: Geometry of elastic model (equivalent mass $\Omega$), Reynolds area $\partial\Omega_c$ and geometry of the non-Newtonian model (sketched by dotted lines). Boundary conditions are marked in blue and red.

The viscosity $\eta(x, y, z)$ and the density $\rho(x, y, z)$ are transformed into the 2D space values $\eta_e(x, y), \eta'_e(x, y), \rho_e(x, y), \rho'_e(x, y)$, and $\rho''_e(x, y)$ via Equation 2.22. These values are then used to solve the generalised Reynolds equation, as shown in Equation 2.21. The solution is carried out in a 3D geometry independent of the equivalent mass, to take into account the distribution of $p$, $T$, and $\dot{\gamma}$ in the film thickness, as shown in the dotted part over contact area $\partial\Omega_c$ in Figure 2.11.

**b Elasticity equation**

The pressure calculated within the contact area $\partial\Omega_c$ serves as a boundary condition for calculating the elastic displacement of the upper surface on the equivalent solid $\Omega$, as shown in Equation 2.23.

$$\nabla \cdot \sigma = 0 \qquad where \qquad \sigma = \begin{bmatrix} \sigma_{xx} & \tau_{xy} & \tau_{xz} \\ \tau_{xy} & \sigma_{yy} & \tau_{yz} \\ \tau_{xz} & \tau_{yz} & \sigma_{zz} \end{bmatrix} \tag{2.23}$$

The Equation 2.23 is solved to obtain the displacement field $U(x, y, z) = \{u, v, w\}$ in the equivalent solid and in the 3 directions of space (x,y,z). The stress tensor $\sigma$ is expressed as a function of the strain tensor and compliance matrix $D_m$.

$$\begin{Bmatrix} \sigma_{xx} \\ \sigma_{yy} \\ \sigma_{zz} \\ \tau_{xy} \\ \tau_{yz} \\ \tau_{zx} \end{Bmatrix} = \underbrace{\frac{E'}{(1+\nu')(1-2\nu')} \begin{bmatrix} 1-\nu' & \nu' & \nu' & 0 & 0 & 0 \\ \nu' & 1-\nu' & \nu' & 0 & 0 & 0 \\ \nu' & \nu' & 1-\nu' & 0 & 0 & 0 \\ 0 & 0 & 0 & \frac{1-2\nu'}{2} & 0 & 0 \\ 0 & 0 & 0 & 0 & \frac{1-2\nu'}{2} & 0 \\ 0 & 0 & 0 & 0 & 0 & \frac{1-2\nu'}{2} \end{bmatrix}}_{D_m} \begin{Bmatrix} \varepsilon_{xx} \\ \varepsilon_{yy} \\ \varepsilon_{zz} \\ \varepsilon_{yz} \\ \varepsilon_{zx} \\ \varepsilon_{xy} \end{Bmatrix} \tag{2.24}$$

Where the $\varepsilon$ is the deformation of the equivalent solid, with $\varepsilon = {}^1\!/_2 \left(\nabla U + \nabla^T U\right)$. The compliance matrix $D_m$ is calculated according to the equivalent body theory [61, 142], with $E_1$ and $E_2$, $\nu_1$ and $\nu_2$ are Young's modulus and Poisson's ratio of the two contacting bodies. The equivalent Young's modulus and equivalent Poisson's ratio are written as Equation 2.25 [61, 142].

$$E' = \frac{E_1^2 E_2 \left(1+\nu_2\right)^2 + E_2^2 E_1 \left(1+\nu_1\right)^2}{\left[E_1\left(1+\nu_2\right) + E_2\left(1+\nu_1\right)\right]^2} \qquad \nu' = \frac{E_1\nu_2\left(1+\nu_2\right) + E_2\nu_1\left(1+\nu_1\right)}{E_1\left(1+\nu_2\right) + E_2\left(1+\nu_1\right)} \tag{2.25}$$

The bottom surface $\partial\Omega_b$ (grey surface in Figure 2.11) is clamped. In the domain $\partial\Omega_c$, the normal stress in z-direction $\sigma_{zz}$ is set to the pressure $-p$ calculated by the generalised Reynolds equation. Other boundaries are set to be free to move.

**c Film thickness and load balance equations**

The film thickness $h$ over the contact area is given by Equation 2.26.

$$h(x,y) = h_0 + \frac{x^2}{2R_x} + \frac{y^2}{2R_y} + \delta(x,y) \tag{2.26}$$

where $\delta(x,y) = w$ is the deformation of the contact surface (x,y,z=0), i.e. on the domain $\partial\Omega_c$ in Figure 2.11. The term $h_0$ is the result of the load balance equation, which relates the pressure generated in the lubricant to the normal load $W$.

$$\iint_S p(x,y)dxdy = W \tag{2.27}$$

The term $\frac{x^2}{2R_x} + \frac{y^2}{2R_y}$ represents the separation due to the original geometry of the contacting solids, under the assumption that the geometry of the sphere can be approximated by a parabola at the point of contact. It is expressed using the radius of curvature of the equivalent geometry [183] $R_x$ and $R_y$. Since the contacts we focus on are sphere-planar contacts, a single equivalent radius of a circle $R$ as $R = R_x = R_y$ could be used in the x and y directions so that the Equation 2.26 becomes:

$$h(x,y) = h_0 + \frac{x^2+y^2}{2R} + \delta(x,y) \tag{2.28}$$

### d Heat equations

The temperature field is given by solving the heat equations within a 3D geometry, as shown in Figure 2.12. It includes the domains $\Omega_t$ and $\Omega_b$, representing the upper and lower solids, and $\Omega_f$ in light grey representing the fluid. Two dark grey areas stand for the solid-fluid interfaces.

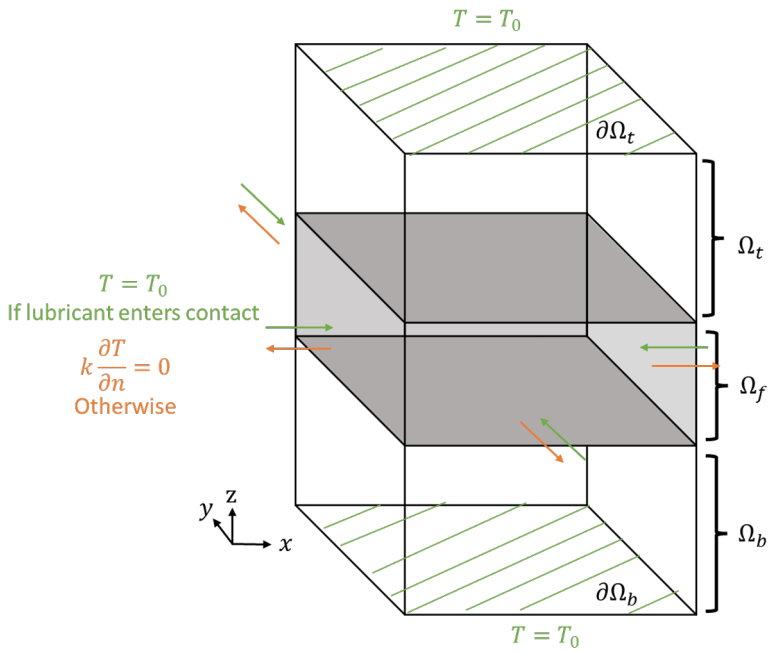


Figure 2.12: Geometry of the thermal model and corresponding boundary conditions for solids and fluid. White areas $\Omega_t$ and $\Omega_b$ represent top and bottom solids, the light grey area $\Omega_f$ represents fluid and dark grey surfaces represent solid-liquid interfaces.

In the solids, with the absence of motion in the y-direction, heat is transferred by conduction, described by Equation 2.29. This equation is solved for both the top and bottom solids.

$$\rho_s c_s u_x \frac{\partial T}{\partial x} - \nabla \cdot (k_s \nabla T) = 0 \tag{2.29}$$

where $u_x$ is the velocity of the solid surface in the x-direction, $c$ is the specific heat capacity and $k$ is the thermal conductivity and subscript $_s$ stands for the properties of the solid.

In the fluid film, according to the thin film assumption, convection in the z-direction is neglected. Moreover, according to Wheeler [75], considering the high Peclet number in EHL, conduction along the x and y directions is also neglected. Furthermore, the heat generation in the fluid film by compression $Q_{comp}$ and shear $Q_{shear}$ needs to be taken into account. The heat equation in the fluid film is written as Equation 2.30.

$$\rho_f c_f \left( u_{fx}(x,y,z)\frac{\partial T}{\partial x} + u_{fy}(x,y,z)\frac{\partial T}{\partial y} \right) - \frac{\partial}{\partial z}\left( k_f \frac{\partial T}{\partial z} \right) = Q_{comp} + Q_{shear} \tag{2.30}$$

where $u_{fx}(x,y,z)$ and $u_{fy}(x,y,z)$ represent the velocity of the fluid at any point in the lubricant film in the x and y directions, as shown in Equation 2.31 [74].

$$
\begin{aligned}
u_{fx}(x,y,z) &= \frac{\partial p}{\partial x}\left(\int_0^z \frac{z}{\eta}dz - \frac{\eta_e}{\eta'_e}\int_0^z \frac{1}{\eta}dz\right) + \eta_e(u_t - u_b)\int_0^z \frac{1}{\eta}dz + u_b \\
u_{fy}(x,y,z) &= \frac{\partial p}{\partial y}\left(\int_0^z \frac{z}{\eta}dz - \frac{\eta_e}{\eta'_e}\int_0^z \frac{1}{\eta}dz\right)
\end{aligned}
\tag{2.31}
$$

$Q_{comp}$ and $Q_{shear}$ represent the compression and shear heat sources, respectively, as shown in Equation 2.32 [74].

$$
\begin{aligned}
Q_{comp} &= -\frac{T}{\rho_f}\frac{\partial \rho_f}{\partial T}\left(\vec{u_f}\cdot\vec{\nabla}p\right) \\
Q_{shear} &= \eta\left[\left(\frac{\partial u_{fx}}{\partial z}\right)^2 + \left(\frac{\partial u_{fy}}{\partial z}\right)^2\right]
\end{aligned}
\tag{2.32}
$$

For the stationary problem in this study, the boundary conditions for the heat equations are the following: for the top and bottom surfaces ($\partial\Omega_t$ and $\partial\Omega_b$ in Figure 2.12), the temperature is set as the initial temperature $T_0$. For the other surfaces, $T = T_0$ if the fluid or the solid enters into the contact area; otherwise, $k\frac{\partial T}{\partial n} = 0$ [74].

### 2.4.2 Non-dimensionalisation of equations

Non-dimensionalisation is a common approach used in multivariate problems that scales variables to a value close to unity and facilitates the understanding of their variation and interactions. It also provides a simpler form to facilitate the numerical solving of the system of equations. This approach is used in the present study.

Since EHD pressure distribution and elastic deformation are very close to the one of a dry contact described by Hertz theory [130], Hertzian dry contact pressure field $p_H(x,y)$ is used to non-dimensionalise the pressure in equations of the contact model. For the circular contact of this study, it is written as Equation 2.33.

$$
p_H(x,y) = \begin{cases} p_h\sqrt{1-\left(\frac{x}{a}\right)^2-\left(\frac{y}{a}\right)^2} & if\ \sqrt{x^2+y^2} \le a \\ 0 & otherwise \end{cases}
\tag{2.33}
$$

where $p_h$ is the Hertzian pressure, representing the maximum pressure in contact, and $a$ is the radius of the contact area, such as:

$$
p_h = \frac{3W}{2\pi a^2} \qquad a = \sqrt[3]{\frac{3WR}{2E'}}
\tag{2.34}
$$

where $E'$ is the equivalent Young's modulus of the contacting solids (see Equation 2.25).

The following dimensionless variables are defined relative to the Hertzian parameters and the density $\rho_0$ and Newtonian viscosity $\eta_0$ value at initial (atmosphere) pressure and ambient temperature $T_0$.

$$X = \frac{x}{a} \quad Y = \frac{y}{a} \quad Z = \frac{z}{a} \quad \overline{u} = \frac{u}{a} \quad \overline{v} = \frac{v}{a} \quad \overline{w} = \frac{w}{a}$$
$$P = \frac{p}{p_h} \quad H = \frac{hR}{a^2} \quad \overline{\rho}_{f,s} = \frac{\rho_{f,s}}{\rho_0} \quad \overline{\eta} = \frac{\eta}{\eta_0} \tag{2.35}$$

Equations in Section 2.4.1 are non-dimensionalised with these dimensionless variables. The dimensionless generalised Reynolds equation is written as:

$$\frac{\partial}{\partial X}\left[\varepsilon\frac{\partial P}{\partial X}\right] + \frac{\partial}{\partial Y}\left[\varepsilon\frac{\partial P}{\partial Y}\right] - \frac{\partial}{\partial x}(\overline{\rho_x^*}) = 0 \tag{2.36}$$

with $\varepsilon = \dfrac{\overline{\rho}_f H^3}{\lambda}\left(\dfrac{\overline{\rho}}{\overline{\eta}}\right)_e$, $\lambda = \dfrac{u_e \eta_0 R^2}{a^3 p_h}$ and $\left(\dfrac{\overline{\rho}}{\overline{\eta}}\right)_e = \left[\dfrac{\overline{\eta}_e}{\overline{\eta}'_e}\overline{\rho}'_e - \overline{\rho}''_e\right]$

$$\overline{\rho}_e = \int_0^1 \overline{\rho}_f dZ$$
$$\overline{\rho}'_e = \int_0^1 \overline{\rho}_f \left(\int_0^Z \frac{1}{\overline{\eta}} dZ'\right) dZ \qquad \overline{\rho}''_e = \int_0^1 \overline{\rho}_f \left(\int_0^Z \frac{Z'}{\overline{\eta}} dZ'\right) dZ \tag{2.37}$$
$$\frac{1}{\overline{\eta}_e} = \int_0^1 \frac{1}{\overline{\eta}} dZ \qquad \frac{1}{\overline{\eta}'_e} = \int_0^1 \frac{Z}{\overline{\eta}} dZ$$
$$\overline{\rho}_x^* = \frac{\overline{\rho}'_e \overline{\eta}_e (u_t - u_b) + \overline{\rho}_e u_b}{u_e}$$

The dimensionless film thickness equation, load balance equation as well as elasticity equation are written as follows:

$$H(X,Y) = H_0 + \frac{X^2 + Y^2}{2R} + \overline{\delta}(X,Y)$$
$$\iint_S P(X,Y) dX dY = \frac{W}{p_h a^2} \tag{2.38}$$
$$\nabla \cdot \overline{\sigma}(\overline{u}, \overline{v}, \overline{w}) = 0$$

The dimensionless heat equations in solids are written as in 2.39:

$$\overline{\rho}_s \, \overline{c}_s \frac{u_x}{u_e}\frac{\partial \overline{T}}{\partial X} - \frac{\partial}{\partial X}\left(\overline{k}_s \frac{\partial \overline{T}}{\partial X}\right) - \frac{\partial}{\partial Y}\left(\overline{k}_s \frac{\partial \overline{T}}{\partial Y}\right) - \frac{\partial}{\partial Z}\left(\overline{k}_s \frac{\partial \overline{T}}{\partial Z}\right) = 0 \tag{2.39}$$

where $\overline{T} = \dfrac{T}{T_0}$. $\overline{c}_s = \frac{c_s}{c_f}$, $\overline{k}_s = \frac{k_s}{\rho_0 c_f u_e a}$. And finally, the dimensionless heat equation in fluids and heat source equations are written as 2.40.

$$\overline{\rho}_f \rho_0 c_f T_0 \left( u_{fx}(X,Y,Z) \frac{\partial \overline{T}}{\partial X} + u_{fy}(X,Y,Z) \frac{\partial \overline{T}}{\partial Y} \right) - \frac{\partial}{\partial Z} \left( \frac{kR^2 T_0}{H^2 a^3} \frac{\partial \overline{T}}{\partial Z} \right) = \overline{Q}_{comp} + \overline{Q}_{shear}$$

$$\overline{Q}_{comp} = -\frac{\overline{T}}{\overline{\rho}_f} \frac{\partial \overline{\rho}_f}{\partial \overline{T}} p_h \left( \vec{u_f} \cdot \vec{\nabla} P \right) \tag{2.40}$$

$$\overline{Q}_{shear} = \frac{\eta_0 \overline{\eta} R^2}{H^2 a^3} \left[ \left( \frac{\partial u_{fx}}{\partial Z} \right)^2 + \left( \frac{\partial u_{fy}}{\partial Z} \right)^2 \right]$$

### 2.4.3 Numerical Solution

As suggested by Habchi [142], a penalty method is used to treat the cavitation problem at the contact outlet.

The solution of the entire non-Newtonian thermal model requires several solution stages. In order to favour the convergence of the solution, the equivalent isothermal Newtonian model by neglecting shear and thermal effects is solved and used as an initial value for subsequent solutions. This approximation is then used as an initial condition to perform the final stage of solving the non-Newtonian thermal model.

Finally, to facilitate the calculations for high-viscosity cases (due to high pressure and/or low temperature), the load ramping method is also used. This means that the simulation is first run at a higher temperature (to obtain lower viscosity) and then gradually reduced to the desired temperature value. The results at the higher temperature will be used as initial conditions for the next iteration, thus improving the convergence of the Newton-type method.

## 2.5 Tribological experiments

To evaluate the quantitative modelling approach, tribological experiments were performed for BB and SQ, using the ball-on-disc tribometer Jerotrib at LaMCoS - INSA de Lyon described in [40]. The bottom of the ball dips into the reservoir full of lubricant to ensure fully flooded conditions. The ball was made of either steel or tungsten carbide, with a roughness of 5 nm and 20 nm, respectively. 3 disks were used, in steel, sapphire and tungsten carbide, with a roughness of 10 nm, 8 nm and 20 nm, respectively. The two specimens (ball and disc) as well as the lubricant tank were thermostatted at three different temperatures for each fluid during the tests, from 293 K to 353 K. Normal loads were widely varied to explore a large range of Hertzian pressures, from 0.8 GPa up to 3 GPa. The two specimens (the ball and the disc) are independently controlled so that tests were performed at constant entrainment speed $u_e$. It induced a central film thickness of the order of 100 nm to ensure EHL condition but varying SRR (see Section 1.2 for definitions of $u_e$ and SRR).

Friction curves measured on the BB and SQ were first provided in [40] and [115] respectively. Because these experiments were realised independently of this thesis by other researchers in LaMCoS, readers should refer to the above references for more details.

## 2.6 Conclusion

This chapter outlines the strategy and methodology pursued throughout this thesis. The two fluids selected for this study are squalane and benzyl benzoate, chosen for their differing characteristics as a lubricant and a traction-like fluid. The intrinsic rheological behaviour of these two fluids needs to be determined independently of friction measurements on tribometers and to be implemented in a model at the continuum scale.

The Eyring viscosity model is chosen for this investigation, with its ability to intrinsically account for an asymptotic limiting shear stress (e.g. in scenarios of high pressure leading to long relaxation times), and because it requires only two parameters for full determination, making it an ideal candidate. In order to establish the Eyring model for both fluids, the Newtonian viscosity $\eta_N$ and Eyring stress $\tau_e$ have to be determined through a contact-independent approach. This is achieved through rheological measurements and molecular dynamics (MD) simulations. The Newtonian viscosity is either measured experimentally or calculated using equilibrium molecular dynamics (EMD) simulations. The response of the fluid to an imposed shear rate at any given pressure and temperature is obtained through non-equilibrium molecular dynamics (NEMD) simulations. $\tau_e$ in terms of pressure $p$ and temperature $T$ for both fluids can be derived from NEMD results. The process of characterisation and results will be presented in Chapter 3.

These fluid characterisations will then be integrated into a thermal EHL non-Newtonian (TEHLnN) contact model at the continuum scale. Friction will subsequently be predicted and compared with experimental data from tribometers. This process will be discussed in detail in Chapter 4.

# Characterisation of fluid

This chapter presents the determination of the parameters namely Newtonian viscosity $\eta_N$ and Eyring stress $\tau_e$ for the Eyring constitutive equation of the two fluids studied. These parameters are crucial for accurately modelling the rheological behaviour of the fluids under EHL conditions.

In the process of determining the Newtonian viscosity, the Stokes-Einstein relation is invoked, and the diffusion coefficient is calculated using equilibrium molecular dynamics (EMD) simulations. This method of estimating Newtonian viscosity will subsequently be compared with results obtained from high-pressure viscometer measurements.

For the determination of the Eyring stress, confined NEMD simulations are employed. These simulations are carried out under isothermal and isobaric conditions, and the shear stress and the corresponding shear rate will be obtained.

Once both parameters are determined, the generalised viscosity (Eyring) models for the two fluids are established taking into account the viscosity variation with pressure, temperature and shear rate. The predicted viscosity is compared with rheological measurements to validate the models. The validated models will then be used in the TEHD contact model to predict friction, which will be presented in Chapter 4.

## 3.1 Newtonian (low shear) viscosity characterisation

EMD simulations were used to determine the Newtonian viscosity of a fluid, as presented in Chapter 2, Section 2.3.3. The resulting Newtonian viscosity values were compared with measurements from the high-pressure viscometer of Bair [116] for SQ and Ndiaye et al. [40] for BB. The simulation conditions of both fluids are summarised in Table 3.1.

| | SQ | BB |
|---|---|---|
| p [MPa] | 0.1 - 2000 | 0.1 - 2000 |
| T [K] | 313 - 2000 | 313 - 2000 |

Table 3.1: Simulation conditions of SQ and BB.

### 3.1.1 Newtonian viscosity by Stokes-Einstein method

The concept of the Stokes-Einstein method is described in Section 2.3.2b. As shown in Equation 2.17, this method requires two pieces of information, the diffusion coefficient $D$ and the characteristic length $r_c$, both can be calculated by EMD simulations. In the present study, $D$ is derived by tracing the MSD curve, and $r_c$ is derived by estimating the volume of each molecule.

$$\eta_N = \frac{k_B T}{6\pi D r_s}$$

#### a Coefficient of diffusion

Previously, Porras-Vazquez [97] performed a wide study of the diffusion behaviour for both BB and SQ by deriving the coefficient of diffusion $D$ from MSD curves, as shown in Figure 3.1(a) and (b).

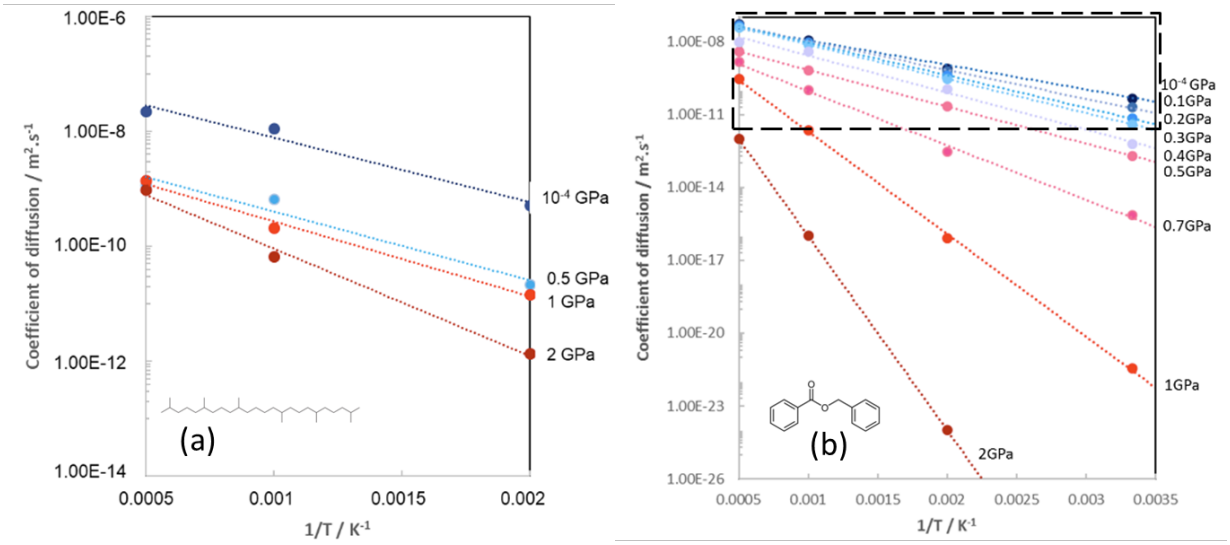


Figure 3.1: Coefficient of diffusion of (a) SQ and (b) BB derived from EMD simulation by tracing MSD curves. Adapted from [97].

He found that the diffusion coefficients of the two fluids show a linear relationship with the inverse of the temperature $\frac{1}{T}$ in a log-lin plot, implying that $D$ satisfies the Arrhenius equation:

$$D = D_0 \exp\left(\frac{-E_a}{k_B T}\right) \tag{3.1}$$

where $D_0$ is a pre-exponential factor of $D$, $k_B$ is the Boltzmann constant $k_B = 1.380649 \times 10^{-23 J/K}$ and $T$ is the temperature. $E_a$ is called the activation energy, which can be related to the energy barrier concept in the SATA theory. Because of the exponential dependency of $D$ with respect to $\frac{1}{T}$, $E_a$ can also be related to the slope of each set of $D$ in the log-lin plot shown in Figure 3.1.

Accordingly, Porras-Vasquez calculated the variation of the activation energy $E_a$ of the two fluids with respect to pressure, as shown in Figure 3.2.

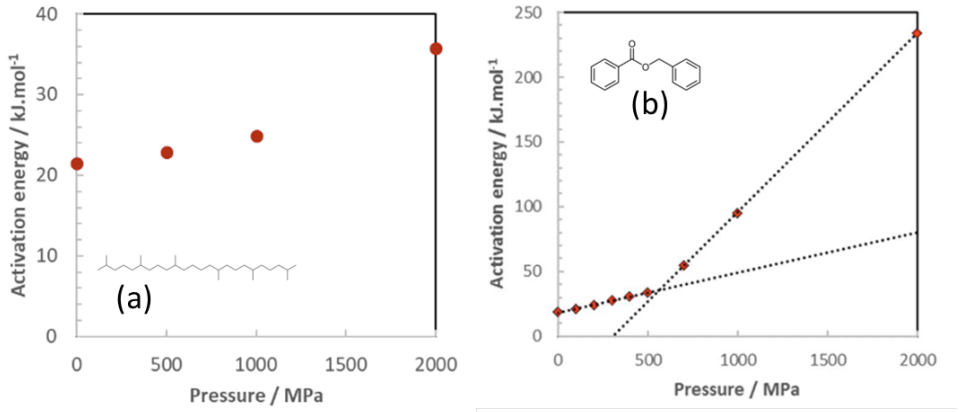


Figure 3.2: Activation energy of (a) SQ and (b) BB derived from diffusion coefficient. Adapted from [97].

This theory provides a first step for viscosity prediction at high pressure. However, care must be taken about the orders of magnitude of the diffusion coefficient, which might have been derived from simulation too short to reach the relaxation time. Indeed, since the calculation of $D$ from the MSD curve is only valid in the diffusive regime (see Section 2.3.2b), the simulation time $t_{simu}$ must be longer than the relaxation time $t_{rel}$. According to Equation 2.18, to reach the diffusion regime ($t_{simu} \geq t_{rel}$) and obtain a diffusion coefficient $D$ of the order of $10^{-25} m^2/s$ (as shown in Figure 3.1(b)) would require a simulation time (not wall-clock time) longer than $t_{rel} \sim {}^{4r_c^2}/_{D} \sim 10^5\ s = 1.2\ days$, as $r_c$ is of the order of several Å ($10^{-10} m$). This is clearly beyond the reach of the computing power ability. Knowing that the typical EMD simulation time we can achieve with the available resources is of the order of nanoseconds or tens of nanoseconds ($10^{-9} s$ to $10^{-8} s$), the minimum diffusion coefficient that can be calculated from EMD simulations in this study is around $10^{-12} m^2/s$. It corresponds to the area framed in a dashed line in Figures 3.1(b).

In the present study, to focus on the diffusive regime of the fluid, EMD simulations have been run without any restriction on the simulation time, simulations run until the maximum wall-clock time is reached, according to our computing facilities of 8 (LaMCoS) or 5.5 (P2CHPD) days, which is the server limit. According to the results, the longest simulation time achieved with this strategy was 71.5 ns, and diffusion is still not reached. During the calculation of the diffusion coefficients in post-processing, a verification step is added to check if the system has entered the diffusive regime. This was done by measuring the last part of the simulation results to see if the slope of the MSD in time is of the order of 1, as described in Section 2.3.2b. Figure 3.3 illustrates this verification step for two systems of SQ at 500 MPa at different temperatures, where case (a) is in the diffusive regime because the power index $b$ is close to 1 and case (b) is not.

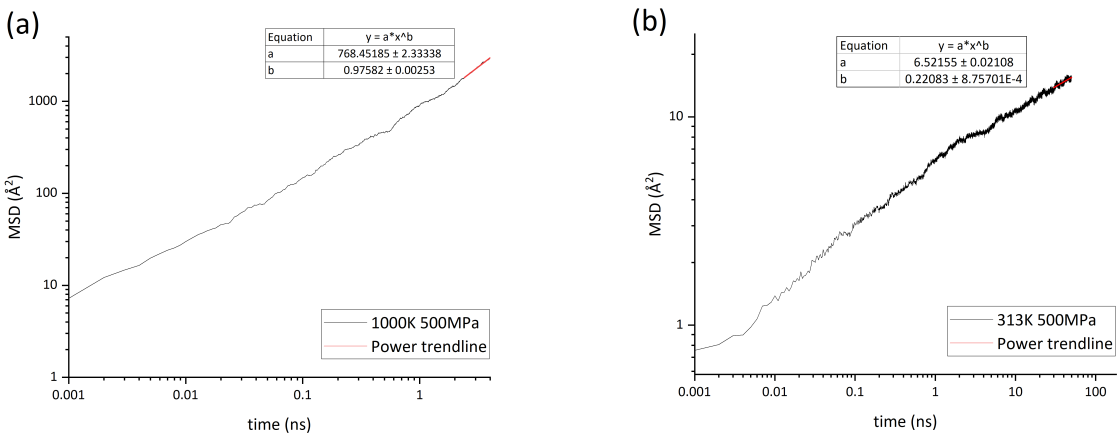


Figure 3.3: Verification for the diffusive regime. (a) SQ 1000K 500 MPa run for 4 ns, (b) SQ 313 K 500 MPa run for 71.5 ns.

Due to the lack of a priori estimates of $t_{rel}$ for the two fluids tested in relation to pressure and temperature, this verification step can only be done a posteriori. In the present study, we use the last 20% to 40% of the total simulation duration for verifying the diffusive regime. For example, for case (a) in Figure 3.3, with a total simulation time of 4 ns, all the last 40% is in the diffusive regime, and the data range for calculating $D$ is the last 40% of results. Whereas in case (b), with a total simulation time of 71.5 ns, even the last 20% is non-diffusive, thus at this condition no $D$ can be calculated. The diffusion coefficients of SQ and BB calculated in the present study with respect to $\frac{1}{T}$ are shown in Figure 3.4.

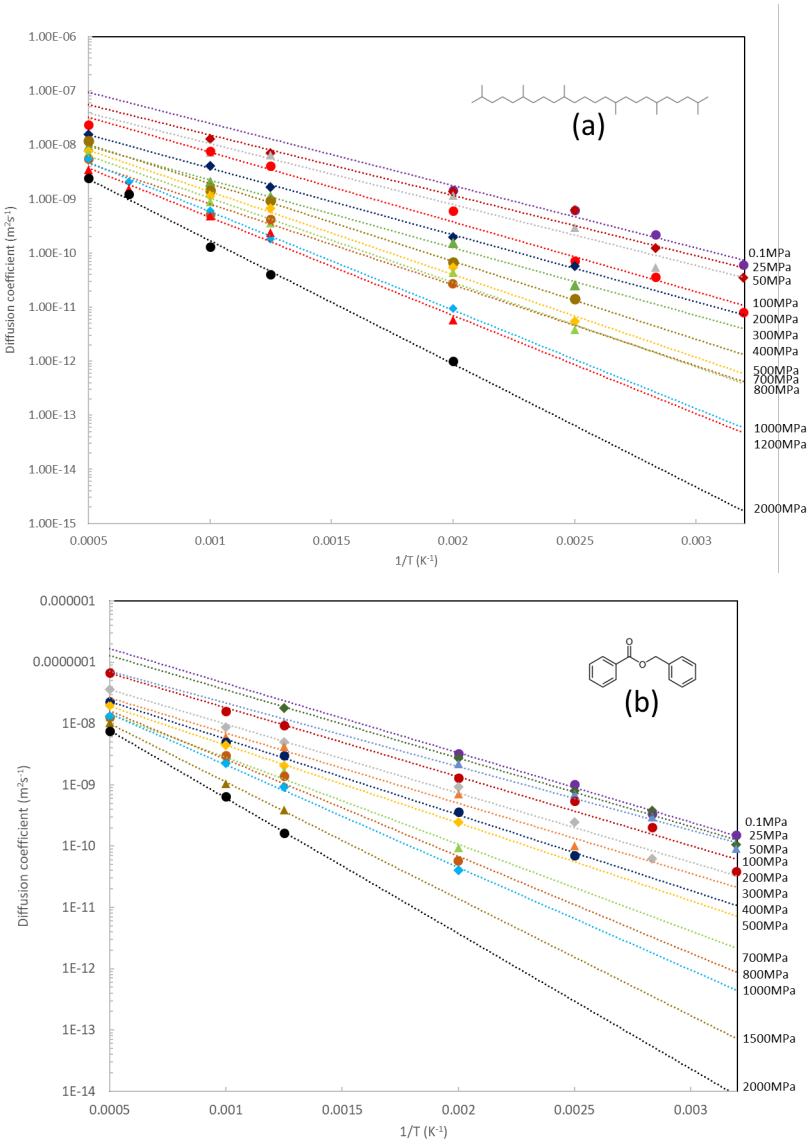


Figure 3.4: Diffusion coefficient calculated from EMD simulations performed in the present study. (a) SQ and (b) BB.

These diffusion data can be considered in relation to literature data. For instance, the experimental measurement from Mondello et al.[184] and simulation result from Prentice et al. [84] and Mondello et al. [184, 185] for $D$ of SQ at 293 K and at atmospheric pressure $p_{atm}$ (0.1 MPa) can be found in the literature. In references [184] and [185], the diffusion coefficient was calculated using constant volume simulations with UA force fields. In reference [84], both UA and AA force fields were used, and the diffusion coefficient was calculated using the same MSD method (see Equation 2.19) as in this study. The experimental results in reference [184] were obtained using the pulsed-field-gradient nuclear magnetic resonance (PFG-NMR) method. These data have been compared with data from this study at atmospheric pressure. The comparison is shown in Figure 3.5.

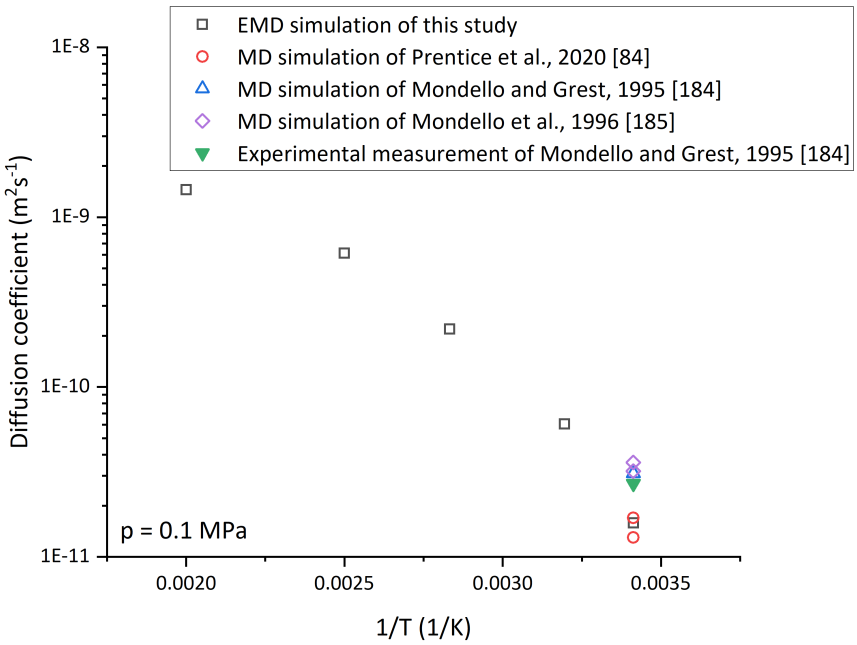


Figure 3.5: Comparison of the diffusion coefficient of SQ $D$ at atmospheric pressure. $D$ is calculated from the EMD simulations performed in the present study (empty black squares), the MD simulation result of Prentice et al. [84] (empty red circles), Mondello and Grest [184] (empty blue triangles), Mondello et al. [185] (purple diamonds), and experimental measurement by Mondello and Grest [184] (full green inverted triangle).

Firstly, the diffusion coefficient $D$ obtained in this study at 293 K and 0.1 MPa is in the same order of magnitude as the experimental and simulation results of Mondello et al. [184, 185]. A particularly good agreement is found with the simulation result of Prentice et al. [84]. This result shows that the EMD simulations give an accurate estimation of $D$ at atmospheric pressure.

Secondly, similar to the results of Porras-Vazquez [97], the $D$ calculated in this study (see Figure 3.4) also show a "linear" relationship with $\frac{1}{T}$ on the log-lin plot, implying that they follow the Arrhenius equation. Thus we can calculate the corresponding values of $D_0$ by fitting the diffusion curves in Figure 3.4 with the Arrhenius equation (see Equation 3.1) and the y-intercept provides $D_0$. The results are shown in Figure 3.6.

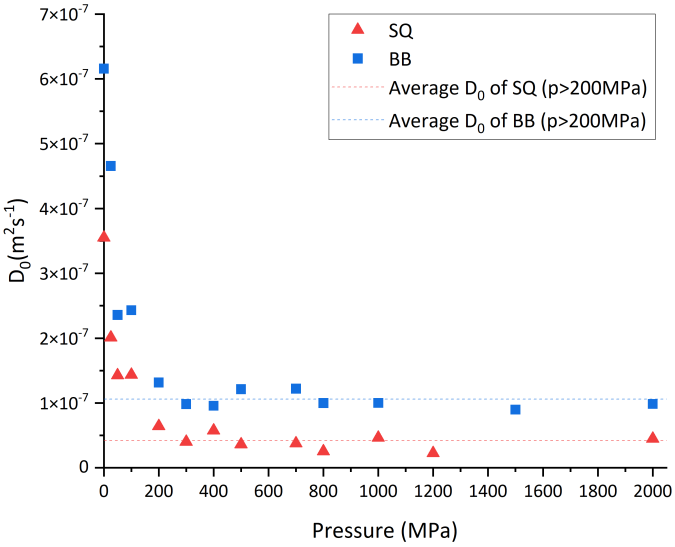


Figure 3.6: Parameter $D_0$ of Arrhenius equation of SQ and BB.

It can be seen that the value of $D_0$ for both fluids varies little with pressure, except at lower pressures (p<200 MPa). This phenomenon is probably due to inaccuracies in calculating the diffusion coefficient at lower pressures. Indeed, as can be seen in Figure 3.4(a) and (b), the lower pressure cases (e.g. 0.1 MPa, 25 MPa and 50 MPa) have fewer data than others. This is because the phase change (boiling) at high temperatures and low pressure made it difficult to calculate $D$. The boiling points of the two fluids at atmospheric pressure can be found in the literature [186] at 694.45 K for SQ and 596.65 K for BB. On the other hand, at low temperatures, it was previously stated that the calculation of $D$ by the MSD requires a longer simulation time. Fewer points and less accuracy have a non-negligible effect on the value of $D_0$ under these conditions. Consequently, in the following calculations, the values of $D_0$ are taken as the average of all data for p>200 MPa. For SQ this value is $4.17 \times 10^{-8} m^2/s^{-1}$ and for BB it is $1.06 \times 10^{-7} m^2/s^{-1}$. They are shown as two dashed lines in Figure 3.6.

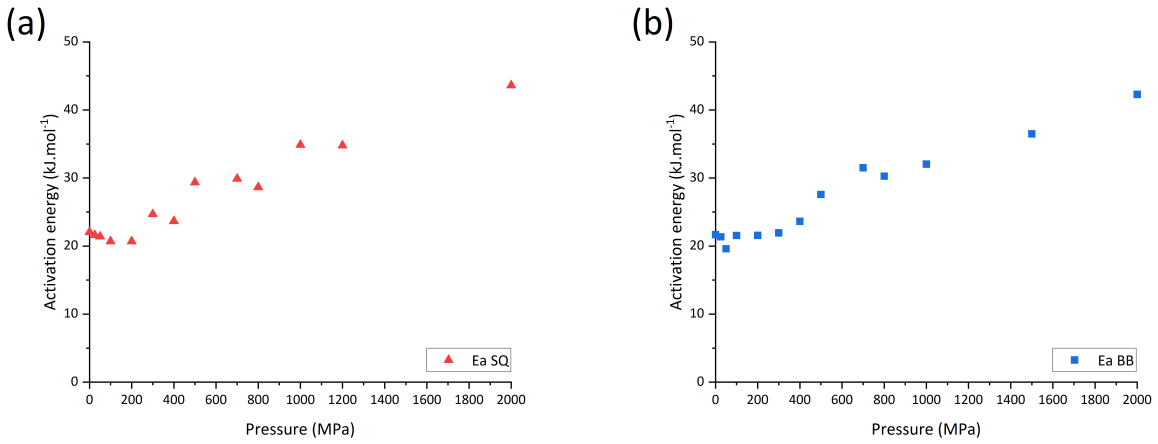


Figure 3.7: Activation energy calculated from $D$ of the present study. (a) SQ and (b) BB.

Thirdly, the corresponding activation energy $E_a$ can be derived from the slope of the Arrhenius fits, as it was already done by Porras-Vazquez [97]. The results are shown in Figure 3.7.

Compared to the $E_a$ of Porras-Vazquez [97], no inflexion point is observed, which is consistent with the left part in Figure 3.2(b). Besides, the order of magnitude in Figure 3.2(a) and the left part in (b) are close to the results from this study. The $E_a(p)$ from this study for both fluids follows a linear law of the type $E_a(p) = A_{Ea} + B_{Ea}p$, where the fitting parameters $A_{Ea}$ and $B_{Ea}$ are shown in Table 3.2.

| Fluid | $A_{Ea}$[kJ/mol] | $B_{Ea}$[kJ/mol.MPa] | $R^2$ |
|---|---|---|---|
| SQ | 20.672 | 0.012 | 0.946 |
| BB | 20.519 | 0.011 | 0.957 |

Table 3.2: The fitting parameters for the $E_a$ equations of BB and SQ.

Finally, the calculated minimum diffusion coefficient by EMD is of the order of $10^{-12}m^2/s$ (for SQ at 500 K and 2000 MPa), which is in agreement with the estimation made earlier in this section. Using $E_a(p)$ and $D_0$, an Arrhenius-type equation for the diffusion coefficient $D$ is established and used later in the Stokes-Einstein equation (Equation 2.17) to predict the Newtonian viscosity.

**b Characteristic length**

The characteristic length $r_c$ is the last parameter to be determined in the Stokes-Einstein equation (Equation 2.17). As stated in Section 2.3.2b, $r_c$ is assumed to be equal to the radius of an equivalent sphere which represents the fluid molecule in the present study. Using the sphere volume formula $V = \frac{4}{3}\pi r_c^3$, $r_c$ can be calculated. In EMD simulation, the total volume $V_t$ of the simulation box is first calculated at a given pressure and temperature. The volume $V$ of each equivalent sphere is then calculated as $V = V_t/N_m$, where $N_m$ is the total number of molecules in the simulation box. It is important to note that $V_t$ is not the total volume of the molecules. Rather, it is the total volume of the molecules plus the free volume between the molecules. This means that the changes in free volume caused by variations in temperature and pressure may introduce significant uncertainties in the calculation of $r_c$. To investigate this influence, $r_c$ values at different pressures (0.1 MPa to 3000 MPa at 293 K and 2000 K) and temperatures (293 K to 2000 K at 3000 MPa) are first calculated. Results are shown in Figure 3.8(a) and (b).

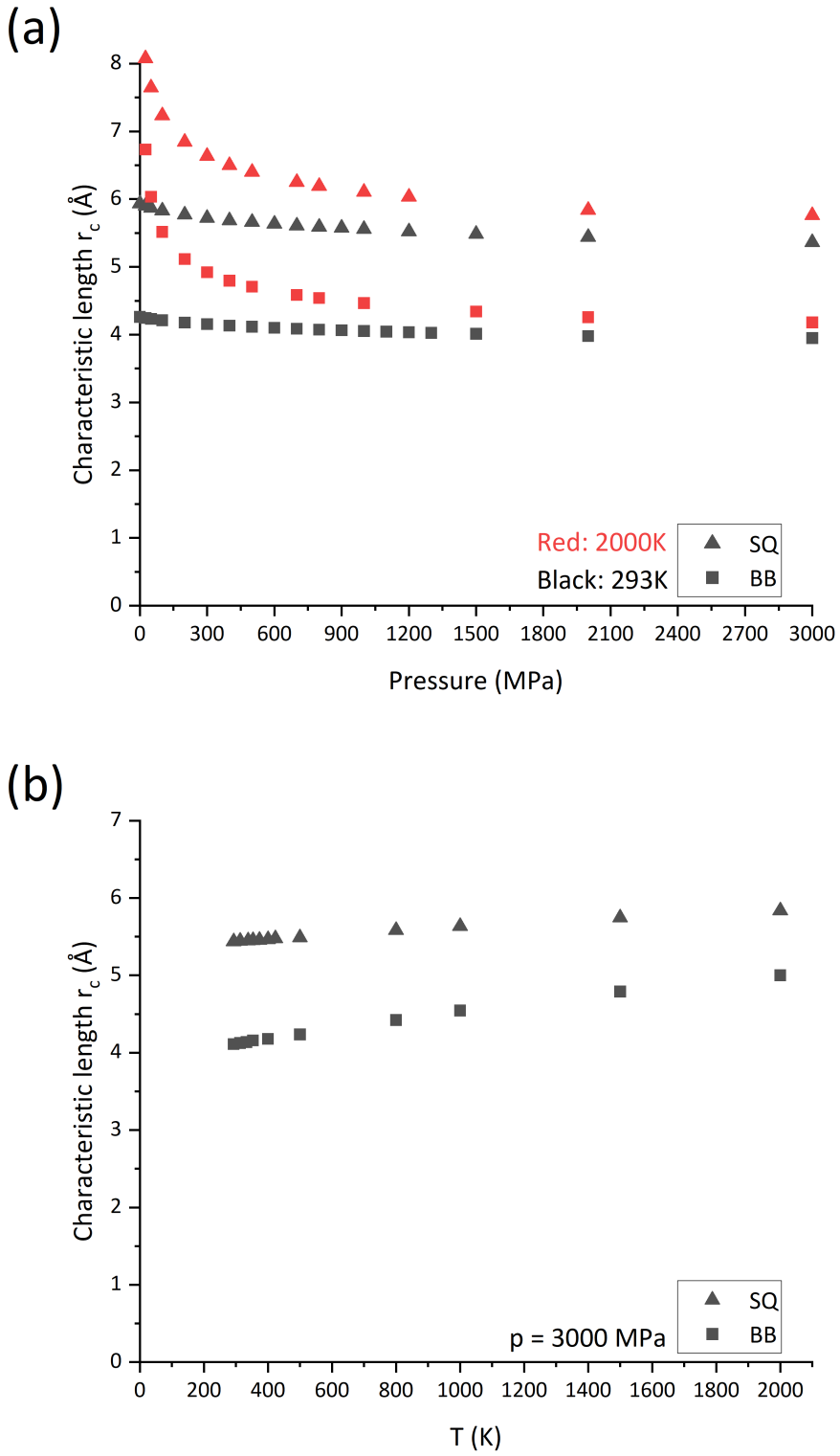


Figure 3.8: Characterisation length of SQ (triangles) and BB (squares) as a function of (a) pressure at 293 K (black) and 2000 K (red), (b) temperature at 3000 MPa.

In Figure 3.8(a), at lower temperatures (293 K), $r_c$ does not show significant changes with pressure. However, at higher temperatures (2000 K), the $r_c$ of both fluids show dramatic changes with pressure at lower pressures (<1000 MPa), likely due to the same phase change (boiling) observed in the calculation of $D_0$. But the values of $r_c$ gradually converge as the pressure increases. Finally, at very high pressures (3000 MPa), the values for both fluids between the two boundary temperatures (293 K and 2000 K) are very close. Upon further analysis of the change in $r_c$ with the temperature at 3000 MPa, as shown in Figure 3.8(b), it can be seen that $r_c$ at high pressure shows an insignificant variation with temperature. From 293 K to 2000 K, the increase in $r_c$ for both fluids is less than 1 Å, which is in agreement with the literature [175, 187]. This result demonstrates that while the change in free volume does have a significant impact on the value of $r_c$, high pressure and the resulting high compression can minimise the space between the molecules, yielding relatively close results. This value at high pressure is then assumed to be the closest approximation of the true $r_c$ value. Therefore, in the present study, values of $r_c$ calculated at the maximum pressure tested in this study (3000 MPa) are used to characterise $r_c$ for both fluids. Since this insignificant difference in the large range of temperature from 293 K to 2000 K (< 1 Å) has little effect on the viscosity calculation result, it is reasonable to assume that $r_c$ is a constant. In practice, it has been taken as the value at room temperature (293 K). For SQ, the value of $r_c$ is 5.44 Å; for BB, it is 4.11 Å.

**c Newtonian viscosity**

EMD simulations have provided a set of Arrhenius equations to model diffusion coefficients from calculated $E_a(p)$, $D_0$ and $r_c$. These parameters are then used in the Stokes-Einstein equations to calculate the Newtonian viscosity as a function of temperature and pressure. A summary of the Newtonian viscosity model is shown in Equation 3.2.

$$\eta_N(p,T)[\text{Pa.S}] = \frac{k_B T}{6\pi D(p,T) r_c}$$

$$D^{SQ}(p,T)[\text{m}^2/\text{s}] = D_0^{SQ} \exp\left(\frac{-E_a^{SQ}(p)}{k_B T}\right) \quad D^{BB}[\text{m}^2/\text{s}] = D_0^{BB} \exp\left(\frac{-E_a^{BB}(p)}{k_B T}\right) \tag{3.2}$$

$$E_a^{SQ}(p)[\text{kJ}/\text{mol}] = 20.672 + 0.012p \qquad E_a^{BB}(p) = 20.519 + 0.011p$$

$$D_0^{SQ}[\text{m}^2/\text{s}] = 4.17 \times 10^{-8} \qquad D_0^{BB}[\text{m}^2/\text{s}] = 1.06 \times 10^{-7}$$

$$r_c^{SQ}[\text{Å}] = 5.44 \qquad r_c^{BB}[\text{Å}] = 4.11$$

The predicted results are compared with the experimental data to validate this approach. Newtonian viscosity measured in the same range of operating conditions by the high-pressure viscometer for SQ [116], and BB [40] are used. Figure 3.9 shows the comparisons.

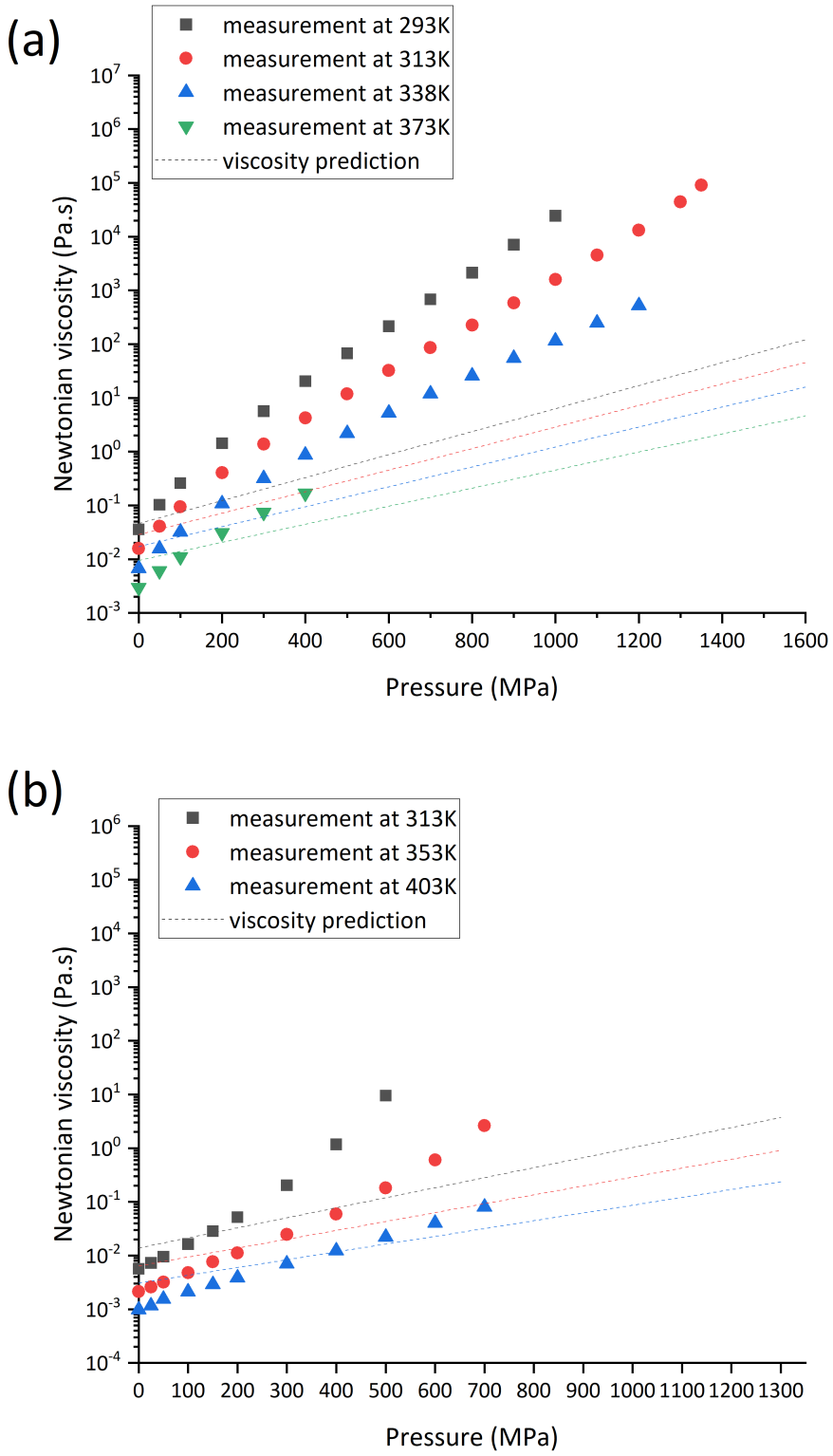


Figure 3.9: Comparison between Newtonian viscosity measurements (symbols, SQ [116] and BB [40]), and prediction by Stokes-Einstein method (dashed lines) of (a) SQ and (b) BB.

As expected, the Stokes-Einstein method predicts an exponential correlation between Newtonian viscosity and pressure, giving a "linear" trend on the log-lin plot. This is due to the Arrhenius equation in the diffusion coefficient. However, the prediction and experimental data show different trends. While this difference between the two data sets is relatively small around atmospheric pressure, where the prediction and measurement are of the same order of magnitude, it increases by several orders of magnitude as the pressure increases. Moreover, the Stokes-Einstein method is not able to predict the faster-than-exponential (or super-Arrhenius behaviour) [87, 88] growth experienced by the fluid at high pressures. Indeed, mainly for BB at 313 K and 353 K, the Newtonian viscosity growth gradually deviates from the original exponential growth and becomes faster with increasing pressure. In other words, for BB, the simple Arrhenius-type law can not describe its viscosity-pressure dependence. For SQ, although the experimental data are broadly consistent with the Arrhenius-type law, a change in the slope can be seen around 100 MPa, with a slight difference in the slope on either side and the same faster-than-exponential trend can be seen at high-pressure (313 K and around 1400 MPa).

An attempt to improve the prediction method is being made. One possibility is to consider the changes in parameters $D_0$, details are provided in Appendix C.

### 3.1.2 Discussion on the Stokes-Einstein/molecular dynamics methods

To discuss the reasons for the difference between measurements and predictions, the first thing that comes to mind is to criticise the physical parameters used to predict Newtonian viscosity. The possible causes of the discrepancy between them via the Stokes-Einstein relation and diffusion coefficient from EMD simulations have been investigated individually.

The first possibility is the inaccurate estimation of the characteristic length $r_c$. As stated before, each molecule is assumed to be a hard sphere (see Section 3.1.2b) and the impact of free volume is integrated. This assumption can lead to a higher value of $r_c$ as the free volume cannot be eliminated. Furthermore, the hard-sphere assumption seems to be a reasonable choice for compact molecules such as BB. However, for molecules such as SQ, which have a chain structure, this assumption may not always hold. In some studies [188], the hydrodynamic radius $r_h$ of such a chain-structured molecule is considered to be the width of the cross-section associated with the fastest motion, i.e., its backbone axis, which is likely to be much shorter than the radius of the equivalent sphere. However, it is difficult to explain the deviation of prediction at high pressures solely by the errors in the estimation of $r_c$ considering the possible difference of several orders of magnitude between the predicted Newtonian viscosity and the actual measured values. Since this length is of such a small order of magnitude, and its variations with pressure and/or temperature are always less than one decade in the tested range, this will not have a significant effect on the prediction results.

The second possibility is errors in the calculation of the diffusion coefficient $D$ and the resulting estimates of $D_0$ and $E_a(p)$. However, our calculation of the diffusion coefficients was conducted strictly in accordance with the original theory [101], and the same method was used in another study [175]. Additionally, we checked the diffusion states before each calculation to avoid potential errors. These measures ensured that the calculated $D$ was very close to the experimental measurements (see Figure 3.4). On the other hand, fitting the prefactor $D_0$ by a constant value could induce a subsequent error at low pressure, as shown in Figure 3.6. A more advanced function to fit $D_0(p)$ has been used and described in Appendix C. This function made it possible to model the sharp decrease of $D_0$ for p<200 MPa. It results in a Stokes-Einstein prediction of $\eta_N$ with $D_0(p)$, as shown in Figure C.2. The new prediction seems to have provided a trend that matches the variation of $\eta_N$ at lower pressures (<

200 MPa). However, the predicted values also seem to be consistently shifted downwards relative to the experimental measurements, which can actually be explained as the overestimation of the value of $r_c$ (see Stokes-Einstein Equation 2.17). The results showed that this approach did not significantly affect the prediction of Newtonian viscosity at high pressure. Therefore, it is unlikely that there is an individual error of sufficient magnitude that could cause a deviation of several orders of magnitude. This possibility is thus ruled out.

As each of these uncertainties taken independently is not sufficient to explain the differences observed, another aspect to consider is the cumulative effect of these uncertainties. There are several steps in the overall method, and each step involves some degree of uncertainty. For instance, errors may occur in the calculation of MSD by molecular dynamics simulations; in the calculation of $D$ from MSD; in the post-processing of the obtained $D$ to gain information about $E_a(p)$, and $D_0(p)$; and in the individual calculation of $r_c$. These errors accumulate step by step and are reflected in the final calculation of the Newtonian viscosity. It is possible that the cumulative error is large enough to cause the observed deviation. However, even taking into account the effect of error accumulation, the Stokes-Einstein (relation involving Arrhenius diffusion law) method still fails to describe the transition from exponential to faster-than-exponential behaviour with increasing pressure. Therefore, a simple Arrhenius-type law would not be sufficient to reproduce the experimental measurements of Newtonian viscosity. A question worth pondering is where this super-Arrhenius behaviour comes from and whether the Stokes-Einstein approach is really comparable to the experimental approach.

The Newtonian viscosity calculated from the diffusion coefficient reflects the properties of the bulk fluid in the diffusive regime, i.e., the properties of a relaxed fluid at equilibrium. Diffusion or flow is a time-scale concept; on sufficiently long timescales, even matter that is considered to be solid can "flow", such as the movement of the crust of Earth. For both experiments and simulations, there is a limit to the calculation of the diffusion coefficient (or viscosity) at equilibrium. This process can become overly lengthy and "too boring to observe" [117], due to the increase in relaxation time $t_{rel}$ caused by the increase in pressure. Examples of this situation can be the inability to enter the diffusion state within the limited simulation time due to the very long $t_{rel}$ ($t_{simu} < t_{rel}$), hence the inability to calculate $D$ (and thus $\eta_N$ based on a diffusion approach), as previously described. In experiments, such as those using a falling ball viscometer, the ball falls too slowly due to the extremely high viscosity, rendering it impossible to measure its value ($t_{obs} < t_{rel}$). Therefore, the experimental measurement of "Newtonian viscosity", in reality, is a measure of low-shear viscosity [116]. Equating the low-shear viscosity and Newtonian viscosity is predicated on the assumption that at very low shear rates, the fluid response is Newtonian. This assumption raises issues in two aspects. Firstly, in low-shear viscosity measurement, external forces are applied to the sample, placing it in a non-equilibrium state. This slightly diverges from the definition of Newtonian viscosity (defined in equilibrium) and the viscosity predicted by the Stokes-Einstein method, which is based on simulations performed at equilibrium. Furthermore, it remains questionable whether the fluid response is Newtonian in all cases, as high pressures result in longer relaxation times and lower critical shear rates. In this latter case, even "low shear" might still initiate shear-thinning. In the former, the increase in $t_{rel}$ may bring problems in the sample state during the measurement. Indeed, under these severe conditions, the relaxation timescale might be equal to or even exceed the duration of the simulation or experiment [118]. In such a case, the experimentally measured viscosity values would not reflect the fluid in a liquid state. Conceivably, these measurements from two different phases are very likely to show different trends, which are reminiscent of the exponential to faster-than-exponential transition that has been widely observed in viscometers with increasing shear rate [88].

Lastly, it is important to note that these two issues may be compounded. This means that in certain

low-shear viscosity measurements, the measured viscosity could correspond to the shear-thinning viscosity of a fluid in a solid-like state, which may differ from the concept of Newtonian viscosity.

As the prediction results show deviations of several orders of magnitude, we can conclude that, at this stage, the Stokes-Einstein method based on parameters derived from EMD simulation cannot provide a satisfactory prediction of friction at EHL conditions. Therefore, an alternative method is chosen to characterise Newtonian viscosity.

### 3.1.3 Determination of Newtonian viscosity model

As mentioned in Section 2.2, the pressures at which the experimental viscosity measurements are made (maximum pressure 1350 MPa for SQ and 700 MPa for BB) are below the pressure found in real EHD contacts. Nevertheless, viscosity models are commonly fitted on these experimental results in the literature to be extrapolated to EHL conditions. The most widely used is the (modified) WLF-Yasutomi model (see Equation 2.11, also displayed below), already published for SQ [85] and BB [40]. Parameters are summarised in Table 3.3.

$$\eta_N = \eta_g \times \exp\left(\frac{-2.303C_1 \times (T - T_g(p)) \times F(p)}{C_2 + (T - T_g(p)) \times F(p)}\right)$$
$$T_g(p) = T_{g0} + A_1 \times \ln(1 + A_2 p)$$
$$F(p) = (1 + B_1)^{B_2}$$

| | $A_1$ [°C] | $A_2$ [GPa$^{-1}$] | $B_1$ [GPa$^{-1}$] | $B_2$ [-] | $C_1$ [-] | $C_2$ [°C] | $T_{g0}$ [°C] | $\eta_g$ [Pa.s] | SD [%] |
|---|---|---|---|---|---|---|---|---|---|
| SQ [85] | 263.8 | 0.3527 | 13.73 | -0.3426 | 11.66 | 39.17 | -88.69 | $1.23 \times 10^7$ | 9.2 |
| BB [40] | 400.19 | 0.363 | 5.391 | -0.399 | 16.00 | 14.55 | -81.73 | $1.00 \times 10^{12}$ | 8.2 |

Table 3.3: Parameters of WLF-Yasutomi law for SQ and BB.

However, as mentioned in Chapter 2, the WLF-Yasutomi law has a mathematical limitation, namely the glass transition pressure $p_g$. Considering the possible high pressure of the EHL conditions on which the present study is focused, this limitation must be bypassed. As a result, an alternative Newtonian viscosity model, the viscosity scaling law created in the present study (see Equation 2.14, also displayed below), is used.

$$\varphi = \left(\frac{T}{T_R}\right)\left(\frac{V}{V_R}\right)^g$$
$$\eta_N = A\exp(B\varphi^{-q} + C\varphi^{-Q}), \qquad 0 < q < 1, \qquad 1 < Q$$

The scaling parameter $\varphi$ of the viscosity scaling law requires knowledge of the relative volume, which is defined by the Tait equation of state (see Equation 2.15, also displayed below). Values of the Tait equation are given in Table 3.4. The parameters for SQ are taken from Bair [116] and the reference density is taken from Mylona et al. [166]. The parameters for BB are derived from the results of the same test as SQ performed by Bair [167] and the reference density of BB is measured at LaMCoS - INSA de Lyon with an Anton Paar DMA4500M density meter.

$$\frac{V}{V_R} = [1 + a_v (T - T_R)] \times \left[1 - \frac{1}{1 + K_0'} \ln\left(1 + \frac{p}{K_0}(1 + K_0')\right)\right]$$

$$\frac{V}{V_R} = \frac{\rho_R}{\rho}$$

| | $K_0'$ | $a_v$[K$^{-1}$] | $K_{00}$[GPa] | $\beta_K$[K$^{-1}$] | $\rho_R$[kg/m$^3$] at 313.15K |
|---|---|---|---|---|---|
| SQ[116] | 11.74 | $8.36 \times 10^{-4}$ | 8.658 | $6.232 \times 10^{-3}$ | 795.8[166] |
| BB[167] | 10.44 | $7.47 \times 10^{-4}$ | 13.707 | $6.107 \times 10^{-3}$ | 1102.3[This study] |

Table 3.4: Parameters of Tait equation of state and density measurements for SQ and BB.

With the scaling parameter $\varphi$ defined, the viscosity scaling law created in this work can be fitted to the experimental viscosity measurements of both fluids, leading to the fitting parameters given in Table 3.5.

| | A[Pa.s] | B[K] | C[K] | q [-] | Q [-] | g [-] | SD [%] |
|---|---|---|---|---|---|---|---|
| SQ[This study] | $3.531 \times 10^{-5}$ | 6.016 | 0.133 | 0.999 | 3.954 | 3.521 | 10.77 |
| BB[This study] | $6.807 \times 10^{-5}$ | 4.280 | 0.155 | 0.871 | 6.037 | 4.569 | 4.13 |

Table 3.5: Parameters of the viscosity scaling law of SQ and BB.

The resulting viscosity curves are shown in Figure 3.10. The experimental viscosity measurements (solid symbols) and two Newtonian viscosity laws (dotted lines for WLF-Yasutomi, dashed lines for viscosity scaling) are compared. It can be observed that for a given temperature, both laws align well with the experimental data, providing a consistent description of Newtonian viscosity at low pressures, 0-1400 MPa for SQ and 0-700 MPa for BB. Notably, neither model seems to accurately predict the faster-than-exponential behaviour around 1400 MPa for SQ, which leads to a possible larger deviation from the experimental measurements with increasing pressures.

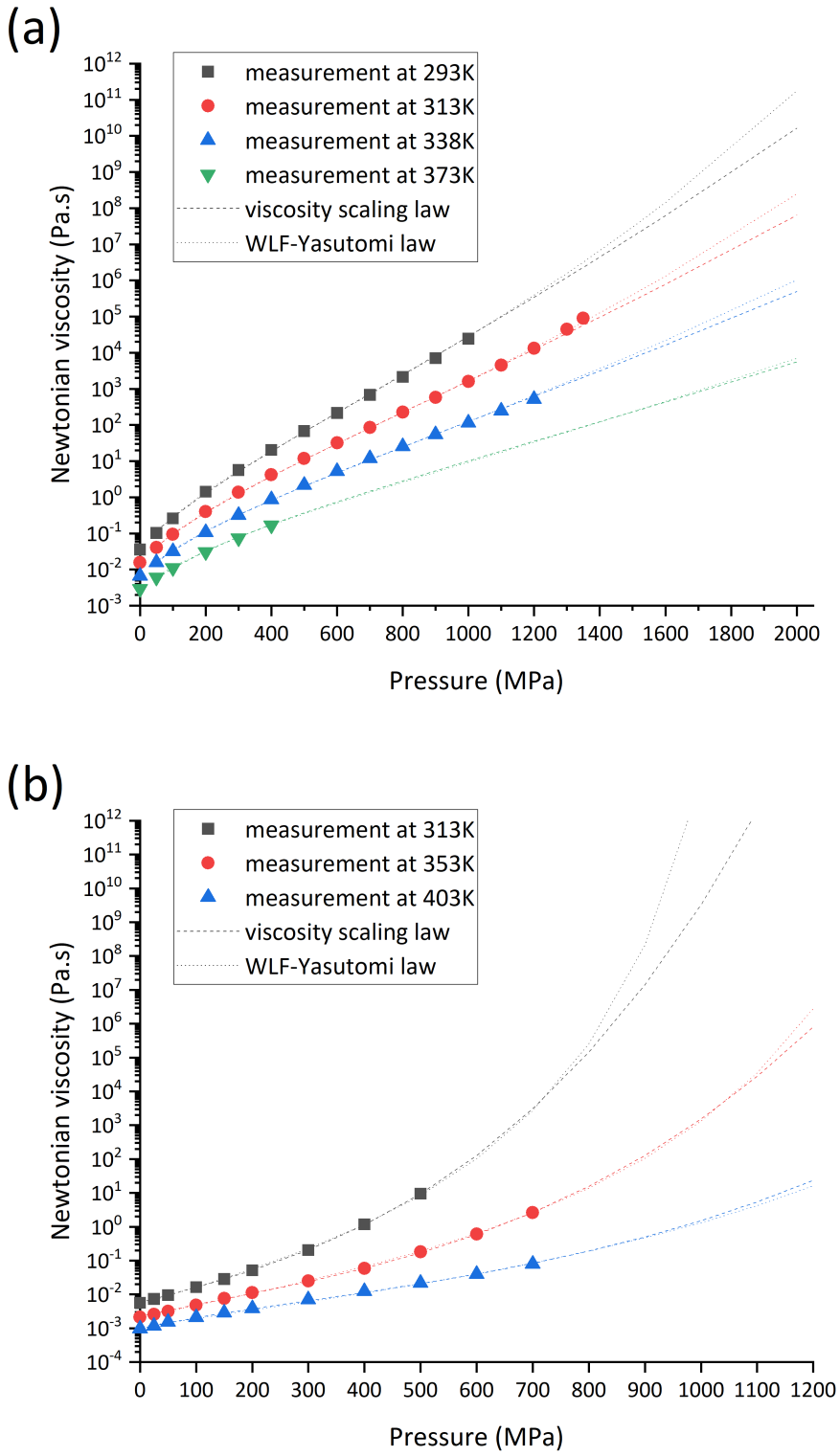


Figure 3.10: Comparison between Newtonian viscosity measurements (symbols, SQ [116] and BB [40]), WLF-Yasutomi law (dotted lines), and viscosity scaling law created in this work (dashed lines) of (a) SQ and (b) BB.

## 3.2 Eyring stress characterisation

NEMD simulations are performed using the method described in Section 2.3.3. To characterise the response of the fluid to shear, it is important to ensure that the simulation gives a good signal-to-noise ratio, which requires the "shear" step of the simulation to be as long as possible. In the actual numerical process, the simulation time was set to at least 5 ns for SQ and 8 ns for BB ($5 \times 10^6$ and $8 \times 10^6$ time steps). The temperature profile of the last 0.5 ns ($5 \times 10^5$ time steps) of each result was traced to check that there were no excessive temperature increases. The velocity profile of the last 2 ns ($2 \times 10^6$ time steps) of each result was traced to check if a Couette velocity profile had been reached. The resulting steady-state stress versus shear rate data in the last 2 ns was used for post-processing to obtain the non-Newtonian viscosity and Eyring stress. The NEMD simulation range of conditions for SQ and BB are shown in Table 3.6. For each given pressure and temperature, at least six different sliding velocities are considered, corresponding to shear rates in the range $10^8 s^{-1}$ to $10^{10} s^{-1}$.

| | T [K] | p [MPa] |
|---|---|---|
| SQ | 293 - 373 | 100 - 2000 |
| BB | 293 - 373 | 200 - 1000 |

Table 3.6: Tested conditions in NEMD of SQ and BB.

The following quantities are obtained from NEMD simulations: film thickness, shear stress, temperature distribution and velocity distribution along the sliding direction and through the film thickness (xz plane) all detailed hereafter. For each case tested, the temperature distribution and velocity profile are checked first. There should be no significant increase in temperature if the system is well thermostatted. For a linear velocity profile (Couette flow), the corresponding shear rate can be calculated from the film thickness and sliding velocity. The non-Newtonian viscosity can be calculated as shear stress divided by shear rate, and the calculation of the Eyring stress is described in Section 3.2.5.

### 3.2.1 Film thickness

The film thickness $h$ of the confined system is calculated as the distance between two surfaces. The rough surfaces used in this study, refer to the distance between the lowest peak of the upper surface and the highest peak of the lower surface, as shown in Figure 3.11. The expression for the film thickness $h$ is given in Equation 3.3:

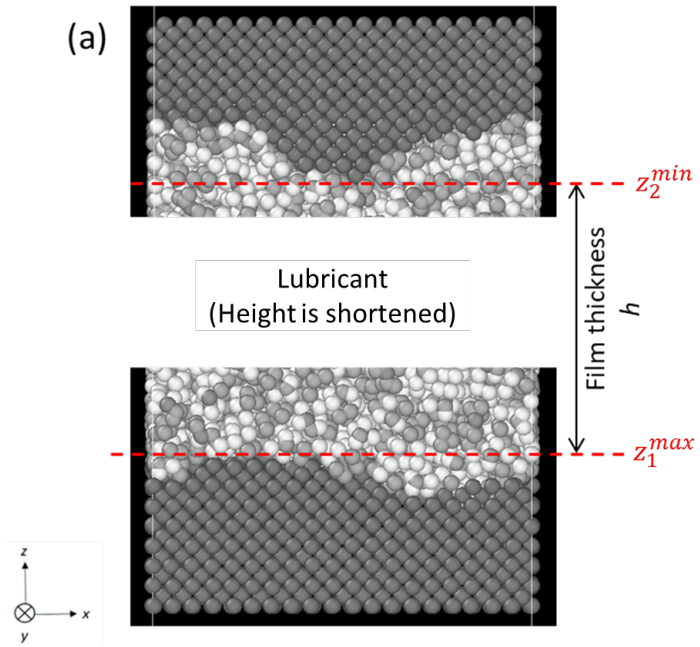


Figure 3.11: Schematic representation of the determination of film thickness in NEMD simulations.

$$h = \left\langle z_2^{min} - z_1^{max} \right\rangle \tag{3.3}$$

where $z_2^{min}$ and $z_1^{max}$ are the minimum and maximum z-coordinates of the bottom and top surfaces respectively, and $\langle ... \rangle$ is the time average. This difference is averaged over the last 2 ns of simulation to give the film thickness value.

### 3.2.2 Temperature profile

In MD simulations, the temperature $T$ is calculated from the kinetic energy $E_k$ of a statistically large group of atoms divided by the degrees of freedom and the Boltzmann constant $k_B$, written as follows:

$$T = \frac{2}{3}\frac{E_k}{k_B} \tag{3.4}$$

To obtain the temperature profile, the simulation box is first divided into individual chunks of thickness $\delta h$ and containing $N_{atom}$ atoms, as shown in Figure 3.12.

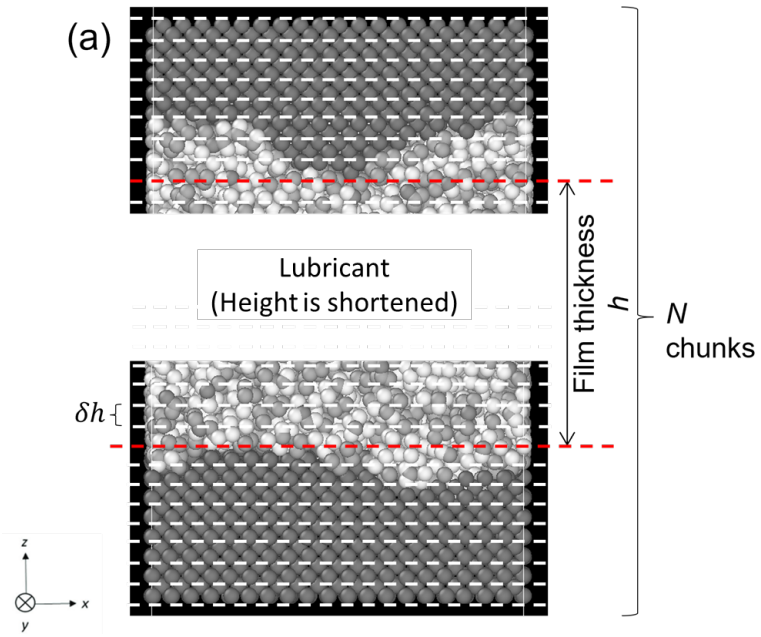


Figure 3.12: Schematic representation of the method used to chunk the system.

The average temperature for each chunk $T_{chunk}$ is calculated as follows:

$$T_{chunk} = \frac{2}{3k_B} \frac{\sum_{i=1}^{N_{atom}} \frac{1}{2} m_i u_i^2}{N_{atom}} \tag{3.5}$$

where $m_i$ and $u_i$ are the mass and velocity of each atom in that chunk.

Calculating each $T_{chunk}$ and plotting it against the number of chunks gives the temperature profile of the entire film thickness $h$. Examples of BB and SQ at different contact conditions are shown in Figure 3.13. For all NEMD simulations in this study, no excessive temperature increase in the film thickness is observed ($\Delta T \leq 5$ K). This demonstrates that the use of the Nosé-Hoover thermostat with an appropriate damping coefficient (see Section 2.3.3) can effectively control the temperature under shear.

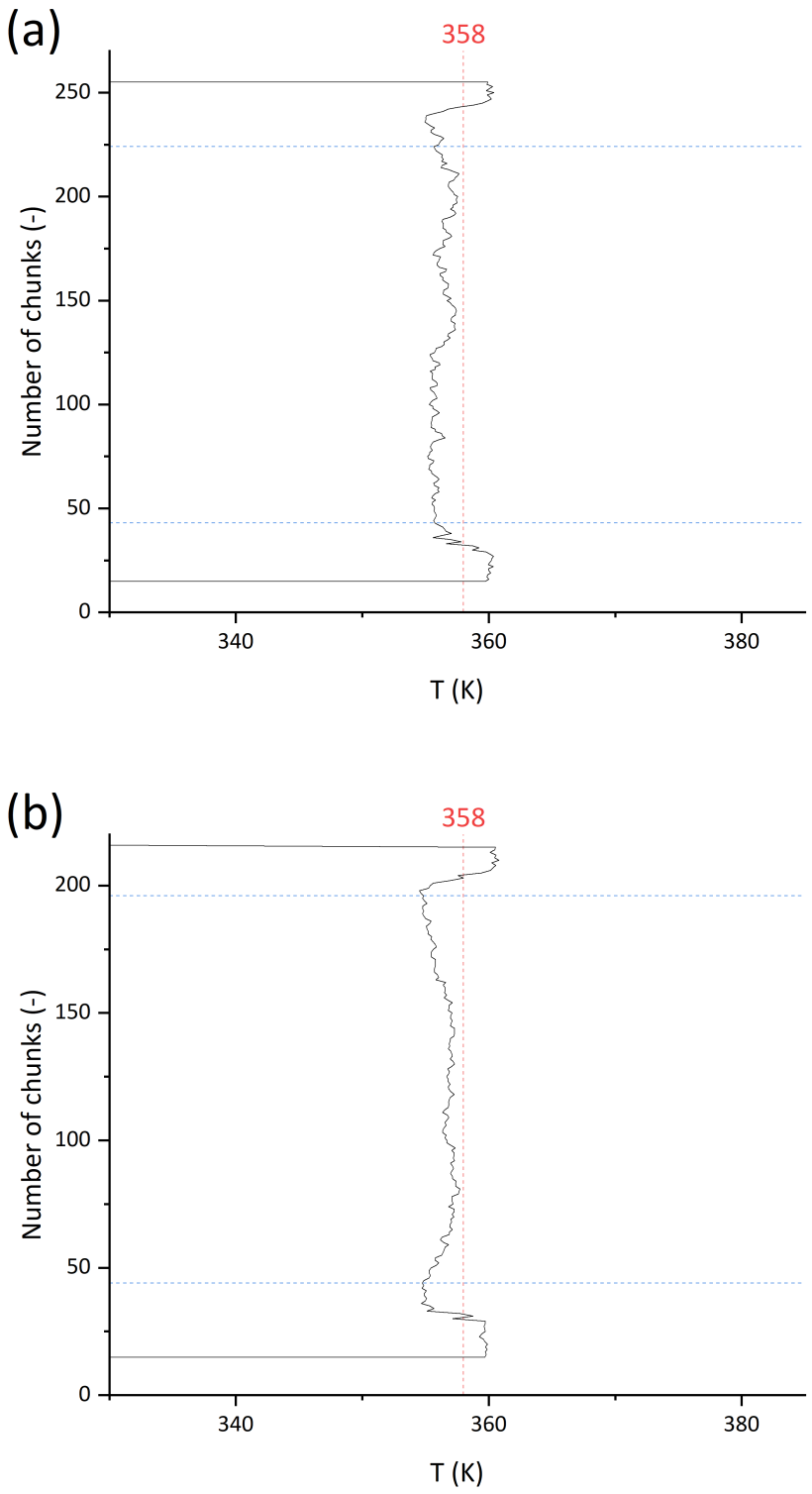


Figure 3.13: Temperature profile of NEMD simulations. (a) SQ at 353 K, 100 MPa, $\Delta u$=0.16Å/ps, (b) SQ at 353 K, 1500 MPa, $\Delta u$=0.16Å/ps. $T$ values are averaged over 2 ns. The red dashed vertical line represents the critical temperature ($T$+5 K) of the given contact condition, and the blue dashed horizontal lines represent the interface between the contact surface and the fluid.

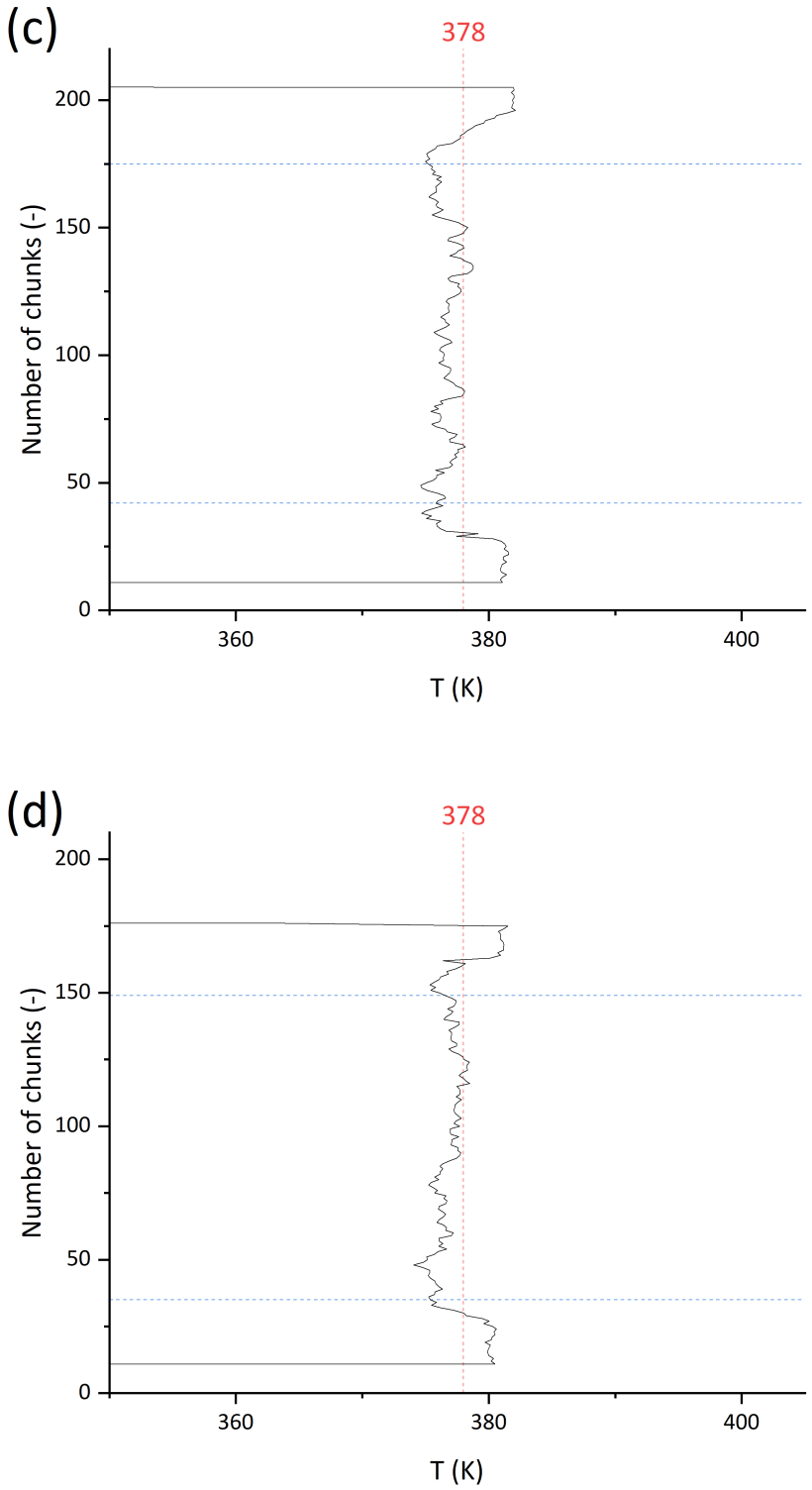


Figure 3.13: Temperature profile of NEMD simulations. (c) BB at 373 K, 100 MPa, $\Delta u$=0.16Å/ps, (d) BB at 373 K , 2000 MPa, $\Delta u$=0.16Å/ps. $T$ values are averaged over 2 ns. The red dashed vertical line represents the critical temperature ($T$+5 K) of the given contact condition, and the blue dashed horizontal lines represent the interface between the contact surface and the fluid.

### 3.2.3 Velocity profile

The chunks used to calculate the temperature profile are also used to calculate the velocity profile. In each chunk, the velocity is calculated by summing the quantity of motion or [mass × velocity] of each atom and dividing it by the sum of the masses. For the profile in the sliding direction, the expression is as follows:

$$u_{chunk} = \frac{\sum_{i=1}^{N_{atom}} m_i u_i}{\sum_{i=1}^{N_{atom}} m_i} \tag{3.6}$$

The shear rate calculation $\dot{\gamma} = \dfrac{\Delta u}{h}$ only holds if the velocity profile is linear. Thus, for each NEMD simulation in this study, the velocity profile is examined to check for a linear profile (Couette flow), as shown in Figure 3.14. As stated in Section 2.3.3, there are no assumptions about the velocity profile in the confined NEMD simulations, so this check is crucial. The shear rate is the basis for the subsequent process of calculating apparent non-Newtonian viscosity. In the present study, all velocity profiles of the simulation results presented have been verified to be linear.

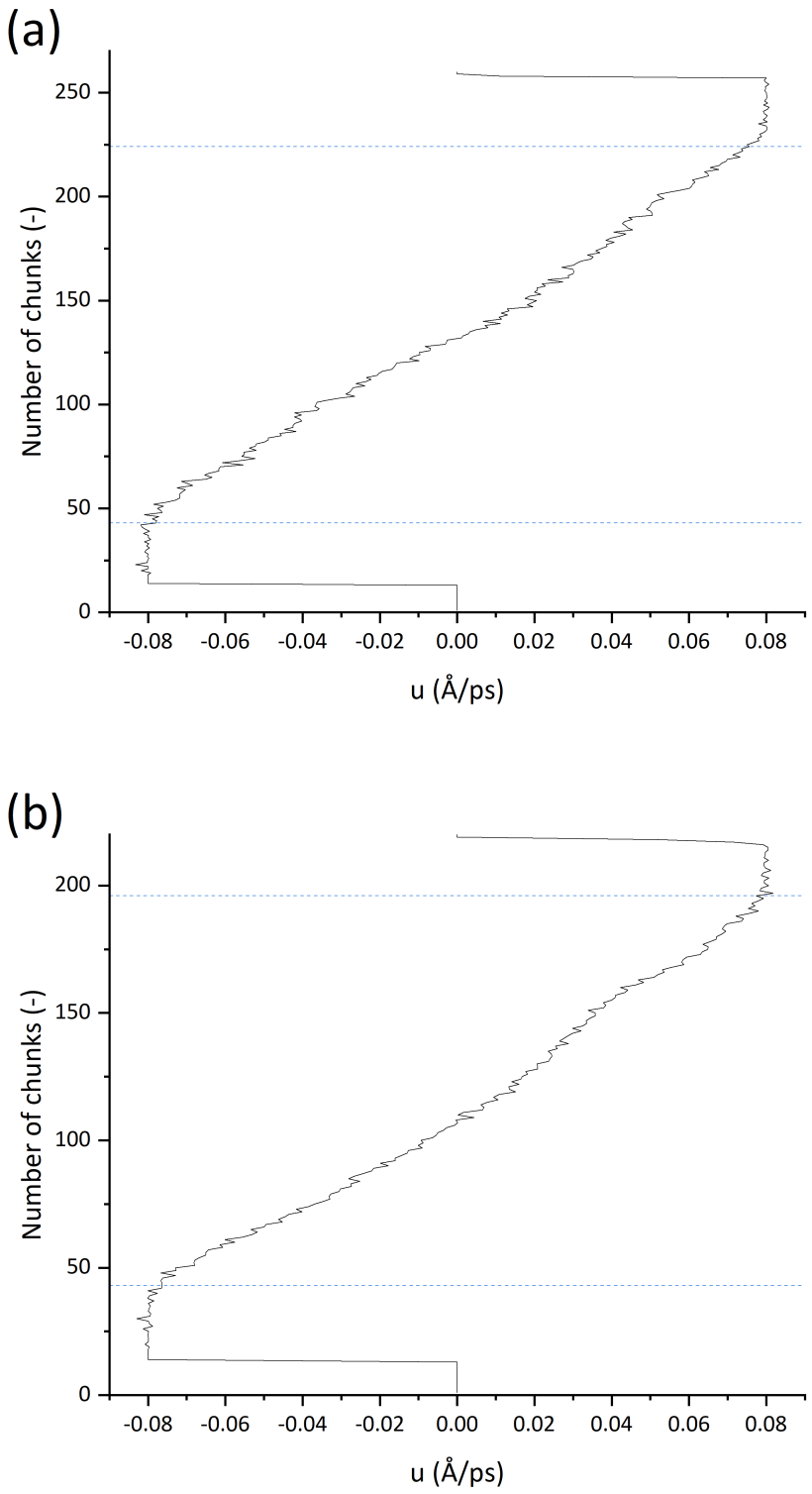


Figure 3.14: Velocity profile of NEMD simulations. (a) SQ at 353 K, 100 MPa, $\Delta u$=0.16Å/ps, (b) SQ at 353 K, 1500 MPa, $\Delta u$=0.16Å/ps. Velocity values are averaged over 2 ns. The blue dashed lines represent the interface between the contact surface and the fluid.

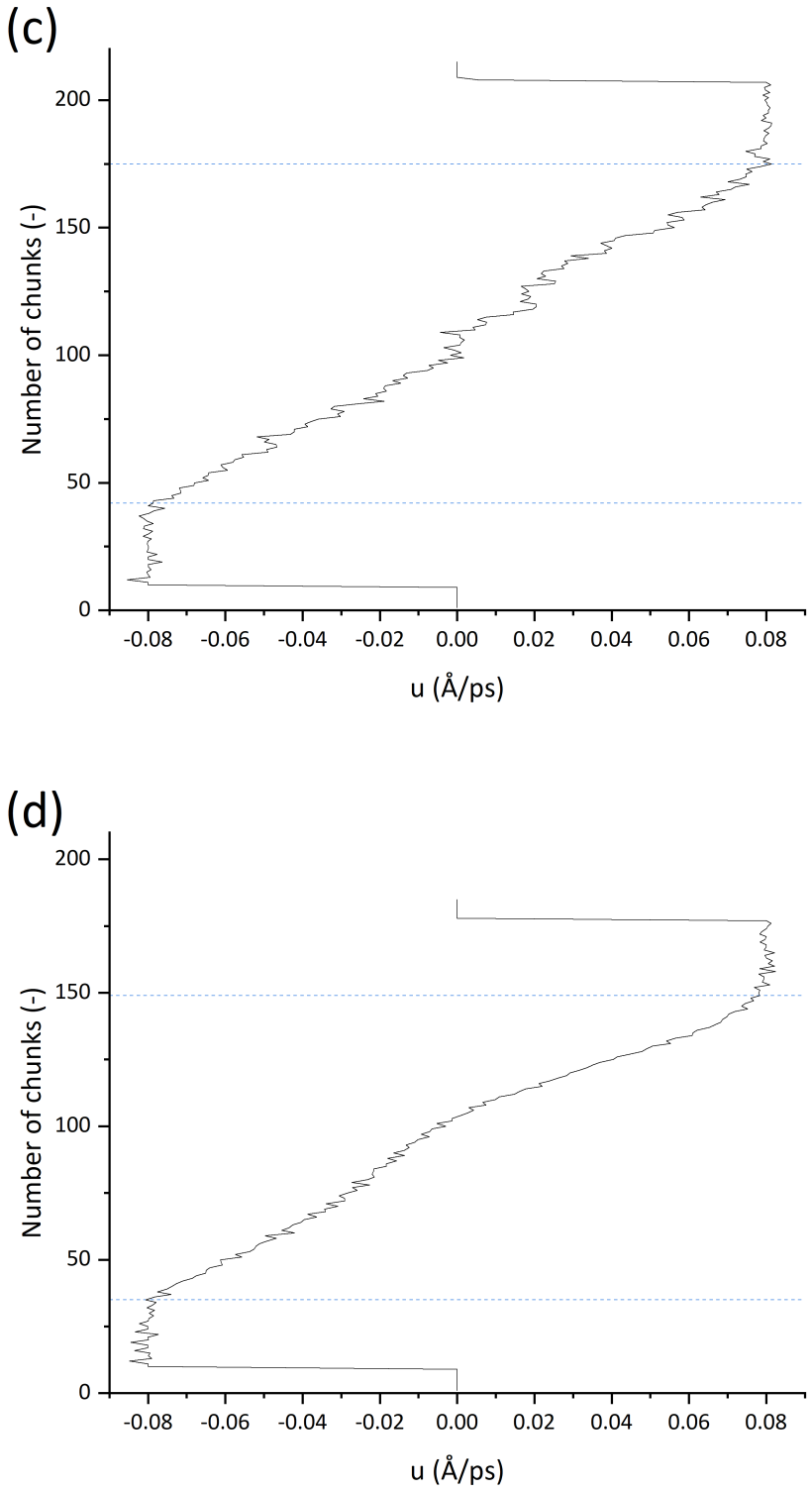


Figure 3.14: Velocity profile of NEMD simulations. (c) BB at 373 K, 100 MPa, $\Delta u$=0.16Å/ps, (d) BB at 373 K , 2000 MPa, $\Delta u$=0.16Å/ps. Velocity values are averaged over 2 ns. The blue dashed lines represent the interface between the contact surface and the fluid.

### 3.2.4 Shear stress

The shear stress $\tau$ is calculated from the tangential force $F_T$ acting on one of the two surfaces moving in the opposite direction of sliding, and the contact area $S = L_x \times L_y$, where $L_x$ and $L_y$ are the lengths of the surface in the x and y directions. $\tau$ is calculated as $\tau = \dfrac{F_T}{S}$. In the NEMD simulation used in this study, $F_T$ is defined as the sum of the forces $F_i$ acting on $N_{surface}$ atoms of the solid surface. Thus, the shear stress is calculated as follows:

$$\tau = \frac{\sum_{i=1}^{N_{surface}} F_i}{S} \tag{3.7}$$

The value $N_{surface}$ corresponds to the number of atoms in the region of the solid surface to which the velocity is imposed (see Section 2.3.3). The shear stress is calculated on each of the two surfaces, and the shear stress value presented in the following sections represents an average of the two.

### 3.2.5 Eyring stress

The previous study by Jadhao and Robbins [80, 119] led to the derivation of the Eyring stress from MD simulations by fitting the Eyring law (approximate form at very high shear rates) on the shear stress-rate data. In the present study, the original Eyring law (Equation 2.10(b), also displayed below) is directly fitted to the shear stress versus shear rate data to calculate the Eyring stress.

$$\tau = \tau_e \sinh^{-1}\left(\frac{\eta_N \dot{\gamma}}{\tau_e}\right)$$

The fitting process can be achieved using the least squares method. However, although the Eyring law has only two parameters: $\tau_e$ and $\eta_N$, the fitting process appears uncertain when both parameters are allowed to vary. This is due to the fact that in Eyring theory the Eyring stress $\tau_e$ is related to the Newtonian viscosity $\eta_N$ by $\tau_e = \eta_N \dot{\gamma}_c$. This internal relationship makes the convergence more difficult, especially under extreme operating conditions where $\eta_N$ becomes very high and $\tau_e$ very low. It makes it difficult in the present study to use this method to determine both parameters simultaneously. Consequently, in practice, this fitting process is simplified by fixing the $\eta_N$ values given by experimental measurement presented in Section 3.1.3, or, if necessary, to the value interpolated by the Newtonian viscosity model chosen for this study. Thus the only parameter to be fitted by the least squares method from the NEMD result is the Eyring stress. This approach is selected in order to derive Eyring stress consistent with $\eta_N$. It means that the pair of parameters ($\eta_N$, $\tau_e$) represents the best fit of the NEMD data by Eyring law (Equation 2.10(a)). However, the disadvantage is that the accuracy of $\tau_e$ depends directly on the relevance of $\eta_N$. As mentioned in Section 3.1.3, the Newtonian viscosity model used for both fluids is derived from the rheological measurements, which are considered reliable.

#### a Squalane

The pressure and temperature conditions for simulations of SQ are given in Table 3.6. For a given pressure and temperature, at least six different sliding velocities were considered, corresponding to shear rates in the range of $10^8 s^{-1} \sim 10^{10} s^{-1}$. At these shear rates, the simulation time ($\geq$5ns) is sufficient to bring the system to a steady state. Fitting Eyring law (Equation 2.10(b)) on the steady-

state shear stress versus shear rate data of the last 2 ns, Eyring stress of SQ $\tau_e^{SQ}$ is obtained. An example of Eyring fit for SQ at 500 MPa is shown in Figure 3.15.

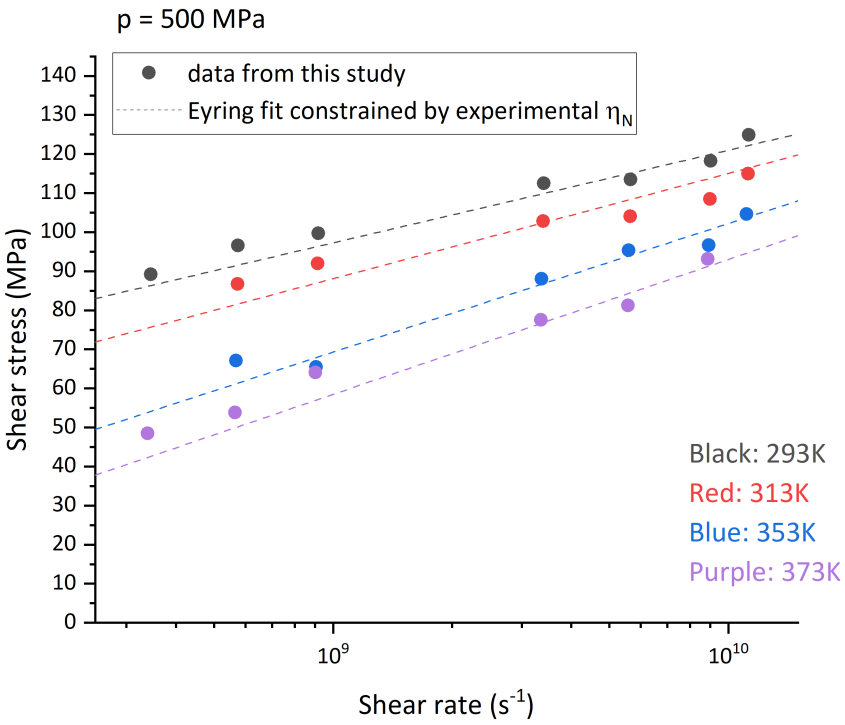


Figure 3.15: SQ shear stress versus shear rate data at 500 MPa. Dots stand for confined NEMD data. Dashed lines stand for the fit of the NEMD data by an Eyring law (Equation 2.10(b)). Different colours indicate different temperatures.

As a complement, $\tau_e^{SQ}$ fitted from bulk NEMD data are given in the study of Jadhao and Robbins [80]. Besides, other NEMD results of SQ can be found, such as confined NEMD by Ewen et al. [31] and Porras-Vasquez et al. [16]. Corresponding $\tau_e^{SQ}$ of these studies have been derived from the fit of these data using the same method proposed in this work. They are superposed to the result from the present study in Figure 3.16.

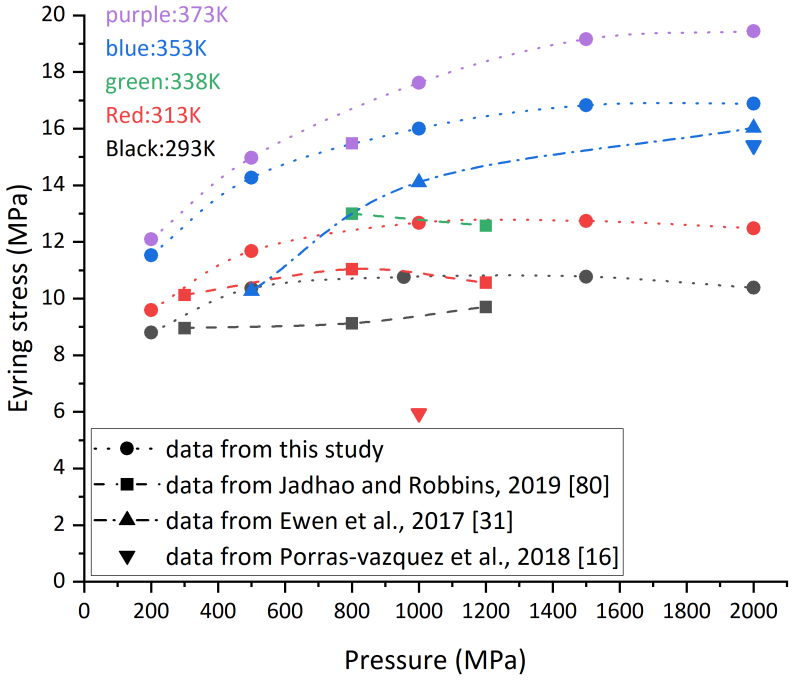


Figure 3.16: SQ Eyring stress versus pressure, and for different temperatures. Comparison between results from this study (confined NEMD, dots and dotted lines) and data from the literature: Jadhao and Robbins [80] (bulk NEMD, squares and dashed lines), Ewen et al. [31] (confined NEMD, triangles and dash-dotted line). Porras-Vazquez et al. [16] (confined NEMD, inverted triangles). Different colours are used to distinguish temperature.

Porras-Vazquez et al. [16] have only two discrete results at two different pressures and temperatures, thus the analysis of the trend is not possible. Jadhao and Robbins [80] reported that $\tau_e^{SQ}$ is independent of pressure for temperatures higher than 250 K and pressures higher than 300 MPa. On the other hand, Ewen et al. [31] and the present study reported data that showed a comparable variation of $\tau_e^{SQ}$ with pressure. The temperature dependency is well reproduced, although the present result overestimates $\tau_e^{SQ}$ when compared to the other studies [31, 80]. Moreover, for SQ as a Group IV base oil (saturated hydrocarbons), this tendency of $\tau_e$ to increase with pressure was also observed recently by Zhang and Spikes [189] from tribology experiments.

The comparison shows that there is no clear consensus on the value of Eyring stress of SQ, and discrepancies exist between the different authors. However, the $\tau_e^{SQ}$ derived from the simulation of the present study are comparable with those from the literature. The discrepancies may arise from differences between NEMD simulations. Indeed, Ewen et al. and Porras-Vazquez et al. [31, 16] applied a Langevin thermostat inside the contact surfaces, which clearly had a limited ability to remove heat compared to the Nosé-Hoover thermostat set on all solids and fluids in the present study (see Section 2.3.3). As Ewen et al. and Porras-Vazquez et al. focused on comparing the NEMD results directly with the tribological experimental results, they had less interest in constraining the thermal effects in contact. They only thermostatted wall atoms to simulate the experimental thermal gradient development [190]. Instead, in this work we attempted to characterise fluid property and construct a constitutive equation for $p$ and $T$. This had to be done in an isothermal, isobaric environment. A

larger temperature rise can thus be anticipated in the NEMD simulations of Ewen et al., causing a decrease of the shear stress and Eyring stress $\tau_e^{SQ}$.

The SLLOD method used by Jadhao and Robbins [80] simulated 125 SQ molecules and used a united-atom (UA) force field to be able to reach low shear rates such as $10^5 s^{-1} \sim 10^6 s^{-1}$. In the present study, only two orders of magnitude in shear rate are explored and a bigger system with 720 SQ molecules constrained by the all-atom (AA) force field is used to avoid layering caused by excessive confinement [16]. On the one hand, the reference work from Jadhao and Robbins, covering four orders of magnitude in rate, shows a substantial logarithmic behaviour of stress at the high shear rate, compared to the present study where the Newtonian viscosity is fixed from the Newtonian viscosity model (Equation 2.14). This may explain the higher Eyring stress values in the present work. On the other hand, when using a more coarse-grained model, the dynamics can be affected by the degree of coarse-graining, thus giving quantitative differences. In addition, the SLLOD method used by Jadhao and Robbins uses the NVT ensemble, whereas the confined NEMD method used in this study ensures pressure stability in the simulated system by applying constant pressure to the unfixed upper contact surface, similar to the NPT ensemble. This may also contribute to the observed difference.

For these reasons, and for the purpose of unifying the research methodology, only the data from the present study are used in the following. The variation of the Eyring stress of SQ $\tau_e^{SQ}$ with respect to pressure $p$ [MPa] and temperature $T$ [K] is fitted by a function given in Equation 3.8. The resulting parameters are given in Table 3.7. This model will be implemented in the FEM contact model. The Eyring stress data from NEMD simulations and the derived equation are superposed in Figure 3.17. It should be noted that this characteristic equation of $\tau_e^{SQ}$ is only valid in the range of tested $p$ (100 MPa to 2000 MPa) and $T$ (293 K to 373 K).

$$\begin{gathered} \tau_e^{SQ}[MPa] = A(T)\left(1 - \exp\left(-\frac{p}{B(T)}\right)\right) + C(T) \\ A(T) = a_1 * T + a_2 \qquad B(T) = b_1 * T + b_2 \qquad C(T) = c_1 * T + c_2 \end{gathered} \tag{3.8}$$

| a1 [MPa/K] | a2 [MPa] | b1 [MPa/K] | b2 [MPa] | c1 [MPa/K] | c2 [MPa] |
|---|---|---|---|---|---|
| 0.0598 | -11.4683 | 4.6973 | -1209 | 0.0505 | -10.0967 |

Table 3.7: Parameters of Eyring stress equation of SQ.

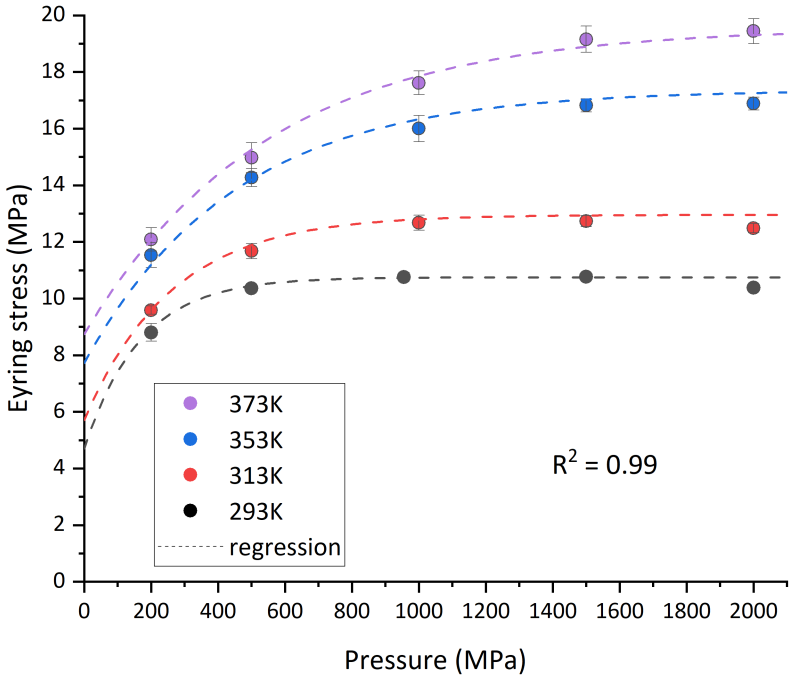


Figure 3.17: SQ Eyring stress from this study (symbols) and Eyring stress equation (written as "regression", dashed lines) as a function of pressure and temperature.

### b Benzyl Benzoate

The pressure and temperature conditions for simulations of BB are also given in Table 3.6. For a given pressure and temperature, at least six different sliding velocities were considered, corresponding to shear rates in the range of $10^8 s^{-1} \sim 10^{10} s^{-1}$. Since BB has been less studied than SQ, no information on its Eyring stress $\tau_e^{BB}$ and no NEMD simulation results are found in the literature to support the present study. The simulation time was long enough ($\geq$ 8 ns) to ensure a steady state. Resulting steady-state shear stress versus shear rate data are post-processed in the same way as SQ to obtain the Eyring stress of BB: $\tau_e^{BB}$. An example of Eyring fit for BB at 500 MPa is shown in Figure 3.18. The obtained $\tau_e^{BB}$ are shown in Figure 3.19.

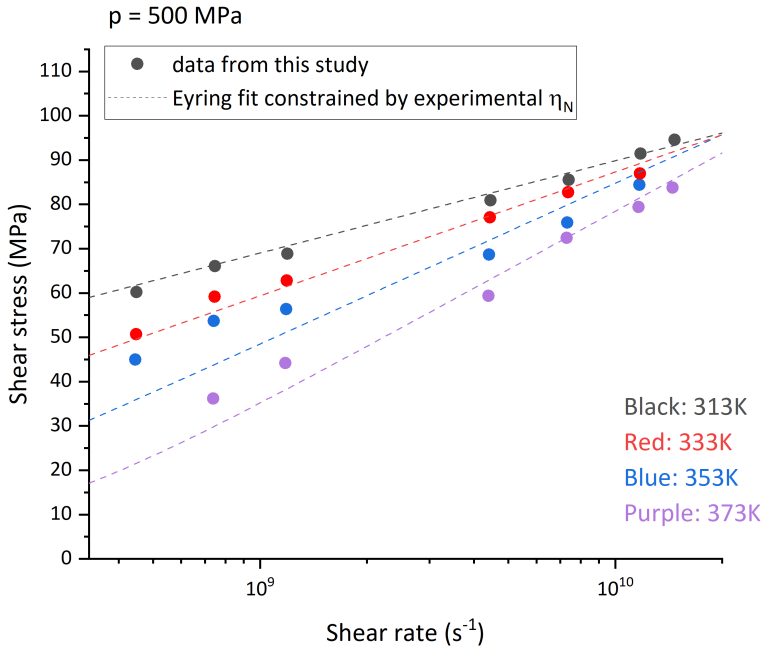


Figure 3.18: BB shear stress versus shear rate data at 500 MPa. Dots stand for confined NEMD data. Dashed lines stand for the fit of the NEMD data by an Eyring law (Equation 2.10(b)). Different colours indicate different temperatures.

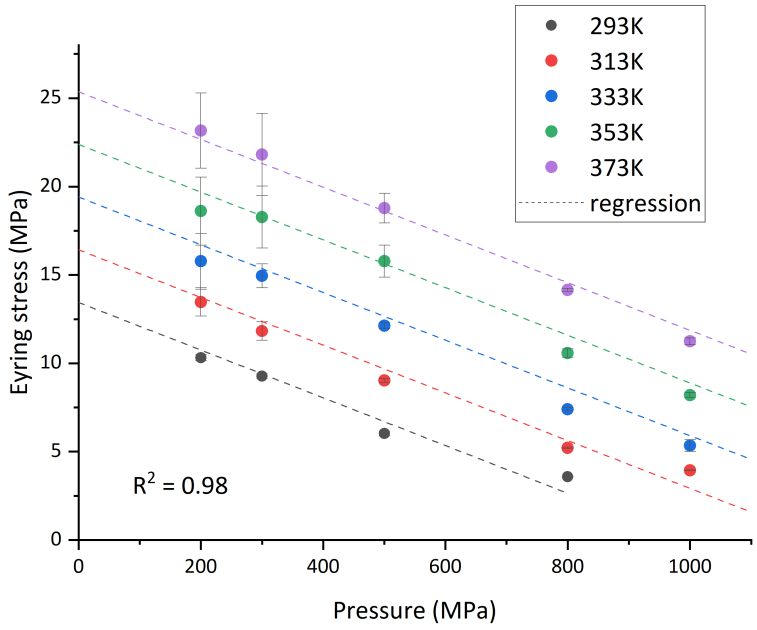


Figure 3.19: BB Eyring stress from this study (symbols) and regression (dashed lines) as a function of pressure and temperature.

According to the results shown in Figure 3.19, $\tau_e^{BB}$ exhibits a rather simple dependence on pressure and temperature: it appears that on the range of tested pressure and temperature, $\tau_e^{BB}$ is proportional to the pressure with a negative slope. A similar observation was made by Evans and Johnson [65] for another traction fluid, Santotrac 50. A linear regression of the results relates $\tau_e^{BB}$ to pressure $p$ [MPa] and temperature $T$ [K] as shown in Equation 3.9.

$$\tau_e^{BB}[MPa] = 0.149T - 0.014p - 30.21 \tag{3.9}$$

Similar to the case of SQ, the characteristic equation of $\tau_e^{BB}$ is only valid in the tested range of $p$ (200 MPa to 1000 MPa) and $T$ (293 K to 373 K). Indeed, obviously, the Eyring stress cannot go to zero or even negative values with increasing pressure. However, when looking closely at Figure 3.19, it appears that $\tau_e^{BB}$ tends towards a low but non-zero asymptotic value. The data at this stage is insufficient to support this assumption, but it could be discussed in future studies.

## 3.3 Synthesis model of fluid viscosity

At this point, two models are established for both fluids studied: the Newtonian viscosity $\eta_N$ model fitted to experimental viscosity measurements (see Equation 2.14), where the fitting parameters are given in Table 3.5; the Eyring stress $\tau_e$ model, which is derived from the NEMD simulation results. For SQ, $\tau_e^{SQ}$ is defined by Equation 3.8, the parameters of which are given in Table 3.7. For BB, $\tau_e^{BB}$ is defined by Equation 3.9. Based on these, the generalised viscosity models (Eyring) for both fluids have been built and are summarised below.

For both fluids, the Eyring generalised viscosity model is written as:

$$\eta(p,T,\dot{\gamma}) = \frac{\tau_e(p,T)}{\dot{\gamma}} \sinh^{-1}\left(\frac{\eta_N(p,T)\dot{\gamma}}{\tau_e(p,T)}\right)$$

For SQ, the two parameters, Newtonian viscosity $\eta_N^{SQ}$ and Eyring stress $\tau_e^{SQ}$ are defined as:

$$\begin{gathered}\eta_N^{SQ}(p,T) = A\exp\left(B\varphi^{-q} + C\varphi^{-Q}\right), \qquad 0<q<1, \qquad 1<Q \\ \varphi = \left(\frac{T}{T_R}\right)\left(\frac{V}{V_R}\right)^g\end{gathered} \tag{3.10}$$

| | A[Pa.s] | B[K] | C[K] | q [-] | Q [-] | g [-] | SD [%] |
|---|---|---|---|---|---|---|---|
| SQ[This study] | $3.531\times10^{-5}$ | 6.016 | 0.133 | 0.999 | 3.954 | 3.521 | 10.77 |

Parameters of the Newtonian viscosity model of SQ.

$$\tau_e^{SQ}(p,T) = A(T)\left(1-\exp\left(-\frac{p}{B(T)}\right)\right) + C(T)$$
$$A(T) = a_1 * T + a_2 \qquad B(T) = b_1 * T + b_2 \qquad C(T) = c_1 * T + c_2$$

| a1 [MPa/K] | a2 [MPa] | b1 [MPa/K] | b2 [MPa] | c1 [MPa/K] | c2 [MPa] |
|---|---|---|---|---|---|
| 0.0598 | -11.4683 | 4.6973 | -1209 | 0.0505 | -10.0967 |

Parameters of Eyring stress equation of SQ.

For BB, the two parameters, $\eta_N^{BB}$ and $\tau_e^{BB}$ are defined as:

$$\begin{gathered}\eta_N^{BB}(p,T) = A\exp\left(B\varphi^{-q} + C\varphi^{-Q}\right), \qquad 0<q<1, \qquad 1<Q \\ \varphi = \left(\frac{T}{T_R}\right)\left(\frac{V}{V_R}\right)^g\end{gathered} \tag{3.11}$$

| | A[Pa.s] | B[K] | C[K] | q [-] | Q [-] | g [-] | SD [%] |
|---|---|---|---|---|---|---|---|
| BB[This study] | $6.807\times10^{-5}$ | 4.280 | 0.155 | 0.871 | 6.037 | 4.569 | 4.13 |

Parameters of the viscosity scaling law of BB.

$$\tau_e^{BB} = 0.149T - 0.014p - 30.21$$

These generalised viscosity models, built to predict the viscosity at given pressure, temperature and shear rate, are based on the Newtonian viscosity and the Eyring stress of the fluids. These two parameters are derived from either experimental measurements (Newtonian viscosity) or simulation results (Eyring stress). For SQ, the Newtonian viscosity data come from high-pressure viscometer [120] performed by Bair [116], while simulation results come from Jadhao and Robbins [80]. For BB, Newtonian viscosity data come from the same measurements by Ndiaye et al. [40] and the simulation results from the present study are used for comparison.

As a final step to validate the generalised viscosity models, the predicted non-Newtonian viscosity has been compared for both fluids to experimental non-Newtonian viscosity measurements performed on high-pressure rheometers. Non-Newtonian viscosity data of SQ come from and Bair et al. [73]. The ones of BB come from rheological experiments carried out at LaMCoS by Bouscharain [121]. Comparisons are shown in Figure 3.20, where (a) is SQ at 293K and pressures from 100 MPa to 955 MPa. (b) is BB at 303 K, 313 K, and pressures of 300 MPa and 400 MPa.

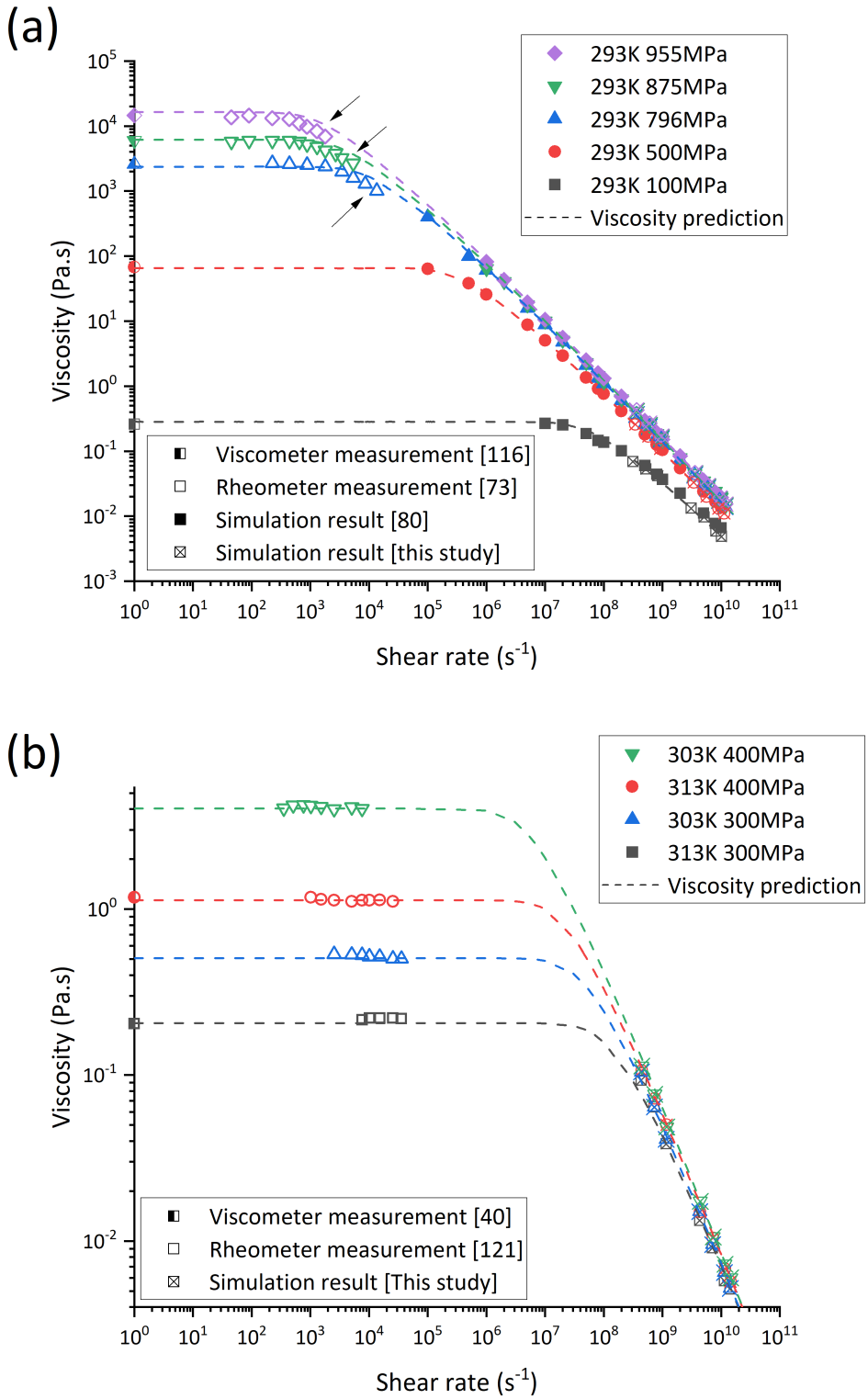


Figure 3.20: (a) Comparison of SQ generalised viscosity prediction (Eyring, dashed lines) at 293 K and pressures from 100 MPa to 955 MPa, with high-pressure viscometer measurements from Bair [116] (half left closed symbols), rheometer measurements from Bair et al. [73] (open symbols), simulation results from Jadhao and Robbins [80] (closed symbols) and from this study (open symbols with a cross) (b) Comparison of BB generalised viscosity prediction (Eyring, dashed lines) at 303 K, 313 K, and pressures of 300 MPa and 400 MPa, with Newtonian viscosity data from Ndiaye et al. [40], rheometer measurements from Bouscharain [121] (open symbols) and simulation results from this study (open symbols with a cross).

The mean absolute percentage error (MAPE) is a commonly used method for measuring the accuracy of predictions [191]. It is the mean relative error between the predicted and measured values, as shown in Equation 3.12, where $M_i$ is the measured value and $P_i$ is the predicted value. Here, the MAPE is calculated for the numerically predicted viscosity and the experimental measurements or NEMD results.

$$MAPE = \frac{100\%}{n} \sum_{i=1}^{n} \left| \frac{M_i - P_i}{M_i} \right| \tag{3.12}$$

It can be seen that the generalised viscosity predicted by the Eyring model is in good agreement with both experimental measurements and NEMD simulation data. For SQ, the MAPE with rheometer measurements from Bair et al. [73] is 22.2%; with simulation data from Jadhao and Robbins [80] is 5.8%; with simulation data from this study is 3.1%. For BB, the MAPE with rheometer measurement from Bouscharain [121] is 3.2%; the MAPE with the simulation data from this study is 6.1%. The models accurately predict the Newtonian viscosity plateau (from high-pressure viscometer measurements), viscosity-rate data at moderate shear rates (from rheometer measurements) and viscosity-rate data at moderate to high shear rates (from the NEMD simulation). A deviation is observed in the prediction of the plateau-shear thinning transition of SQ compared with the rheometer measurements from Bair et al. at 796 MPa, 875 MPa and 955 MPa (indicated by the black arrow in Figure 3.20). The experimental non-Newtonian transition is delayed compared to the predicted one. Jadhao and Robbins reported a similar result [80] when they attempted to fit the Eyring model to the same experimental data, they also found that for these data from Bair et al. [73], the Carreau model fits better in this region.

These quantitative predictions of generalised viscosity demonstrate the feasibility and reliability of the viscosity modelling approach proposed in this study. Friction prediction can then be carried out with these models at the contact scale, which is the topic of the next chapter.

## 3.4 Conclusion

This chapter was devoted to the determination of the parameters for the generalised viscosity (Eyring) model, which are the Newtonian viscosity $\eta_N$ and the Eyring stress $\tau_e$.

Initially, the EMD simulations were used to determine the Newtonian viscosity, considering the diffusion coefficient and the Stokes-Einstein relation. The Stokes-Einstein method is grounded on three parameters: the diffusion coefficient $D$, the activation energy $E_a$, and the characteristic length $r_c$. Through the analysis of the mean square displacement (MSD) curve obtained from the EMD simulations, $D$ was calculated. Following this, an Arrhenius equation for $D(p,T)$ was established linking $D$ with $1/T$. This process led to the determination of the pre-exponential factor $D_0$ and the activation energy $E_a(p)$. The characteristic length $r_c$ was estimated by assessing the volume of each atom.

The Stokes-Einstein viscosity predictions did not yield the expected accuracy compared to the experimental data, since it failed to take into account the faster-than-exponential behaviour of viscosity. Even though this attempt at predicting Newtonian viscosity through EMD simulations has enriched our understanding of EHD viscosity prediction, it did not provide satisfactory viscosity simulations. Therefore, experimental measurements represented the only reliable source of Newtonian viscosity data. Hence, a viscosity model was constructed by fitting an adequate law to these data.

In the second part of this chapter, the Eyring stress $\tau_e$ was determined via NEMD simulations. The temperature profile of each NEMD simulation result was verified to ensure that there was no significant temperature increase (less than 5 K). Following this, the velocity profile within the film thickness was verified to be linear. The shear rate was then calculated based on the velocity of the two contact surfaces and the film thickness fully separating these two. The verification of the temperature profile ensured that the simulated system was in a steady state, isothermal, isobaric environment. Finally, the steady-state shear stress was calculated from the forces acting on the contact surfaces in the direction of shear and the contact surface area. The obtained shear stress along with its corresponding temperature, pressure, and shear rate were used to derive the Eyring stress for the respective conditions. During this process, the Newtonian viscosity was fixed to the value provided by the previously established Newtonian viscosity model. The obtained Eyring stress values were then subjected to regression analysis, thereby constructing the Eyring stress model as a function of pressure and temperature. This approach allowed us to incorporate the complex dependence of Eyring stress on these two key variables, making the model robust for a wide range of conditions.

Finally, the generalised viscosity (Eyring) models for the two fluids were established. The prediction of viscosity versus shear rate data of the two studied fluids was compared with experimental measurements (viscometer and rheometer) and NEMD simulation results from the literature and this study. The results showed a good match, validating the generalised viscosity model which will be used in the contact model for friction prediction. The results of these studies will be presented in Chapter 4.

# EHD friction prediction

In this chapter, the results of EHD friction predictions are presented. The Eyring viscosity model including the pressure and temperature variation of its two parameters has been implemented into the thermal-elastohydrodynamic non-Newtonian (TEHLnN) contact model described in Chapter 2 to predict friction.

The EHD friction prediction is carried out for steel-steel contacts and under the same operational conditions as tribology experiments. The numerical results are then compared with experimental data from ball-on-disc tribometers to evaluate the quality of the prediction. Potential sources of error are analysed.

Finally, to further explore the generation of the friction plateau, the influence of the thermal effects and shear thinning effects on the friction mechanism is investigated. This is done through two additional simulations: isothermal non-Newtonian and thermal Newtonian simulations.

## 4.1 Additional material properties

Material properties also need to be specified to solve the system of equations. For example, in order to solve the elasticity equation, Young's modulus $E$ and Poisson's ratio $\nu$ are required. Similarly, for the heat equation, the thermodynamic properties of both solids and fluids, such as specific heat $c$ and thermal conductivity $k$, are needed.

In the present study, lubricated friction from steel-steel contacts is numerically predicted and compared with experimental measurement. Corresponding material properties, such as $E$, $\nu$, $k$, $\rho$ and $c$ are given in Table 4.1.

| **Solid** | Ball | Disc 1 |
|---|---|---|
| Material | Steel | |
| Young's modulus $E$ [GPa] | 210 | |
| Poisson's ratio $\nu$ [-] | 0.3 | |
| Thermal conductivity $k$ [$^{W}/_{mK}$] | 21 [192] | |
| Specific heat $c$ [$^{J}/_{kgK}$] | 470 | |
| Density $\rho$ [$^{kg}/_{m^3}$] | 7850 | |
| **Fluid** | SQ | BB |
| Thermal conductivity $k$ [$^{W}/_{mK}$] | 0.14 | 0.13 |
| Specific heat $c$ [$^{J}/_{kgK}$] | 1040 | 2058 |

Table 4.1: Materiel properties of the contacting solids and lubricant thermodynamic properties.

## 4.2 Friction prediction from the TEHLnN model

With the help of these additional material properties, the full Eyring viscosity model established in Section 3.3 is implemented into the TEHLnN contact model described in Section 2.3 to predict friction. The numerical simulations of the contact are selected to be carried out in the same operating conditions as the experimental friction measurement described in Section 2.2, in order to compare numerical prediction with experiment data. The experiment conditions are summarised in Table 4.2.

| **Fluid** | SQ | BB |
|---|---|---|
| Ambiant temperature $T_0$ [K] | 313 | 313, 333 |
| Contact load $W$ [N] | 46, 108, 254 | 32, 61 |
| Max Hertzian pressure $p_h$ [MPa] | 900, 1200, 1600 | 800, 1000 |
| Entrainment speed $u_e$ [$^{m}/_{s}$] | 0.8 | 2.5(313 K), 5(333 K) |
| Slide to roll ratio SRR [%] | 0.1-80 | 0.1-50 |

Table 4.2: Tribological experiment conditions of SQ and BB.

These tribological conditions are first plotted against the Newtonian viscosity data to see how representative they are. They are presented as black crosses in Figure 4.1. These represent the Newtonian viscosity of SQ or BB at the ambient (lubricant reservoir) temperature and the Hertzian pressure of the tribometer experiments. The viscosity values are obtained based on the experimental viscometer measurement or extrapolated using the selected viscosity model (refer to Chapter 2). In the contact area, the pressure increases from atmospheric to Hertzian pressure, resulting in a change in viscosity of several orders of magnitude. As shown in Figure 4.1, for SQ the test conditions correspond to viscosity inside or close to the experimental measurement range, whereas for BB the test conditions are located further into the extrapolated area.

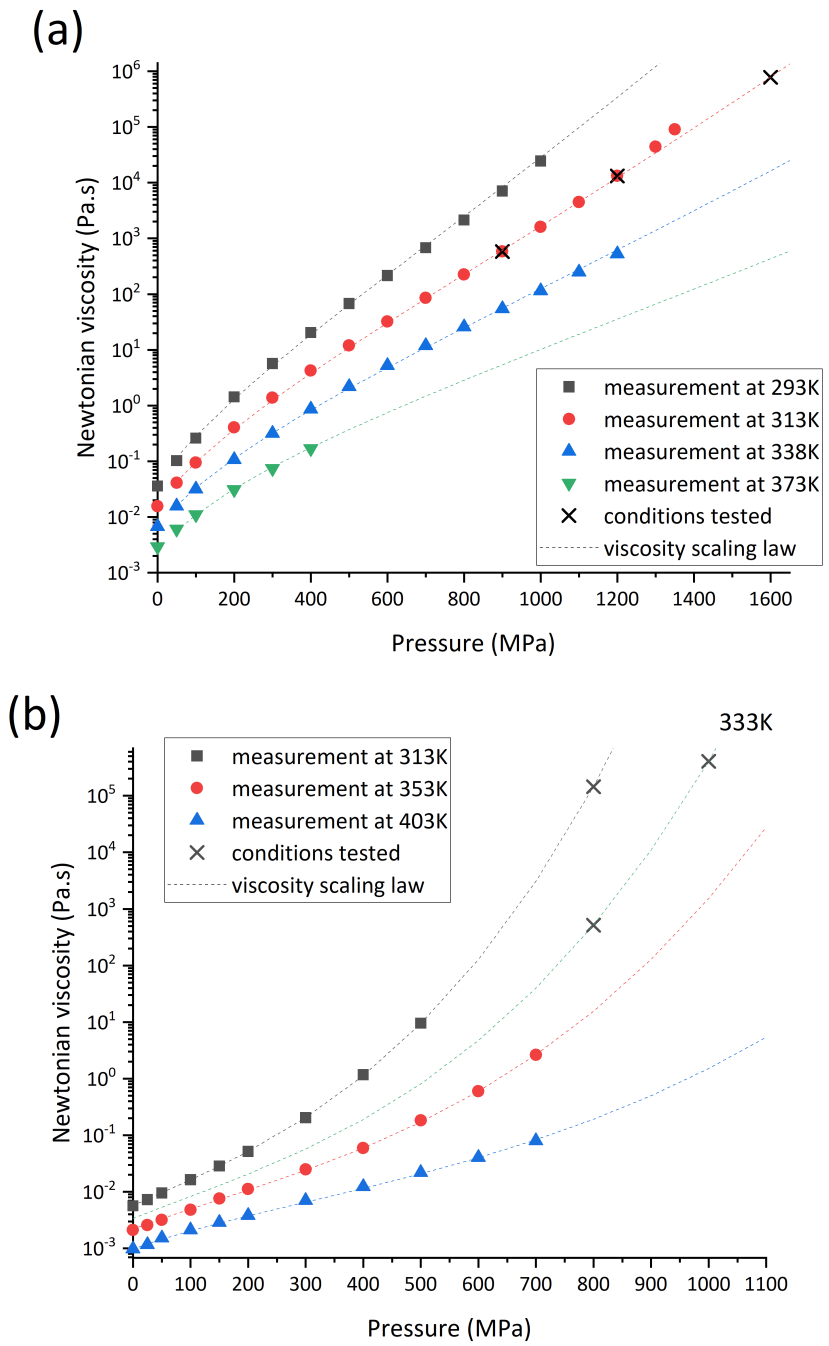


Figure 4.1: Comparison between viscosity measurements (filled symbols) and the viscosity scaling law predictions (dash lines). (a) SQ, experimental data from [116]. (b) BB, experimental data from[40]. The operating conditions for the friction experiments of the present study are marked as black crosses.

For steel-steel contact, the measured and predicted friction curves are shown in Figure 4.2 and Figure 4.3. Figure 4.2(a), (b), and (c) stand for SQ whereas Figure 4.3(a), (b), and (c) stand for BB. TEHLnN predictions are shown as red dots, and tribological measurements are shown as black squares.

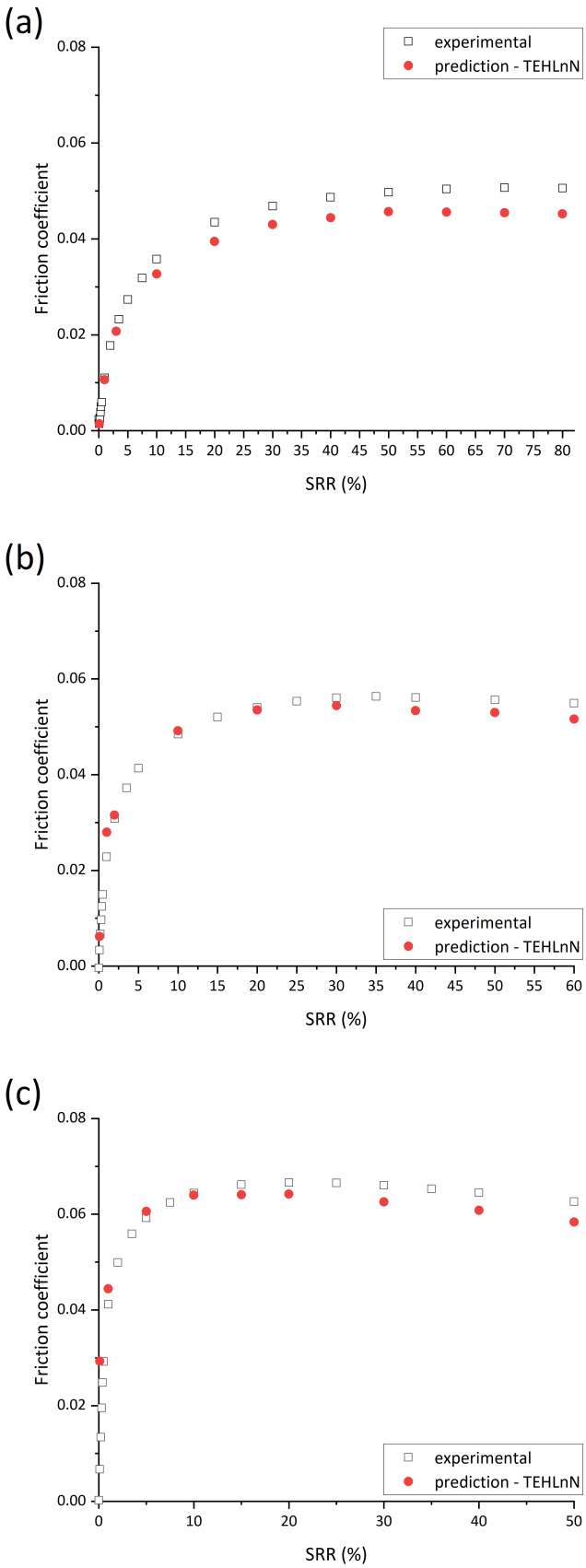


Figure 4.2: Comparison between experimental friction measurements from this study (black squares) and numerical predictions of TEHLnN simulation (red dots). (a) SQ $T_0$=313K, $p_h$=900MPa. (b) SQ $T_0$=313K, $p_h$=1200MPa. (c) SQ $T_0$=313K, $p_h$=1600MPa.

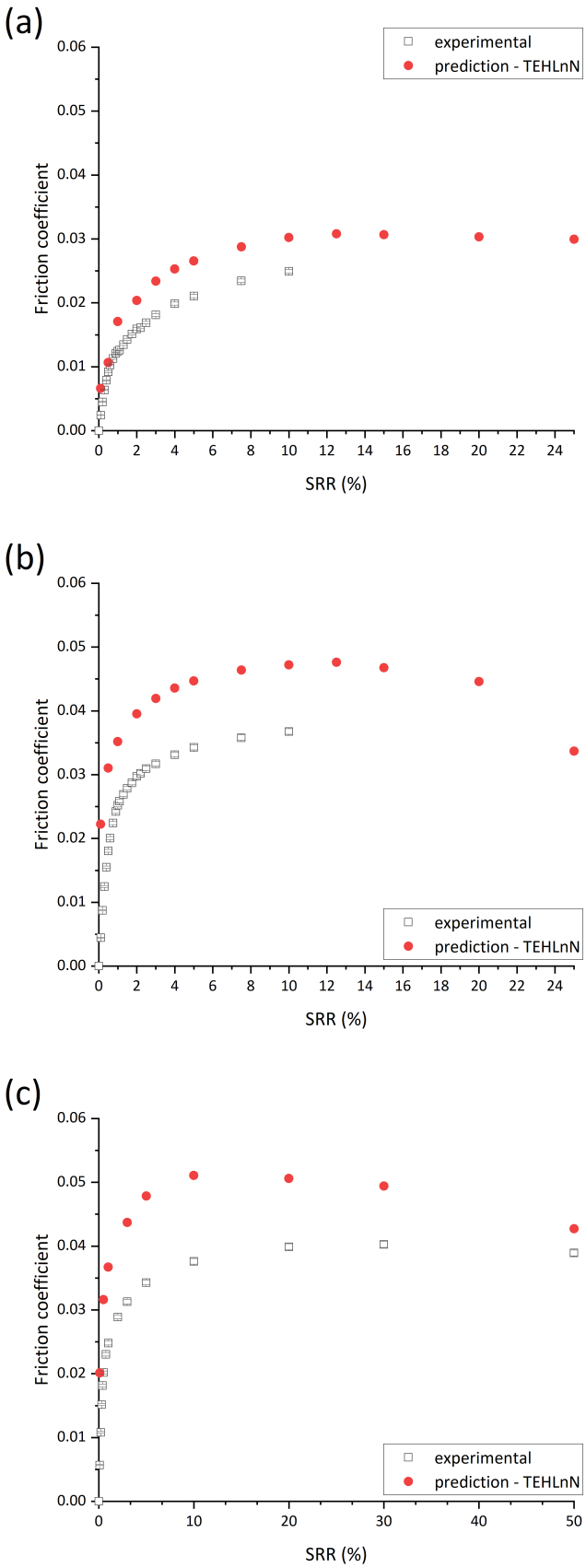


Figure 4.3: Comparison between experimental friction measurements from [40] (black squares) and numerical prediction of TEHLnN simulation (red dots). (a) BB $T_0$=333K, $p_h$=800MPa. (b) BB $T_0$=333K, $p_h$=1000MPa. (c) BB $T_0$=313K, $p_h$=800MPa.

The quality of the predictions is evaluated by mean absolute percentage errors detailed in Section 3.3. In this context, the MAPE is calculated for the coefficient of friction numerically predicted at the same condition as the tribological measurement.

In the case of SQ (Figure 4.2), the MAPE (for SRR>1%), as well as the maximum relative error between the experimental measurements and TEHLnN predictions, is always lower than 10%. Also, the simulations reproduced very well the linear and shear thinning regimes of the friction curves. More interestingly, they successfully predicted the friction plateau and the thermal thinning regime on a quantitative basis.

For BB (Figure 4.3), the TEHLnN predictions show a MAPE (for SRR>1%) of 25% to 34%, with a maximum relative error up to 60% in the last case (Figure 4.3(c)) at SRR=5%. Despite being less accurate than for SQ, the TEHLnN prediction still provides a suitable order of magnitude of the friction coefficient and reproduces qualitatively the linear and shear thinning regimes, as well as the plateau regime (Figure 4.3(a) and (b)) and the thermal thinning regime (Figure 4.3(c)). It is also worth noting that for cases (a) and (b), the highest experimental SRR is 10%. The maximum SRR was extended to 25% in simulations, and the results show the occurrence of the thermal thinning regime in cases (a) and (b).

It is clear from the MAPE results that the magnitude of the deviation between the predicted and measured values varies for the two types of fluids. Due to the complexity of EHD contacts, many factors can affect the accuracy of friction force prediction. The most likely cause of the deviation is the accuracy of the viscosity model; in other words, the accuracy of the two parameters of the Eyring model: the Newtonian viscosity at contact pressure and the Eyring stress.

To further investigate this issue, additional simulations were carried out. The robustness of the Eyring model was tested by altering its two parameters. Different Eyring stress laws were initially tested while using the same Newtonian viscosity model. For SQ, two Eyring stress laws can be recognised: Equation 3.8 from this study, which depends on both $p$ and $T$ and a law derived from the results of Jadhao and Robbins [80] (see Figure 3.16). According to [80], the Eyring stress of SQ might be independent of $p$ for $T$ greater than 250 K and $p$ higher than 300 MPa. Hence, a linear regression versus only $T$ was derived from the Eyring stress data, as shown in Equation 4.1.

$$\text{From[80]}: \quad \tau_e^{SQ}[\text{MPa}] = 0.074T - 12.483 \tag{4.1}$$

As shown in Figure 4.4, the red dots represent the predictions using the Eyring stress from this study, while the purple inverse triangles represent the predictions using the Eyring stress of Jadhao and Robbins. The same viscosity scaling model is used for Newtonian viscosity. Numerical prediction from the two different Eyring stresses only shows a difference in friction coefficient of around 5%, while the difference in Eyring stress can reach 20%. This friction prediction approach does not appear to be highly sensitive to the value of the Eyring stress. Instead, its accuracy is more dependent on the Newtonian viscosity of the lubricant at contact pressure conditions.

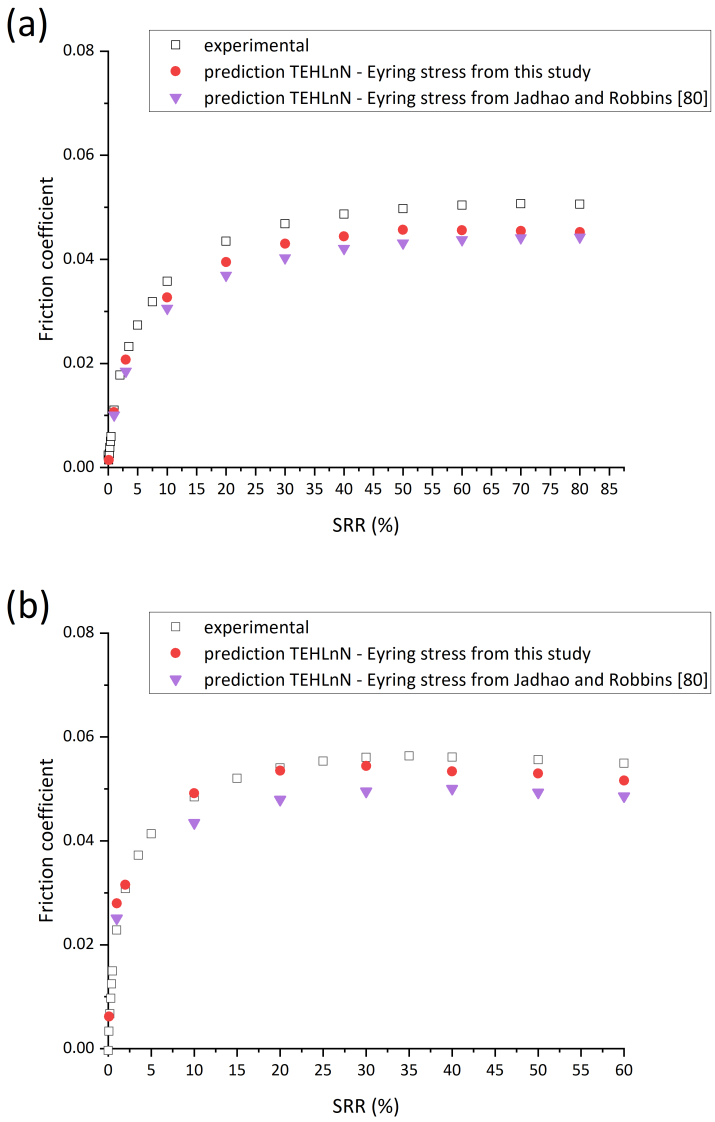


Figure 4.4: Comparison between experimental measurements from this study (black squares) and TEHLnN predictions using Eyring stress from this study (red dots) and from Jadhao and Robbins [80] (purple inverse triangles). (a) SQ $T_0$=313K, $p_h$=900MPa. (b) SQ $T_0$=313K, $p_h$=1200MPa.

Based on this robustness analysis, the reasons why predictions for SQ are more accurate than those for BB can be explained. For SQ the Hertzian pressure probed in the tribological test led to pressure distribution within the range of $p$ and $T$ that have been probed in rheological tests, as indicated in Figure 4.1(a). For BB, as shown in Figure 4.1(b), the Newtonian viscosity under test contact conditions is considerably outside the experimental measurement range, leading to significantly extrapolated viscosity data.

More importantly, the different fast-than-exponential behaviour exhibited by the two fluids also contributes to the differences observed in the predictions. For BB, its transition occurs at lower pressures (from 300 MPa to 700 MPa), which, combined with the restricted range of rheological test conditions that there are very little of the data lies within its fastest-than-exponential range. This makes its

extrapolation to higher pressures more precarious. Moreover, all the tribological test conditions for BB lie within this extrapolated zone. Conversely, for SQ, this transition happens at higher pressures (around 1300 MPa). This makes its extrapolation more secure and results in higher accuracy for the Newtonian viscosity prediction.

From this perspective, a better quantitative friction prediction for BB is still an open challenge.

## 4.3 Investigation of the friction plateau generation

Despite the observed discrepancies for BB, the TEHLnN simulation still quantitatively predicts the experimentally measured friction of the two fluids and in particular of the friction plateau. In other words, the friction plateau can be reproduced in a realistic contact model that takes into account both non-Newtonian effects modelled by the Eyring viscosity model and thermal effects due to compression and shear heat source in the energy equation. To be able to discuss in more detail the origin of the friction plateau, these two effects had to be uncoupled. For that, two additional simulations are performed for each operating condition in Figures 4.2 and 4.3.

Isothermal non-Newtonian simulations prevent temperature rise due to heat generation. Such simulations have been run by removing the thermal model in the TEHLnN contact model (see Section 2.3.3) and fixing all temperatures $T$ to the ambient (lubricant reservoir) temperature $T_0$. On the other hand, thermal Newtonian simulations were run by considering only the shear-independent viscosity (taken as $\eta_N$), thus preventing shear thinning. Results of these two simulations are reported in Figures 4.5 and 4.6, where isothermal non-Newtonian simulations are shown as blue triangles and thermal Newtonian simulations are shown as green diamonds. TEHLnN predictions and experimental measurements are also shown in the same figures as red dots and black squares.

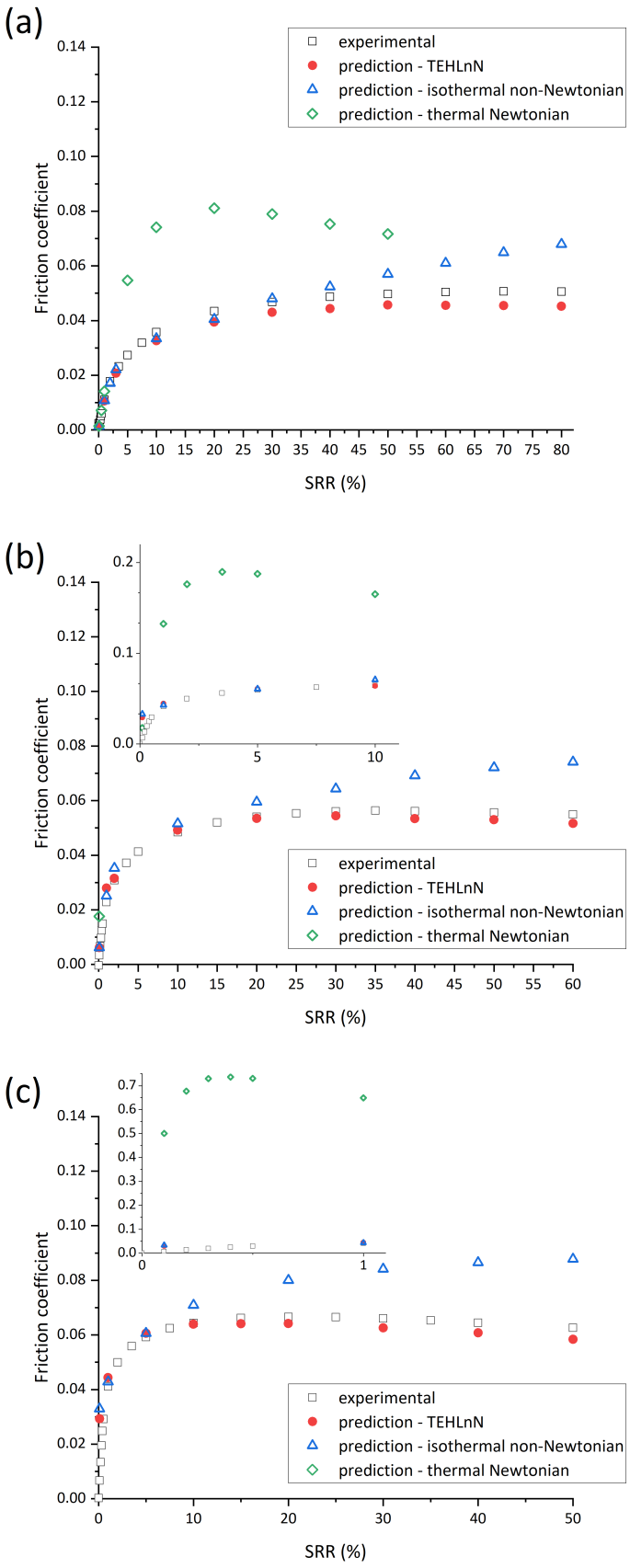


Figure 4.5: Comparison between experimental measurements from this study (black squares) and prediction results of thermal non-Newtonian simulation (red dots), isothermal non-Newtonian simulation (blue triangles) and thermal Newtonian simulation (green diamond). (a) SQ $T_0$=313K, $p_h$=900MPa. (b) SQ $T_0$=313K, $p_h$=1200MPa. (c) SQ $T_0$=313K, $p_h$=1600MPa.

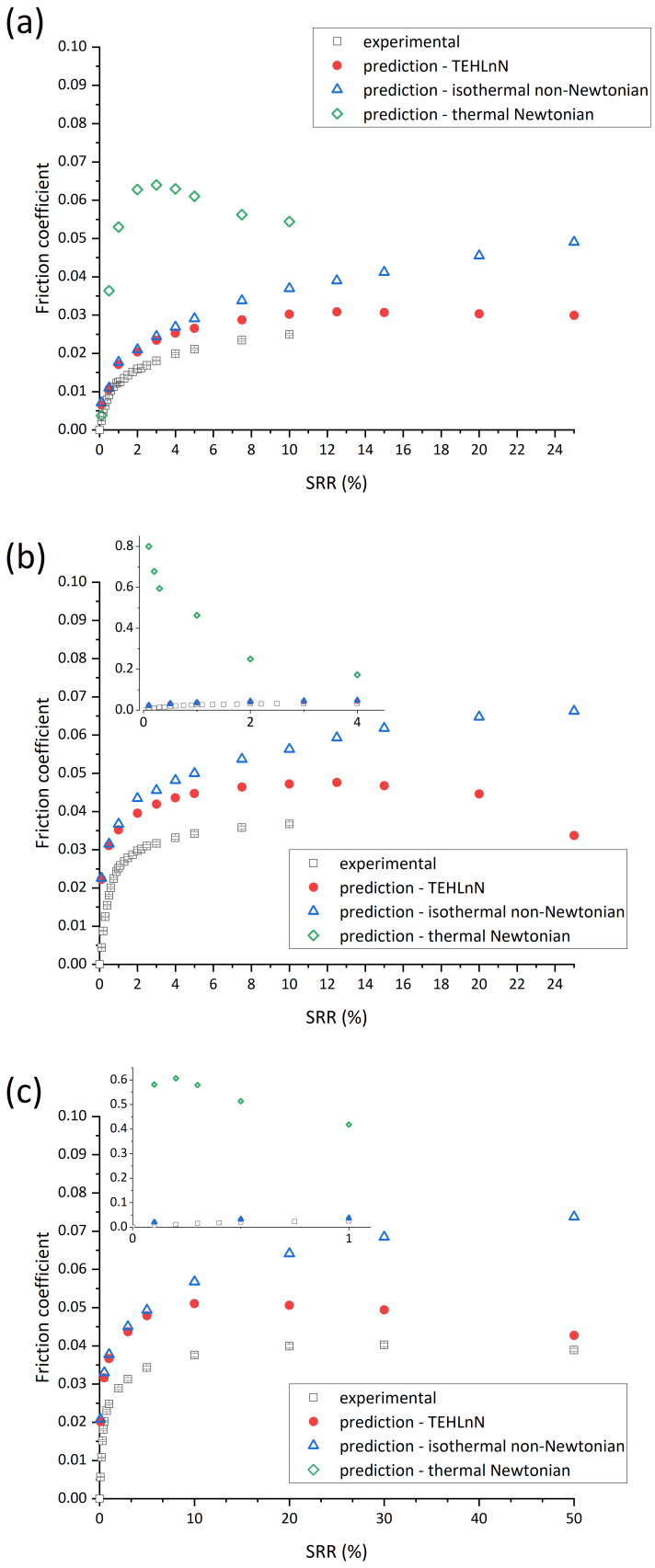


Figure 4.6: Comparison between experimental measurements from [40] (black squares) and prediction results of thermal non-Newtonian simulation (red dots). (a) BB $T_0$=333K, $p_h$=800MPa. (b) BB $T_0$=333K, $p_h$=1000MPa. (c) BB $T_0$=313K, $p_h$=800MPa.

Unsurprisingly, for both fluids, the thermal Newtonian simulations show a rapid linear rise of friction coefficient at very low SRR. For example, Figure 4.6(b) shows that the friction coefficient of BB at $T_0$=333 K and $p_h$= 1000 MPa goes from 0 to 0.8 in just 0.1% of SRR. Then due to the thermal effects, the friction slope gradually decreases with increasing SRR until it becomes negative, meaning that the thermal thinning in this friction regime has a more significant impact than the natural increase of shear stress with shear rate. The initial friction slope, as well as the maximum friction coefficient, increases with pressure (Figure 4.5(a), (b), (c) and Figure 4.6(a), (b)) and decrease with temperature (Figure 4.6(a), (c)) due to the dependence of the Newtonian viscosity model on pressure and temperature.

Since there are several orders of magnitude differences between the friction coefficients obtained from the thermal Newtonian simulation and the experimental data, it is clear that a Newtonian constitutive equation alone does not make it possible to reproduce the experimental friction curves, neither quantitatively nor even qualitatively. The non-Newtonian constitutive equation (here the Eyring relation) plays a significant role in the onset of the friction plateau observed in experiments.

On the other hand, the isothermal non-Newtonian simulations perfectly reproduced the experimental measurement and TEHLnN data at low to moderate SRR (up to SRR = 20% for SQ and a significantly lower SRR value for BB). Beyond this range, the thermal effects become significant and the isothermal non-Newtonian simulations overestimate more and more the friction coefficients in comparison to both TEHLnN simulation and experimental data. These numerical simulations underline the fact that heat generation and dissipation can play a non-negligible role in friction in the shear-thinning regime. This is particularly visible for the BB in Figure 4.6 (b) and (c), where discrepancies between non-Newtonian isothermal and non-Newtonian thermal predictions occur at low SRR (around 1%). It can also be noted that these discrepancies occur at SRR lower for the BB than for the SQ, meaning that thermal effects are more pronounced for traction-like fluid BB than lubricant SQ. This effect was already noted on the BB in [40] where the maximum friction value showed a decrease of around 4% for increasing entrainment velocities, meaning increasing heating.

Thermal effects play an even more important role in limiting friction phenomena. Figures 4.5 and 4.6 show that neither thermal nor non-Newtonian effects alone can reproduce the friction plateau observed experimentally. As a consequence, the friction plateau appears to be due to a combination of shear thinning (non-Newtonian effect) and thermal thinning (thermal effect). The “plateau-like” regime of the friction curves does not seem to be due solely to an intrinsic property of the lubricant. It also depends on the viscous heating in the contact, including the materials constituting the solid bodies and contact conditions.

This conclusion can also be related to the variation of $\dot{\gamma}_{red.} = \dfrac{\dot{\gamma}}{\dot{\gamma}_c}$ in the contact area. In fact, when the contact conditions change, the critical shear rate $\dot{\gamma}_c$ also changes. Consequently, the $\dot{\gamma}_{red.}$ changes for the same SRR. Combined with the thermal effect, this determines friction under specific conditions. It may explain why friction plateaus tend to occur at high contact pressures (for the same SRR): a lower critical shear rate due to high pressure makes it easier to reach high $\dot{\gamma}_{red.}$, and the higher viscosity also makes the thermal effect more pronounced. Furthermore, the assumption could be made based on these inferences that the occurrence of friction plateaus is generic. A sufficiently high $\dot{\gamma}_{red.}$ and a sufficiently strong thermal effect (at a high shear rate) will eventually lead friction to saturate or even drop. Although which of these two effects is in the dominant position in this process remains unclear because the present study demonstrates that neither can independently reproduce the friction plateau observed in the experiment.

Furthermore, the empirical friction plateau laws presented in Section 1.4 are questionable and hardly reflect a general characterisation of the fluid. They phenomenologically represent both the shear thinning of the fluid and the thermal dissipations in the contact where they are characterised. This prevents them from being extrapolated to other contacts. However, as the present work shows, thermal effects play an important role in the generation of the friction plateau, i.e. it depends not only on the lubricant but also on the test conditions (temperatures, training speed and thermal properties of the solid bodies). The model proposed in this work is more relevant as it can be extrapolated to other conditions.

Given the non-negligible influence of thermal effects on EHD friction, it is a reasonable conjecture that, under the same contact conditions (pressure, temperature, and shear rate/SRR), different thermodynamic characteristics introduced by varying contacting solids may alter thermal dissipation and thus cause differing frictional responses. Thus, friction in a set of steel-sapphire contacts was also predicted and compared with those in steel-steel contacts under the same conditions, details of which are given in Appendix D. Unfortunately, the difference in the thermal properties of the two solids is not significant enough to strongly conclude their influence on their friction, further studies are needed.

## 4.4 Limitations and perspectives

With a contact-independent established Eyring model for both fluids, the present approach quantitatively predicted the friction of experimental EHD contact. Different regimes for both fluids, including the plateau regime and the thermal thinning regime, are very well reproduced. Compared with classical EHD friction prediction [55, 56, 57, 63], the present approach does not require reference to any friction measurement. This makes it an important step towards the "true" friction prediction and quantitative EHL [88].

However, the proposed approach does come with its own limitations, stemming both from the characterisation of fluid intrinsic properties and the contact model at the continuum scale.

Firstly, there are technical limitations, both experimentally and numerically. The characterisation of Newtonian viscosity $\eta_N$ is a challenging task. Experimentally, this process can be time-consuming and the experimental equipment required may not be readily available. For instance, high-pressure viscometer measurements are often limited in their range of pressures and temperatures, often falling short of EHD conditions (see Section 3.1.3). On the other hand, numerical methods are also constrained by computational power, which may restrict the coverage of all contact conditions. Indeed, building a comprehensive Eyring stress model covering a wide range of temperatures and pressures it is a lengthy process.

The second source of limitations comes from the Eyring model considered. Our method of calculating Eyring stress requires the involvement of Newtonian viscosity, its accuracy depends directly on the accuracy of the Newtonian viscosity model, making this the most complex and challenging aspect of the entire approach. Obtaining Eyring stress using only NEMD results (as done by Jadhao et al. [80]) seems to be a worthwhile approach to try. However, for this method to give reliable Newtonian viscosity, simulations would have to run to reach a low range of shear rates, making them tremendously longer, and not accessible with the local computing facilities.

Moreover, the question of the range of validity of the BB Eyring stress (denoted $\tau_e^{BB}$ see Figure 3.19) arises. We postulate that it will eventually converge to a smaller value with increasing pressure,

but this assumption is not substantiated by any supporting evidence. In the present study, the $\tau_e^{BB}$ displays a linear trend over its applicable range (0-1000 MPa) and is inversely proportional to the pressures. Beyond this range, the value of $\tau_e^{BB}$ could potentially decrease to a negative value with increasing pressure. This would imply that the fluid would exhibit shear-thinning behaviour at a shear rate lower than zero, which is not possible in reality. As such, the current $\tau_e^{BB}$ model cannot be utilised to predict friction for pressures higher than 1000 MPa. On the other hand, for SQ, as $\tau_e^{SQ}$ exhibits a plateau with increasing pressure, its model can be extrapolated to higher pressures (see Figure 3.17).

In addition to the limits stated, the following perspectives are envisaged to bring versatility to this work.

First, this method has only been tested on pure substances, and its applicability to mixtures is uncertain.

Second, since this study found that the generation of the friction plateau results from a combination of non-Newtonian and thermal effects, the contact conditions are expected to influence friction. For now, the proposed approach mainly considers steel-steel contact. It has also been applied to steel-sapphire contact for limited contact conditions (see Appendix D) and very good results have been obtained. This study should now be extended to more types of contacts, especially those involving solids with significantly different thermodynamic properties to prove the versatility of the approach.

Finally, the current TEHLnN contact model employs simplified material properties for both the fluid and the solid. For instance, constant values are used for thermal conductivity ($k$) and specific heat capacity ($c$). Given our demonstration of the significant role that thermal effects play in the EHD friction response, this approach could incorporate the use of pressure and temperature-dependent material properties, as recommended by Habchi et al. [52]. This could more accurately represent heat dissipation in the contact area, thereby improving the quality of the prediction.

## 4.5 Conclusion

This chapter presented friction prediction results obtained using the TEHLnN contact model along with the Eyring law established independently in Chapter 3 based on rheometer measurements and molecular dynamics simulations. Predictions were performed under the same operating conditions as tribology experiments. The results showed a promising degree of consistency when compared with experimental data. The model successfully reproduced the experimentally observed friction regimes, including the friction plateau and thermal regime.

For SQ, the mean absolute percentage error (MAPE) of the prediction was consistently less than 10%, while for BB, this value was relatively higher, around 30%. An analysis of the robustness of the Eyring law was conducted, demonstrating that among the two parameters used to construct the Eyring model, the prediction was more sensitive to the Newtonian viscosity model. This was therefore identified as the primary source of deviation.

To investigate the genesis of the friction plateau, thermal and non-Newtonian effects in the contact were isolated. The results indicated that neither of these two effects could individually reproduce the friction plateau observed in the experiments, suggesting that the friction plateau results from a combination of these effects. Hence, the generation of the friction plateau could be seen as (whatever the fluid), as a sufficiently high shear thinning and thermal effect under certain contact conditions.

Furthermore, the study also revealed how thermal effects can impact the friction response, potentially starting at a very low SRR.

Finally, the limitations and potential future directions of the proposed approach were discussed. It could be extended to more contacts involving different materials, particularly solids with significantly different thermodynamic properties. Extending the range of pressures to which this approach can be applied is a necessary enhancement. Lastly, the use of temperature and pressure-dependent material thermodynamic properties could be an improvement in the model.

# General conclusion

This thesis aims to bring an original strategy to predict friction in the elastohydrodynamic (EHD) contact, based on the a priori fluid characterisation.

- Chapter 1 develops the state of the art concerning EHD friction. In particular, it emphasises the difficulty of correctly modelling the friction threshold observed experimentally, while the physical origin remains unclear. Researchers previously used empirical models based on tribological experiments to artificially introduce friction plateaus, thereby limiting their progression from being truly "predictive".

- The proposed strategy is developed in Chapter 2. It consists of two parts. The first part focuses on the determination of the rheological properties of the fluid, with a particular focus on generalised viscosity. This involves establishing the constitutive equation for viscosity as a function of pressure, temperature, and shear rate. The Eyring viscosity model is chosen for its simple form, featuring only two parameters which greatly facilitates the characterisation process. The second part consists of building a thermal EHD contact model, able to reproduce the pressure and temperature fields experienced in the real contact area. The constitutive viscosity equation established in the first part will be implemented into the contact model to predict friction.

  Characterisation of fluid rheological properties under elastohydrodynamic lubrication (EHL) conditions is by itself a challenge. It is crucial to determine these rheological properties in a contact-independent manner within the volume of fluid. But at the same time, rheological conditions applied to the fluid should be as close as possible to the contact condition. However, at this stage, due to the limitation of experimental methods, molecular dynamics simulations (MD) are utilised to attempt to extend the existing literature data. To illustrate the versatility of the proposed friction prediction method, two fluids with different characteristics are selected: a classical lubricant squalane (SQ) and benzyl benzoate (BB), the latter is chosen to mimic the properties of traction fluid.

- The two parameters of the Eyring model, i.e., the Newtonian viscosity and the Eyring stress, are then determined in Chapter 3. Equilibrium molecular dynamics (EMD) simulations are initially employed for the determination of Newtonian viscosity. The Stokes-Einstein relationship is first coupled with the diffusion coefficient characterisation via EMD. Unfortunately, this method is limited by the sharp increase of relaxation time with pressure, making it too long to be computed under EHL conditions. Consequently, a Newtonian viscosity model derived from experimentally measured Newtonian viscosity is used.

  Non-equilibrium molecular dynamics (NEMD) simulations are used for the determination of

Eyring stress. NEMD simulations are conducted under isothermal and isobaric conditions. Steady-state shear stress and corresponding shear rate are obtained, and the Eyring stress is calculated by fitting the Eyring equation to the obtained stress-rate data. Once the two parameters are determined, the generalised (Eyring) viscosity models for the two fluids are established.

- In Chapter 4, the thermal EHL non-Newtonian (TEHLnN) contact model is developed to predict friction. It simultaneously solves four fully coupled equations: the generalised Reynolds equation, the elasticity equation, the film thickness equation, and the heat equation. The Eyring viscosity model, established in Chapter 3 is implemented into the model, allowing the prediction of friction using contact-independent physical quantities.

  The prediction results are compared with measurements from tribological experiments, demonstrating that despite some deviations, the friction coefficients of both fluids have been quantitatively predicted. Moreover, all friction regimes, including the friction plateau, are accurately predicted. Later, the causes of deviations between numerical predictions and experimental measurements are analysed. The Eyring viscosity model is considered to be the cause of the deviation, and subsequent robustness tests revealed that one of its parameters, the Newtonian viscosity, is the primary factor affecting the accuracy of predictions.

  Two additional simulations, isothermal non-Newtonian and thermal Newtonian, are performed to disentangle non-Newtonian and thermal effects. The results indicate that neither of them can independently reproduce the friction plateau observed in the experiments. Thus, the friction plateau is a result of the combined effect of non-Newtonian and thermal effects. This analysis also reveals the influence of thermal effects on the fluid friction response: contrary to the traditional belief that thermal effects have a significant impact only under high shear rates, they manifest almost simultaneously with non-Newtonian effects and continuously influence the friction response.

## Achivements

Compared to existing literature, the present study has made advancements in the following aspects:

- **Development of a new EHD friction prediction method**, through the determination of the rheological constitutive laws of fluids, in particular the generalised viscosity. By organically combining the contact-independent constitutive laws with the existing TEHLnN contact model, this approach allowed friction prediction to move from reliance on experimental results to true prediction based on material constitutive equations and intrinsic properties. This approach led to the first quantitative prediction of EHD friction, including friction plateau and thermal thinning regime.
- **Versatility of the approach**: This approach has been applied to two fluids of very different nature, lubricant SQ and traction-like fluid BB, to highlight the versatility of the approach to make it independent of the nature of the fluid.
- **Prediction of the friction plateau**: Utilising the Eyring viscosity model and the TEHLnN contact model, this study successfully predicted the friction plateau, which was observed experimentally for many years but had never been predicted by previous EHD friction models.
- **Generation of the friction plateau**: The role of non-Newtonian and thermal effects in friction

plateau generation is numerically investigated by switching off either the thermal model or the non-Newtonian model. The results demonstrate that the friction plateau is a combined effect of non-Newtonian and thermal effects.

Additionally, while efforts to characterise Newtonian viscosity through EMD simulations and the Stokes-Einstein relation did not yield plausible values under EHL conditions, they significantly advanced our understanding of the fluid state in such conditions.

We discovered that the genuine impact of changes in contact conditions (pressure and temperature) on the fluid is reflected in alterations to its relaxation time $t_{rel}$ and critical shear rate $\dot{\gamma}_c$, which is associated with the state and flow behaviour of the fluid.

- The state of the fluid depends on the ratio between the relaxation time $t_{rel}$ and the observation time $t_{obs}$ (the simulation time $t_{simu}$ in our case). It determines whether the fluid will be in a liquid-like or solid-like state.
- To better understand the behaviour of the fluid under shear (non-equilibrium), the shear rate $\dot{\gamma}$ should be compared to a critical shear rate $\dot{\gamma}_c$ which would be defined as $\frac{1}{t_{rel}}$.

## Limitations and perspectives

Despite making significant strides towards "true" friction prediction and quantitative EHL, this study does have certain limitations, which originate primarily from the characterisation of fluid intrinsic properties and the continuum-scale contact model. Moving forward, there are several perspectives for future work to address these limitations.

- **Characterisation of fluid**: The EMD method does not accurately describe Newtonian viscosity under EHL conditions; therefore, the Newtonian viscosity model used in this study was obtained by fitting the viscosity scaling law to experimental data over a limited range of pressure and temperature. Yet, our specific interest lies in high-pressure and/or low-temperature conditions, which often require a great extrapolation of the Newtonian viscosity model, as seen in the case of BB. Besides, robustness testing reveals that the prediction approach is highly sensitive to Newtonian viscosity, suggesting that the extrapolation of Newtonian viscosity is likely to impact the accuracy of the prediction.

  One possibility for exploring friction plateau regimes without extrapolating Newtonian viscosity involves maintaining moderate pressure but working at very high shear rates. However, achieving such high shear rates experimentally poses a significant challenge.

  While an Eyring stress model for both fluids was constructed using NEMD simulations, it is only applicable within a limited pressure-temperature range. In addition, the method employed for calculating Eyring stress is highly dependent on the determination of Newtonian viscosity. Therefore, its accuracy is largely tied to the viscosity model, consistent with the problems encountered with the Newtonian viscosity model.

  Furthermore, in some cases, calculating Eyring stress through NEMD simulations might not be the most optimal solution. For the two fluids selected in this study, NEMD simulations were less challenging due to their simple molecular structure and the fact that they are pure substances. This is not the case for NEMD simulations of complex fluids, compounds, or mixtures. In these instances, using MD simulations might not be the most economical or straightforward approach,

considering that even the relatively simple NEMD simulations used in this study were already constrained by computational power.

The experimental approach may be a better solution for these cases. In theory, a fully experimental and contact-independent method for determining Eyring stress is conceivable. Assuming $\tau_e = \eta_N \dot{\gamma}_c$ and $\dot{\gamma}_c = \frac{1}{t_{rel}}$, the Eyring stress model could be constructed by experimentally measuring both $t_{rel}$ and $\eta_N$. Brillouin scattering appears to be a potential experimental method for measuring $t_{rel}$; however, as of now, no substantiated results support this approach.

- **EHD contact modelling**: Given the significant role of thermal effects in friction response, a potential and necessary optimisation for the existing TEHLnN model is to replace the simplified material properties (currently treated as constants, e.g. $k$, $c_p$) with values that are dependent on pressure and temperature, as recommended by Habchi et al. [63]. This modification would render the thermal effects in the simulations more aligned with reality, thereby improving the accuracy of the predictions. Additionally, while friction predictions for steel-steel and steel-sapphire contacts have been performed, further validation of this method across a broader range of contact materials.

- **Further investigation of thermal effects**: One of the most important conclusions of this study is the revelation that friction plateaus arise as a result of a combination of non-Newtonian and thermal effects. A reasonable conjecture is that in the absence of thermal effects, contacts between different types of surfaces under identical conditions would exhibit the same friction responses due to the same non-Newtonian effects. Any observed discrepancies in friction response, if present, can be wholly attributed to differences in thermal effects (due to differences in the thermal properties of different surfaces). The former has been confirmed by comparing the results of isothermal non-Newtonian simulations of steel-steel and steel-sapphire contacts (see Appendix D). However, proving the latter by comparing the experimental or TEHLnN results becomes challenging because of the similar thermal diffusivity of steel and sapphire. It would be valuable to explore other contact surfaces in the future, particularly those surfaces with substantial differences in thermal properties. This would make it possible to validate the influence of thermal effects on friction and enrich our understanding of the thermal and shear-thinning behaviours of these contacts.

  To do this, we need to find materials that are compatible with the limits of each of the tribology tests and numerical approaches. Tungsten Carbide, for example, is being considered.

# Calculation of reduced viscosity slope

To derive the viscosity slope from the representation in figure 2.5 (log scale), let's set $x = \frac{\dot{\gamma}}{\dot{\gamma}_e} = \dot{\gamma}_{red.}$, and $y = \frac{\eta}{\eta_N} = \eta_{red.}$. The corresponding logarithmic form are $X = \log_{10} x$ and $Y = \log_{10} y$. Then, the reduced viscosity slope is defined as the variation rate $R(x)$, written as:

$$R_{visco}(x) = \frac{\mathrm{d}Y}{\mathrm{d}X} = \frac{\mathrm{d}Y}{\mathrm{d}y} \times \frac{\mathrm{d}y}{\mathrm{d}x} \times \frac{\mathrm{d}x}{\mathrm{d}X} = \frac{x}{y}\frac{\mathrm{d}y}{\mathrm{d}x} \tag{A.1}$$

In Eyring equation 2.10(a), substituting $\dot{\gamma}_e$ and $\eta_N$ for $\tau_e$, one obtains an alternative form of Eyring viscosity equation:

$$\frac{\eta}{\eta_N} = \frac{\dot{\gamma}_e}{\dot{\gamma}} \sinh^{-1}\left(\frac{\dot{\gamma}}{\dot{\gamma}_e}\right) \tag{A.2}$$

By replacing the reduced viscosity by $y$ and the reduced shear rate by $x$, one obtains:

$$y = \frac{\sinh^{-1}(x)}{x} \tag{A.3}$$

Substituting equation A.3 into equation A.1, the variation rate of reduced Eyring viscosity as function of $\dot{\gamma}_{red.}$ finally became:

$$R_{visco}(x) = \frac{x}{\sqrt{1+x^2}\sinh^{-1}(x)} - 1 \tag{A.4}$$

# Newtonian viscosity by Green-Kubo method

The concept of the Green-Kubo (GK) method is described in Section 2.3.2a. In this study, GK is first tested on SQ, due to unsatisfactory results and other drawbacks, which are explained later, no further tests were carried out on the SQ and BB.

The output of the GK method is the viscosity value in a given step length (every 200,000 time steps or 0.2 ns in the present study). This result needs to be averaged again for a longer period to obtain the representative viscosity at the given $p$ and $T$. In the present study, all the GK simulations for SQ are run for 10 ns and the viscosity value is taken from the average of the last 2 ns. The simulation results are compared with viscosity measurements from Bair [116], as shown in Figure B.1. The solid squares represent the experimental measurements, the hollow diamonds represent the simulation results, and the colours distinguish temperatures. Dashed lines are used to connect the simulation results to identify the trend.

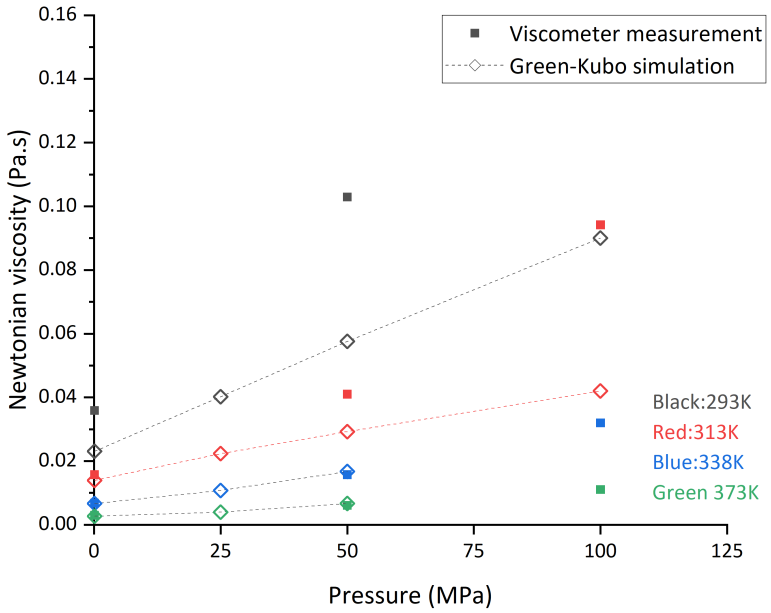


Figure B.1: Comparison between viscosity measurements (filled squares) and viscosity from GK method (hollow diamonds and dashed lines). Experimental data of SQ comes from [116].

It can be seen that the Newtonian viscosity calculated by the GK method has relatively good accuracy at atmospheric pressure. For 313 K, 338 K, and 373 K, the mean absolute percentage error (MAPE) between the two sets is consistently less than 10%. The highest MAPE is found at 293 K, at around 30%. However, it appears that the deviation between the two sets of data increases with pressure. For example, at 293 K and 313 K, and 50 MPa and 100 MPa, the maximum MAPE can reach 65%. The simulation results and the experimental data show a very different trend, and the deviation may increase with pressure by several orders of magnitude. Although simulations were not carried out for other temperatures, the same trend is likely to occur.

The GK method calculates viscosity using the autocorrelation function of the stress tensor. Ideally, with increasing time, the autocorrelation function of the stress tensor should decay to zero, implying that the integral in Equation 2.16 converges to a constant value - the viscosity of the fluid under the given conditions. However, the full convergence of the viscosity sometimes requires a long simulation time [193]. However, in the present study, the simulation time for GK methods is limited to several nanoseconds due to computational limitations. This limitation leads to functions that do not converge under certain conditions, especially at lower temperatures and/or higher pressures where particle fluctuations are slower, resulting in a prolonged fluctuation duration. Conversely, an overly long simulation time can cause another issue. In some cases, the autocorrelation function may not decay to zero and instead presents a “long tail”, causing the integration to diverge and introducing new errors [193, 194].

These challenges limit the applicability of the GK method in the current study. As a result, we opted for the Stokes-Einstein method, which is based on diffusion coefficients.

# Improvement of Stokes-Einstein method

An attempt to improve the prediction method is being made. One possibility is to consider the changes in parameters ($D_0$ and $r_c$) with pressure. For $r_c$, given that in our calculation method, it is the free volume that is most influenced by changes in pressure. And when the effect of free volume is excluded as much as possible, the value of $r_c$ becomes nearly independent of temperature and pressure, as previously analysed. Hence, its value remains constant. The only parameter to be refined is $D_0$. The $D_0$ values obtained from EMD simulations (as shown in Figure 3.6) are fitted with Equation C.1. The resulting fitting parameters for both fluids are presented in Table C.1. The $D_0$ values and their corresponding fits are depicted in Figure C.1.

$$D_0(p)[\mathrm{m^2/s}] = D_{00} + A\left(1 - \exp\left(\frac{-p}{B}\right)\right) + C\left(1 - \exp\left(\frac{-p}{D}\right)\right) \tag{C.1}$$

| Fluid | $D_{00}$ [$\mathrm{m^2/s}$] | A [$\}rm^{m^2}/s$] | B [MPa] | C [$\mathrm{m^2/s}$] | D [MPa] | $R^2$ |
|---|---|---|---|---|---|---|
| SQ | $3.57 \times 10^{-7}$ | $-1.45 \times 10^{-7}$ | 11.28 | $-1.77 \times 10^{-7}$ | 134.29 | 0.98 |
| BB | $6.26 \times 10^{-7}$ | $-2.18 \times 10^{-7}$ | 106.08 | $-3.06 \times 10^{-7}$ | 32.91 | 0.97 |

Table C.1: The parameters of the equation for $D_0$ of SQ and BB.

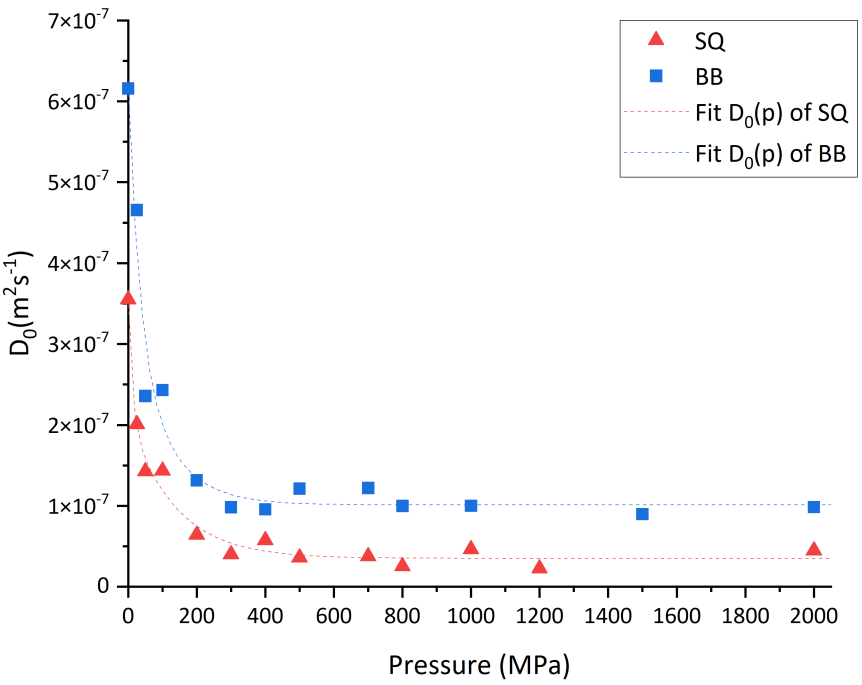


Figure C.1: Parameter $D_0$ and their corresponding fits as function of pressure of SQ and BB.

Based on the $D_0(p)$ defined by Equation C.1, and the same $E_a(p)$ and $r_c$ values, the refined Stokes-Einstein equation can provide a new prediction of $\eta_N(p,T)$. This new prediction, experimental measurements, and previous predictions using constant $D_0$ values are plotted in Figure C.2.

According to Figure C.2(a), the new method does not significantly improve the quality of the prediction for SQ. However, in (b), the new method enhances the prediction quality at lower pressures (<300 MPa). The comparison between the new predictions and experimental data at these pressures can be seen in the small inset of Figure C.2(b). At these pressures, the new prediction gives a significantly better prediction of experimental measurements. But as the pressure increases, the value of $D_0(p)$ approaches the constant value used in the previous method, thus the two predictions converge. The same difference of up to several orders of magnitude is observed, yet these higher pressures are typical operating conditions of the EHD contacts. In addition, adjusting the parameters $D_0(p)$ does not help to capture the faster-than-exponential behaviour observed in the experimental measurements of both fluids. We can conclude at this point that, at least for the two fluids studied, the Stokes-Einstein method cannot accurately predict the value or the order of magnitude of their Newtonian viscosity under EHL conditions.

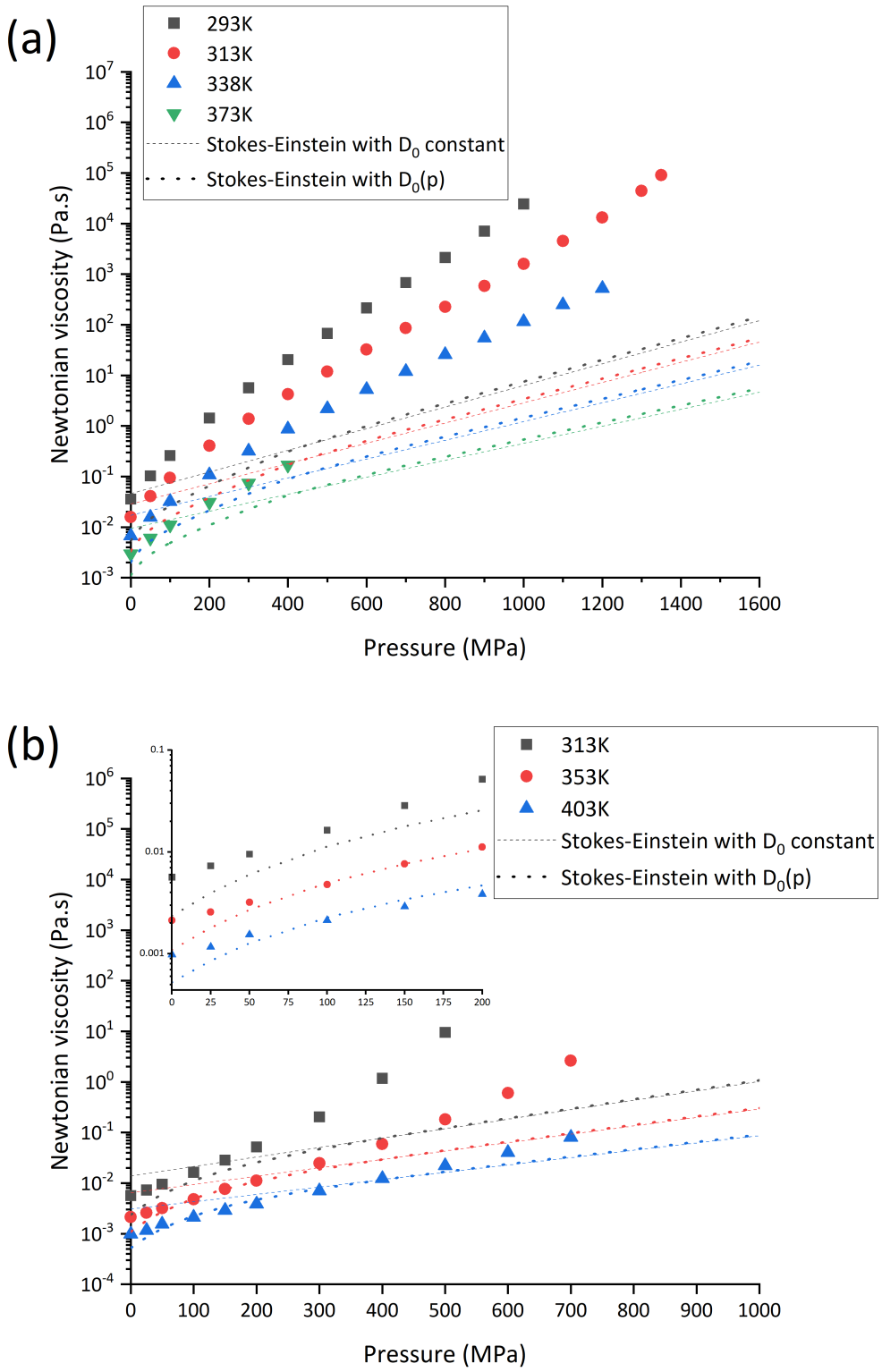


Figure C.2: Comparison between Newtonian viscosity measurements (symbols, SQ [116] and BB [40]), prediction by Stokes-Einstein law with constant $D_0$ (dashed lines) and prediction by Stokes-Einstein law with $D_0(p)$ (dotted lines) of (a) SQ and (b) BB.

# Friction prediction on steel-sapphire contacts

In the tribological experiments of SQ cited in this study, another set of contact materials, a Steel ball and a Sapphire disc, were tested. The material properties of this new set are shown in Table D.1. Utilising this new material combination, the same TEHLnN and isothermal non-Newtonian friction predictions were performed. The TEHLnN results will be used to compare differences in friction response due to varying thermal effects. The isothermal results aim to verify whether thermal effects are the only factor contributing to the observed differences (since the isothermal non-Newtonian simulation results should remain consistent under the same contact conditions). Comparable contact conditions to steel-steel contact shown in Figure 4.5 were selected and summarised in Table D.2.

| **Solid** | Ball & Disc 1 | Disc 2 |
|---|---|---|
| Material | Steel | Sapphire |
| Young's modulus $E$ [GPa] | 210 | 360 |
| Poisson's ratio $\nu$ [-] | 0.3 | 0.34 |
| Thermal conductivity $k$ [$^{W}/_{mK}$] | 21 [192] | 45 |
| Specific heat $c_p$ [$^{J}/_{kgK}$] | 470 | 1171 |
| Density $\rho$ [$^{kg}/_{m^3}$] | 7850 | 3980 |
| Thermal diffusivity $\frac{k}{c_p\rho}$ [$^{m^2}/_{s}$] | $5.69 \times 10^{-6}$ | $9.66 \times 10^{-6}$ |

Table D.1: Materiel properties of the new contacting solids.

| Contact combination | steel-steel | steel-sapphire |
|---|---|---|
| Ambient temperature $T_0$ [K] | 313 | |
| Contact load $w$ [N] | 108, 254 | 68, 159 |
| Corresponding Hertzian pressure $p_h$ [MPa] | 1200, 1600 | |
| Entrainment speed $u_e$ [$^{m}/_{s}$] | 0.8 | |

Table D.2: Contact conditions used for comparison between steel-steel and steel-sapphire contacts.

Experimental measurements and numerical predictions for two different contacts are shown in Figure

D.1, where (a) stands for $ph = 1200$ MPa and (b) stands for $ph = 1600$, solid symbols represent steel-steel contact and open symbols represent steel-sapphire contact. Experimental measurements are denoted by black squares, TEHLnN results are denoted by red dots, and isothermal non-Newtonian results are denoted by blue triangles. Note that in the isothermal results, the steel-sapphire symbols (open blue triangles) are enlarged to improve readability as the results almost coincide.

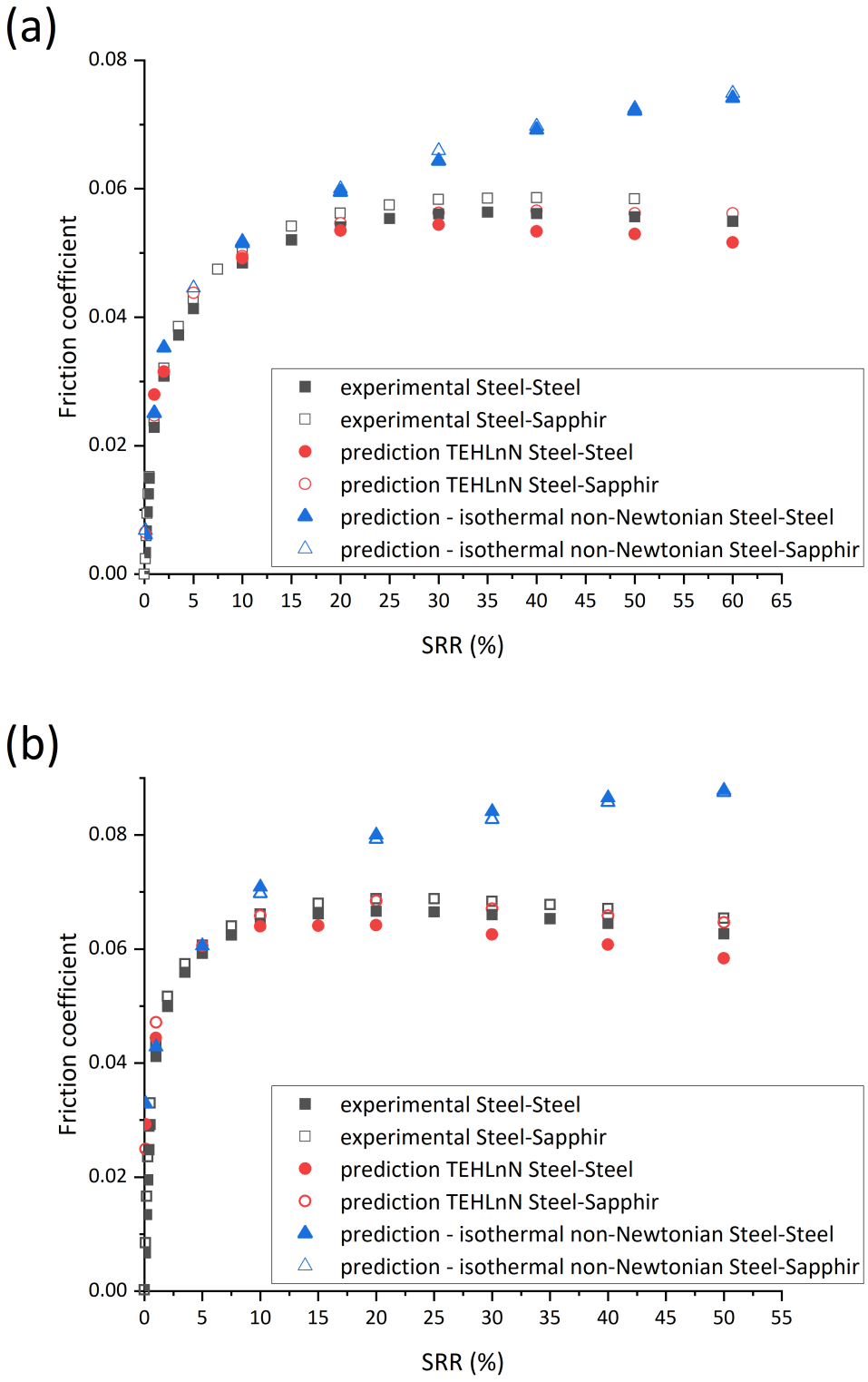


Figure D.1: Comparison between steel-steel (solid symbols) and steel-sapphire (open symbols) contact. Experimental measurements (black squares) TEHLnN prediction results (red dots) and isothermal non-Newtonian simulation (blue triangles). (a) SQ $T_0$=313K, $p_h$=1200MPa. (b) SQ $T_0$=313K, $p_h$=1600MPa.

Similar to the predictions for steel-steel contacts, the TEHLnN friction prediction for steel-sapphire contact yielded very satisfactory results. The friction and different friction regimes (including the friction plateau) were quantitatively predicted with the MAPE (for SRR $>$ 1%) always being less than 4%.

In Figure D.1(a) and (b), the experimental results (black squares) show a slight difference in the coefficient of friction between steel-steel and steel-sapphire contacts under the same conditions, with the results from steel-steel contact consistently lower than those from steel-sapphire. A similar minor difference is also observed in the TEHLnN simulation results (red dots). However, in TEHLnN, not only is the coefficient of friction for the steel-steel contact lower, but it also shows a faster decrease in the friction coefficient at relatively high SRRs (30% to 65%). This indicates a more pronounced thermal thinning effect compared to the steel-sapphire contact.

Simultaneously, the isothermal non-Newtonian results (blue triangles) for the two different contacts align both quantitatively and qualitatively. This observation confirms our assumption that, in the absence of thermal effects, the same contact conditions should yield consistent non-Newtonian effects and, therefore, consistent friction. Hence, the differences in friction coefficients observed previously in both experiments and TEHLnN simulations between the two contacts can be attributed to variations in thermal effects.

Indeed, the difference in thermal diffusivity between steel and sapphire is not significant (see Table D.2), being only about 41%. This minor difference explains why the two contacts do not exhibit considerable differences in experimental measurements and TEHLnN predictions under identical contact conditions. Still, it is predictable that the higher thermal diffusivity of sapphire enables more rapid dissipation of heat generated in the contact area via the solid surface than steel. Nonetheless, due to the complexities of real contact, it is not uncritical to say that the temperature in a steel-sapphire contact will be lower than in a steel-steel contact under the same conditions simply because the heat dissipation capacity is greater. Given the coupling of temperature, viscosity, and heat generation in the contact area, a lower temperature might result in higher viscosity, which could intensify shear heating. This suggests that a quantitative analysis of changes in thermal effects (and thus friction response difference) due to different contacting solids would likely necessitate calculations of both heat generation and dissipation rates, which is beyond the scope of this current study.

# Bibliography


[1] K. Holmberg and A. Erdemir, "Global impact of friction on energy consumption, economy and environment," *FME Transactions*, vol. 43, pp. 181–185, 2015. iv, 1

[2] K. Holmberg, P. Andersson, and A. Erdemir, "Global energy consumption due to friction in passenger cars," *Tribology International*, vol. 47, pp. 221–234, 3 2012. [Online]. Available: http://dx.doi.org/10.1016/j.triboint.2011.11.022 iv, 1

[3] K. Holmberg and A. Erdemir, "Influence of tribology on global energy consumption, costs and emissions," *Friction*, vol. 5, pp. 263–284, 2017. iv, 1

[4] H. A. Spikes, "Sixty years of EHL," *Lubrication Science*, vol. 18, pp. 265–291, 10 2006. [Online]. Available: https://onlinelibrary.wiley.com/doi/10.1002/ls.23 vii, 7, 32

[5] F. W. Smith, "Lubricant behaviour in concentrated contact systems - the castor oil-steel system," *Wear*, vol. 2, pp. 250–263, 1959. vii, 8

[6] S. S. Bair, *High pressure rheology for quantitative elastohydrodynamics*. Elsevier, 2019. viii, 9, 24

[7] S. Bair, "A traction (friction) curve is not a flow curve," *Lubricants*, vol. 10, 9 2022. ix, 10

[8] W. Hirst and A. Moore, "Non-newtonian behaviour in elastohydrodynamic lubrication," *Proceedings of the Royal Society of London. A. Mathematical and Physical Sciences*, vol. 337, pp. 101–121, 3 1974. [Online]. Available: https://royalsocietypublishing.org/doi/10.1098/rspa.1974.0040 ix, 10

[9] K. L. Johnson and J. L. Tevaarwerk, "Shear behaviour of elastohydrodynamic oil films." *Proc R Soc London Ser A*, vol. 356, pp. 215–236, 1977. ix, xii, xiii, 10, 18, 19, 20, 21

[10] L. Houpert, "New results of traction force calculations in elastohydrodynamic contacts," *Journal of Tribology*, vol. 107, pp. 241–245, 4 1985. [Online]. Available: https://asmedigitalcollection.asme.org/tribology/article/107/2/241/436330/New-Results-of-Traction-Force-Calculations-in ix, 10

[11] L. Martinie and P. Vergne, "Lubrication at extreme conditions: A discussion about the limiting shear stress concept," *Tribology Letters*, vol. 63, 8 2016. ix, x, xi, xii, 10, 12, 14, 17, 18

[12] S. N. Ndiaye, "Ultimate behavior of confined fluids under very high pressure and shear stress," Ph.D. dissertation, INSA de Lyon, 2017. [Online]. Available: https://tel.archives-ouvertes.fr/tel-02061350 ix, xii, 10, 18, 19, 30

[13] V. S. Craig, C. Neto, and D. R. Williams, "Shear-dependent boundary slip in an aqueous newtonian liquid," *Physical Review Letters*, vol. 87, pp. 54 504–1–54 504–4, 2001. ix, 11

[14] Y. Zhu and S. Granick, "Limits of the hydrodynamic no-slip boundary condition," *Physical Review Letters*, vol. 88, p. 4, 2002. ix, 11

[15] P. A. Thompson and S. M. Troian, "A general boundary condition for liquid flow at solid surfaces," *Nature*, vol. 389, pp. 360–362, 1997. ix, 11

[16] A. Porras-Vazquez, L. Martinie, P. Vergne, and N. Fillot, "Independence between friction and velocity distribution in fluids subjected to severe shearing and confinement," *Physical Chemistry Chemical Physics*, vol. 20, pp. 27 280–27 293, 2018. ix, xi, xii, xxii, xxxiii, xxxiv, 11, 14, 16, 17, 18, 30, 34, 38, 75, 76, 77

[17] E. Schnell, "Slippage of water over nonwettable surfaces," *Journal of Applied Physics*, vol. 27, pp. 1149–1152, 1956. ix, 11

[18] R. Pit, H. Hervet, and L. Léger, "Direct experimental evidence of slip in hexadecane: solid interfaces," *Physical Review Letters*, vol. 85, pp. 980–983, 2000. ix, x, 11, 12

[19] H. Hervet and L. Léger, "Flow with slip at the wall: From simple to complex fluids," *Comptes Rendus Physique*, vol. 4, pp. 241–249, 2003. ix, 11

[20] C. W. Wu, P. Zhou, and G. J. Ma, "Squeeze fluid film of spherical hydrophobic surfaces with wall slip," *Tribology International*, vol. 39, pp. 863–872, 2006. ix, 11

[21] X. M. Li, F. Guo, and P. L. Wong, "Shear rate and pressure effects on boundary slippage in highly stressed contacts," *Tribology International*, vol. 59, pp. 147–153, 2013. ix, 11

[22] M. Kaneta, H. Nishikawa, and K. Kameishi, "Observation of wall slip in elastohydrodynamic lubrication," *Journal of Tribology*, vol. 112, pp. 447–452, 1990. x, 11

[23] M. A. Plint, "Third paper: Traction in elastohydrodynamic contacts," *Proceedings of the Institution of Mechanical Engineers*, vol. 182, pp. 300–306, 1967. x, xii, 8, 12, 18

[24] S. Bair, F. Qureshi, and W. O. Winer, "Observations of shear localization in liquid lubricants under pressure," *Journal of Tribology*, vol. 115, pp. 507–513, 1993. x, xii, 12, 18

[25] L. Chang, "On the shear bands and shear localizations in elastohydrodynamic lubrication films," *Journal of Tribology*, vol. 127, pp. 245–247, 1 2005. [Online]. Available: https://asmedigitalcollection.asme.org/tribology/article/127/1/245/462984/On-the-Shear-Bands-and-Shear-Localizations-in x, xii, 12, 18

[26] S. Bair and C. McCabe, "A study of mechanical shear bands in liquids at high pressure," *Tribology International*, vol. 37, pp. 783–789, 10 2004. x, xii, 12, 13, 18

[27] H. Kobayashi and Y. Fujita, "Mechanisms for three kinds of limiting shear stresses appearing in the traction modes of viscous, viscoelastic, and glassy states of lubricants," *Journal of Applied Physics*, vol. 115, 2014. x, 12

[28] B. Jacobson, "An experimental determination of the solidification velocity for mineral oils," *ASLE Transactions*, vol. 17, pp. 290–294, 1974. x, 13

[29] P. Šperka, I. Křupka, and M. Hartl, "Evidence of plug flow in rolling-sliding elastohydrodynamic contact," *Tribology Letters*, vol. 54, pp. 151–160, 2014. x, 13, 14

[30] A. Ponjavic, L. D. Mare, and J. S. Wong, "Effect of pressure on the flow behavior of polybutene," *Journal of Polymer Science, Part B: Polymer Physics*, vol. 52, pp. 708–715, 2014. x, 13

[31] J. P. Ewen, C. Gattinoni, J. Zhang, D. M. Heyes, H. A. Spikes, and D. Dini, "On the effect of confined fluid molecular structure on nonequilibrium phase behaviour and friction," *Physical Chemistry Chemical Physics*, vol. 19, pp. 17 883–17 894, 2017. x, xi, xxii, xxxiii, xxxiv, 14, 15, 34, 38, 39, 75, 76

[32] C. Gattinoni, D. M. Heyes, C. D. Lorenz, and D. Dini, "Traction and nonequilibrium phase behavior of confined sheared liquids at high pressure," *Physical Review E - Statistical, Nonlinear, and Soft Matter Physics*, vol. 88, pp. 1–10, 2013. xi, 14, 34

[33] S. Bair and W. O. Winer, "A rheological model for elastohydrodynamic contacts based on primary laboratory data," *Journal of Tribology*, vol. 101, pp. 258–264, 1979. [Online]. Available: http://www.asme.org/about-asme/terms-of-use xi, 14

[34] J. Zhang, A. Tan, and H. Spikes, "Effect of base oil structure on elastohydrodynamic friction," *Tribology Letters*, vol. 65, pp. 1–24, 2017. xi, 14, 15

[35] S. Ndiaye, L. Martinie, D. Philippon, M. Gonon-Caux, J. Margueritat, and P. Vergne, "On the influence of phase change in highly loaded frictional contacts," *Tribology Letters*, vol. 68, pp. 1–23, 2020. xi, 14, 16

[36] M. Alsaad, S. Bair, D. M. Sanborn, and W. O. Winer, "Glass transitions in lubricants: Its relation to elastohydrodynamic lubrication (ehd)," *Journal of Tribology*, vol. 100, pp. 404–416, 7 1978. [Online]. Available: https://asmedigitalcollection.asme.org/tribology/article/100/3/404/382589/Glass-Transitions-in-Lubricants-Its-Relation-to xi, 16

[37] K. L. Johnson and R. Cameron, "Fourth paper: Shear behaviour of elastohydrodynamic oil films at high rolling contact pressures," *Proceedings of the Institution of Mechanical Engineers*, vol. 182, pp. 307–330, 1967. xi, 16

[38] K. L. JOHNSON and A. D. ROBERTS, "Observations of viscoelastic behaviour of an elastohydrodynamic lubricant film." *Proc. Roy. Soc. London a*, vol. 337, pp. 217–242, 1974. xi, 16

[39] N. Ohno, N. Kuwano, and F. Hirano, "Effect of bulk modulus of solidified oils under high pressure on tractional behavior," *Japanese Journal of Tribology*, vol. 38, pp. 1361–1372, 1993. xi, 16

[40] S. N. Ndiaye, L. Martinie, D. Philippon, N. Devaux, and P. Vergne, "A quantitative friction-based approach of the limiting shear stress pressure and temperature dependence," *Tribology Letters*, vol. 65, pp. 1–14, 12 2017. xi, xii, xxvii, xxviii, xxix, xxxi, xxxii, xxxvi, xxxviii, xl, xlii, xlv, 16, 20, 31, 47, 50, 59, 60, 63, 65, 81, 82, 88, 90, 95, 96, 111

[41] S. Bair and W. O. Winer, "Shear strength measurements of lubricants at high pressure," *Journal of Tribology*, vol. 101, pp. 251–257, 1979. xi, 9, 17

[42] ——, "The high pressure high shear stress rheology of liquid lubricants," *Journal of Tribology*, vol. 114, pp. 1–9, 1992. xi, xii, 17, 19

[43] H. S. Cheng and B. Sternlicht, "A numerical solution for the pressure, temperature, and film thickness between two infinitely long, lubricated rolling and sliding cylinders, under heavy loads," *Journal of Basic Engineering*, vol. 87, pp. 695–704, 9 1965. [Online].

Available: https://asmedigitalcollection.asme.org/fluidsengineering/article/87/3/695/396991/A-Numerical-Solution-for-the-Pressure-Temperature xii, 17

[44] H. S. Cheng, "A refined solution to the thermal-elastohydrodynamic lubrication of rolling and sliding cylinders," *A S L E Transactions*, vol. 8, pp. 397–410, 1 1965. [Online]. Available: https://www.tandfonline.com/doi/full/10.1080/05698196508972110 xii, 17

[45] K. Johnson and J. Greenwood, "Thermal analysis of an eyring fluid in elastohydrodynamic traction," *Wear*, vol. 61, pp. 353–374, 6 1980. [Online]. Available: https://linkinghub.elsevier.com/retrieve/pii/0043164880902987 xii, 17

[46] S. Wang, C. Cusano, and T. F. Conry, "Thermal analysis of elastohydrodynamic lubrication of line contacts using the ree-eyring fluid model," *Journal of Tribology*, vol. 113, pp. 232–242, 4 1991. [Online]. Available: https://asmedigitalcollection.asme.org/tribology/article/113/2/232/434555/Thermal-Analysis-of-Elastohydrodynamic-Lubrication xii, 17

[47] H. J. Kim, P. Ehret, D. C. Dowson, and C. M. Taylor, "Thermal elastohydrodynamic analysis of circular contacts part 2: Non-newtonian model," *Proceedings of the Institution of Mechanical Engineers, Part J: Journal of Engineering Tribology*, vol. 215, pp. 353 – 362, 2001. xii, 17

[48] D. Dowson and G. Higginson, "A numerical solution to the elasto-hydrodynamic problem," *Journal of mechanical engineering science*, vol. 1, no. 1, pp. 6–15, 1959. xii, 7, 17

[49] A. Grubin, "Fundamentals of the hydrodynamic theory of lubrication of heavily loaded cylindrical surfaces," *Investigation of the Contact Machine Componets*, vol. 2, 1949. xii, 7, 17

[50] A. W. Crook, "The lubrication of rollers iii. a theoretical discussion of friction and the temperatures in the oil film," *Philosophical Transactions of the Royal Society of London. Series A, Mathematical and Physical Sciences*, vol. 254, pp. 237–258, 12 1961. [Online]. Available: https://royalsocietypublishing.org/doi/10.1098/rsta.1961.0016 xii, 18

[51] ——, "The lubrication of rollers iv. measurements of friction and effective viscosity," *Philosophical Transactions of the Royal Society of London. Series A, Mathematical and Physical Sciences*, vol. 255, pp. 281–312, 1 1963. [Online]. Available: https://royalsocietypublishing.org/doi/10.1098/rsta.1963.0005 xii, 18

[52] W. Habchi, P. Vergne, S. Bair, O. Andersson, D. Eyheramendy, and G. E. Morales-Espejel, "Influence of pressure and temperature dependence of thermal properties of a lubricant on the behaviour of circular tehd contacts," *Tribology International*, vol. 43, pp. 1842–1850, 10 2010. [Online]. Available: http://dx.doi.org/10.1016/j.triboint.2009.10.002 xii, 18, 98

[53] J. P. Ewen, D. M. Heyes, and D. Dini, "Advances in nonequilibrium molecular dynamics simulations of lubricants and additives," *Friction*, vol. 6, pp. 349–386, 12 2018. xii, 18, 37

[54] F. L. Plant, E. J. Hutchinson, and D. Ben-Amotz, "Raman measurements of localized pressure variations in lubricants above the glass transition pressure," *Journal of Tribology*, vol. 119, pp. 817–822, 1997. xii, 18

[55] M. Björling, W. Habchi, S. Bair, R. Larsson, and P. Marklund, "Towards the true prediction of EHL friction," *Tribology International*, vol. 66, pp. 19–26, 2013. [Online]. Available: http://dx.doi.org/10.1016/j.triboint.2013.04.008 xii, xiii, xiv, 10, 18, 21, 22, 25, 97

[56] H. C. Liu, B. B. Zhang, N. Bader, C. H. Venner, and G. Poll, "Simplified traction prediction for highly loaded rolling/sliding EHL contacts," *Tribology International*, vol. 148, 8 2020. xii, xiii, xv, 10, 18, 21, 25, 97

[57] B. Jacod and C. H. Venner and P. M. Lugt, "Extension of the friction mastercurve to limiting shear stress models," *Journal of Tribology*, vol. 125, pp. 739–746, 10 2003. xii, xiii, 18, 21, 25, 97

[58] A. V. Olver and H. A. Spikes, "Prediction of traction in elastohydrodynamic lubrication," *Proceedings of the Institution of Mechanical Engineers, Part J: Journal of Engineering Tribology*, vol. 212, pp. 321–332, 5 1998. [Online]. Available: http://journals.sagepub.com/doi/10.1243/1350650981542137 xii, xiii, 18, 21, 25

[59] G. E. Morales-Espejel and A. W. Wemekamp, "An engineering approach on sliding friction in full-film, heavily loaded lubricated contacts," *Part J: J. Engineering Tribology*, vol. 218, 2004. xii, xiii, 18, 21, 25

[60] W. Habchi, I. Demirci, D. Eyheramendy, G. Morales-Espejel, and P. Vergne, "A finite element approach of thin film lubrication in circular ehd contacts," *Tribology International*, vol. 40, pp. 1466–1473, 2007. xii, xiii, xv, 18, 21, 25

[61] W. Habchi, D. Eyheramendy, P. Vergne, and G. Morales-Espejel, "A full-system approach of the elastohydrodynamic line/point contact problem," *Journal of Tribology*, vol. 130, pp. 1–10, 4 2008. xii, xiii, xiv, xv, 18, 21, 22, 25, 30, 43

[62] Y. Liu, Q. J. Wang, S. Bair, and P. Vergne, "A quantitative solution for the full shear-thinning EHL point contact problem including traction," *Tribology Letters*, vol. 28, pp. 171–181, 11 2007. xii, xiii, 18, 21, 25

[63] W. Habchi, D. Eyheramendy, S. Bair, P. Vergne, and G. Morales-Espejel, "Thermal elastohydrodynamic lubrication of point contacts using a newtonian/generalized newtonian lubricant," *Tribology Letters*, vol. 30, pp. 41–52, 4 2008. xii, xiii, xv, xxiv, 18, 21, 25, 40, 97, 104

[64] S. Bair and A. Laesecke, "Normalized ashurst-hoover scaling and a comprehensive viscosity correlation for compressed liquids," *Journal of Tribology*, vol. 134, 2012. xii, xix, 18, 25, 31, 33

[65] C. R. Evans and K. L. Johnson, "The rheological properties of elastohydrodynamic lubricants," *Proceedings of the Institution of Mechanical Engineers, Part C: Journal of Mechanical Engineering Science*, vol. 200, pp. 303–312, 1986. xii, xiii, xxxv, 19, 20, 21, 80

[66] E. Höglund and B. Jacobson, "Experimental investigation of the shear strength of lubricants subjected to high pressure and temperature," *Journal of Tribology*, vol. 108, pp. 571–577, 10 1986. [Online]. Available: https://asmedigitalcollection.asme.org/tribology/article/108/4/571/437614/Experimental-Investigation-of-the-Shear-Strength xii, 19, 20

[67] E. Höglund, "The relationship between lubricant shear strength and chemical composition of the base oil," *Wear*, vol. 130, pp. 213–224, 1989. xii, 19, 20

[68] W. Hirst and A. J. Moore, "Elastohydrodynamic lubrication at high pressures." *Proc R Soc London Ser A*, vol. 360, pp. 403–425, 1978. xii, 19, 20

[69] S. Bair and W. O. Winer, "The high shear stress rheology of liquid lubricants at pressures of 2 to 200 mpa," *Journal of Tribology*, vol. 112, pp. 246–252, 4 1990. [Online]. Available: https://asmedigitalcollection.asme.org/tribology/article/112/2/246/437616/The-High-Shear-Stress-Rheology-of-Liquid xii, 19

[70] H. Spikes and Z. Jie, "History, origins and prediction of elastohydrodynamic friction," *Tribology Letters*, vol. 56, pp. 1–25, 2014. xiii, xv, xviii, 21, 26, 28, 31

[71] C. R. Evans and K. L. Johnson, "Regimes of traction in elastohydrodynamic lubrication," *Proceedings of the Institution of Mechanical Engineers, Part C: Journal of Mechanical Engineering Science*, vol. 200, pp. 313–324, 9 1986. [Online]. Available: http://journals.sagepub.com/doi/10.1243/PIME_PROC_1986_200_135_02 xiii, 21

[72] B. Jacod, C. H. Venner, and P. M. Lugt, "A generalized traction curve for EHL contacts," *Journal of Tribology*, vol. 123, pp. 248–253, 4 2001. xiii, 21

[73] S. Bair, C. McCabe, and P. T. Cummings, "Calculation of viscous EHL traction for squalane using molecular simulation and rheometry," *Tribology Letters*, vol. 13, pp. 251–254, 2002. xiii, xv, xxxvi, xxxvii, xxxviii, 21, 25, 34, 81, 82, 83

[74] T. Doki-Thonon, "Thermal effects in elastohydrodynamic spinning circular contacts," Ph.D. dissertation, INSA de Lyon, 2012. [Online]. Available: https://tel.archives-ouvertes.fr/tel-00749882 xiii, xiv, xxiv, xxvii, 21, 22, 40, 44, 45

[75] J.-D. Wheeler, "Non-elliptical point contacts : The torus-on-plane conjunction," Ph.D. dissertation, INSA de Lyon, 2016. [Online]. Available: https://tel.archives-ouvertes.fr/tel-01791538 xiii, xxiv, 7, 21, 40, 44

[76] P. J. Carreau, "Rheological equations from molecular network theories." *Trans Soc Rheol*, vol. 16, pp. 99–127, 1972. xiii, 21

[77] H. Eyring, "Viscosity, plasticity, and diffusion as examples of absolute reaction rates," *The Journal of Chemical Physics*, vol. 4, pp. 283–291, 1936. xiii, xv, 22, 25, 26, 29

[78] N. Voeltzel, "Molecular simulation of an ionic liquid as lubricant: from bulk rheology to nanoconfinement," p. 143, 2016. xiv, 21

[79] S. Bair, *"Recent Developments in High-Pressure Rheology of Lubricants"*, 1995, vol. 30. [Online]. Available: https://linkinghub.elsevier.com/retrieve/pii/S016789220870628X xiv, 22

[80] Vikram Jadhao and Mark O. Robbins, "Rheological properties of liquids under conditions of elastohydrodynamic lubrication," *Tribology Letters*, vol. 67, pp. 1–20, 9 2019. [Online]. Available: https://doi.org/10.1007/s11249-019-1178-3 xiv, xvi, xvii, xxxiii, xxxiv, xxxvi, xxxvii, xxxviii, 22, 29, 30, 34, 38, 74, 75, 76, 77, 81, 82, 83, 91, 92, 97

[81] L. Prandtl, "Ein gedankenmodell zur kinetischen theorie der festen körper," *Zamm-zeitschrift Fur Angewandte Mathematik Und Mechanik*, vol. 8, pp. 85–106. xv, 25

[82] V. L. Popov and J. Gray, "Prandtl-tomlinson model: History and applications in friction, plasticity, and nanotechnologies," *ZAMM-Journal of Applied Mathematics and Mechanics/Zeitschrift für Angewandte Mathematik und Mechanik*, vol. 92, no. 9, pp. 683–708, 2012. xv, 25

[83] L. Lin and M. A. Kedzierski, "Density and viscosity of a polyol ester lubricant: Measurement and molecular dynamics simulation," *International Journal of Refrigeration*, vol. 118, pp. 188–201, 2020. [Online]. Available: https://doi.org/10.1016/j.ijrefrig.2020.07.004 xvi, 29

[84] I. J. Prentice, X. Liu, O. A. Nerushev, S. Balakrishnan, C. R. Pulham, and P. J. Camp, "Experimental and simulation study of the high-pressure behavior of squalane and poly- -olefins," *Journal of Chemical Physics*, vol. 152, 2020. [Online]. Available: https://doi.org/10.1063/1.5139723 xvi, 29, 54, 55

[85] S. S. Bair, O. Andersson, F. S. Qureshi, and M. M. Schirru, "New EHL modeling data for the reference liquids squalane and squalane plus polyisoprene," *Tribology Transactions*, vol. 61, pp. 247–255, 2018. [Online]. Available: http://dx.doi.org/10.1080/10402004.2017.1310339 xviii, xxxi, 30, 63

[86] D. C. Dowson and G. R. Higginson, *Elasto-hydrodynamic lubrication : the fundamentals of roller and gear lubrication*. Pergamon Press, Oxford, 1966. [Online]. Available: https://www.sciencedirect.com/science/article/pii/004316486790018X xviii, 31

[87] P. Vergne and S. Bair, "Classical EHL versus quantitative EHL: A perspective part I - real viscosity-pressure dependence and the viscosity-pressure coefficient for predicting film thickness," *Tribology Letters*, vol. 54, pp. 1–12, 2014. xviii, xxx, 24, 31, 61

[88] S. Bair, L. Martinie, and P. Vergne, "Classical EHL versus quantitative EHL: A perspective part II — super-arrhenius piezoviscosity, an essential component of elastohydrodynamic friction missing from classical EHL," *Tribology Letters*, vol. 63, 9 2016. xviii, xxx, 24, 31, 61, 62, 97

[89] S. Bair, C. Mary, N. Bouscharain, and P. Vergne, "An improved yasutomi correlation for viscosity at high pressure," *Proceedings of the Institution of Mechanical Engineers, Part J: Journal of Engineering Tribology*, vol. 227, pp. 1056–1060, 2013. xix, 31, 32

[90] S. Bair, *Compressibility and the Equation of State*. Elsevier, 2019. xix, 32

[91] A. T. Hayward, "Compressibility equations for liquids: A comparative study," *British Journal of Applied Physics*, vol. 18, pp. 965–977, 7 1967. [Online]. Available: https://iopscience.iop.org/article/10.1088/0508-3443/18/7/312 xix, 32, 33, 41

[92] A. P. Thompson, H. M. Aktulga, R. Berger, D. S. Bolintineanu, W. M. Brown, P. S. Crozier, P. J. in 't Veld, A. Kohlmeyer, S. G. Moore, T. D. Nguyen, R. Shan, M. J. Stevens, J. Tranchida, C. Trott, and S. J. Plimpton, "Lammps - a flexible simulation tool for particle-based materials modeling at the atomic, meso, and continuum scales," *Computer Physics Communications*, vol. 271, p. 108171, 2 2022. xix, 34

[93] M. P. Allen and D. J. Tildesley, *Computer simulation of liquids*. Oxford university press, 2017. xix, xxi, 34, 36, 37

[94] J. P. Ewen, C. Gattinoni, F. M. Thakkar, N. Morgan, H. A. Spikes, and D. Dini, "A comparison of classical force-fields for molecular dynamics simulations of lubricants," *Materials*, vol. 9, 8 2016. xix, 34

[95] K. Pluhackova, H. Morhenn, L. Lautner, W. Lohstroh, K. S. Nemkovski, T. Unruh, and R. A. Böckmann, "Extension of the lopls-aa force field for alcohols, esters, and monoolein bilayers and its validation by neutron scattering experiments," *The Journal of Physical Chemistry B*, vol. 119, no. 49, p. 15287–15299, 2015. xix, 34

[96] S. W. Siu, K. Pluhackova, and R. A. Böckmann, "Optimization of the opls-aa force field for long hydrocarbons," *Journal of Chemical Theory and Computation*, vol. 8, pp. 1459–1470, 2012. xix, 34

[97] A. P. Vázquez, "A molecular approach to the ultimate friction response of confined fluids," Ph.D. dissertation, INSA de Lyon, 2019. [Online]. Available: https://tel.archives-ouvertes.fr/tel-02882466 xix, xxi, 6, 30, 31, 34, 36, 39, 51, 52, 55, 56, 57

[98] D. J. Evans and B. L. Holian, "The nose-hoover thermostat," *The Journal of Chemical Physics*, vol. 83, pp. 4069–4074, 1985. xx, 35

[99] M. S. Green, "Markoff random processes and the statistical mechanics of time-dependent phenomena. ii. irreversible processes in fluids," *The Journal of Chemical Physics*, vol. 22, pp. 398–413, 1954. xx, 35

[100] R. Kubo, "Statistical-mechanical theory of irreversible processes. i. general theory and simple applications to magnetic and conduction problems," *Journal of the Physical Society of Japan*, vol. 12, no. 6, pp. 570–586, 1957. xx, 35

[101] A. Einstein, "Über die von der molekularkinetischen theorie der wärme geforderte bewegung von in ruhenden flüssigkeiten suspendierten teilchen," *Annalen der physik*, vol. 4, 1905. xx, 36, 61

[102] G. G. Stokes *et al.*, "On the effect of the internal friction of fluids on the motion of pendulums," 1851. xx, 36

[103] D. Keffer, "The working man's guide to obtaining self diffusion coefficients from md simulations," *Program*, 2001. xxi, 37

[104] D. J. Evans and G. P. Morriss, "Nonlinear-response theory for steady planar couette flow," *Physical Review A*, vol. 30, pp. 1528–1530, 9 1984. [Online]. Available: https://link.aps.org/doi/10.1103/PhysRevA.30.1528 xxi, 37

[105] F. Müller-Plathe, "A simple nonequilibrium molecular dynamics method for calculating the thermal conductivity," *The Journal of Chemical Physics*, vol. 106, pp. 6082–6085, 4 1997. xxii, 37

[106] J. P. Ewen, H. A. Spikes, and D. Dini, "Contributions of molecular dynamics simulations to elastohydrodynamic lubrication," *Tribology Letters*, vol. 69, pp. 1–15, 3 2021. [Online]. Available: https://doi.org/10.1007/s11249-021-01399-w xxii, 29, 34, 37, 38

[107] S. Bair, C. McCabe, and P. T. Cummings, "Comparison of nonequilibrium molecular dynamics with experimental measurements in the nonlinear shear-thinning regime," *Physical Review Letters*, vol. 88, pp. 583 021–583 024, 2002. xxii, 37, 38

[108] P. Spijker, G. Anciaux, and J.-F. Molinari, "The effect of loading on surface roughness at the atomistic level," *Computational Mechanics*, vol. 50, pp. 273–283, 9 2012. xxii, 38

[109] S. Foiles, M. Baskes, and M. S. Daw, "Embedded-atom-method functions for the fcc metals cu, ag, au, ni, pd, pt, and their alloys," *Physical review B*, vol. 33, no. 12, p. 7983, 1986. xxii, 38

[110] M. I. Mendelev, S. Han, D. J. Srolovitz, G. J. Ackland, D. Y. Sun, and M. Asta, "Development of new interatomic potentials appropriate for crystalline and liquid iron," *Philosophical Magazine*, vol. 83, pp. 3977–3994, 12 2003. xxii, 38

[111] L. Zhao, L. Liu, and H. Sun, "Semi-ionic model for metal oxides and their interfaces with organic molecules," *The Journal of Physical Chemistry C*, vol. 111, no. 28, pp. 10 610–10 617, 2007. xxii, 38

[112] J. Raisin and J.-D. Wheeler, *CONSTRUCTION D'UN MODELE NUMERIQUE POUR LA SIMULATION THERMO-ELASTOHYDRODYNAMIQUE DE CONTACTS LUBRIFIES 3D (PONCTUEL/ELLIPTIQUE/TORIQUE) OPERANT EN REGIME TRANSITOIRE*, 2015. xxiv, 40

[113] Y. Peiran and W. Shizhu, "A generalized reynolds equation for non-newtonian thermal elastohydrodynamic lubrication," *Journal of Tribology*, vol. 112, pp. 631–636, 10 1990. [Online]. Available: https://asmedigitalcollection.asme.org/tribology/article/112/4/631/435009/A-Generalized-Reynolds-Equation-for-NonNewtonian xxiv, 40

[114] O. Reynolds, *IV. On the theory of lubrication and its application to Mr. Beauchamp tower's experiments, including an experimental determination of the viscosity of olive oil*, 12 1886, vol. 177. [Online]. Available: https://royalsocietypublishing.org/doi/10.1098/rstl.1886.0005 xxiv, 5, 41

[115] R. Xu, L. Martinie, P. Vergne, L. Joly, and N. Fillot, "An approach for quantitative ehd friction prediction based on rheological experiments and molecular dynamics simulations," *Tribology Letters*, vol. 71, p. 69, 6 2023. [Online]. Available: https://link.springer.com/10.1007/s11249-023-01740-5 xxvii, 47

[116] S. Bair, "Reference liquids for quantitative elastohydrodynamics: Selection and rheological characterization," *Tribology Letters*, vol. 22, pp. 197–206, 5 2006. xxviii, xxix, xxx, xxxii, xxxvi, xxxviii, xl, 30, 31, 33, 50, 59, 60, 62, 63, 64, 65, 81, 82, 88, 107, 108, 111

[117] K. Chang, "The nature of glass remains anything but clear," Jul 2008. [Online]. Available: https://www.nytimes.com/2008/07/29/science/29glass.html xxx, 62

[118] L. Berthier and G. Biroli, "Theoretical perspective on the glass transition and amorphous materials," 11 2010. [Online]. Available: http://arxiv.org/abs/1011.2578http://dx.doi.org/10.1103/RevModPhys.83.587 xxx, 62

[119] V. Jadhao and M. O. Robbins, "Probing large viscosities in glass-formers with nonequilibrium simulations," *Proceedings of the National Academy of Sciences of the United States of America*, vol. 114, pp. 7952–7957, 7 2017. xxxiii, 34, 38, 74

[120] C. Mary, D. Philippon, L. Lafarge, D. Laurent, F. Rondelez, S. Bair, and P. Vergne, "New insight into the relationship between molecular effects and the rheological behavior of polymer-thickened lubricants under high pressure," *Tribology Letters*, vol. 52, pp. 357–369, 2013. xxxvi, 81

[121] N. BOUSCHARAIN, private communication, 1 2023. xxxvii, xxxviii, 81, 82, 83

[122] P. Jost, "Jost report," https://api.parliament.uk/historic-hansard/written-answers/1966/aug/11/jost-report, 1960. 5

[123] I. Hutchings, "Fifty years of tribology," http://www.eng.cam.ac.uk/news/fifty-years-tribology, 2016. 5

[124] J. Gao, W. D. Luedtke, D. Gourdon, M. Ruths, J. N. Israelachvili, and U. Landman, "Frictional forces and amontons' law: From the molecular to the macroscopic scale," *Journal of Physical Chemistry B*, vol. 108, pp. 3410–3425, 2004. 5

[125] E. Popova and V. L. Popov, "The research works of coulomb and amontons and generalized laws of friction," *Friction*, vol. 3, pp. 183–190, 2015. 5

[126] "A history of lubricants." [Online]. Available: https://link.springer.com/content/pdf/10.1557/S0883769400055895.pdf 5

[127] "The ultimate historical timeline of mechanical lubrication." [Online]. Available: https://mil-comm.com/lubricants/the-ultimate-historical-timeline-of-mechanical-lubrication/ 5

[128] D. Dowson, *History of tribology*. Addison-Wesley Longman Limited, 1978. 5

[129] K. J. Anderson, "A history of lubricants," *MRS Bulletin*, vol. 16, no. 10, p. 69–69, 1991. 5

[130] H. Hertz, *On the Contact of Rigid Elastic Solids and on Hardness*. MacMillan, 1882. 5, 7, 45

[131] R. STRIBECK, "Die wesentlichen eigenschaften der gleit and rollenlager, vdi zitschrift, vol. 46," 1902. 6

[132] B. J. Hamrock, S. R. Schmid, and B. O. Jacobson, "Fundamentals of fluid film lubrication," *Fundamentals of Fluid Film Lubrication*, 2004. 7

[133] W. Habchi, S. Bair, F. Qureshi, and M. Covitch, "A film thickness correction formula for double-newtonian shear-thinning in rolling EHL circular contacts," *Tribology Letters*, vol. 50, pp. 59–66, 2013. 7

[134] J. D. Wheeler, P. Vergne, N. Fillot, and D. Philippon, "On the relevance of analytical film thickness ehd equations for isothermal point contacts: Qualitative or quantitative predictions?" *Friction*, vol. 4, pp. 369–379, 12 2016. 7

[135] F. W. Smith, "The effect of temperature in concentrated contact lubrication," *ASLE Transactions*, vol. 5, pp. 142–148, 1962. 8

[136] C. Roelands, "Correlational aspects of the viscosity-temperature pressure relationship of lubricating oils," Ph.D. dissertation, 1966. [Online]. Available: https://asmedigitalcollection.asme.org/tribology/article/93/1/209/419010/Correlational-Aspects-of-the-Viscosity-Temperature 8

[137] M. L. Williams, R. F. Landel, and J. D. Ferry, "The temperature dependence of relaxation mechanisms in amorphous polymers and other glass-forming liquids," *Journal of the American Chemical Society*, vol. 77, pp. 3701–3707, 7 1955. [Online]. Available: https://pubs.acs.org/doi/abs/10.1021/ja01619a008 8, 32

[138] N. F. Bader, "Traction in EHL-contacts: the influence of local fluid rheology and temperatures," Ph.D. dissertation, Hannover: Institutionelles Repositorium der Leibniz Universität Hannover, 2018. 9

[139] S. Bair and W. O. Winer, "Experimental investigation of the shear strength of lubricants subjected to high pressure and temperature," *Journal of Tribology*, vol. 112, p. 744, 1990. 9, 20

[140] A. W. Crook, "Elastohydrodynamic lubrication of rollers," *Nature*, vol. 190, pp. 1182–1183, 1961. 9

[141] S. Bair and R. Casalini, "A scaling parameter and function for the accurate correlation of viscosity with temperature and pressure across eight orders of magnitude of viscosity," *Journal of Tribology*, vol. 130, pp. 1–7, 10 2008. 9

[142] W. Habchi, "A full-system finite element approach to elastohydrodynamic lubrication problems : Application to ultra-low-viscosity fluids," Ph.D. dissertation, INSA de Lyon, 2008. [Online]. Available: http://theses.insa-lyon.fr/publication/2008ISAL0038/these.pdf 10, 43, 47

[143] P. L. Wong, X. M. Li, and F. Guo, "Evidence of lubricant slip on steel surface in EHL contact," *Tribology International*, vol. 61, pp. 116–119, 2013. 11

[144] J. Richmond, O. Nilsson, and O. Sandberg, "Thermal properties of some lubricants under high pressure," *Journal of Applied Physics*, vol. 56, pp. 2065–2067, 1984. 11

[145] Y. Zhang and K. T. Ramesh, "On the compressibility of a glass-forming lubricant: Experiments and molecular modeling," *Journal of the Mechanics and Physics of Solids*, vol. 46, pp. 1699–1722, 1998. 11

[146] K. Hentschel, "The influence of molecular structure on the frictional behaviour of lubricating fluids," *Journal of Synthetic Lubrication*, vol. 2, pp. 143–165, 1985. 14

[147] M. Muraki, "Molecular structure of synthetic hydrocarbon oils and their rheological properties governing traction characteristics," *Tribology International*, vol. 20, pp. 347–354, 1987. 15

[148] T. Tsubouchi, H. Hata, and Y. Yoshida, "Optimisation of molecular structure for traction fluids," *Lubrication Science*, vol. 16, pp. 393–403, 2004. 15

[149] M. D. Ediger, C. A. Angell, and S. R. Nagel, "Supercooled liquids and glasses," *Journal of Physical Chemistry*, vol. 100, pp. 13 200–13 212, 1996. 16, 32

[150] B. Jacobson, "A high pressure-short time shear strength analyzer for lubricants," *Journal of Tribology*, vol. 107, pp. 220–223, 1985. 19

[151] L. Houpert, L. Flamand, and D. Berths, "Rheological and thermal effects in lubricated e.h.d. contacts," *Journal of Tribology*, vol. 103, pp. 526–532, 1981. 20

[152] H. S. S. Hsiao and B. J. Hamrock, "A complete solution for thermal-elastohydrodynamic lubrication of line contacts using circular non-newtonian fluid model," *Journal of Tribology*, vol. 114, pp. 540–551, 1992. 20

[153] S. Bair, "The high pressure rheology of some simple model hydrocarbons," *Proceedings of the Institution of Mechanical Engineers, Part J: Journal of Engineering Tribology*, vol. 216, pp. 139–149, 3 2002. [Online]. Available: http://journals.sagepub.com/doi/10.1243/1350650021543960 24

[154] A. Paknejad, R. Mohammadkhani, and H. Zarei, "Experimental high-temperature, high-pressure density measurement and perturbed-chain statistical associating fluid theory modeling of dimethyl sulfoxide, isoamyl acetate, and benzyl alcohol," *Journal of Chemical and Engineering Data*, vol. 64, pp. 5174–5184, 2019. 24

[155] H. Eyring, T. Ree, and N. Hirai, "The viscosity of high polymers—the random walk of a group of connected segments," *Proceedings of the National Academy of Sciences*, vol. 44, no. 12, p. 1213–1217, 1958. 28

[156] M. J. Comuñas, X. Paredes, F. M. Gaciño, J. Fernández, J. P. Bazile, C. Boned, J. L. Daridon, G. Galliero, J. Pauly, and K. R. Harris, "Viscosity measurements for squalane at high pressures to 350 mpa from t = (293.15 to 363.15) k," *Journal of Chemical Thermodynamics*, vol. 69, pp. 201–208, 2014. [Online]. Available: http://dx.doi.org/10.1016/j.jct.2013.10.001 30

[157] S. Bair and F. Qureshi, "Accurate measurements of pressure-viscosity behavior in lubricants," *Tribology Transactions*, vol. 45, pp. 390–396, 1 2002. 31

[158] I. R. Walker, "Nonmagnetic piston–cylinder pressure cell for use at 35 kbar and above," *Review of Scientific Instruments*, vol. 70, pp. 3402–3412, 8 1999. 31

[159] S. Yasutomi, S. Bair, and W. O. Winer, "Application of a free volume model to lubricant rheology. 1 - dependence of viscosity on temperature and pressure." *Journal of Tribology, Transactions of the ASME*, vol. 106, pp. 291–303, 1984. 32

[160] A. K. Doolittle, "Studies in newtonian flow. ii. the dependence of the viscosity of liquids on free-space," *Journal of Applied Physics*, vol. 22, pp. 1471–1475, 1951. 32

[161] C. M. Roland, "Characteristic relaxation times and their invariance to thermodynamic conditions," *Soft Matter*, vol. 4, pp. 2316–2322, 2008. 32

[162] P. G. Debenedetti and F. H. Stillinger, "Supercooled liquids and the glass transition," *Nature*, vol. 410, no. 6825, p. 259–267, 2001. 32

[163] S. Bair and P. Kottke, "Pressure-viscosity relationships for elastohydrodynamics," *Tribology Transactions*, vol. 46, pp. 289–295, 2003. 32

[164] F. D. Murnaghan, "The compressibility of media under extreme pressures," *Proceedings of the National Academy of Sciences*, vol. 30, pp. 244–247, 9 1944. [Online]. Available: https://pnas.org/doi/full/10.1073/pnas.30.9.244 33

[165] R. Casalini and C. M. Roland, "Thermodynamical scaling of the glass transition dynamics," *Physical Review E*, vol. 69, p. 062501, 6 2004. [Online]. Available: https://link.aps.org/doi/10.1103/PhysRevE.69.062501 33

[166] S. K. Mylona, M. J. Assael, M. J. Comuñas, X. Paredes, F. M. Gaciño, J. Fernández, J. P. Bazile, C. Boned, J. L. Daridon, G. Galliero, J. Pauly, and K. R. Harris, "Reference correlations for the density and viscosity of squalane from 273 to 473 k at pressures to 200 mpa," *Journal of Physical and Chemical Reference Data*, vol. 43, 3 2014. 33, 63, 64

[167] S. Bair, private communication, 7 2016. 33, 63, 64

[168] D. M. Heyes, E. R. Smith, D. Dini, H. A. Spikes, and T. A. Zaki, "Pressure dependence of confined liquid behavior subjected to boundary-driven shear," *Journal of Chemical Physics*, vol. 136, 2012. 34

[169] S. Maćkowiak, D. M. Heyes, D. Dini, and A. C. Brańka, "Non-equilibrium phase behavior and friction of confined molecular films under shear: A non-equilibrium molecular dynamics study," *Journal of Chemical Physics*, vol. 145, 2016. [Online]. Available: http://dx.doi.org/10.1063/1.4965829 34

[170] D. Savio, N. Fillot, and P. Vergne, "A molecular dynamics study of the transition from ultra-thin film lubrication toward local film breakdown," *Tribology Letters*, vol. 50, no. 2, pp. 207–220, 2013. 34

[171] J. P. Ewen, S. E. Restrepo, N. Morgan, and D. Dini, "Nonequilibrium molecular dynamics simulations of stearic acid adsorbed on iron surfaces with nanoscale roughness," *Tribology International*, vol. 107, pp. 264–273, 3 2017. 34, 38

[172] A. I. Jewett, D. Stelter, J. Lambert, S. M. Saladi, O. M. Roscioni, M. Ricci, L. Autin, M. Maritan, S. M. Bashusqeh, T. Keyes, R. T. Dame, J.-E. Shea, G. J. Jensen, and D. S. Goodsell, "Moltemplate: A tool for coarse-grained modeling of complex biological matter and soft condensed matter physics," *Journal of Molecular Biology*, vol. 433, p. 166841, 5 2021. 34, 38

[173] A. H. Larsen, J. J. Mortensen, J. Blomqvist, I. E. Castelli, R. Christensen, M. Dułak, J. Friis, M. N. Groves, B. Hammer, C. Hargus, E. D. Hermes, P. C. Jennings, P. B. Jensen, J. Kermode, J. R. Kitchin, E. L. Kolsbjerg, J. Kubal, K. Kaasbjerg, S. Lysgaard, J. B. Maronsson, T. Maxson, T. Olsen, L. Pastewka, A. Peterson, C. Rostgaard, J. SchiØtz, O. Schütt, M. Strange, K. S. Thygesen, T. Vegge, L. Vilhelmsen, M. Walter, Z. Zeng, and K. W. Jacobsen, "The atomic simulation environment - a python library for working with atoms," *Journal of Physics Condensed Matter*, vol. 29, 6 2017. 34, 38

[174] P. Atkins, P. W. Atkins, and J. de Paula, *Atkins' physical chemistry*. Oxford university press, 2014. 36

[175] F. Rizk, S. Gelin, A. L. Biance, and L. Joly, "Microscopic origins of the viscosity of a lennard-jones liquid," *Physical Review Letters*, vol. 129, 8 2022. 36, 59, 61

[176] I. S. Gutzow, *Glasses And Glass Transition*, 2011. 36

[177] M. Cappelezzo, C. A. Capellari, S. H. Pezzin, and L. A. F. Coelho, "Stokes-Einstein relation for pure simple fluids," *The Journal of Chemical Physics*, vol. 126, no. 22, p. 224516, 6 2007. [Online]. Available: http://dx.doi.org/10.1063/1.2738063 36

[178] N. Ohtori, H. Uchiyama, and Y. Ishii, "The Stokes-Einstein relation for simple fluids: From hard-sphere to Lennard-Jones via WCA potentials," *The Journal of Chemical Physics*, vol. 149, no. 21, p. 214501, 12 2018. [Online]. Available: http://dx.doi.org/10.1063/1.5054577 36

[179] L. B. Weiss, V. Dahirel, V. Marry, and M. Jardat, "Computation of the hydrodynamic radius of charged nanoparticles from nonequilibrium molecular dynamics," *Journal of Physical Chemistry B*, vol. 122, pp. 5940–5950, 2018. 36

[180] N. Voeltzel, "Molecular simulation of an ionic liquid as lubricant : From bulk rheology to nanoconfinement," Ph.D. dissertation, 2016. [Online]. Available: http://lamcos.insa-lyon.fr/files/theses/1195-thesepdf.pdf 37

[181] W. T. Ashurst and W. G. Hoover, "Dense-fluid shear viscosity via nonequilibrium molecular dynamics," *Phys. Rev. A*, vol. 11, pp. 658–678, Feb 1975. [Online]. Available: https://link.aps.org/doi/10.1103/PhysRevA.11.658 38

[182] P. Liu, J. Lu, H. Yu, N. Ren, F. E. Lockwood, and Q. J. Wang, "Lubricant shear thinning behavior correlated with variation of radius of gyration via molecular dynamics simulations," *Journal of Chemical Physics*, vol. 147, 2017. 38

[183] B. J. Hamrock and D. Dowson, "Isothermal elastohydrodynamic lubrication of point contacts part i-theoretical formulation," 1976. [Online]. Available: http://www.asme.org/about-asme/terms-of-use 43

[184] M. Mondello and G. S. Grest, "Molecular dynamics of linear and branched alkanes," *The Journal of Chemical Physics*, vol. 103, pp. 7156–7165, 1995. 54, 55

[185] M. Mondello, G. S. Grest, A. R. Garcia, and B. G. Silbernagel, "Molecular dynamics of linear and branched alkanes: Simulations and nuclear magnetic resonance results," *Journal of Chemical Physics*, vol. 105, pp. 5208–5215, 1996. 54, 55

[186] W. M. Haynes, D. R. Lide, and T. J. Bruno, *CRC handbook of chemistry and physics*. CRC press, 2016. 56

[187] T. D. Langridge, M. J. Tarver, and S. T. Whitten, "Temperature effects on the hydrodynamic radius of the intrinsically disordered n-terminal region of the p53 protein," *Proteins: Structure, Function, and Bioinformatics*, vol. 82, no. 4, p. 668–678, 2013. 59

[188] M. Iwahashi, Y. Yamaguchi, Y. Ogura, and M. Suzuki, "Dynamical structured of normal alkanes, alcohols, and fatty acids in the liquid state as determined by viscosity, self-diffusion coefficient, infrared spectra, and 13c nmr spin-lattice relaxation time measurements," *Bulletin of the Chemical Society of Japan*, vol. 63, pp. 2154–2158, 1990. 61

[189] J. Zhang and H. Spikes, "Measurement of ehd friction at very high contact pressures," *Tribology Letters*, vol. 68, 3 2020. 76

[190] R. Khare, J. de Pablo, and A. Yethiraj, "Molecular simulation and continuum mechanics study of simple fluids in non-isothermal planar couette flows," *The Journal of Chemical Physics*, vol. 107, pp. 2589–2596, 8 1997. 76

[191] R. J. Hyndman and G. Athanasopoulos, *Forecasting: Principles and practice*. OTexts, 2021. 83

[192] T. Reddyhoff, A. Schmidt, and H. Spikes, "Thermal conductivity and flash temperature," *Tribology Letters*, vol. 67, pp. 1–9, 2019. [Online]. Available: http://dx.doi.org/10.1007/s11249-018-1133-8 87, 112

[193] L. d. S. Oliveira and P. A. Greaney, "Method to manage integration error in the green-kubo method," *Phys. Rev. E*, vol. 95, p. 023308, Feb 2017. [Online]. Available: https://link.aps.org/doi/10.1103/PhysRevE.95.023308 108

[194] T. Petrosky, "Transport theory and collective modes ii: Long-time tail and green± kubo formalism," *Foundations of Physics*, vol. 29, 1999. 108

FOLIO ADMINISTRATIF

THÈSE DE L'INSA LYON

**NOM** : XU **Date de soutenance** : 10 Nov 2023

**Prénom** : Ruibin

**Titre** : A Quantitative Approach to EHD Friction Prediction Based on Rheometry and Molecular Dynamics Simulations

**Nature** : Doctorat **Numéro d'ordre** : 2023ISAL0086

**École doctorale** : Mécanique, Énergétique, Génie Civil et Acoustique (MEGA)

**Spécialité** : Génie Mécanique

**Résumé** : Cette thèse présente une approche quantitative de la prédiction du frottement élastohydrodynamique (EHD), en employant une combinaison de rhéométrie et de simulations de dynamique moléculaire (MD). L'approche est établie en utilisant deux fluides de natures différentes : le lubrifiant squalane (SQ) et le benzoate de benzyle de type traction (BB). La viscosité Newtonienne des fluides est déterminée à l'aide de mesures provenant de viscosimètres à haute pression (VHP) trouvés dans la littérature, et un nouveau modèle de viscosité Newtonienne créé basé du modèle existant dans la littérature. Un modèle de contrainte d'Eyring, couvrant une large gamme de températures et de pressions, est construit à l'aide de simulations de dynamique moléculaire hors équilibre (NEMD). Les viscosité Newtonienne et les contraintes d'Eyring obtenus sont utilisés pour construire les modèles de viscosité généralisée de type Eyring pour les deux fluides. Les modèles de viscosité développés sont implémentés dans un modèle de contact de thermo-élastohydrodynamique lubrification non-Newtonien (TEHLnN) avec method des éléments finis (MEF) pour prédire le frottement, et les résultats sont comparés avec frottement mesurés dans les tribomètres sous les mêmes conditions de contact. Notamment, le plateau de frottement et le régime d'amincissement thermique observés expérimentalement sont reproduits avec précision par le modèle TEHLnN. Des recherches supplémentaires ont été menées pour révéler la génération de plateaux de frottement, les résultats suggèrent que les plateaux de frottement sont générés à la suite d'une combinaison d'effets non-Newtoniens et thermiques. Les travaux révèlent également l'influence des effets thermiques, contrairement à la compréhension traditionnelle, il apparaît presque simultanément avec l'effet non-Newtonien. Ce travail représente une étape cruciale vers la prédiction "véritable" du frottement et de quantitatif EHL, en rassemblant la rhéométrie expérimentale, les simulations de dynamique moléculaire et la modélisation du contact.
**Mots clés** : Frottement EHD, Plateau de frottement, Modèle Eyring, Simulations dynamique moléculaire (DM)

**Laboratoire de recherche** : Laboratoire de Mécanique des Contacts et des Structures (LaMCoS)

**Directeur de thèse** : Nicolas FILLOT, Laetitia MARTINIE

**Président de jury** : Ashlie MARTINI

**Composition du jury** : Ashlie MARTINI, Gerhard POLL, Norbert BADER, Noël BRUNETIERE